UNIVERSIDADE DE SÃO PAULO
INSTITUTO DE FÍSICA DE SÃO CARLOS

Altamir Gomes Bispo Junior

Leveraging improved approaches for the investigation of patterns and randomness in digital chaos

São Carlos

2024

Altamir Gomes Bispo Junior

Leveraging improved approaches for the investigation of patterns and randomness in digital chaos

Thesis presented to the Graduate Program in Physics at the Instituto de Física de São Carlos da Universidade de São Paulo, to obtain the degree of Doctor in Science.

Concentration area: Computational Physics

Advisor: Prof. Dr. Odemir Martinez Bruno

Corrected version

(Original version available on the Program Unit)

São Carlos

2024

Bispo Junior, Altamir Gomes
Leveraging improved approaches for the investigation of patterns and randomness in digital chaos / Altamir Gomes Bispo Junior; advisor Odemir Martinez Bruno – corrected version -- São Carlos 2024.
290 p.

Thesis (Doctorate – Graduate Program in Computational Physics) -- Instituto de Física de São Carlos, Universidade de São Paulo – Brasil , 2024.

1. Dynamical systems. 2. Chaos. 3. Pattern recognition. I. Bruno, Odemir Martinez, advisor. II. Title.

Este trabalho é dedicado aos meus familiares, amigos, colegas e à Deus.

ACKNOWLEDGEMENTS

Obrigado a todos aqueles, que de alguma maneira, fizeram e fazem parte da minha vida. Aos professores, colegas, ao meu orientador Professor Doutor Odemir, ao Scientific Computing Group e ao meu irmão Alexandre de toda caminhada. Ao Luciano Mitidieri, Humberto Moraes e Gabriel Lucidio. Ao Ministério Universidades Renovadas. Meus agradecimentos às agências de fomento CNPq, FAPESP e CAPES pelo auxílio financeiro e material.

"A boa educação é moeda de ouro. Em toda a parte tem valor."
Padre José de Anchieta

ABSTRACT

BISPO JUNIOR, A.G. **Patterns and randomness in digital chaos**. 2024. 290 p. Thesis (Doctor in Science) - Instituto de Física de São Carlos, Universidade de São Paulo, São Carlos, 2024.

Dynamical deterministic systems with chaotic properties have been actively studied and new applications are established as the qualities of these systems are tested and proved. The k-logistic map is a variation of the logistic map that presents interesting properties for applications in generating pseudo-random numbers (PRNGs) and encryption. Given that the orbits generated by the k-logistic map present characteristics of high entropy and uniform distribution under statistical tests, question arises on which transformations and projections on the orbit of the k-logistic map are able to reveal patterns that are imperceptible in the original space. And another question also arises about which combinations of computer-based and mathematics-based techniques and methods of the arsenal of mathematics should be included into the toolset. This proposal has applications in the areas of cryptoanalysis, dynamical systems analysis and pattern recognition. The following methods were employed: generation of orbits with the k-logistic map, statistical test suites, local density measurements, topological graphs on objects contained in metric spaces, Dynamic Time Warping, spectral analysis, random matrix theory and machine learning. When projecting an orbit or distributions of orbits in metric spaces, and constructing topological graph distributions from these projections, even simple and conventional statistical tests revealed previously imperceptible patterns that were considered to be mere random noises. The results that were found from this development have relevance in improving test batteries for number sequences and analysis of dynamical systems.

Keywords: Dynamical systems. Chaos. Pattern recognition.

RESUMO

BISPO JUNIOR, A.G. **Alavancando abordagens melhoradas para a investigação de padrões e aleatoriedade no caos digital**. 2024. 290 p. Tese (Doutorado em Ciências) - Instituto de Física de São Carlos, Universidade de São Paulo, São Carlos, 2024.

Sistemas dinâmicos determinísticos com propriedades caóticas vêm sendo estudados ativamente e novas aplicações são estabelecidas à medida em que as qualidades desses sistemas são postas à prova e aclamadas. O k-mapa logístico é uma variação do mapa logístico que apresenta propriedades interessantes para aplicações em geração de números pseudoaleatórios (PRNGs) e criptografia. Dado que as órbitas geradas pelo k-mapa logístico apresentam características de alta entropia e distribuição uniforme sob testes estatísticos, surge a questão sobre quais transformações e projeções sobre a órbita do k-mapa logístico são capazes de revelar padrões que são imperceptíveis no espaço de origem. E também surge a questão sobre quais combinações de técnicas e métodos do arsenal da matemática e da computação devem ser incluídos no ferramental. A presente proposta possui aplicação nas áreas de criptoanálise, análise de sistemas dinâmicos e reconhecimento de padrões. Os seguintes métodos foram empregados: geração de órbitas com o k-mapa logístico, suítes de testes estatísticos, medidas de densidade local, grafos topológicos sobre objetos contidos em espaços métricos, Dynamic Time Warping, análise espectral, teoria de matrizes aleatórias e aprendizado de máquina. Ao se projetar a órbita ou distribuições de órbitas em espaços métricos, e construindo-se distribuições de grafos topológicos a partir dessas projeções, mesmo testes estatísticos simples e convencionais revelaram padrões antes imperceptíveis e considerados como meros ruídos aleatórios. Os resultados encontrados a partir desse desenvolvimento possuem relevância no aperfeiçoamento de baterias de testes para sequências de números e análise de sistemas dinâmicos.

Palavras-chave: Sistemas dinâmicos. Caos. Reconhecimento de padrões.

LIST OF FIGURES

LIST OF TABLES

LIST OF ABBREVIATIONS AND ACRONYMS

CNP	Correlation Network Projection
DTW	Dynamic Time Warping
FPP	First Passage Percolation
IBM	International Business Machines Corporation
KS	Kolmogorov-Sinai
LIS	Longest Increasing Subsequence
LLNA	Life-like Network Automata
LLNA-BP	Life-like Network Automata based on Bit Patterns
LLNA-DTEP	Life-like Network Automata based on Density Time Evolution Patterns
LPP	Last Passage Percolation
MP	Matrix Profile
NIST	National Institute of Standards and Technology of the United States of America
PCA	Principal Component Analysis
PRNG	Pseudorandom Number Generator
QRNG	Quantum Random Number Generator
RADAR	Residual Analysis for Anomaly Detection in Attributed Networks
RNG	Random Number Generator
SRB	Sinai-Ruelle-Bowen
SVM	Support Vector Machine
ulp	unit in the last place
USP	University of São Paulo

LIST OF SYMBOLS

$\dot{x}$	First derivative of x
$\ddot{x}$	Second derivative of x
$\sim$	Value of the variable in its left-hand side is similar to that of the variable in its right-hand side, and vice-versa
$\doteq$	Variable in the left-hand side approaches the limit to the value of the variable in the right-hand side
$\boldsymbol{A}'$	Transpose of matrix $\boldsymbol{A}$
$tr(\boldsymbol{A})$	Trace of the square matrix $\boldsymbol{A}$
$\|\boldsymbol{a}\|_2 = \sqrt{\boldsymbol{a}'\boldsymbol{a}}$	ℓ_2-norm of the vector $\boldsymbol{a}$
$\|\boldsymbol{A}\|_{2,1} = \sum_{i=1}^{n} \sqrt{\sum_{j=1}^{d} \boldsymbol{A}_{i,j}^2}$	$\ell_{2,1}$-norm of the matrix $\boldsymbol{A} \in \mathbb{R}^{n \times d}$
$\|\boldsymbol{A}\|_F = \sqrt{\sum_{i=1}^{n} \sum_{j=1}^{d} \boldsymbol{A}_{i,j}^2}$	Frobenius norm of the matrix $\boldsymbol{A} \in \mathbb{R}^{n \times d}$
M^{σ}	Thermal conjugate to β_{σ}
β_{σ}	Thermal conjugate to M^{σ}
$K(x)$	Entropy for the functional x
$\mathscr{P}(x)$	Topological pressure or free energy for the functional x
Z_N^{top}	Partition function associated with the topological pressure

CONTENTS

1 INTRODUCTION

Chaos theory has a curious history. During centuries, passing through the Middle Ages (centuries V to XV) and the Modern Age (centuries XV to XVIII), scientific exponents such as Kepler and Galileo and their peers studied the predictability of motion in nature and its laws, specialising themselves in the calculation of the orbits of planets and stars. It was later observed that such movements do not occur precisely as expected by the stated laws which, so far, were not proved incorrect (13). The observation of this fact shows us that there are, in nature, variables of difficult quantification and analysis that influence the behavior of natural systems with virtually unpredictable results.

More recently, Edward Lorenz incidentally discovered during his lab experiments at MIT, in the 1960s, that very small changes in non-linear equations' input values can produce results or outputs sporting high discrepancy one another. Until then, it was thought that changes affecting output values were approximately proportional to changes affecting input values. This discovery opened a range of studies related to the behavior of dynamical systems. It was later discovered that the logistic map and its variations model with significant adherence the evolution of systems found in nature. Figure 1 illustrates the Lorenz system, also known as a strange attractor.

Such systems, in their initial stages, are forecasteable. However, past a certain evolution interval of the system, its behavior may become unpredictable. Applications

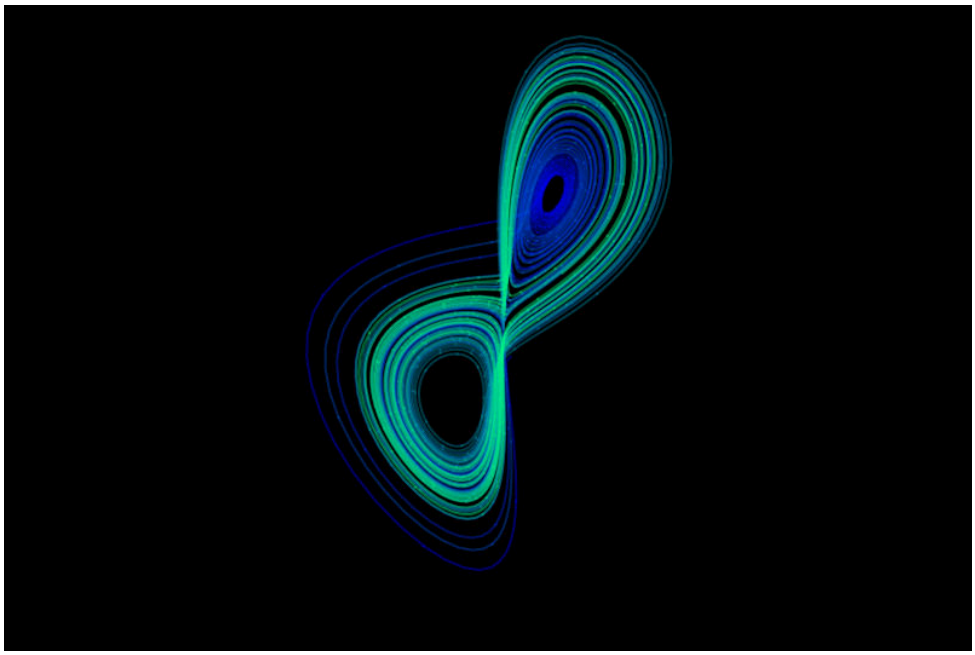

Figure 1 – Lorenz attractor.
Source: By the author.

in computer modeling confer objects of study to researchers: the system's future state, according to their initial conditions. Following the study of those systems, it becomes possible to know under which conditions the system remains stable and under which such stability is lost, conducting the system to chaos (14, 15). There are applications of dynamical systems and chaos being actively researched. An example is the generation of pseudo-random numbers. Another example are techniques and methods of machine learning that have become very powerful. Chaos is a source of studies and experiments that is being paired with techniques and methods of the state of the art in machine learning (16,17). The study of nonlinear systems such as deterministic dynamical systems under chaotic regime is, in considerable part, an exploratory analysis restricted to a given dataset extracted off the system's evolution. Together, it is subjected to numerical and storage precision restrictions. Physics deals with high dimensionality systems, such as those formed by electromagnetic waves, which are nevertheless tractable when unfolded into linear equations, for which there is a capable toolset for the task of pattern extraction, including temporal patterns. Such a toolset is not directly applicable to non-linear systems and it is rarely known non-linear general solutions in closed form, hence the need to develop specific techniques and methods (18), such as heuristics, which work at least reasonably well for scenarios of interest.

Furthermore, the dynamics of natural environments and ecological systems can be understood in more depth with the development of dynamical systems theory and methods (5). A recent study built upon qualitative analysis concluded that chaos is much more common in nature than previously thought (19). More specifically, one of the important applications for the study of interacting animal populations within the ecosystem and also of their movement and proliferation regimes is pest control (20,21). Events of interest may arise at very long timescales and be abrupt (22). Given the inter and multidisciplinary theme of the dynamical systems, that encompasses fields as diverse as Physics, Biology, Chemistry, Mathematics and Computer Science, it is only natural that research and development in any of these impacts other fields.

There is no clear delimitation between random and chaotic sequences. Chaotic sequences may hide patterns and self-similarity that are sometimes not obvious. The logistic map has chaotic configurations that, however, present intricate patterns and the distribution of its orbit does not obey the uniform distribution. Cellular automata (CA) under rule 30 are used as PRNGs (23), despite generating several (discarded) regions with undesirable patterns.

There is a proficuous development for the natural extension of the study of chaotic dynamical systems in their representation via complex networks. A large number of tools have been developed for the study of complex networks. However, deficits in metrics and measurements with objective meaning regarding the statistical parameters extracted

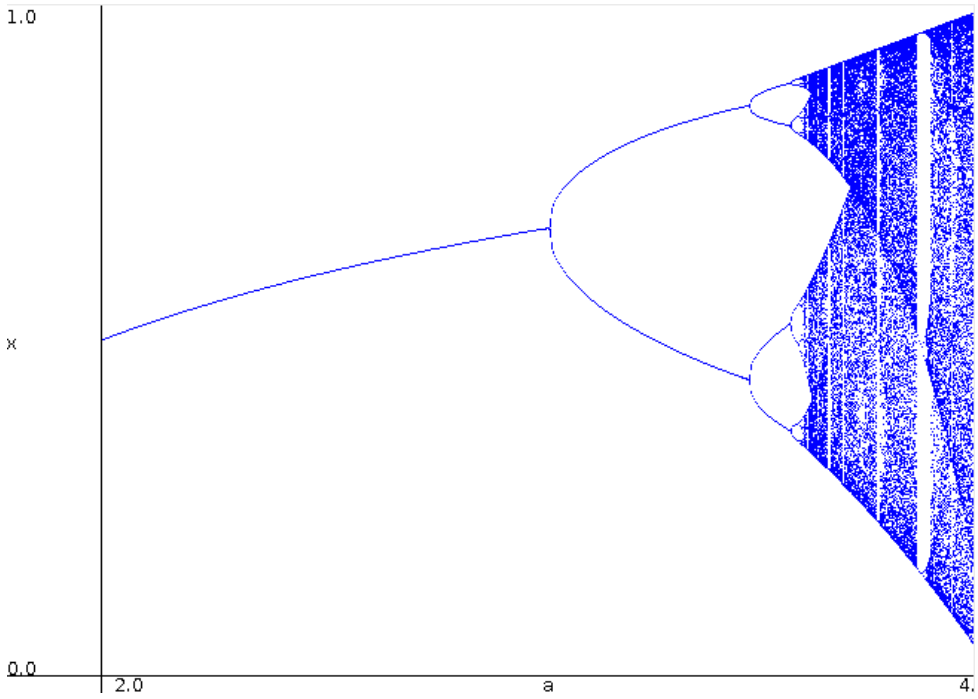

Figure 2 – Bifurcation diagram for the logistic map.
Source: By the author.

under use of a significant portion of such complex network analysis tools hinder the interpretability of results and the comparability between systems (24). At first, we will limit ourselves to design or transform orbits into mathematical objects that are more receptive to simple and traditional statistical methods, progressively passing on to more complex approaches, envisaging their application in cryptography and cryptanalysis.

This work may be summarised as an effort for the advancement of methodologies and techniques for the study of patterns in dynamical systems that can model natural environments and their biological aspects. One of our aims is to elucidate, at first empirically, the conditions under which the patterns, may periodic or chaotic, emerge. Patterns, by their very nature, are predictable. We apply techniques that improve contrast, displaying thus such patterns. As the numerical precision is finite in computers, computer simulations of orbits of dynamical systems are guaranteed to be periodic. Care must be taken with computer simulations as numerical artifacts can lead to misleading results (25) and the shadowing lemma, e.g. chaotic-like perturbed periodic orbits, is guaranteed to apply only to hyperbolic dynamical systems.

The main objectives of this D.Sc. project are, succinctly:

- To analyze dynamical systems, to find patterns and describe constraints related to their surge.

- To shed a clarifying light on chaotic orbits: about their periodicity and statistical

aspects of dynamical systems implemented under the constraints of finite machine precision.

- To improve on the chaotic orbits for the purpose of building improved PRNGs.
- To unravel a capable toolset composed of techniques and methods from Computing, Physics and Mathematics that serves as a means of achieving the desired purpose.

2 DEVELOPMENT

2.1 Literature review

In this section, we highlight historical, scientific and technical facts that are important to our endeavor. This work takes advantage of developments in the following areas of knowledge: dynamical systems, topology, machine learning, statistics, random matrix theory and complex networks. There is a vast bibliography regarding each of these disciplines. The need to couple statistics and statistical tests for small or medium-sized, low-dimensional, samples to dynamical systems comes from explanatory studies on the structure and the laws of evolution for a given dynamical system. The techniques and methods of machine learning that deal with a large number of samples and high-dimensionality, with a potentially higher cost on computing resources, serve better for exploratory studies.

2.1.1 Dynamical systems

Autonomous differential equations of the form

$$\dot{x} = f(x(t))$$

give rise to continuous-time dynamical systems (26). As the regimes in real-life evolve through continuous time, they can be faithfully modelled by nonlinear differential equations like the Lorenz and Lotka-Volterra systems. Lotka-Volterra is particularly a predator-prey system (27) that can be described by the equation

$$\dot{x} = \alpha x - \beta xy$$

$$\dot{y} = \delta xy - \gamma y$$

where

- x is the number of prey;
- y is the number of predators;
- $\dot{x}$ and $\dot{y}$ are the instantaneous growth rates of the populations;
- α, β, γ, δ are positive real parameters describing the interaction between species.

For the context of simulation of phenomena, we can either opt to model their individual interactions or to quantify population density, that is, the ratio of individuals of interest to the area of interest. The latter, for the purposes of ecological modelling, is regarded as the better approach (28). Other choices are the inclusion of a diffusive regime for the species and movement of the species over the space itself. Modelling of movement may account for transport of specimen groups by wind and even by other species. When diffusion-reaction is also taken into consideration, the system can be described by the following general form:

$$\frac{\partial U_i(\boldsymbol{R}, T)}{\partial T} = D_i \nabla^2 U_i(\boldsymbol{R}, T) + f_i(U_1, \ldots, U_n)$$

for i assuming values from 1 to n, U_i as population density, $\boldsymbol{R}$ as the three-dimensional spatial position, D_i as the diffusion coefficient of the ith species and where the Laplace operator, ∇^2, is denoted by

$$\nabla^2 = \frac{\partial^2}{\partial X^2} + \frac{\partial^2}{\partial Y^2} + \frac{\partial^2}{\partial Z^2}$$

Despite differences between discrete and continuous-time systems, simple discrete dynamical systems still retain much of the qualitative behavior and complexity of their high-dimensional continuous-time dynamical systems counterparts, including bifurcations, periodicity and onset of chaos, making them useful for the study of dynamical systems theory.

A conjunction of diverse equations may apply to a single dynamics. Also, some noise and stochasticity that do not make part of the attempted modelling may diverge phenomena from typical asymptotical behaviors that are predicted by these models (29), giving rise to transients. Figure 2.1.1 presents some examples of complex interactions found in nature (5, 30). A number of researchers rely intensively upon computational prowess to investigate dynamics. There is currently a misconception that analytical approaches are limiting and of little practical value. Unbeknownst is that numerical methods are prone to a disadvantage due to the vast array of parameter values to investigate (31) and also due to exposure to numerical artifacts. Analytical forms of dynamics can furnish exact solutions and breadth of knowledge about parameter influence. Dynamics in analytical form also lead to an elegant and comprehensive presentation of the problems themselves and their constraints (25).

Some authors model ecological contexts as mostly or purely stochastic processes. For an example, see Garcia *et al.* (21), but it is known that beings like insects do not always move randomly and their behavior is influenced by food resources, habitats, prey, predators, or competitors (32–35). Along stochasticity, there are also other important companion phenomena like synchronization and resonance in dynamical systems (36–38).

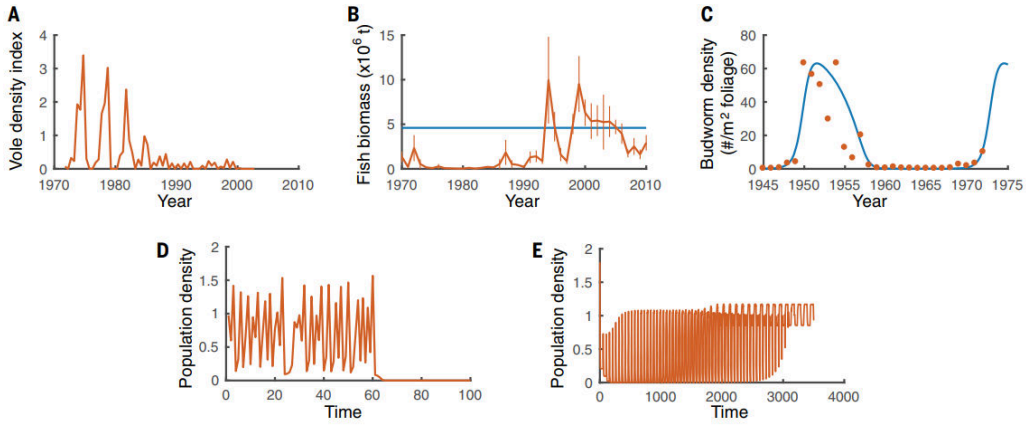

Figure 3 – Some examples of transient dynamics. **(A to C)** Empirical examples of regime shifts after long transients. **(A)** Population abundance of voles in northern Sweden [redrawn from (1)]. **(B)** Biomass of forage fishes in the eastern Scotian Shelf ecosystem; redrawn from (2)]. (C) Spruce budworm [dots; data from Imperial College London] has a fast generation time that results in extended periods of low budworm density interrupted by outbreaks. The blue line with fast budworm dynamics and slow foliage dynamics agrees with the data (3). **(D and E)** Examples of long transients on population dynamics: **(D)** apparently sustainable chaotic oscillation suddenly results in species extinction (2); **(E)** high-energy periodic oscillations that persist over several generations transition to oscillations with a much smaller amplitude and non-stationary regime (4). Source: HASTINGS *et al.* (5).

2.1.1.1 Chaotic orbits

Chaos theory tries to explain unpredictable behaviors of a deterministic dynamical system as it is case of the logistic map after a certain number of iterations. The logistic map, that is studied and debated intensively in the literature (39–45), has the form $x_{n+1} = rx_n(1 - x_n)$. Its input parameters are r and x_0, with the following restrictions: $r \in U = (0, 4)$ and $x_n | n \in \mathbb{N}_0 \in M = (0, 1)$. Another example of dynamical system is the tent map $x_{n+1} = \mu \min(x_n, 1 - x_n)$ (46, 47). Dynamical systems as maps are also discrete. Orbits are collections of points related to the evolution function $f : M \to M$ of a dynamical system. An orbit of a discrete dynamical system can be formalized by:

$$\mathcal{O}(\mu, x_0) = x_0, x_1, \ldots, x_t$$

Two interesting properties of deterministic dynamical systems are causality and determination.

- Causality: a given advanced stage of a deterministic dynamical system is caused by previous systems of the system itself.

- Determination: given intial conditions and an evolution function, the orbit is fixed.

For a certain class of dynamical systems, taken that they progressed significantly in time, another characteristic is that its statistic is invariant, being influenced by the initial state of the system no more (14,48). The logistic map is a an example of such class and an interesting model for study of systems found in nature, such as the biological (40,49). For example, reproduction of microorganisms. But, the logistic map can only be calculated without errors with arbitrarily high numerical precision. Reductions in numerical precision can result in arbitrarily large calculation errors. Those errors are due to a "butterfly effect", in which the error propagation is locally exponential in relation to the evolution of the system, as noted by Lorenz (50). This problem occurs with an orbit type of special interest: chaotic orbits (51,52). The Lyapunov exponent characterizes the separation rate between distinct trajectories. In chaotic orbits, changes that are at first insignificant in the input parameters lead to unrecognizable trajectories and, thus, to high values of the Lyapunov exponent for a given limited interval of the trajectory.

Lyapunov Exponent (vector spaces): given a map Φ, a direction vector e_i and a perturbation δ, if δ travels in the e_i direction, then $\Phi(x+\delta) - \Phi(x)$ also travels in that direction. Like this, under repeated map applications we observe

$$\frac{\|\Phi^n(x+\delta) - \Phi^n(x)\|}{\|\delta\|} = (A_i(x))^n = e^{n \log(A_i(x))}$$

We will use the abbreviation Λ instead of $\log A_i$. The set of d numbers

$$\Lambda_1(x), \Lambda_2(x), \ldots, \Lambda_d(x)$$

represent the local Lyapunov exponents in x. e_i directions where $\Lambda_i > 0$ are locally unstable, directions where $\Lambda_i < 0$ are locally stable and those for which $\Lambda_i = 0$ are neutral. Let $\Lambda_i(x)$ be a function of the coordinates in the space of states. The average calculated through the trajectory will be

$$\frac{1}{T} \sum_{n=1}^{T} \Lambda_i(x_n)$$

If the dynamics are independent of the initial conditions of the system, then the sum will converge to an invariant

$$\lambda_i \equiv \int \Lambda_i(x) \rho(x) dx$$

$\rho(x)$ is the invariant measure. The expected values λ_i are the global Lyapunov exponents.

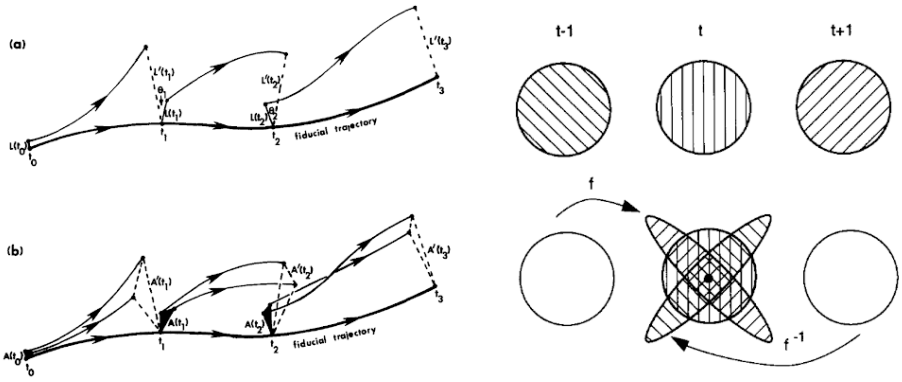

Figure 4 – On the left, fiduciary trajectory on the calculation algorithm for the Lyapunov exponent, on the right, chaos control via framing or "linearization" of attractors.
Source: WOLF *et al.*; FARMER; SIDOROWICH (6, 7).

Several developments related to the Lyapunov exponents led to developments in chaos control and stabilization (53–60) accompanied by the surge of the discipline of cybernetical physics (61). The heart of proposals like Wolf *et al.* and Farmer and Sidorowich (6,7) is to assume that the system behaves (approximately) linearly under certain domains (Figure 4). Farmer and Sidorowich's proposal, in particular, explores computation in varieties for chaos control by exploring attraction or repulsion properties as the system evolves. Techniques as delay-coordinate embedding obeying Takens' theorem for soft attractors preserve topology in the orbits of the dynamical systems after transformations such as diffeomorphisms that change the orbit's measures (48, 62, 63).

Chaoticity in dynamical systems aroused interest of researchers in view of their application in encryption (64–70). Construction of a random number generator is widely known as one of the key parts in developing encryption tools (71).

A limited sequence of values $\{x_i\}^{\infty}$ of a map is chaotic if

- $\{x_i\}$ is not asymptotically periodic.
- No Lyapunov exponent vanish.
- The largest Lyapunov exponent is strictly positive.

Random or stochastic processes are fundamentally different to chaos, understood here as deterministic chaos (46). Even if two initial states for a stochastic process are identical to each other, successive realizations of a stochastic process will result in different sequences with probability $1-\epsilon$, ϵ being the probability for the occurrence of two identical sequences. As a stochastic process is not deterministic, in this case there is no strict definition for computing of the Lyapunov exponent. The Wolf approach applied to a

sequence seeks the nearest neighbor $y_0 = x_k$ of a point x_j and uses it as the initial value of another sequence. The expected value of the separation rate is

$$\ln\left(\frac{\|x_{k+1} - x_{j+1}\|}{\|x_k - x_j\|}\right)$$

and it is used as a measure of the Lyapunov exponent.

Let us consider the case where the x_i are randomly and evenly distributed within a limited range in $\mathbb{R}^+$. If the values x_i are truly random then the denominator of the expected value can be arbitrarily small while the numerator remains large. As new values are drawn, the minimum separation distance tends to zero, while the expected separation distance between any two values remains limited and far from zero. As a result, the Lyapunov exponent will increase without limit as the amount of values tends to infinity. Despite this important difference between chaos and randomness, chaotic maps whose Lyapunov exponent may not tend to infinity, as it is the case with the logistic map, are studied in the construction of pseudorandom number generators.

2.1.2 Sources of randomness

Several sources of randomness can be found in nature. (38,40) They are intimately related to modern physics and thermodynamics. It is known that the state transitions for matter under thermodynamics are largely unpredictable and that the quantum noise behaves like a true random generator (72,73). Quantum noise obeys fundamental principles of quantum mechanics and arises from the indeterminate state of matter, two of those fundamental principles are the uncertainity principle and fluctuations of the lowest possible energy held on a quantum mechanical system. Quantum noise has also the advantage that for an actual well-designed quantum system it is exceedingly difficult to tap into the process of its state transitions (74), which is a desirable property for many applications.

2.1.2.1 Applications of sources of randomness

Sources of randomness are needed wherever unpredictability is desired (75). Accuracy of approximate algorithms may benefit from random initializations or random state transitions. Approximate algorithms such as K-means for clustering, simulated annealing for solution of optimization problems and Monte Carlo for solution of numerical problems are of paramount importance in the fields of the sciences, engineering, financial applications, gaming, gambling and last but not least, cryptography. Life-Like Network Automata (76–78) assigns initially a random value of 0 or 1 to every cell of its domain network.

Dice, shuffling playing cards, and roulette wheels are all examples of applications of mechanical random generators. Interestingly, a small bias can be detected when flipping

coins (79). But even when the random generator is practically perfect, clustering and pathologies like apophenia, which is seen at type I errors in statistical tests, causes great burden to finance, and in our own experience it also affects negatively the analysis of patterns in chaotic dynamics, since the detection of false patterns is undesirable.

2.1.2.2 Pseudorandom number generation

The main issue with true random generation of numerical values is that the whole process would churn out an entirely different set of values each time, thus harming repeatability and replicability of experiments. To circumvent this limitation, pseudorandom number generators (PRNG) were idealized and came to conception (80, 81).

PRNGs are conceived to behave deterministically, contrary to true random generators that behave stochastically (82). Which means every time the PRNG is fed with a certain seed parameter, and given that the inner workings of the machine obey some protocol e.g. the static discipline and guarranted logical operation, it is guarranted that the PRNG will always churn out the exact same set of values for the same input sequence, thus ensuring repeatability and replicability for experiments. On Chapter 3, we conduct experiments using a composition of the LFSR and the logistic map for showing how PRNGs of diverse natures show better results together than each one of them alone.

2.1.2.3 Cryptography

Cryptology, that is, the study of codes or secret systems of words or numbers, has been used through the millennia for the purpose of hiding secret messages. The systematic study of cryptology is more recent but, nonetheless, remarkable and took during the last century. The first known evidence, somewhat in dispute (83), of an application of encryption was found in an inscription circa 1900 BC in Egypt, most exactly in the main chamber of the nobleman Khnumhotep II. It is not clear what the purpose of encryption, even if it was to obfuscate the message in the inscription at all. However, it is worthy of note. "Arthashastra", a classic work on statecraft credited to Kautalya, describes the espionage service in ancient India and some form of "secret writing" given as assignments to spies is mentioned there.

Circa 100 BC, the Roman army under the command of Julius Caesar employed some form of encryption to convey secret messages between high-ranking combatants. Such an example is given in Figure 2.1.2.3.

It is what is now known as a substitution cipher, the Caesar cipher. A cipher is an algorithm used for encryption or decryption. In a substitution cipher, each character of the message which has to be encrypted, which we call the plain text, is substituted by another character to form the encrypted message or cipher text. Each character was shifted by 3 places, so the character 'A' was replaced by 'D', 'B' was replaced by 'E', and so on.

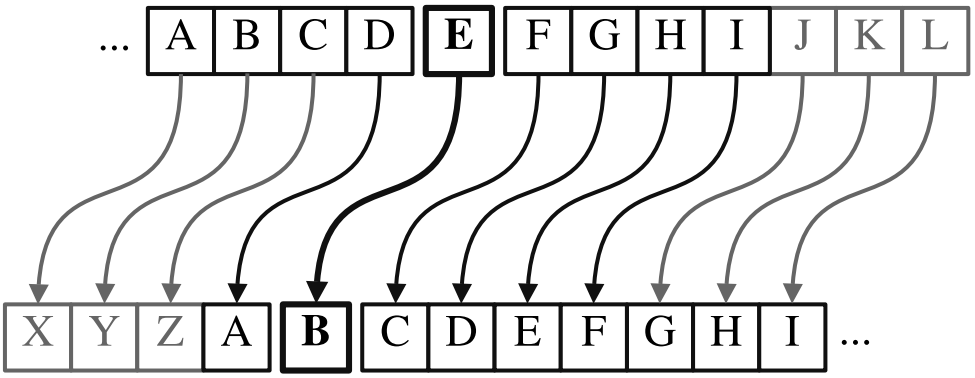

Figure 5 – Symbol-to-symbol mapping for the Caesar cipher.
Source: By the author.

The characters would wrap around at the end, so 'X' would be replaced by 'A'. Later into the 20th century, beginning from World War II, leadership on encryption techniques and reverse engineering would play pivotal role for intelligence regarding battlefield awareness and combat actions.

Diffie and Hellman in 1976 (84) introduced the concept of public-key cryptography, solving the problem of key exchange, and also paved the way for our current digital signatures (85). Every person involved in message exchange has a key constructed by the pair $k = (pk, sk)$, pk being the public encryption key and sk the secret decryption key. in order to send a message m to Bob, Alice encrypts m into a ciphertext by means of Bob's pk. To read the message, Bob decrypts the ciphertext by means of his personal encryption key sk. In a nutshell,

$$D(sk, E(pk, m)) = m$$

Public-key encryption is an one-way function with a trapdoor that presents easeness to its user when encrypting any message using a known public key, but ups the ante when decryption is required, as the decryption key is maintained in secretion. Before public-key cryptography, which is assymetric, meaning different keys are used for encryption and decryption, symmetric methods where a single key is used for the means of both encryption and decryption were in vogue. Cryptography is nowadays used in secure communications employed in everyday's financial transactions, mailing systems and the internet.

Kerckhoffs' principle of cryptography (86) states that a cryptography should remain secure even if anything save the key about the cryptographic system is known. Let parameters x and r of the logistic map as parts of an encryption key. Starting from every value admissible for x_0 up to subsequent values, the orbit with nevertheless always reach to the same attractor. That is due to the own definition of attractor in chaotic orbits. Thus, values of x are irrelevant as much as cryptographic features of state are concerned. Furthermore, while the shadowing lemma on a hyperbolic set guarrantees that a simulated

chaotic orbit remains for all purposes chaotic (87, 88) , on the other side, the simulated orbit is now in practice periodic. r is left as a possible key for chaotic cyphers. We know from the bifurcation diagram that some regions are pathological and should be avoided.

As a safeguard against improper decryption of the ciphertext, if two different keys are close enough to each other, the sensitivity to parameters must guarantee that two orbits starting with slightly different parameters will diverge early enough, and the secret parameter should be sensitive enough to guarantee the so-called avalanche property: under even the smallest parameter change, the ciphertext will change dramatically (66)

Some authors (65,66) do not stress that many chaotic maps are not merely fractal, being in truth multifractal and endowed with a singularity spectrum. In many cases found in nature their non-random patterns are easy to spot, but they can also assume random formations under certain configurations (89) and, as such, they are usable as PRNGs save the set of their loci with poor randomness qualities. For applications of cipher generation in real-time, processing speed is also a concern, as it is not doable to perform calculations in arbitrarily high precisions and maintain sustained high performance. Speaking of symmetric methods for cryptography, they are generally faster than their assymetric counterparts.

2.1.2.4 Logistic and k-logistic maps and their application in cryptography

The interest for the logistic map arose in considerable part due to the scientific endeavor of tackling complex phenomena via simple mathematical descriptions (45, 90) . The logistic map has as one of its predecessors the logistic function

$$f(x) = \frac{L}{1 + e^{-k(x-x_0)}}$$

that is well-known in the field of ecology.

One interesting relationship is the topological conjugacy between the logistic map with parameter $r = 4$ and the tent map

$$x_{n+1} = f_\mu(x_n) = \begin{cases} \mu x_n & \text{for } x_n < \frac{1}{2} \\ \mu(1 - x_n) & \text{for } x_n \geq \frac{1}{2} \end{cases}$$

with parameter $\mu = 2$. A description for topological conjugacy is that a given function f can be mapped into a function g via a homeomorphism, that is, a bijective and continuous function between topological spaces that has a continuous inverse. Figures 6 and 7 present bifurcation diagrams of these maps.

Other relationship of the logistic map is the Feigenbaum constant – ratios for successive bifurcations in a nonlinear map. Something remarkable in this modern realization in the discipline of mathematics is that computer-assisted proofs of the Feigenbaum con-

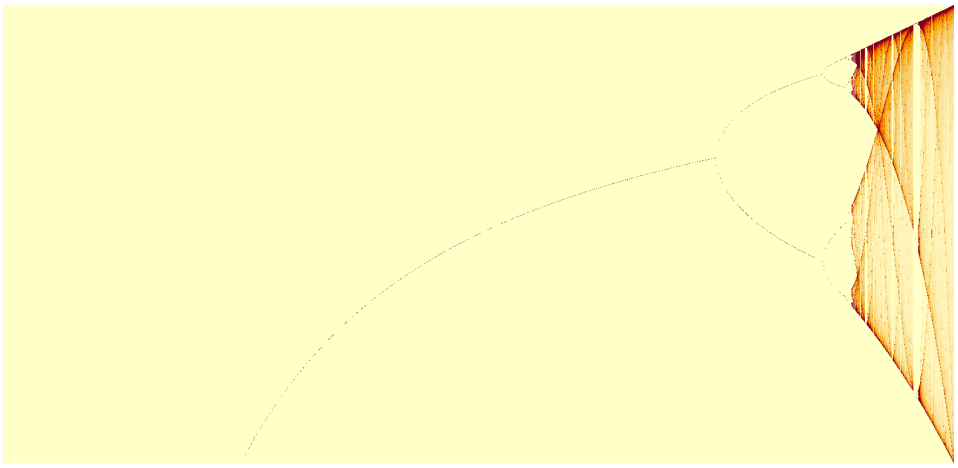

Figure 6 – Bifurcation diagram for the logistic map.
Source: By the author.

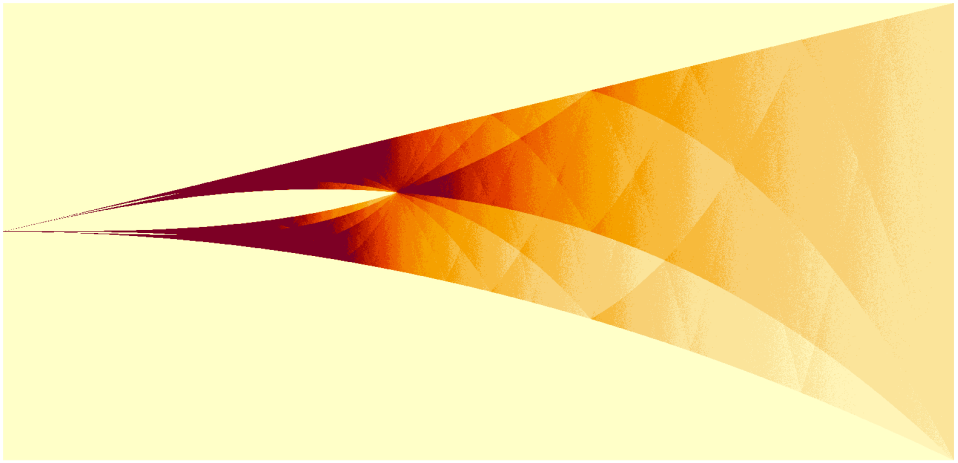

Figure 7 – Bifurcation diagram for the tent map.
Source: By the author.

jectures followed (91), thus marking the era of the supporting role of the digital computer in mathematics research. The logistic map, for its simplicity and ease of implementation and verification, was one of the ingredients that led to the Feigenbaum result.

For pedagogical reasons, it is rather common to find examples of measures of qualitative behavior and chaoticity like the calculation of the Lyapunov exponent and the cobweb plot applied on the logistic map as in Figure 8. Concentrated pathways in blue mean low-period attractors and unconcentrated pathways mean high-period or chaotic attractors.

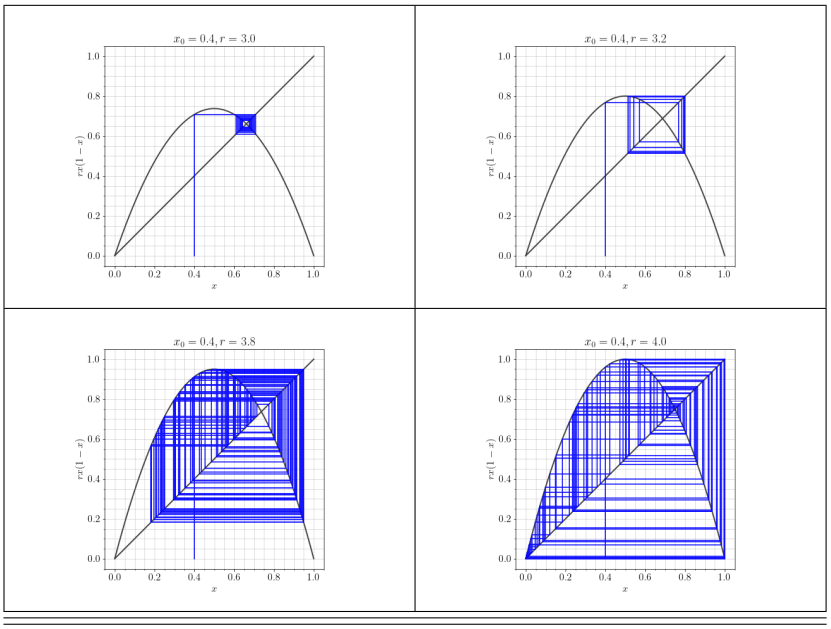

Figure 8 – Cobweb diagrams for the logistic map.
Source: By the author.

Given parameters r and x_0 for some logistic map we observe that changing r even minimally leads to the system's evolution function to become another, unrecognizable with respect to the previous. As r approaches four, the number of possibilities for the map grows exponentially and without bound. We can say, therefore, that chaos is infinite. Then, the usage of r as a control parameter is cogitated. The proposal of the seminal work (64) determines thresholds x_{min} and x_{max} of the logistic map, $x_{min} < x_{max}, x_{min} > 0, x_{max} < 1$, and mapping of the set of n input symbols $S = s_1, s_2, \ldots, s_n$ within interval $[x_{min}, x_{max})$. Therefore, each symbol s_y is represented by the range

$$\left[(y-1)\frac{x_{max}-x_{min}}{|S|} + x_{min}, y\frac{x_{max}-x_{min}}{|S|} + x_{min}\right), y \in I_s = \{1, 2, \ldots, n\}$$

of the logistic map. The value for i in the i-th iteration of the logistic map with symbolic value s_y is registered in the cipher. In this step the value for i reverts to zero and a new count is done. Still, the map is iterated at least N_0 times before the next numeric value under s_y gets registered. There are objections about the proposal mentioned here. It is questioned that, without additional care for cryptography security, the proposed method is not strong and neither recommendable for production cryptographic systems (65, 66, 92).

Pseudorandom numbers are ideally generated under a perfectly uniform distribution. The uniform distribution has invariant density measure equal to

$$\frac{1}{b-a}$$

(conservative) mean equal to

$$\frac{a+b}{2}$$

and standard deviation equal to

$$\frac{b-a}{\sqrt{12}}$$

The logistic map, however, presents invariant density measure equal to

$$\frac{1}{\pi\sqrt{x(1-x)}}$$

whose distribution is not uniform, being this one of the factors that prevent its use in encryption.

One of the proposed solutions to improve the distribution characteristics for the orbit of the logistic map in terms of numerical implementation is Deep Zoom (8, 69, 70). Deep Zoom is an elegant computational solution consisting of the calculation of a dynamical system, for example, the logistic map, with the following changes. The k to the left of the separator in numerical representation in decimal base are removed. The Figure 9 illustrates, base-2 instead of base-10, how certain digits present better randomness characteristics than others. The vertical bar indicates the tests of NIST SP 800-22 Rev. 1a successful for each bit position in 48-bit and 104-bit words.

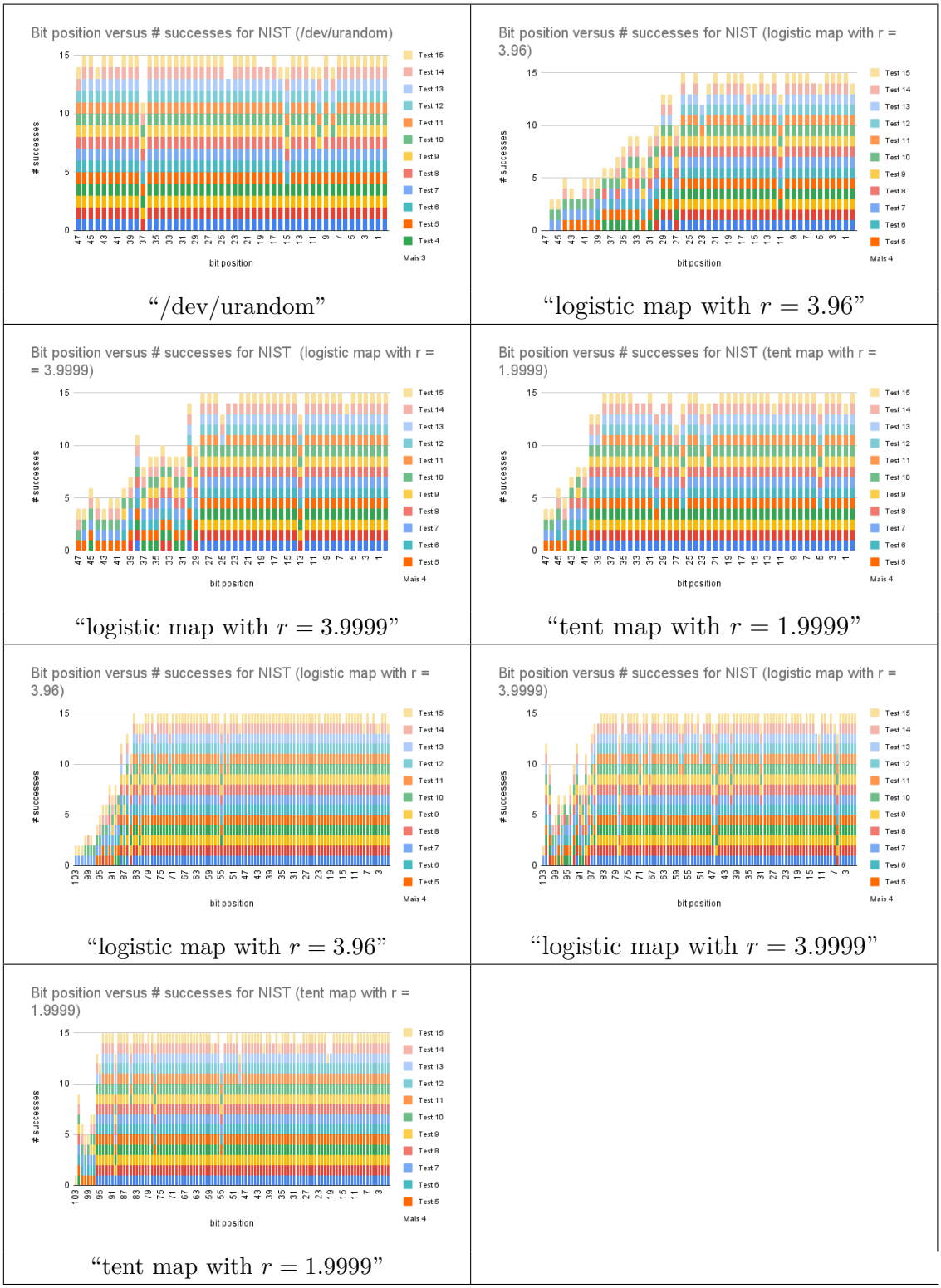

Figure 9 – NIST SP 800-22 Rev. 1a. -based tests, bit position vs. # successes. Source: By the author.

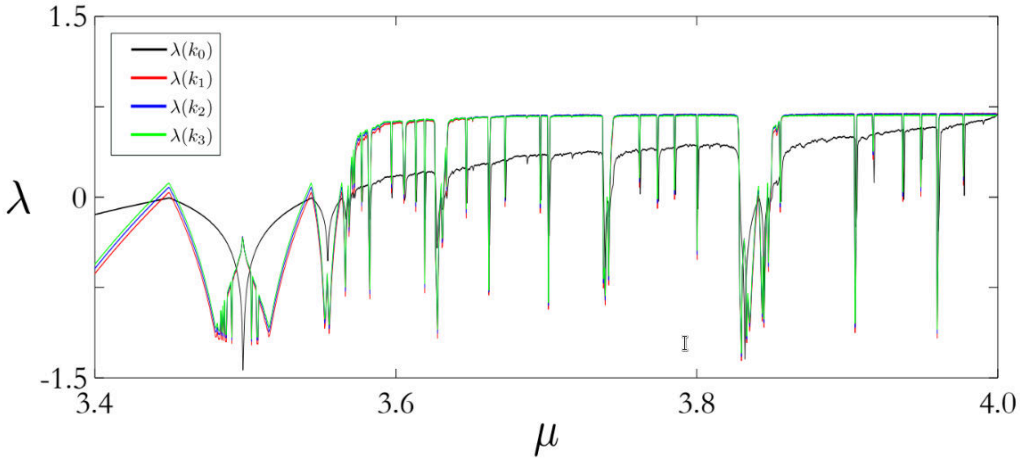

Figure 10 – Stability of the Lyapunov exponent for the k-logistic map.
Source: MACHICAO; BRUNO (8).

A precision of L digits is kept after the separator. The new map with transformed orbit is defined as the k-logistic map, and formally defined by the following equation:

$$x_t^{k+L} = \frac{\lfloor x_t 10^{k+L} \rfloor}{10^L} - \lfloor x_t 10^k \rfloor$$

Experiments demonstrate reinforcement of pseudorandom characteristics of a dynamical system via Deep Zoom (69, 70). It is a robust state-of-the-art method for applications of chaos theory wherever pseudorandomness is desired. However, it does not improve on the short periodicity of the orbits of the original logistic map.

Figure 10 shows the values of the Lyapunov exponent λ for different values μ and 4 distinct values for k with the k-logistic map. Values of $\lambda \geqslant 0$ indicate chaotic orbits, $\lambda \approx 0$ indicates chaotic orbits and $\lambda \leqslant 0$ indicates stable orbits. Figure 11 shows a bifurcation diagram for 4 distinct values for k. The diagram for k_2 and k_3 shows that the distribution for the values of the k-logistic map is approximately uniform.

2.1.3 Patterns

While the intuitive notion of patterns is not hard to grasp, as they are for the human eye distinctive and intricate in a particular way at a glance, how do we define and/or measure patterns? Tiffany Winn and Paul Calder say (93) "In the current climate, pattern is an often misused buzzword. However, there is no clear definition of patternness, perhaps because patterns do not lend themselves to prescriptive, formal definitions." Although we do not yet have a clear and robust formal definition as for what is a pattern, we are bound to recognize immediately that patterns are, by definition, bound to repeat themselves over and over upon a given object of interest, and the object in question might be a physical system or a mathematical structure. For that reason, and for the purposes of this investigation, we act our studies upon relatively small samples of orbits of a dy-

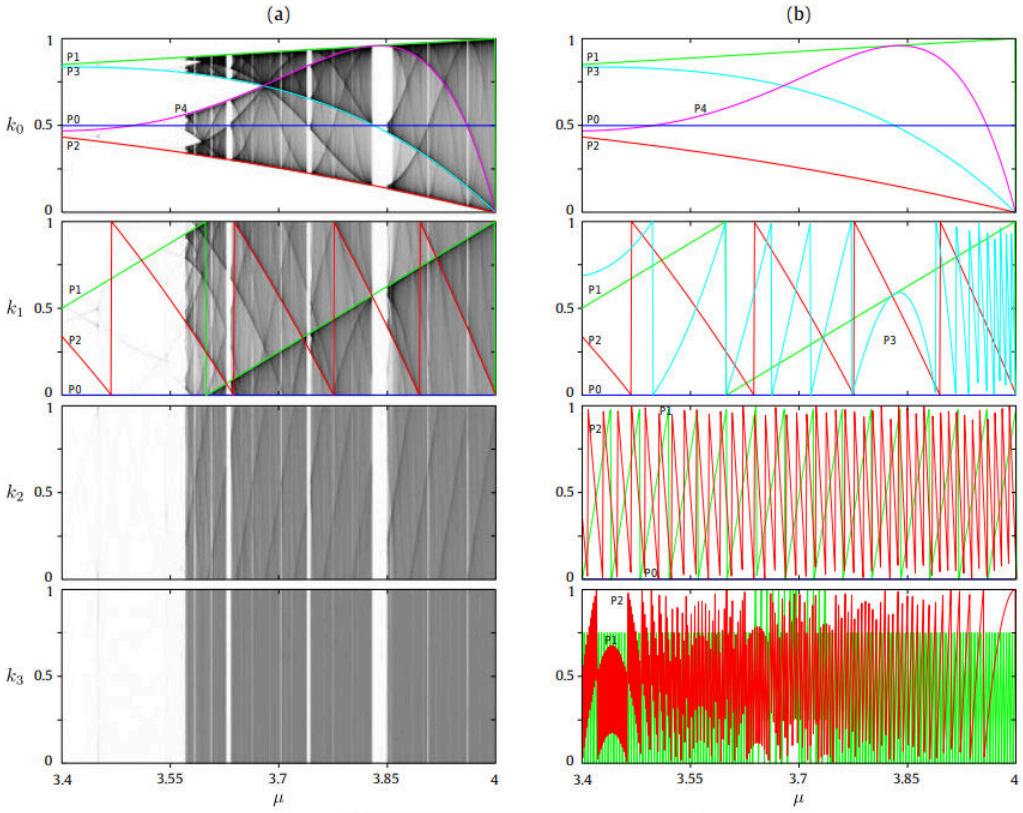

Figure 11 – Stability of the Lyapunov exponent for the k-logistic map.
Source: MACHICAO; BRUNO (8).

namical system, although we make efforts to make sample sizes large enough, assuming these patterns are repetitive enough. Attempts to spot what are the dominant patterns is also important. If a pattern is dominant, that also means we can use it as a proxy for defining our object of interest itself.

The task of pattern recognition is a complex problem that is attacked inter and multidisciplinarily via an intermix of graph theory, dynamical systems theory, measurements on complex networks, texture analysis and fractal measures (94–98).

Patterns may arise from spatial or temporal data. The computerized definition of pattern search applies for patterns in a numerical setting. There are programs developed for the purpose of analysis of chaos, as in Figure 12.

2.1.3.1 Digital degradation of a computer-generated map

When run on a digital computer, dynamical systems are subject to a phenomenon called digital degradation. Orbits that were ideally to be chaotic turn into periodic and as the digital precision is limited it impoverishes the calculations that have to be done (99). Let's remember that arbitrary-precision calculations are not really arbitrary since the maximum number of digits that can be allocated at any given time for the numerical representation is limited. The mean period length $\langle L \rangle$ scales with machine precision Δ

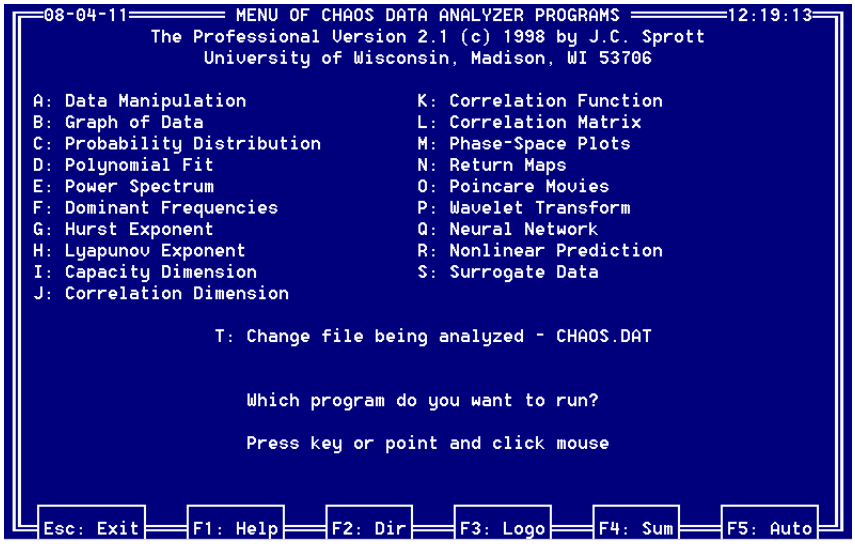

Figure 12 – Chaos Data Analyzer by J.C. Sprott.
Source: CHAOS ...(9).

as $\langle L \rangle \approx \Delta^{-D(2)/2}$ (100, 101) under certain assumptions (102). What remains is to certify that the results obtained via computer simulations are *precise enough* to qualitatively describe the same systems that were formally idealized via mathematical abstractions. Dynamical systems theory is useful here as it provides formal guarrantees just like the *shadowing lemma*.

2.1.3.2 Diffusion phenomena in media and long-range correlations

Published works present and explain the breadth of examples of diffusion phenomena in media and long-range correlations (103, 104). They were discovered to happen in a variety of settings: nucleotide sequences, sequences of letters in several famous books, heart beats in healthy patients, bits of a computer storage with subsequent editing and drop forming times off a leaky tap (105–109). When the characteristic diffusion exponent deviates significantly off the value of 1/2, the sequence of consecutive events sport some kind of correlation with high probability.

Systems with reaction-diffusion properties are extensively used in modelling chemistry and biophysics problems (110). In Section 2.2 we present an analysis based on diffusive principles that makes it possible to treat the logistic map, instead of a noisy signal, as a time series in the conventional sense, and thus enables conventional time series analysis methods to succeed, for example, methods of separation of components such as singular spectrum analysis.

2.1.4 Complex networks

Complex networks can be traced back to the field of graph theory. In 1735, the mathematician Euler developed the first rigorous proof using a representation by means

of graphs of the seven bridges across the river Pregel that surrounded the merchant city of Königsberg in Eastern Prussia as a step. Between the two branches of the Pregel and connected by five of these bridges to the mainland there was the island Kneiphof. The remaining two bridges crossed the two branches of the river to each side. The question to be answered was if one could walk across all seven bridges and never cross the same one twice. Euler demonstrated that the answer is no.

Formally, a graph can be represented as a pair $G = (V, E)$ where V is a set of vertices and E is a set of unordered pairs v_1, v_2 called edges. An adjacency matrix A with elements $a_{i,j}$ where the i-th row and the j-th column denote an edge connecting vertex i to vertex j.

In modern times, graph theory has a very important place in spite of its widespread applicability and connections to linear algebra, providing complementary formalism for the mathematical modelling of physical phenomena (111).

Advantages of using graphs for data representation include:

- Graphs can represent about any kind of relationship.
- A variety of known and straightforward algorithms can be applied to graphs.

As the number of vertices and edges grows and the combinational properties of such graphs are also enriched, one of the questions that arise is what kind or form the aforementioned properties assume when the graph is sufficiently large? Another question is, when the parameters for the nodes and vertices of the graph are dynamically modified, what kind of new behavior is to be seen? Dynamic graph models are routinely seen in compilers, databases, fault tolerance, artificial intelligence and computer networks (112, 113). Finally, when we move from relatively simple and well-defined toy network structures to representations of real systems via network modelling, what phenomena can be seen (114)? The discipline of complex networks deals with such questions.

Graphs in the usual academic sense were for a long time treated mostly as mathematical structures subject to a kind of formalism in the way of proofs and algebraic formulae (115, 116). The field of complex networks, much due to input of social and biological sciences, gets more concerned about the statistical properties of graphs (24, 117). During the development of the discipline of complex networks, themes such as complex network characterization (95, 97, 118–121), machine learning (122), pattern recognition (120, 123) and resonance (124, 125) in complex networks gained traction.

We describe here two properties of complex networks: the scale-free property and the small-world property. We also comment briefly on spatial networks, a structure that extends the array of purely topological properties of a graph and is fundamental for the purposes of the present work.

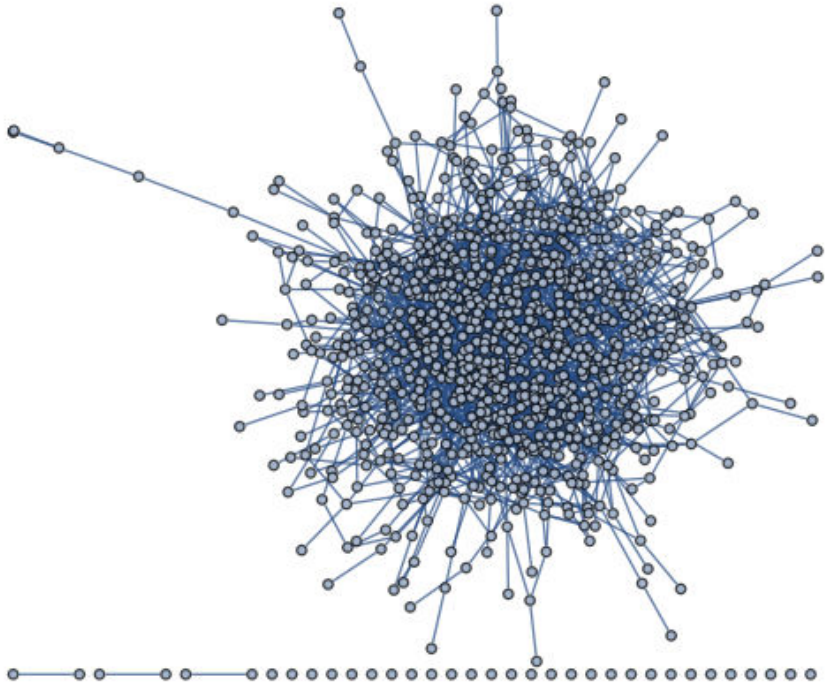

Figure 13 – Random network with 1,000 nodes.
Source: By the author.

Some measures for networks (126), assuming the graph is undirected.

- Measures of network connectivity:

  The degree k_i of the vertex i, is the number of its connections with other nodes or even itself, that can be defined as

$$k_i = \sum_{j=1}^{n} a_{i,j}.$$

  The maximum possible degree for every node in a simple graph, that is, a graph where every pair of nodes has at most one edge leads to a *complete graph*.

  The degree distribution $P(k)$ denotes the fraction of nodes with degree k, where

$$P = \sum_{i} k_i.$$

  Stranting from the degree distribution we derive other measures such as

$$\langle k^n \rangle = \sum_{k} k^n P(k)$$

  is the moment of order n. Starting from order $n = 1$, we derive the mean degree $\langle k^n \rangle$ of the network, from order $n = 2$ we derive the mean variance which is a measure of fluctuations in the network connectivity and so on.

Entropy H_k of the degree distribution, related to network complexity and also an indicator of robustness, where

$$H = -\sum_{k=k_{min}}^{k_{max}} P(k) \log P(k).$$

Hierarchical degree k_h. Obtained by traversing the network recursively until reach every node at hierarchy level h, compute their respective numbers of neighbors and then sum them all.

$$\langle k_h \rangle = \frac{1}{N} \sum_i k_h(i)$$

- Measures of correlation:

  Average degree of the nearest neighbors

  $$k_{nn}(i) = \frac{1}{k_i} \sum_{j \in \mathcal{N}_i} k_j = \frac{1}{k_i} \sum_{j=1}^{N} a_{i,j} k_j$$

  Pronounced differences in the average degree of the NNs in relation to the current vertex indicate a dynamical generating regime for the graph.

  Pearson correlation coefficient

  $$\rho_P = \frac{(1/M) \sum_{j>i} k_i k_j a_{i,j} - [(1/M) \sum_{j>i} (1/2)(k_i + k_j) a_{i,j}]^2}{(1/M) \sum_{j>i} (1/2)(k_i^2 + k_j^2) a_{i,j} - [(1/M) \sum_{j>i} (1/2)(k_i + k_j) a_{i,j}]^2}$$

- Measures of clustering:

  Average clustering coefficient

  $$\langle cc \rangle = \frac{1}{N} \sum_i cc_i$$

  It can be seen that in most real-world networks, an object of study for complex networks, nodes tend to create tightly knit groups of nodes where the edges represent the links, this probability higher than the probability of a randomly established link between any two nodes (127, 128). Akin to the concepts of a multifractal, there are under disposition either global or local measures of clustering. As every subnetwork can also be analyzed as a whole network, local measures of clustering can lead to multiscale analysis techniques.

- Measures of distance:

  Average geodesic distance

  $$\langle l \rangle = \frac{1}{N(N-1) \sum_{i \neq j} d_{i,j}}$$

  Network efficiency

  $$E = \frac{1}{N(N-1)} \sum_{i \neq j} \frac{1}{d_{i,j}}$$

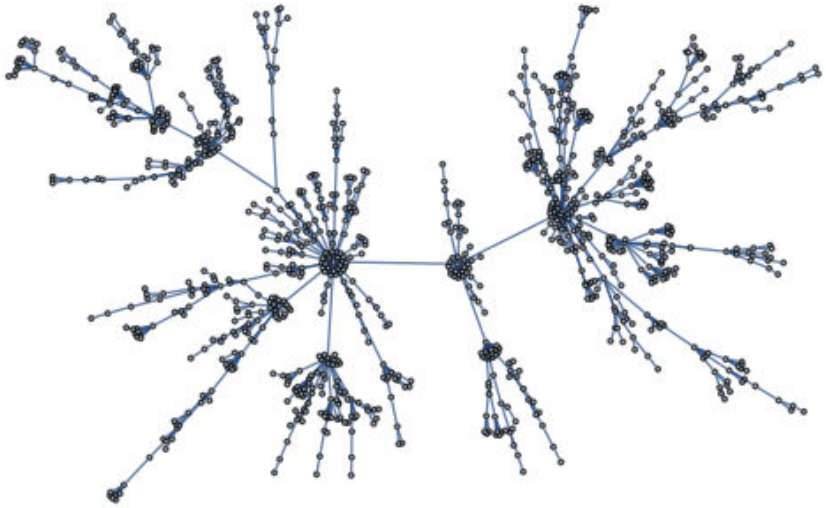

Figure 14 – Example of Barabási-Albert network with 1,000 nodes and proeminent scale-free and small-world properties.
Source: By the author.

- Measures of centrality:

  Betweenness

$$b_i = \sum_{j \neq k} \frac{n_{jk}(i)}{n_{jk}}$$

  Normalized betweenness

$$b_i = \frac{1}{n^2} \sum_{j \neq k} \frac{n_{jk}(i)}{n_{jk}}$$

2.1.4.1 Scale-free property

Networks with the scale-free property are known to be robust to random failures but, on the other side, they are highly susceptible to anomalous spreads (129) which, if of viruses or other harmful entity, would prove problematic in a real setting. Figure 14 gives one example of a network with proeminent scale-free property, in contrast with the random network in Figure 13. Another distinctive feature of such networks is that their local degree distributions cannot be predicted from the global degree distribution for the network. Node degrees with the scale-free property follow not a Poisson distribution but a power law distribution. One implication of the power law is that the degree distribution of these networks has no characteristic scale. In contrast, networks with a single well-defined scale like random graphs are alike to lattices in that the mean degree of the network can roughly predict the degree of every node. Current terminology defines nodes with sufficiently large degrees as hubs of the network, although the definition is somewhat arbitary in virtue of the scale-free feature itself.

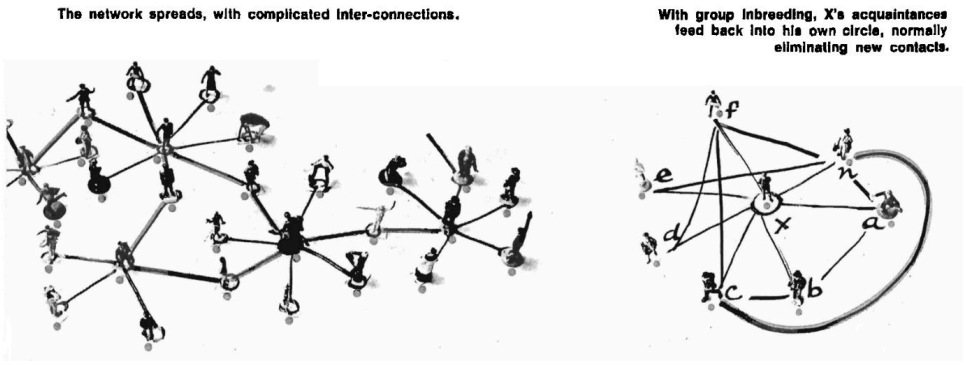

Figure 15 – Milgram's description of social connections with small-world property. Source: MILGRAM (10)

2.1.4.2 Small-world property

The scale-free property gives rise to another property, the small-world property. In networks with the small-world property, few hops can lead to a travel from some vertex of the graph to virtually any other, even in arbitrarily large graphs. A hop is a jump from one vertex of the graph to another via one edge. Stanley Milgram tested this property experimentally while at Harvard (130), see Figure 15, leading researchers to analyses of degrees of connectedness. The famous six degrees of separation concept derived from their research. In a real-world setting, we witness that modern advances in communications and travel enabled the growing and widening span of relationship networks. This ever-increasing connectedness of human beings, despite considerable physical distances between the individuals and their large total number, results in a growing density of social networks that increases significantly the possibilities for any two individuals to connect or to be tighly related in some form.

Formally, the typical number of hops needed to connect any two nodes in a network with the small-world property grows proportionally to the logarithm of the number of nodes in the network, and most pairs of nodes will be connected by at least one hop. Other properties are often associated with small-world networks are the over-abundance of concentration nodes or hubs serving as the common connections mediating the short paths between vertices. A metric, namely the degree distribution of the network, allows one to analyze this property by taking into account the fraction of nodes in the network that have a particular number of incoming connections.

2.1.4.3 Spatial networks

Spatial network is a graph endowed with spatial properties as coordinates, length and area. Its vertices and edges are associated with geometric objects in a metric space. Topological properties are very important for the purposes of making analyses of universal properties across a plethora of network instances, but they alone are not capable to

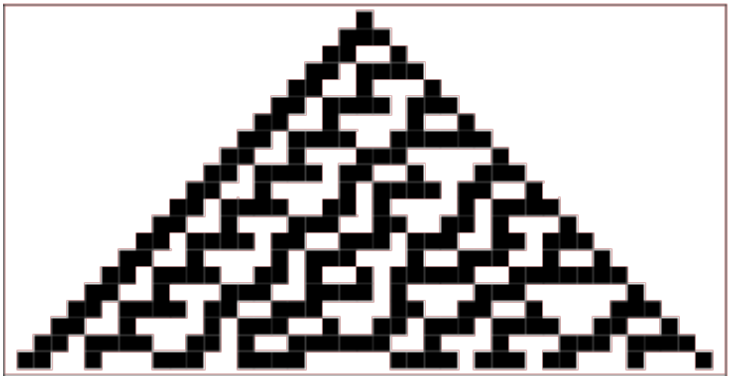

Figure 16 – Example of elementar cellular automata.
Source: ELEMENTARY ...(11).

provide every information that is actually relevant. Transportation and mobility networks, Internet, mobile phone networks, power grids, social and contact networks, and neural networks, are all examples of the high relevance of spatial properties (131) and to project networks onto geometric objects helps where topology alone does not contain all the information when a cost is associated with the length of edges as it is induced in the case of spatial network, and such cost will in turn effect the topological structure of these networks (132). Thus, to characterize and to understand structural and evolutionary aspects of spatial networks is crucial for many different fields.

One of the most straightforward examples are objects like cities, streets, avenues, estate neighborhoods, transport lines etc. that are equipped with a metric and can be represented as networks (133) and are also conductible to network analysis techniques (134). However, the definition of spatial does not convey spaces in the usual physical sense solely, but also spaces of probabilities or spaces of functions.

2.1.5 Cellular Automata

Cellular automata, which are examples of dynamical systems, have remarkable computational advantages over classic numerical implementations of dynamical systems formulae, due to their all-around discrete nature. Cellular automata do not suffer severe limitations in terms of numerical accuracy when they are represented through the use of computers.

Cellular automata are defined by a d-dimensional grid of cells. Each cell is associated with an on-off state. The evolution of a cellular automaton is associated with evolution rules, which determine the next state of a given cell from its current state and that of its neighbors. The application of rules in a cellular automaton, depending on its complexity, it can be computationally costly in terms of time, even without the severe issues regarding numerical accuracy and the use of available storage. Figure 16 exemplifies an elementary cellular automaton of dimension 1, considering the dimension of evolution

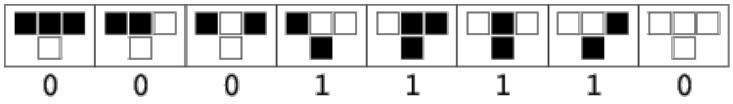

Figure 17 – Possibilities for rule 30.
Source: ELEMENTARY ...(11).

aside. An elementary cellular automaton considers only its immediate neighbors. Cellular automata are most useful for the simulation of individual interactions in discrete time and discrete space. A classical example of cellular automaton that is known to have universal computing capabilities is John Conway's Game of Life (135).

Figure 17 shows a table that breaks down the evolution possibilities for rule 30 of an elementary cellular automaton. This rule is formerly used by the Wolfram application to generate pseudorandom numbers (136), due to the fact that it is chaotic and presents interesting pseudorandomness. There are works that exploit cellular automata to simulate complex reaction-diffusion behavior as it is seen in a class of chemical experiments (137).

2.1.5.1 Life-like Network Automata

Life-like Network Automata (LLNA) is a technique conceived for the analysis and study of complex networks (76–78). Much of the collected data that is stored nowadays can be projected onto networks for an informative and sophisticated representation. Issue is, this data, in sole virtue of its sheer volume might be untractable and thus it is imperative to have efficient algorithms that help harvest the data for the purposes of machine learning and knowledge discovery (138). The pivotal concept in LLNA is that living beings are capable of performing intelligent actions. If this behavior is simulated to some extent by a computer, then automated analysis on the data is effected.

LLNA may be considered as a generalization of John Conway's Game of Life (Figure 18) that exploits life-like intelligent performance in order to help effect analysis over complex networks. The parameters for this type of cellular automaton assume the form of rules, whose notation is of the form Bx/Sy, where x and y are strings of digits. The rule notation for the standard Game of Life is assumed as the string B3/S23. A cell assumes state 1 at time t is it is alive or state 0 if it is dead, it is born if it has three neighbors, survives if it has two or three living neighbors, and dies otherwise. The main difference here is that while for the standard Game of Life the graph is represented as grid of cells, where every cell equals one node, each with a maximum of eight neighbors, for LLNA graphs whose nodes have an arbitrary number of neighbors and potentially imbalanced connections are employed.

The pivotal idea behind LLNA is to expand the application of rules from the game of life to a more general form that acknowledges connectivity imbalances and a

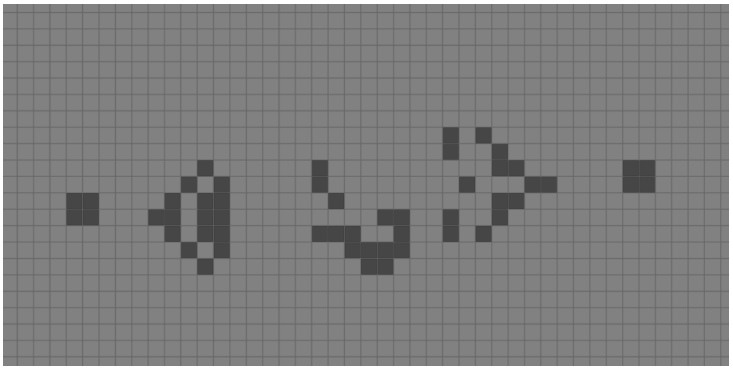

Figure 18 – John Conway's Game of Life.
Source: By the author.

huge variety of network types. Formally, we have cells c_i in the graph each evolving over time t and assuming state values $s(c_i, t)$ 1 or 0. For each cell c_i, it is applied the density measure

$$\rho(c_i, t) = \frac{1}{k_i} \sum_j s(c_i, t) A(i, j) \in [0, 9]$$

where A is the adjacency matrix of the graph whose elements with value equal to 1 denote an existing edge between nodes i and j, and value equal to 0 otherwise. Density information in turn determines the next state according to the rules Bx/Sy, and transition function $\phi : s(c_i, t) \to s(c_i, t + 1)$.

$$s(c_i, t+1) = \begin{cases} 1, & \text{if } s(c_i,t) = 0 \text{ and } \frac{x_x}{r} \leqslant \rho(c_i,t) < \frac{x_x+1}{r} \to \text{ Born (B)} \\ 1, & \text{if } s(c_i,t) = 0 \text{ and } \frac{y_y}{r} \leqslant \rho(c_i,t) < \frac{y_y+1}{r} \to \text{ Survive (S)} \\ 0, & \text{otherwise} \end{cases}$$

where $r = 9$. At time $t = 0$ LLNA performs a random initialization of cell states where the expected value for the probability of dead or alive cells at the beginning is equal to 0.5. Iterations are effectively counted only after a small transient period ψ of about 20 iterations needed for the automaton to attempt achieved equilibrium.

Measurements extracted from LLNA and converted in histograms as feature vectors are the Shannon entropy, Word Length and Lempel-Ziv complexity.

LLNA-BP improves on the original LLNA by the means of histograms for the 2^n possible bit patterns, where n is the fixed length for the bit patterns. In this fashion, combinatorial properties of evolution-related bit patterns can be developed into a statistic and provide alternative information about a network.

LLNA-DTEP leads to another improvement, as it explores temporal patterns. A binary $T \times N$ matrix $\mathcal{T}$ with elements $s(c_i, t)$ depicts the state for each cell over the evolution steps, where N is the number of cells of the network automaton and T

is the number of timesteps for the evolution process. One description for TEP is the concatenation of the states of cells of an automaton as the automaton evolves. TEP employs two matrices D-TEP and SD-TEP. The D-TEP matrix $\mathcal{D}$ is a $N \times T$ matrix whose elements are equal to $\rho(c_i, t)$. SD-TEP provides additional information to complement D-TEP, withstanding nevertheless the same basic principles of exploiting temporality. The SD-TEP matrix $\mathcal{S}$ is a $N \times T$ matrix equal to $\mathcal{D} \odot 2\mathcal{T} - 1$, where $\odot$ is the Hadamart product between matrices.

2.1.6 Random matrix theory

John Wishart and Eugene Wigner presented original work envisaging how to better understand the interacting nuclei of atoms (139,140), taking into account that strongly interacting particles at the quantum level cannot be easily described at the level of the individual particle. Thus, it should be more fruitful to attack the problem leveraging statistical descriptions of the highly-correlated nuclei, analog to application of thermodynamics ensembles as in the case of classic matter.

Wishart's work went into the realm of modelling statistical descriptions as matrices, namely sample covariance matrices. It was found to be very useful in the field of Statistics (141–143), however his work has also a physics underpinning that must be taken into account, and which developed into random matrix theory (144). Random matrix theory finds applications also in the fields of Engineering, Mathematical statistics and numerical analysis, Number theory, Combinatorics, Finance, Free probability, theoretical neuroscience, Optimal control and computational mechanics (145).

One of the objects of interest related to random matrix theory is the theory's generalization and the profound implications for a wide range of phenomena of the properties embedded deep into the structure of the mathematical entities considered in the theory (146–152).

2.1.6.1 Wigner matrices and semicircle distribution

Wigner matrices or random matrices are symmetric and every of its entries $M_{i,j}{}_{1 \leqslant i,j \leqslant n}$ is a random variable. One interesting application of Wigner matrices in image processing and computer vision is image denoising.

The Wigner semicircle distribution is the probability distribution on the interval $[-R, R]$ with probability density function f which is a semicircle with center at $(0, 0)$.

$$f(x) = \frac{2}{\pi R^2}\sqrt{R^2 - x^2}, -R \leqslant x \leqslant R, f(x) = 0 \,\forall |x| > R$$

The semicircle distribution is related to the Wigner semicircle law (140,153) stated below:

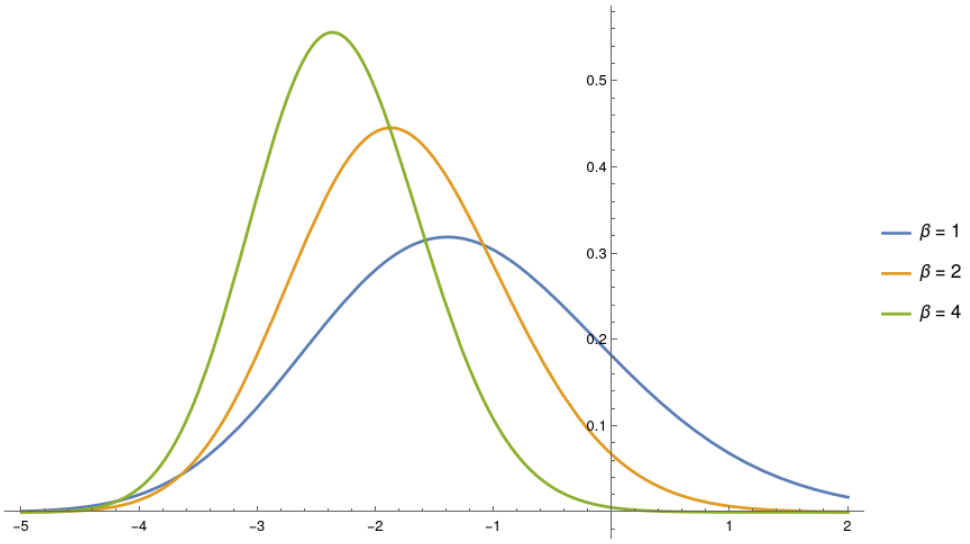

Figure 19 – Tracy-Widom distribution and parameters β for the three gaussian ensembles, GOE ($\beta = 1$), GUE ($\beta = 2$), and GSE ($\beta = 4$).
Source: By the author.

Let $\{M_n\}_{n=1}^{\infty}$ be a sequence of Wigner matrices, and for each n denote $X_n = M_n/\sqrt{n}$. Then the mean of X_n converges weakly, in probability to the semicircle distribution.

The elements of M_n must be random and i.i.d. with identical values for densities, second moments m^2 and n-th moments bounded by constants B_n independent of i, j and N. Let $S = S_{\alpha,\beta}(v, N)$ be the number of eigenvalues of M_n that lie in the interval $(\alpha\sqrt{N}, \beta\sqrt{N})$ for $\alpha < \beta \in \mathbb{R}$. Then

$$\lim_{N\to\infty} \frac{E[S]}{N} = \frac{1}{2\pi m^2} \int_{\alpha}^{\beta} \sqrt{4m^2 - x^2}dx$$

2.1.6.2 Tracy-Widom distribution on the asymptotic limit for the length of Longest Increasing Subsequence for random sequences

The Tracy-Widom distribution is related to the Wigner semicircle distribution. In the seminal paper by Robert May (154), the critical point $1/\alpha_c = \sqrt{2}$ described for the matrix of species' interactions incides on the upper edge of the semicircle distribution, and happens when $\mu\lambda_{max} = \sqrt{2}$. In fact, a region of the left tail of the Tracy-Widom distribution intersects with the Wigner semicircle.

There are typically three Tracy-Widom distributions, F_β, with $\beta \in \{1, 2, 4\}$. They correspond to the three gaussian ensembles: orthogonal ($\beta = 1$), unitary ($\beta = 2$), and symplectic ($\beta = 4$) (Figure 19). GOE is related to projections over the real set, GUE over the complex set and GSE over the quartenion set, which hints to their important relations and fundamental properties (155).

The distribution of the maximal eigenvalue λ_{max} for the Wigner matrices and for the dynamics of certain phenomena converges to the Tracy-Widom distribution in the asymptotic limit. The distribution of the Longest Increasing Subsequence for random variables also converge into this distribution in the asymptotic limit (156). The Tracy-Widom distribution for LIS specifically belongs to the unitary ensemble.

2.1.6.3 Phase transitions and the Tracy-Widom distribution

Statistical distributions for critical phenomena like phase transitions (150) that approach the Tracy-Widom distribution at its centre need not follow it through their range (157). Strange events might affect both tails of the distribution, pointing to phase transitions that are unusual and unexpected. We will use this assumption further in order to devise complex networks that capture certain behaviors of RNGs and the k-logistic map. Furthermore, stochastic processes are often characteristical of phase transitions in physical systems. As such, there is justification for studying the phase transitions, the Tracy-Widom distribution and random number generation in tandem.

2.1.6.4 The Dynamic Time Warping algorithm

The Dynamic Time Warping algorithm (DTW) has found widespread use in time series classification tasks, more specifically the nearest neighbor time series classification task. Time series classification is a form of the classification task where temporal precedence and subsequence of points possess a meaning that is taken into account by some algorithm's calculations on similarity.

A formal definition for the L_2-DTW follows:

$$DTW_2(x, y) = \min_{\pi \in \mathcal{A}(x,y)} \left(\sum_{(i,j)\in\pi} |x_i - y_j|_2 \right)$$

π is an alignment path of length k, equivalently, it is a sequence of k pairs of indices $((i_1, j_1), (i_2, j_2),..., (i_k, j_k))$ and $\mathcal{A}(x, y)$ is the set of all admissible paths.

DTW and its computational efficiency are built upon the paradigm of dynamic programming. Dynamic programming reduces the exponential complexity of the naive approach to worst-case polynomial complexity. However, practical runtimes for time series of even moderate length are still significant and impede large-scale applications. Approximate approaches and parallel implementations have been developed in order to placate this issue (158, 159).

Furthermore, other algorithms have been developed with the goal of superseding DTW in terms of classification accuracy. It is worthy of note that even conceptually more advanced alternatives to DTW could not readily beat it in overall terms, largely due to

Algorithm 1 Algorithm for Dynamic Time Warping.

Require: Vectors s and t;
Ensure: Matrix DTW;
  for $i \leftarrow 2$ to $n+1$ **do**
    for $j \leftarrow 2$ to $m+1$ **do**
      $DTW_{i,j} \leftarrow \infty$
    end for
  end for
  $DTW_{1,1} \leftarrow 0$
  for $i \leftarrow 2$ **to** $n+1$ **do**
    for $j \leftarrow 2$ **to** $m+1$ **do**
      $cost \leftarrow d(s_i, t_j)$
      $DTW_{i,j} \leftarrow cost + \min(DTW_{i+1,j}, DTW_{i,j-1}, DTW_{i+1,j-1})$
    end for
  end for

both DTW's ease of implementation and its noted robustness and general effectiveness for a large and varied set of inputs (160–162).

2.1.6.5 The Matrix Profile

The Matrix Profile (163) is a data structure that allows for largely parameter-free in-depth time series analysis. Several time series analysis tasks can be performed through means of exploiting this data structure. Akin to the DTW it is based upon, MP allows for practical results that are not necessarily the most accurate, but it is admirably flexible and shares with DTW its largely robust behavior. Devoted research and development efforts have been leased in order to reduce the burden of calculations related to MP on computational resources through reductions in computational complexity and novel high-performance algorithm implementations like STAMP, STAMPI, STOMP, SCRIMP, SCRIMP++, SWAMP, DAMP, SCAMP, GPU-STOMP, TranSCRIMP, TranSCAMP and TranSCAMPfpga (164) have paving the way for a more widespread adoption of MP in both academic research and also day-to-day non-academic-related routine tasks. The basic data structure is built off computations of the DTW between non-intersecting windows of a fixed size m and between any given time series, even within the sole time series itself. Every window has a predefined fixed size and they all contain a subsequence of the original values.

The matrix profile data structure is constructed by means of fixed-size windows. A vector of pairs stores the distances of time series windows to their respective nearest neighbor and also the indices of the nearest neighbors. Using mathematical notation: W represents the window size, TS the time series vector, MP the matrix profile vector where each element is the distance d of the time sequence $(TS_p)_{i \leqslant p \leqslant i+W-1}$ starting at i and bounded by $i+W$ to its nearest neighbor, and IDX the indices of the time sequences

$(TS_q)_{j \leqslant q \leqslant j+W-1}$ starting at j and bounded by $j+W$ which are nearest neighbors to each $(TS_p)_{i \leqslant p \leqslant i+W}$ starting at i and bounded by $i+W$, $j \notin [i-W+1, i+W-1]$. Algorithm 2 is depicted.

Algorithm 2 Naive algorithm for matrix profile.

Require: Time series vector ts, window size W;
Ensure: Vectors MP and IDX;

```
for i ← 1 to T do
    MP_i ← ∞
    IDX_i ← −∞
end for
for i ← 1 to T − W + 1 do
    for j ← 1 to T − W + 1 do
        if j ∉ [i−W+1, i+W−1] and DTW((TS_p)_{i≤p≤i+W−1}, (TS_q)_{j≤q≤j+W−1}) < MP_i
then
            IDX_i ← j
            MP_i ← min_{MP_i, DTW((TS_p)_{i≤p≤i+W−1}, (TS_q)_{j≤q≤j+W−1})}
        end if
    end for
end for
```

2.1.6.6 Anomaly detection

A widely-accepted definition of outlier states that an outlier is "an observation that deviates so much from other observations as to arouse suspicion that it was generated by a different mechanism" (165). Research has been devoted into developing and refining automated methods for anomaly detection (166–176) and also to placate ever-growing issues – due to the exponential increase of stored data – such as the high dimensionality curse (177–179).

One possible grasp of anomaly detection, also known as outlier detection, is to understand it as a very specific form of classification. The classification task in its most general form is comparatively loose and does not usually deal with highly imbalanced classes. Several important challenges follow relaxing constraints due to imbalanced classes. If the instantiation of a class comprise of a very small set of points, every false positive and false negative shows up with magnified weight. Furthermore, a given classification method may engulf altogether one low cardinality class within another high cardinality class. For the general classification task, it is even desirable to remove outliers before instantiating the task, since they steer the classification method into deviating from the expected result (180, 181).

Therefore, imbalanced classes and outlying points are problematic in much of the context of machine learning. The diverse class instantiations tend to comprise approximately the same cardinality for several tasks. Classification methods take clever advantage of this constraint by simplifying the problem, but they end up not tuned to deal with the

scenarios belonging to anomaly detection. Outlier detection as a classification task deals precisely with such difficult issues. In the context of machine learning, outlier detection is not as widespread as clustering and classification. However, when outlier detection is called into action, it is usually of paramount importance. Under the context of a factory, outliers mean severe failures in a production facility; under the context of neighboring natural events, outliers might be dangerous tornadoes or giant sea waves; under the context of a medical faciltiy, outlers mean unusual electrocardiograms and patient abnormal cardiac rhythm and, under the context of a financial transaction, outliers mean costly frauds and abuse of the system (181).

In practice, the bias sensitivity that is collateral to outlier detection methods inhibits efforts to formal generalization for the notion of outlierness. Methods that perform well under certain groups of anomaly/outlier detection tasks tend to perform poorly in other tasks, leading thus to the increasing interest in outlier ensembles (180), as ensembles adapt better to the diverse kinds of tasks. Because assumptions cannot be simplified too much for any given outlier detection method that is aimed to perform with at least reasonable accuracy, these methods cannot be easily sped up unlike the bulk of classification methods. And an additional caveat is the manner the literature approaches the experimental facet of scientific validation. Experiments are performed under very controlled environments and synthetic datasets, without too much regard to common and important real-world tasks. Comparisons between methods are hardened by the lack of standardized benchmarks (182, 183).

2.1.6.7 Applications of computational geometry methods

Modern computational geometry theory and methods have significant recognition due to widespread computer graphics and computer-aided design and manufacturing (CAD/CAM) uses. The field of application for computational geometry is stretched on by the classical nature of many of its problems, which also come from the task of visualization of mathematical structures. Other important applications of computational geometry comprise robotics, geographic information systems (GIS), integrated circuit design, computer-aided engineering and computer vision.

Purely topological methods provide network measurements that prove useful. Nonetheless, applied fields related to computational geometry are interesting two-fold: to provide output that taps further upon human sensory abilities (184) and to project object properties in a way that an array of further analyses can be conducted and other methods and techniques now can be applied (185), shedding light on the data in a new perspective.

Alves and Bruno (12) projected networks originating from the k-logistic map using computational geometry concepts and methods. On Figures 20 and 21, the deployment of network links or edges between vertices within a radius r centered at vertex i and the

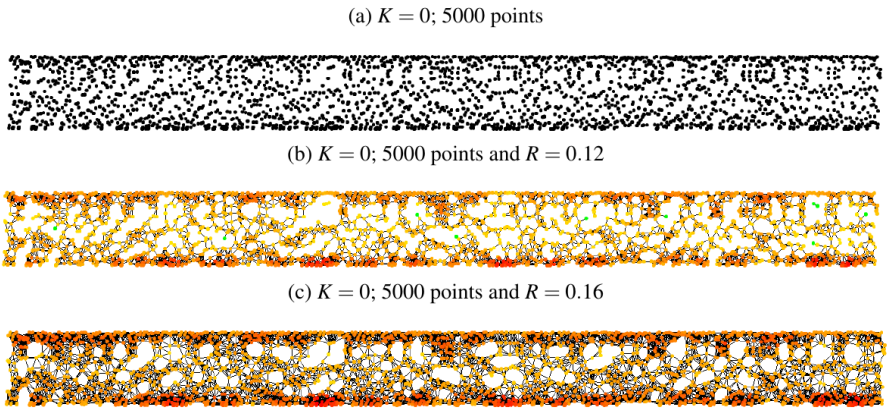

Figure 20 – Plots from the k-logistic map with $k = 0$.
Source: ALVES; BRUNO (12).

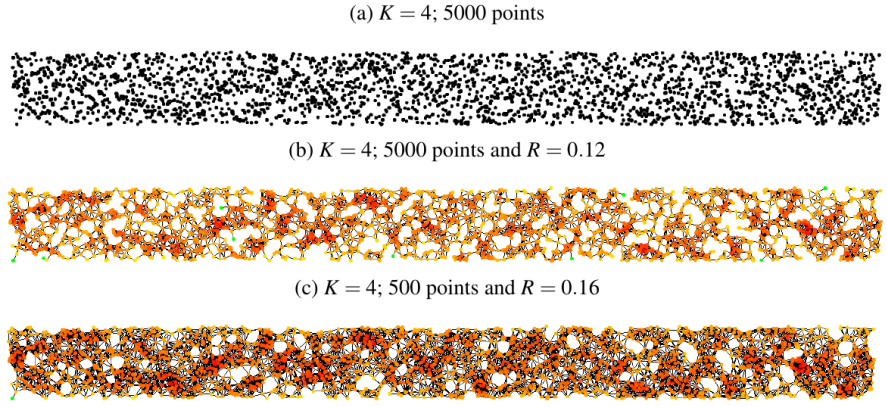

Figure 21 – Plots from the k-logistic map with $k = 4$.
Source: ALVES; BRUNO (12).

vertex i itself on the $\mathbb{R}^2$ plane, for all i, is seen.

A graph is constructed over vertices that are derived from a sequence of n points p_i selected out of some orbit of the k-logistic map. The geometry on the $\mathbb{R}^2$ plane is projected by repeating the edge creation process for every vertex. Axis x is valued by the indices $i \in \mathbb{N}$ of the points in the sequence and axis y is valued by $p_i \in \mathbb{R}$. Scaling factors are applied to each of the axes and then a coordinate (x, y) is assigned to every point. Finally, the maximal component of the graph is computed.

On Figure 22, it is seen the Delaunay Triangulation on the $\mathbb{R}$ plane that is computed over the network.

2.1.6.8 Residual Analysis for Anomaly Detection in Attributed Networks

RADAR (186) was developed with the goal of performing anomaly detection on networks, given attribute information associated with the network. It is based on the

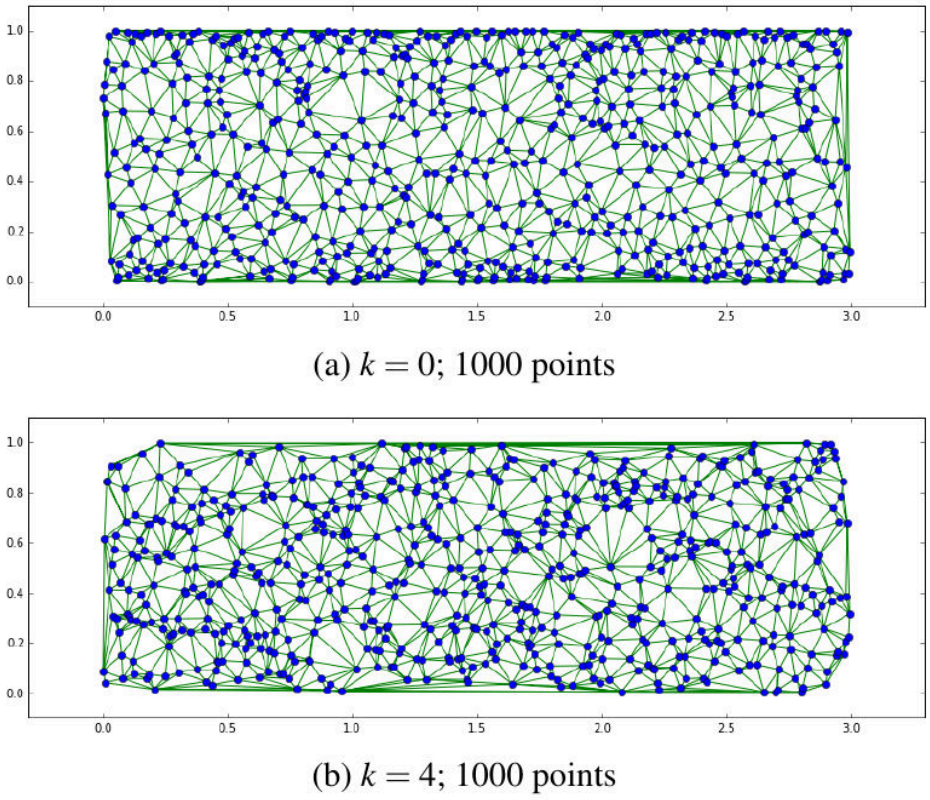

(a) $k = 0$; 1000 points

(b) $k = 4$; 1000 points

Figure 22 – Delaunay triangulation from the k-logistic map.
Source: ALVES; BRUNO (12).

assumption that to combine attribute information of nodes and structural information of the network is a powerful method to locate anomalous nodes. The usefulness of anomaly detection in the context of complex networks is clear. Anomalous nodes, in a certain way, serve as a signature for the network.

It relies on an iterative optimization algorithm that attempts to reconstruct the original attribute matrix associated with the network. The catch here is that the residual error of the reconstruction process tends to vary significantly between inlier and outlier instances, that is, the attribute patterns between anomalous instances and normal instances are quite different each other.

Let the set of n interconnected instances $\mathcal{U} = \{u_1, u_2, \ldots, u_n\}$ with interconnection represented by edges e_j. And associate every instance with a feature set in d dimensions $\mathcal{F} = \{f_1, f_2, \ldots, f_d\}$. Attribute information of all n instances is denoted by $\boldsymbol{X} \in \mathbb{R}^{n \times d}$. Furthermore, let $\tilde{\boldsymbol{X}}$ denote the estimated attribute matrix and let $\boldsymbol{R}$ denote the residual matrix of approximation errors $\boldsymbol{X} - \tilde{\boldsymbol{X}}$. If representative instances at hand conduct to accurate estimates of the attribute information matrix, then it is improbable that such instances are anomalous. On the other side, a large value for the norm of $\boldsymbol{R}_i$ indicates that a given instance has a high probability to be an anomaly and this result is used to

spot anomalies.

The objective function for RADAR is

$$\min_{\boldsymbol{W},\boldsymbol{R}} \|\boldsymbol{X} - \boldsymbol{W}'\boldsymbol{X} - \boldsymbol{R}\|_F^2 + \alpha\|\boldsymbol{W}\|_{2,1} + \beta\|\boldsymbol{R}\|_{2,1} + \gamma tr(\boldsymbol{R}'\boldsymbol{L}\boldsymbol{R}) \tag{2.1}$$

And the update equations are

$$\boldsymbol{R} = (\boldsymbol{I} + \beta\boldsymbol{D}_R + \gamma\boldsymbol{L})^{-1}(\boldsymbol{X} - \boldsymbol{W}'\boldsymbol{X}) \tag{2.2}$$

$$\boldsymbol{W} = (\boldsymbol{X}\boldsymbol{X}' + \alpha\boldsymbol{D}_{\boldsymbol{W}})^{-1}(\boldsymbol{X}\boldsymbol{X}' - \boldsymbol{X}\boldsymbol{R}') \tag{2.3}$$

Algorithm 3 describes the workings of the concept.

Algorithm 3 The RADAR algorithm for anomaly detection in attributed networks.

Require: Attribute matrix $\boldsymbol{X}$, adjacency matrix $\boldsymbol{A}$, parameters α, β, γ.
Ensure: Top m instances with the highest anomaly scores.
  Build Laplacian matrix $\boldsymbol{L}$ from the adjacency matrix $\boldsymbol{A}$;
  Initialize $\boldsymbol{D}_{\boldsymbol{R}}$ and $\boldsymbol{D}_{\boldsymbol{W}}$ to be identity matrix;
  Initialize $\boldsymbol{R} = (\boldsymbol{I} + \beta\boldsymbol{D}_{\boldsymbol{R}} + \gamma\boldsymbol{L})^{-1}\boldsymbol{X}$;
  while objective function in Eq. 1 does not converge **do**
    Update $\boldsymbol{W}$ by Eq. 3;
    Update $\boldsymbol{D}_{\boldsymbol{W}}$ by setting $\boldsymbol{D}_{\boldsymbol{W}_{i,i}} = \dfrac{1}{2\|\boldsymbol{W}_i\|_2}$;
    Update $\boldsymbol{W}$ by Eq. 2;
    Update $\boldsymbol{D}_{\boldsymbol{R}}$ by setting $\boldsymbol{D}_{\boldsymbol{R}_{i,i}} = \dfrac{1}{2\|\boldsymbol{R}_i\|_2}$;
  end while
  Calculate the anomaly score for the i-th instance as $\|\boldsymbol{R}_i\|_2$
  Return top m instances with the highest anomaly score.

2.2 Methodology

Here we describe the concepts and methods devised to tackle the problem of leveraging improved methods for pattern search and detection in chaotic orbits and seemingly random outputs.

2.2.1 Multi-tap logistic map

Weaknesses in encryption can be used by techniques that exploit the algebraic properties of the map, properties such that conventional statistical tests are not able to detect. One example are the weaknesses found in elliptical curves. We do not know formulations that successfully exploit possible algebraic weaknesses of the k-logistic map. However, numerical and computational methods for exploitation of these weaknesses are

not to be excluded. An ingenious direct application of machine learning is glimpsed, noting that values of any random sequence with uniform distribution will not present patterns beyond casual and random clusters. Unexpected patterns can be considered as a "signature" for the dynamical system. Machine learning algorithms can be divided among those based on global optimization, such as support vector machines (SVM), and those of local optimization, such as decision trees, random forests (RF) and multilayered perceptron (MLP).

We present here an application of the logistic map and the k-logistic map for pseudorandom number generation (PRNG) which we refer to as the Multi-Tap Logistic Map (MTLM), where the orbits constructed from multiple parameters are fused. Due to the fact that the orbit of the k-logistic map derives directly from the orbit of the original logistic map, the characteristic cycle lengths of the digital form are retained. This characteristic presents issues to number generation applications, since periods for each individual orbit might be too small to be of any use, or the runtime may be prohibitive and impractical. We show how the use of a coupled Linear Feedback Shift Register (LFSR) improves number generation application along with the logistic map and the k-logistic map.

The logistic map, due to its orbits of high complexity and chaotic behavior, has been studied for the purposes of pseudorandom number generation. It warrants non-linear relationship between elements inside the orbit set, however, the digital form of the logistic map suffers from degradation. One such issue related to digital degradation is that lengths of the periods formed upon the basin of attraction, which are small and do not span well over the space of possible values. The k-logistic map, as already presented in Section 2.1.2.4 is a variant of the logistic map that extracts the statistically most relevant digits of the orbit, thus improving both non-linearity and statistical distribution of the orbit, however, issues that are related to small periods remain unabatted. The Linear Feedback Shift Register, known by the acronym LFSR, is commonly used for pseudorandom number generation. With a correct polynomial it spans every numerically doable value over the space, with its value statistics representative of a distribution adequate for number generation, with certain limitations e.g., the relationship between elements is linear and when full word size is taken into account, the fact that no value repeats itself until the full realization of the period is of concern. If the qualities of non-linearity inherent to the logistic map and of long period length from the LFSR are combined, then we can improve pseudorandom number generation.

Many works execute digital perturbations over the chaotic orbit in order to improve period length. In a number of these works, the digital perturbation is essentially a parameter value switch during the execution of the algorithm. Such perturbation imposes

a constraint and expose the run to characteristic pathological cases, if there are no guarrantees as for the sanity of orbits under the parameter change. Also, depending on the size of the state space and the function space, not all cases could be determined empirically. In our proposal, we run maps in parallel. Since it is probable that no relationship can be found between the orbits, beside the LFSR selector of bits in orbit elements, the probability of the PRNG being dominated by a rare pathological case is reduced. The entropy bits are collected from several orbits via multi-tap procedure and concatenated sequentially.

Computing the k-logistic map with precision of several thousands of digits should attain long periods. However, the computational cost is significant and even more so for time-sensitive cryptographic operations. We provide a brief analysis of the weaknesses of digital chaos and describe our steps taken to improve on it. Due to the fractal nature of the logistic map and similar dynamical systems, under certain parameters the period repeats itself too early. We describe these situations as pathological cases. This limitaton is directly related to the set of attractors with small period lengths which, are simply put, not adequate for cryptographic applications. It is important to note that simply switching from the logistic map to the k-logistic map does not alleviate this issue.

As already said, a measure that can be taken to improve both period length and reduce digital degradation is to employ arbitrary length arithmetic which demands more computing resources and, due to the inherently serial nature of the logistic map, might impede high performance real time applications. Since our proposal runs several maps in parallel, commonplace multi core computers can be taken advantage of.

Considering numerical representation with many digits, it is increasingly necessary to develop methods for lengthening cycles in lieu of the needs of cryptographic applications.

LFSR's and the logistic map, despite showing desirable statistical properties, they do not operate or behave like a true RNG e.g. after producing a certain value, the map will redo itself from there, therefore generating a period. Some techniques can be applied to make these maps simulate more closely a true RNG, e.g. discard a subset of digits off the map's numerical image.

If the shortest period of the generator is large enough, then it is little cause for concern. For the logistic map, Table 2.2.1 presents mean period lengths.

The period is a measure of the predictability of the PRNG. For PRNGs based upon deterministic algorithms and run by a deterministic machine, its next state after one pass of the execution of the algorithm is completely defined by its current state. The period also presumes a cyclic operation of the machine. See Figures 23, 24, 25 and 26. One pass after the last state under the period and the PRNG begins to repeat itself, with

Table 1 – Digital precision for logistic map calculations under base 10 followed by mean period length.

Base 10 digital precision	Mean period length
10	39,086.32
11	119,717.11
12	366,510.19
13	1,099,759.87
14	3,374,700.89
15	10,315,441.27
16	31,697,223.91
17	99,019,100.52

Source: By the author.

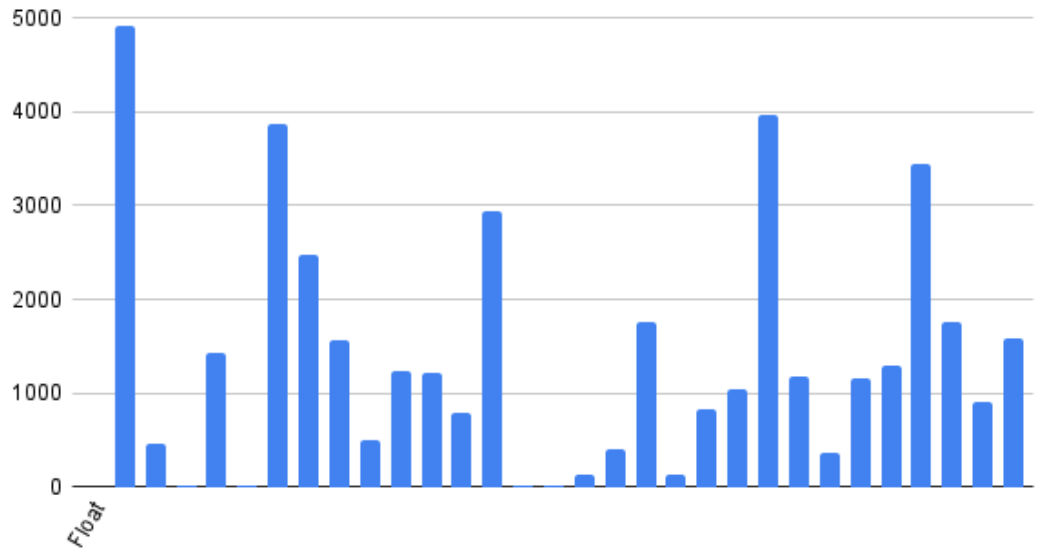

Figure 23 – Period length for logistic map, machine IEEE-754-compliant single precision from $r = 3.7$ to $r = 3.99$.
Source: By the author.

all its subsequent output values perfectly matched by equality to a given previous output sequence. The average period of a PRNG is directly related to the number of symbol streams, however. Thus, combining outputs from several k-logistic map sources increases the period by the order of the least common multiple of all periods. Combining outputs it is also more computationally efficient because the time complexity for every base-n digit added increases only linearly, and the time complexity for the k-logistic map, due to a costly multiplication operation, increases by order of the square of n, if schoolbook multiplication algorithm is employed.

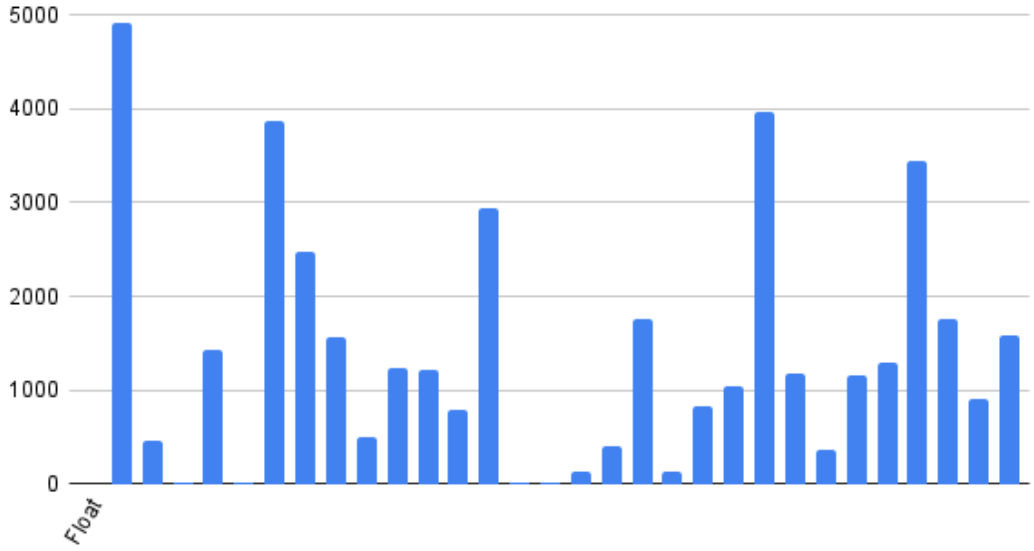

Figure 24 – Period length for logistic map, machine IEEE-754-compliant single precision from $r = 3.7$ to $r = 3.99$.
Source: By the author.

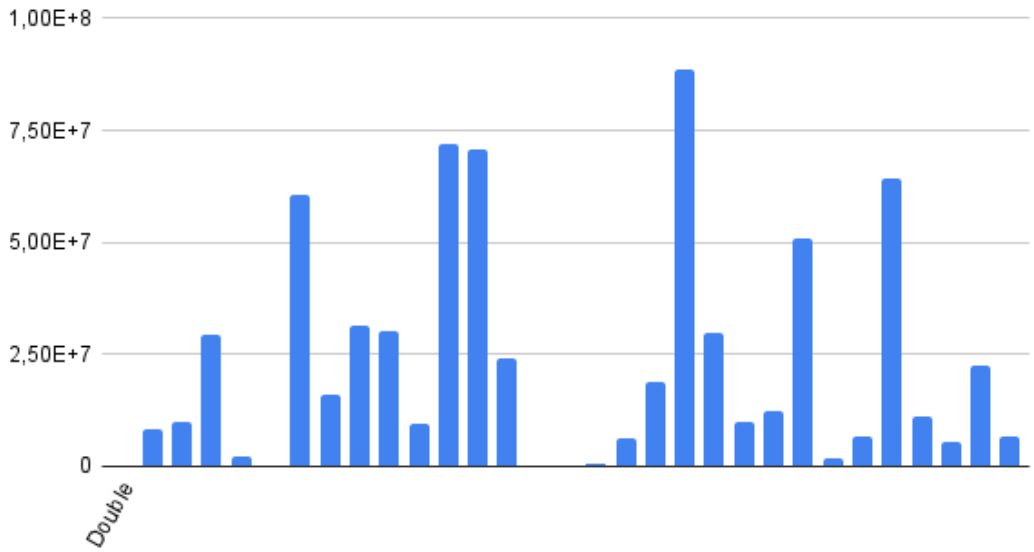

Figure 25 – Period length for logistic map, machine IEEE-754-compliant double precision from $r = 3.7$ to $r = 3.99$.
Source: By the author.

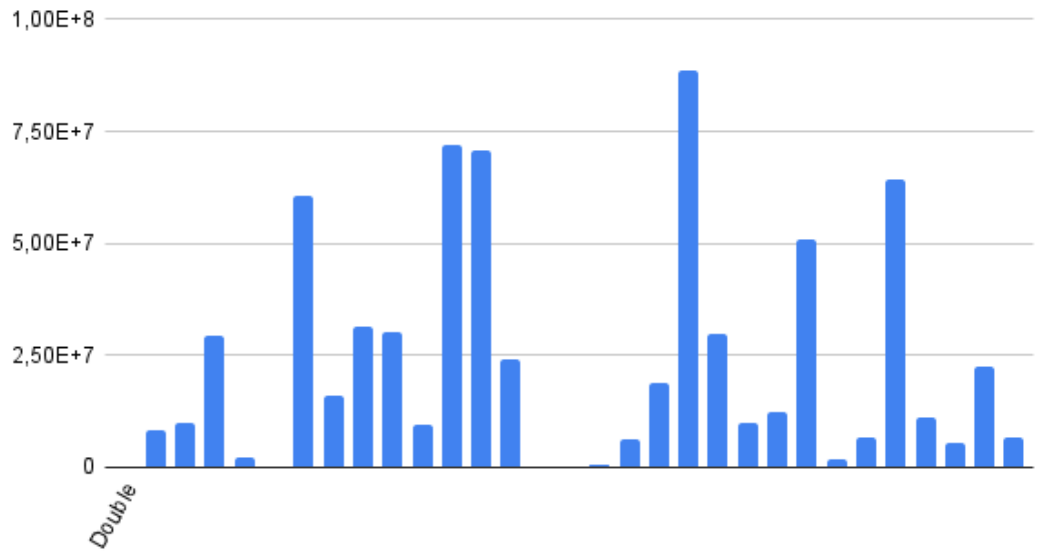

Figure 26 – Period length for logistic map, machine IEEE-754-compliant double precision from $r = 3.7$ to $r = 3.99$.
Source: By the author.

LFSRs obey the Golomb statistical properties for maximal length sequences, namely, the balance property, the run property and the autocorrelation property. They resemble certain properties one expect to find in random sequences (187). Due to these properties, they are extensively employed in communication and data/stream ciphers. The generation of binary sequences in GF(2) is a well-known use case.

Let a run in a binary sequence be a subsequence of consecutive zeros or ones. We denote a run of zeros a gap and a run of ones a block. A gap of length k is a set of k consecutive zeros flanked by ones. A block of length k is a set of k consecutive ones flanked by zeros. A run of length k is either a gap or block, of length k. Then, we present three randomness postulates of a periodic sequence:

Balance property:

In a period of the sequence, the number of ones and the number of zeros differ by at most one. Run property:

In every period, half the runs have length 1, one-fourth have length 2, one-eight has length 3, etc., as long as the number of runs so indicated exceeds 1. Moreover, for each of these lengths, there are equally many gaps and blocks. Autocorrelation property:

The out-of-phase autocorrelation of the sequence always has the same value.

It is important to note that we see in truly random sequences a wider spread of values.

The LFSR is endowed with desirable properties, furthermore, non-linear outputs that do not sport such properties but otherwise present other interesting properties can be coupled to this class of generators. However, there are known weaknesses of the LFSR that exploit its conception as a linear combination of polynomials in a field. Of special interest, there is the iterative Berlekamp-Massey algorithm that can be applied to a sequence of (not necessarily consecutive) $2n$ or more stream bits.

One method we employ is to conceal what the LFSR output in fact is, as the k-logistic map is non-linear, using a LFSR as a selector into bits of the k-logistic map output makes it therefore harder to find a suitable function to reverse the output into a primitive generator, since the relationship of the output to the input is purely linear no more.

For the k-logistic map, we output its value times 256 as a cast 8-bit integer. For the LFSR-sourced k-logistic map, we run one LFSR and one map at a time and we extract sequentially eight triples of bits off the LFSR. The value of each triple is used to select one bit off each value output by the map. All eight bits are concatenated and their value is output as a cast 8-bit integer. For the multi-source k-logistic map, we run eight maps in parallel and output sequentially their values times 256 as a cast 8-bit integer. For the

LFSR-multi-source k-logistic map, we run eight maps and eight LFSRs in parallel. For each LFSR, in proper sequence, eight triples of bits are read and their value is used to select the bit off the 8-bit value output by each of the maps. All bits are concatenated and their value is output times 256 as a cast 8-bit integer.

2.2.1.1 Estimation of probability density functions

Knowing the exact value for the natural invariant density, then we also know which symbols are more likely to appear in a given sequence and also which sequences are more or less common among all. For conventional symbolic dynamics the state space is partitioned into regions, and each region is associated to a symbol. The regions may not necessarily be of the same size.

A histogram is built upon the symbolic dynamics information. Sufficiently many points are needed for a precise estimation for the value of $*p$, the true probability. Argument can be made that in the case of the logistic map it is possible to sample up to millions of points, which leads to a precise estimation, but this possibility is not necessarily true for every dynamical system or process. And we cannot always take for granted that we know the natural invariant density in analytical fashion for every case, as it is the case of the Ulam map, that is, the logistic map with $r = 4$. We are down to one of the following issues that make difficult to determine precise values for $*p$: a selection of resolutions for the regions of the state space are coarse-grained and, as such, of little use for practical purposes, or higher resolutions require prohibitively high computational resources, or certain dynamical processes of interest are intrinsically restricted as the number of samples that can be obtained tends to be very low.

We now argue, under these assumptions, that an alternative concept used very successfully for the task of unsupervised machine learning, when boiled down into a practical method, is able to present improved results for the one-dimensional case in comparison to conventional symbolic dynamics and also the Lyapunov exponent alone. We partition the phase space and apply measures on a ball of radius ϵ or ϵ-ball to obtain estimates for the dynamical system. Interpreting the symbolic dynamics in the light of numerical representation, we now consider a point and its iterations in the state space, computed numerically down to its ulp, and we associate a strict region to this point centering onto it a ϵ-ball, and count the number of points inside the ball. In practice, we are estimating a measure related to $*p$, but not the value of $*p$ directly. If certain topological characteristics of the system or process, such as relative ordering of the points under the measure, are more important than the measure itself, then one collateral is that the bias of the estimator used in this fashion can be neglected.

We stress that our alternative numerical approach is experimental by concept as the estimate might be far off the value of the true local measure. In this case, it is needed

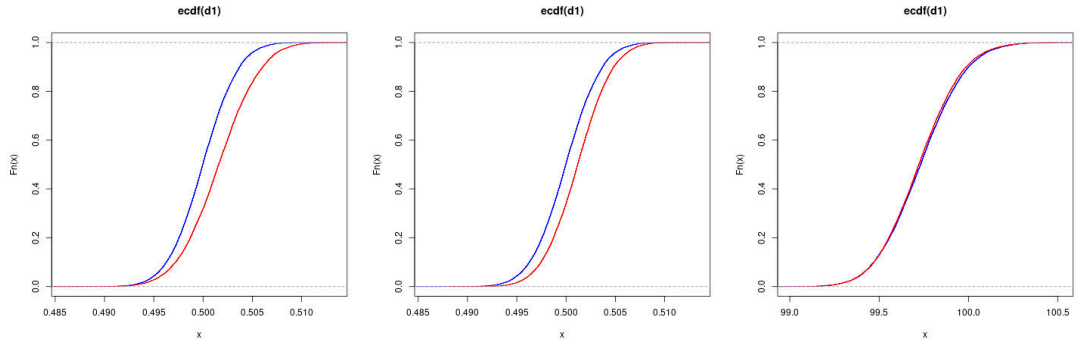

Figure 27 – Three cumulative empirical orbit distributions. Octave PRNG, k-logistic map $k = 0$ and $k = 3$
Source: By the author.

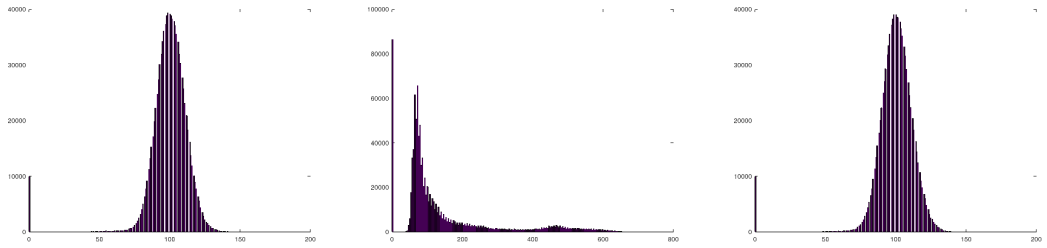

Figure 28 – Three density distributions. Octave PRNG, k-logistic map $k = 0$ and $k = 3$
Source: By the author.

to increase sample sizes and shrink the ϵ-ball.

An ϵ-neighbourhood is the collection of points that reside at most ϵ units away from a given point. A local density measure is a estimate for the probability of points belonging to any metric space X to be contained in a given region of the whole domain A, $X \in A$. Such a measure allows to infer correlations between points. As it is computationally very expensive to scour the entire space for the calculation of densities, samples are used. An estimate of local density over A works as follows: given a point p, calculate how many points are contained in the neighbourhood of p. Local density measures are consecrated by their high sensitivity in the detection of anomalous patterns in challenging data sets (188–190).

2.2.1.2 Topological counterparts of density estimators

Figures 27, 28 and 29 give distinct perspectives on the same dynamical system or stochastic process.

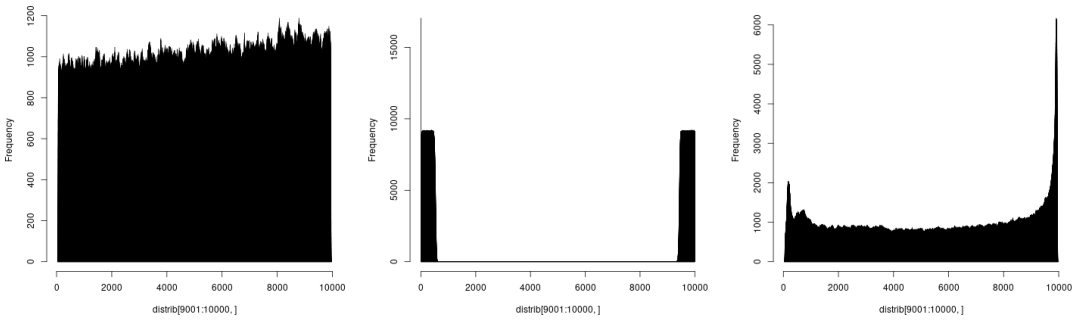

Figure 29 – Three "topological" distributions. Octave PRNG, k-logistic map $k = 0$ and $k = 3$
Source: By the author.

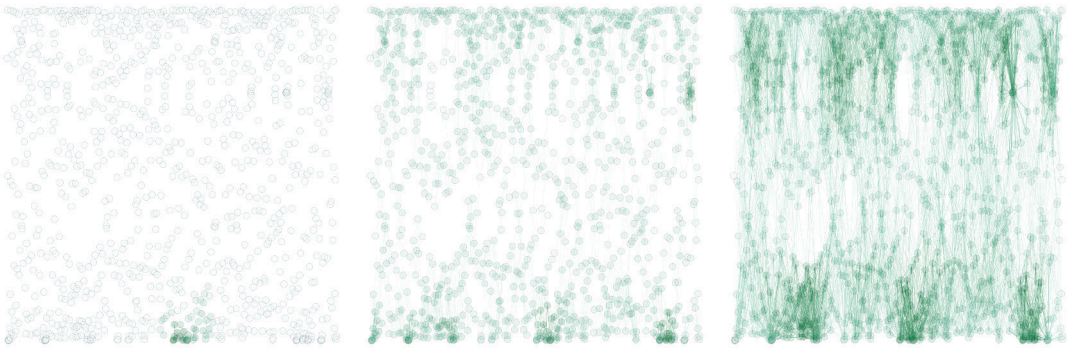

Figure 30 – Graphs built from the orbit of the k-logistic map with neighbor radius at values 0.06, 0.12 and 0.24.
Source: By the author.

From the attraction basin for the logistic map $x_{n+1} = rx(1-x)$ a structure is generated for some given parameter value r. For arbitrary values of r, the logistic map will generate periodic or chaotic orbits. Works have approached the evolution of logistic map with attention to orbit terms, that we call a horizontal approach. The Figure 30 exemplifies this approach with graphs built from 1,000 orbit points to the k-logistic map with $k = 3$ and $\mu = 3.99999$. In this exploration in dense matrices, we will use an horizontal and vertical approach. Horizontal because it scans a given orbit, and vertical because it scans the different parameters μ of the dynamical system. In encryption applications, the parameters may be used as part of the key, so it is interesting to study the evolution of the dynamical system also in the direction of the parameters.

An important observation. In computational terms, the logistic map presents low efficiency in leveraging the range of floating point values, even more considering the repeats of exponents for normalized numbers in the IEEE-754 standard within range $(0, 1)$. In finite accuracy, every computed orbit is periodic, although the shadowing lemma, restrictions applied, ensures that periodic behavior is the closest to the chaos as the machine accuracy lets on. Hence the importance of using arbitrary accuracy numbers whenever feasible. Some proposals suggest the insertion of orbit disturbances in order to increase efficiency. Taking cycle size averages for μ in the range of 3.7 to 3.99, step 0.01, the mean for double precision is equal to 23,288,148.13, for simple precision is equal to 1,377.96. The range of standardised floating point values for double precision in IEEE-754 standard is on the order of 2^{56}, and simple precision floating point is on the order of 2^{25}. This means that, on average, for the cases studied, utilization in double precision is about 1 in 400,000,000,000, and in simple precision, it gets to about 1 in 1,000,000.

We now present the following concepts:

- Local density measure: A measure of local density can be induced. The orbit of a chaotic dynamical system is contained within some range, presumably within the set

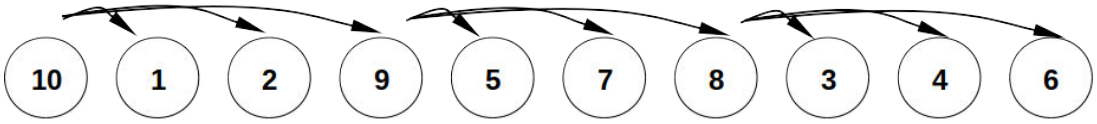

Figure 31 – A topological graph.
Source: By the author.

of the real numbers. For some map $x_{n+1} = f(x_n)$ the collection of points is discrete and therefore countable. By projecting this collection, we obtain a distribution of points in space. M is the projection of the orbit from the attraction basin and d is the Euclidean distance. From each point, we calculate its local density measure. Put informally, given that a stone thrown by the dynamical system fell on the coordinates x_A, how many of the other stones thrown had fallen within the region at most ϵ units away from x_A? Regions over which no stone has fallen are not especially informative about the behavior of the dynamical system, especially for sparse sets.

- Topological graphs on objects contained in metric spaces: A topology preserves mathematical information about some mathematical object. Through employing topology methods and techniques, we try to cancel or at least compensate the interference of precision and sampling errors in the distribution of numerical values. Numerical indices are conferred on the n density values distributed on the real line, order 1 for the lowest numeric value or weight attributed to a vertex and order n for the largest, in increasing order by weight, respecting the total order in the continuous line. In a topological graph, if vertex i comes before the vertex j, then the vertex index i will also come before the vertex index j on the tuple.

Consider a frequency computation of indices over m distinct density distributions. Given odds p, frequencies f and indices A and B withdrawn from the same uniform distribution, then $P(f_A \leqslant f_B) = P(f_B \leqslant f_A)$ for any pair of indices. This is a equivalence relation for the ideal RNG. The histogram of an ensemble of several orderings illustrates the distribution of the vertices of the graph. Obviously, if the ensemble includes the entire topological graph population, then the histogram distribution will be uniform. The global distribution is invariant, however the distribution for a portrait that includes only a small sample of the population may not be equal to distribution for the complete set of ensembles. For the ideal RNG, it is expected that the distribution for any ensemble of topological graphs approaches that of the complete ensemble, given that the density estimates, the amount of topological graphs and the sample range all have achieved a high level of statistical significance. By analyzing a piece of the system with a high level of statistical significance for the histograms, it is also possible to evaluate the topological randomness of the values.

P	1	2	3	4	5	6	7	8	9	10
D	4	4	6	6	5	6	5	5	4	3

Figure 32 – An unordered vector.
Source: By the author.

P	10	1	2	9	5	7	8	3	4	6
Do	3	4	4	4	5	5	5	6	6	6

Figure 33 – An ordered density estimate vector.
Source: By the author.

We observe in the time series approach experiments that the trends of the logistic map orbit or the data after decomposition of the diffused logistic map orbit vary from one sample to another, therefore, it is justified to use several orbits or sections of orbits in the analysis. The topological matrix is built upon topological graphs, with each graph representing an orbit. In thermodynamics formalism, each realization of the system, with its orbit $\mathcal{O}$, is a state. So, the topological matrix works as an ensemble of states where each estimate is represented by one histogram bar and it is assigned to one matrix column. Figures 33, 32, 31 and 34 picture the method. P represents the set of positions, D is the unordered sequence of density estimates and Do is the ordered sequence of density estimates.

In a nutshell, we take m sequences of n orbits as one ensemble. Every sequence of n values is taken as one microstate. In our implementation, the 10% highest density values are highlighted as peak representatives in the distribution that estimates the invariant density measure.

Take into account the following orbits:

$$\mathcal{O}_1 = (x_{1,1}, x_{1,2}, ..., x_{1,n})$$

$$\mathcal{O}_2 = (x_{2,1}, x_{2,2}, ..., x_{2,n})$$

$$\mathcal{O}_m = (x_{m,1}, x_{m,2}, ..., x_{m,n})$$

The topological matrix is formalized as follows: given functions density $\rho_r(x)$, index $i(x)$ such that $1 \leq i(x) \leq n \in \mathcal{N}$, sort $\hat{\rho}_r(x)$ such that if $\hat{\rho}_r(x) < \hat{\rho}_r(y)$, then

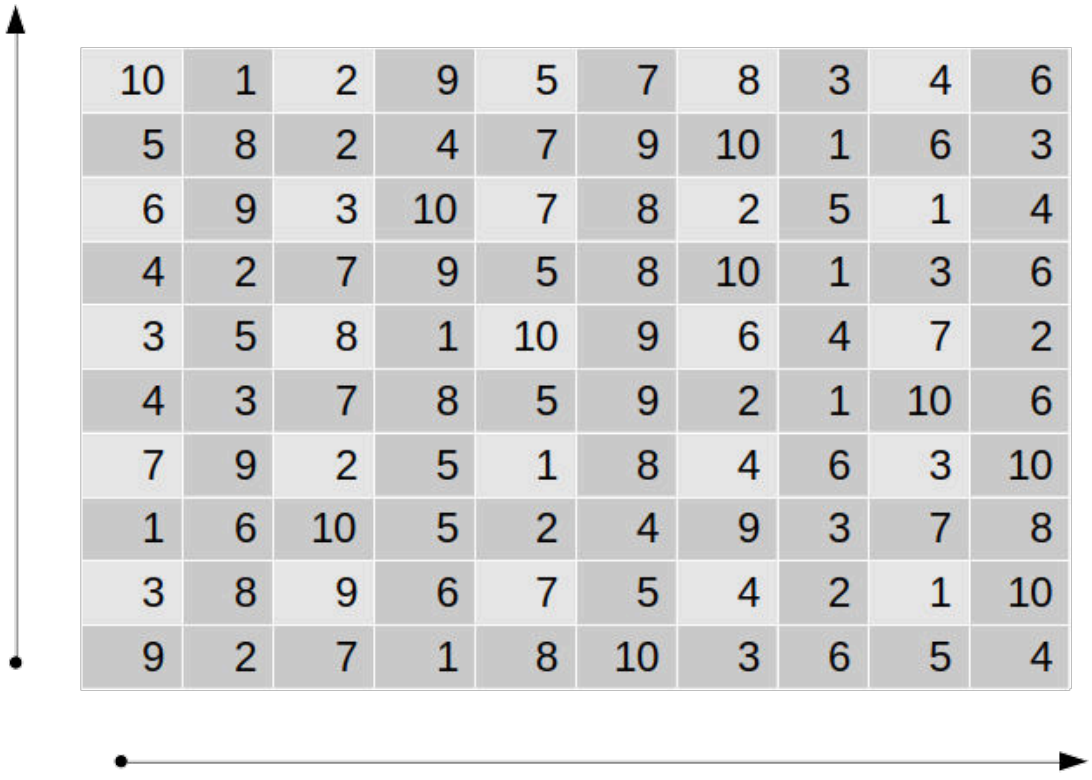

Figure 34 – A topological matrix.
Source: By the author.

$i(\hat{\rho}_r(x)) < i(\hat{\rho}_r(y))$ for all x, y, and count $c(x)$:

- Given that $x \in \mathcal{O}$ is random:

$$\begin{bmatrix} x_{1,1} & x_{1,2} & ... & x_{1,n} \\ ... & ... & ... & ... \\ x_{m,1} & x_{m,2} & ... & x_{m,n} \end{bmatrix} \Longrightarrow \begin{bmatrix} \rho_r(x_{1,1}) & \rho_r(x_{1,2}) & ... & \rho_r(x_{1,n}) \\ ... & ... & ... & ... \\ \rho_r(x_{m,1}) & \rho_r(x_{m,2}) & ... & \rho_r(x_{m,n}) \end{bmatrix}$$

$$\Longrightarrow \begin{bmatrix} (\rho_r(x_{1,1}), i(x_{1,1})) & (\rho_r(x_{1,2}), i(x_{1,2})) & ... & (\rho_r(x_{1,n}), i(x_{1,n})) \\ ... & ... & ... & ... \\ (\rho_r(x_{m,1}), i(x_{m,1})) & (\rho_r(x_{m,2}), i(x_{m,2})) & ... & (\rho_r(x_{m,n}), i(x_{m,n})) \end{bmatrix}$$

$$\Longrightarrow \begin{bmatrix} i(x_{1,i(x)|i(\hat{\rho}_r(x))=1}) & i(x_{1,i(x)|i(\hat{\rho}_r(x))=2}) & ... & i(x_{1,i(x)|i(\hat{\rho}_r(x))=n}) \\ ... & ... & ... & ... \\ i(x_{m,i(x)|i(\hat{\rho}_r(x))=1}) & i(x_{m,i(x)|i(\hat{\rho}_r(x))=2}) & ... & i(x_{m,i(x)|i(\hat{\rho}_r(x))=n}) \end{bmatrix}$$

$$\Longrightarrow \begin{bmatrix} c_1(i(x_{j,k}) = 1) \\ c_2(i(x_{j,k}) = 2) \\ ... \\ c_n(i(x_{j,k}) = n) \end{bmatrix} \sim \begin{bmatrix} c_{\lfloor 9n/10 \rfloor + 1}(i(x_{j,k}) = \lfloor 9n/10 \rfloor + 1) \\ c_{\lfloor 9n/10 \rfloor + 2}(i(x_{j,k}) = \lfloor 9n/10 \rfloor + 2) \\ ... \\ c_n(i(x_{j,k}) = n) \end{bmatrix} \Longrightarrow \begin{bmatrix} m \\ m \\ ... \\ m \end{bmatrix}$$

$$1 \leq j \leq m$$

$$1 \leq k \leq n$$

2.2.1.3 Diffusion-based time series analysis

It is readily acknowledged that a dissipative and chaotic map like the k-logistic map does not lend itself to standard time series analysis and tools. Reason is that the orbit of an highly chaotic system is usually indistinguishable from random noise. Let us remind that the eigenvalues for a diffusive chaotic dynamical system expand and contract. The expansion and contraction processes take place during the continued iteration of the system. If we take a snapshot of a given iteration of the system, it is like if the system ceased dissipation momentarily, and it is now energy-preserving.

The (one-dimensional) heat equation

$$\frac{\partial U}{\partial t} = \Delta U$$

is diffusive but, contrary to chaos, the diffusion process here moves towards equilibrium. Therefore, if we apply the heat equation onto a snapshot of a chaotic orbit, in a sense, we are reordering or "dechaotizing" the system.

Let the finite difference approach

$$\frac{\partial U}{\partial t} = c^2 \frac{\partial^2 U}{\partial x^2} \Rightarrow$$

$$U_t = U_{xx}, c = 1 \Rightarrow$$

$$\frac{u_i^{n+1} - u_i^n}{k} = \frac{u_{i+1}^n - 2u_i^n + u_{i-1}^n}{h^2}, k = \Delta t, h = \Delta x = 1 \Rightarrow$$

$$u_i^{n+1} = k(u_{i-1}^n + u_{i+1}^n) + (1 - 2k)u_i^n.$$

Now we set the boundary conditions, assuming the first point of the orbit lies at 0 and the last point lies at L, to

$$U(0, t) = 0,$$

$$U(L, t) = 0,$$

$$t > 0.$$

And the initial condition

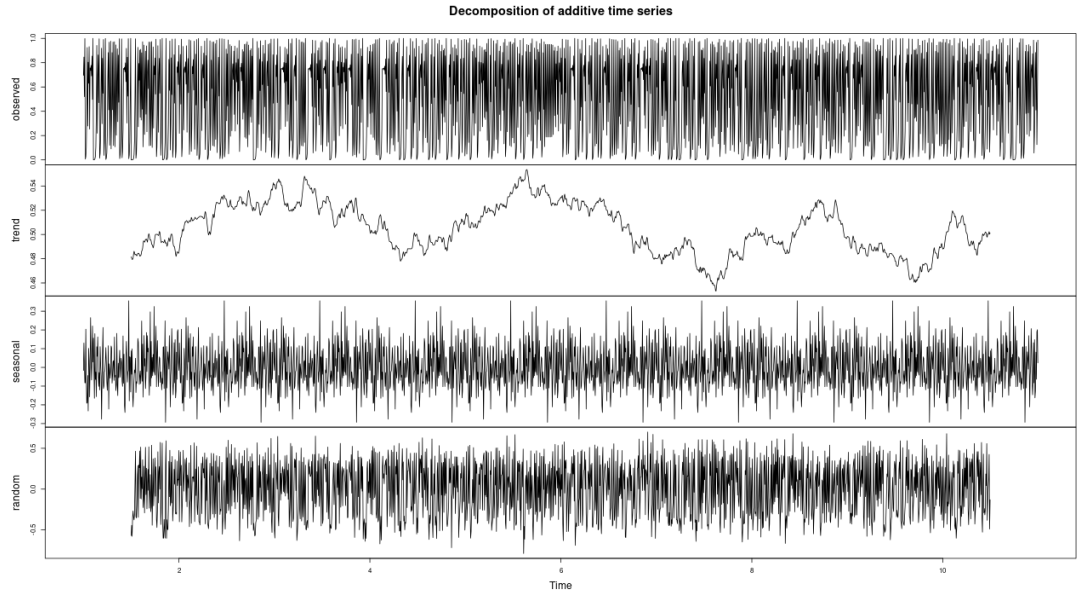

Figure 35 – Time series decomposition on the k-logistic map with $k = 0$.
Source: By the author.

$$U(x, 0) = U_0(x)$$

in order to transform the snapshot.

Note: after we apply the heat equation, the system is still energy-preserving.

Figure 35 examplifies time series decomposition on the original k-logistic map and Figure 36 for the k-logistic map after heat equation is applied.

As the heat equation is linear and diffusion in dynamical systems is non-linear, decomposition methods would readiliy distinguish between their respective diffusive bands. Thus, after application of the heat equation, the system is still amenable to an array of methods for chaos analysis.

Motif is a technical term that essentially defines patterns in time series. Motif search is an important task on time series (191). It was previously unattainable for the original k-logistic map, however we show in Chapter 3 that after rounds of the one-dimensional heat difference equation we now can search for motifs in chaotic orbits in a fashion that is coherent. For more information on motifs induced from time series we refer to the work of Xu *et al.* (192).

2.2.1.4 Reduction of Longest Increasing Subsequence to Dynamic Time Warping

Sakai and Inenaga demonstrated that the dynamic time warping distance for any given pair of value sequences can be calculated as the longest increasing subsequence of an input variable that is a transformation of the original input (193). The converse

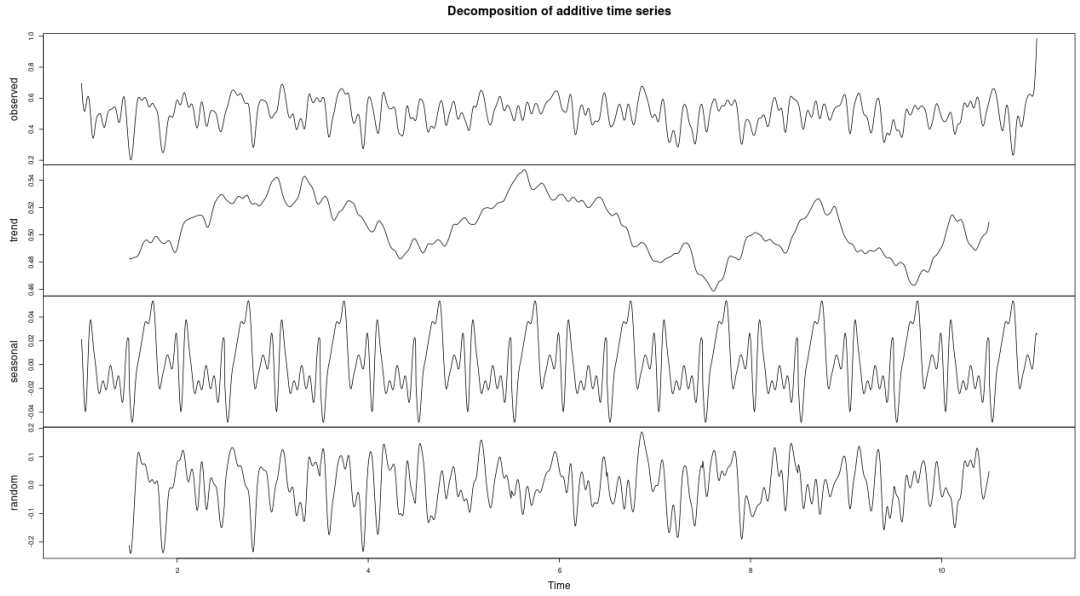

Figure 36 – Time series decomposition on the diffused k-logistic map with $k = 0$.
Source: By the author.

must be true, that is, the longest increasing subsequence of a given input variable can be calculated as the dynamic warping distance of a pair of input variables that is the inverse transformation applied. As this relationship is biunivocal, an equivalence relation, it is doable that both output values from different algorithms share the same statistical distribution, that is known for the LIS problem to be in the asymptotic limit the Tracy-Widom distribution if the input variables are random. There is the issue that the DTW input variables go through a sequence of transformations for this exchange. The original variables are in $\mathbb{R} \times \mathbb{R}$ and the transformed variables are in $\mathbb{R}$. This fact does not immediately negate our assumption, if the distribution for the random DTW input variables is *measure-preserving* transformable from a joint probability distribution to an univariate probability distribution. It can be readily seen that further transformations in the reduction process are of linear type and, as such, it effects for some distributions such as the Gaussian and uniform types only the parameters of the distribution but not its family.

Let us construct the following to show that the relationship between the outputs for the DTW and the transformed LIS is indeed linear: we set the constant c for the reduction from DTW to LIS to any arbitrary value for any $x \geqslant 0 \in \mathbb{R}$. It is straightforward that scalings for the LIS input variables depend only on the constant c. As we change c, every input variable for the corresponding problem is scaled accordingly.

The transformation also relies on the length m of the first DTW (vector) input variable and the length n of the second DTW input variable for the resulting $(m + (m - 1)(n - 1)) \times (n + (m - 1)(n - 1))$ graph. It leads to a joint probability distribution for

the transformed input variable. The probability distribution for the pair of DTW input variables can also be interpreted as a joint probability distribution of the same family as that of the transformed input variables. By means of performing a *measure-preserving* transformation from the joint probability distribution to $\mathbb{R}$, as we change the values for m or n, the map for the joint probability distribution for input variables is scaled accordingly in $P(X) \in [0, 1] \subset \mathbb{R}$. As for the convergence of the joint probability distribution, if one random variable is drawn from a distribution X, and the other from a distribution Y, and either distribution converges, then the joint characteristic function

$$E[e^{i(uX_n+vY_n)}] = E[e^{iuX_n}]E[e^{ivY_n}] \Rightarrow$$

$$E[e^{iuX}]E[e^{ivY}] = E[e^{i(uX+vY)}]$$

also converges.

For the case of the convergence for the distribution of inputs that are random variables, the distribution of outputs in the asymptotic limit converges to the Tracy-Widom distribution. Alternatively, there is the combinatorial argument that two discrete random variables X and Y independently drawn from univariate distribution $\mathcal{U}$ each in probability space $(\Omega, \mathcal{F}, \mathbb{P})$ over Ω of cardinality equal to 2^n have a joint probability distribution isomorphic to $\mathcal{U}$ for the variable Z whose probability space over Ω of cardinality equal to 2^{2n}.

One consequence of importance is related to the First Passage Percolation and Last Passage Percolation over the directed $\mathbb{Z}^2$ lattice where the distances from some point at (x, y) to its neighbors at $(x + 1, y)$ and at $(x, y + 1)$ are randomly weighted. Walks are allowed only in the north and east directions. FPP relates to the optimal path or geodesic between $(0, 0)$ and (m, n). Conversely, LPP relates to the maximal path without cycles. For LPP the distribution of maximum is known to converge to the Tracy-Widom distribution for some cases (194). It is conjectured that the distribution of the geodesic also converges to this distribution (195). We see that a solution for the DTW can also be represented over a $\mathbb{Z}^2$ lattice. The essential difference between DTW and FPP paths is that FPP allows "north" and "east" walks only, whereas DTW allows "north", "northeast" and "east" walks. Figure 37 shows experimentally the similarity of the distributions for FPP and DTW. It can be observed that the constraint of i.i.d. random weights for the FPP and LPP is not satisfied as weights for the DTW lattice are drawn from the distance function $(x-y)^2$ between points x and $y \in \mathbb{R}$ applied over $\mathbf{X} \times \mathbf{Y}$, where $\mathbf{X}, \mathbf{Y}$ are random vectors, $\mathbf{X} \in \mathbb{R}^m$, $\mathbf{Y} \in \mathbb{R}^n$. However, Figure 38 makes it noticeable that the distribution of weights obtained is virtually indistinguishable from the empirical random distribution of $(x - y)^2$, $x \in \mathbf{X}$, $y \in \mathbf{Y}$.

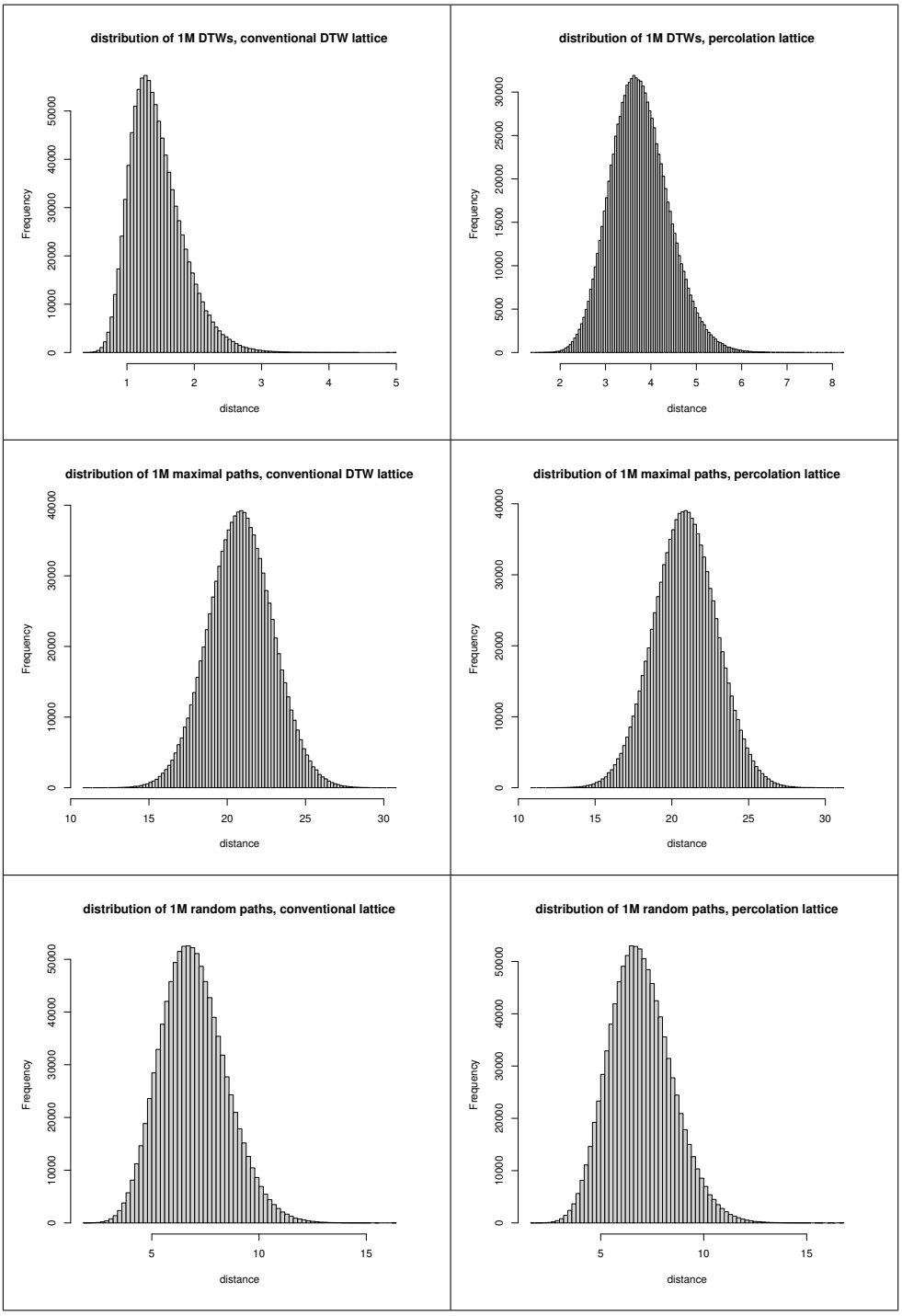

Figure 37 – Distributions for DTW, maximal path length and random path length. By "conventional" we mean the standard DTW lattice walkable in the "north", "northeast" and "east" directions. By "percolation" we mean the FPP and LPP lattices in Z^2.
Source: By the author.

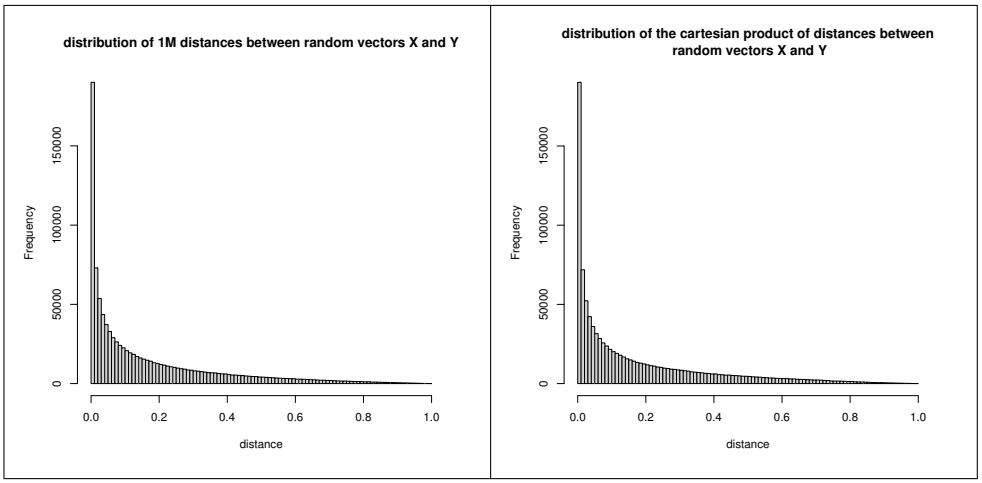

Figure 38 – Distributions for weights and random variables.
Source: By the author.

Thus, assuming equivalence between the DTW and LIS we use concepts and methods from random matrix theory to perform analyses upon chaotic orbits and RNGs.

2.2.1.5 Projections over Complex Networks

Deterministic flavors and the application of the map both induce obvious correlations that interfere with the investigation by means of immediate or nearby strong correlations. For example, for the logistic map, there is the quadratic curve space represented per Poincaré plot between two adjacent orbit points that is a very obvious pattern. Therefore, two any adjacent points are somehow correlated, however that is not the behavior of our interest. It is desirable to find objects related to a memory of the system or patterns that are preserved even after several iterations of the evolution of the dynamical system. i.e. long-range correlations characteristic of one-dimensional systems that are preseved even after the decay of the nearby correlations.

We can mark potential correlations as relations in a graph (196). For the graph to be as information-rich as possible, we must consider as many non-straightforward correlations as possible. Non-straightforward correlations can be interesting due to the property of decay, which is expected to be of exponential order for one-dimensional chaotic dynamical maps. In the Alves and Bruno approach (12), nodes that represent the point iterates i and $i+1$ with straightforward quadratic correlation are linked together along with other nodes within a radius. We want to get rid of this type of network connection in order to depthen our study of the long-range correlations. Luchesi and Bruno demonstrated via empirical experiments that the expected correlation strength for the logistic map weakens significantly after ten iterations or more (197). Therefore, we introduce a modification in the proposed method of Alves and Bruno (12), which we now call the *baseline* method, and set a gap of 10 points in the original phase space between any nodes on the projected

Table 2 – Mean and standard deviations for diverse measures. RANDU is a legacy random number generator that was developed by IBM.

generator	DTW	$> 1\sigma$	$< -1\sigma$	$> 2\sigma$	$< -2\sigma$	euclidean
$k = 0$	3.93±0.73	5.04±0.34	2.43±1.00	5.68±0.28	1.10±1.10	0.50±0.35
$k = 1$	5.38±0.74	6.52±0.36	3.64±1.49	7.18±0.30	1.83±1.78	0.50±0.31
$k = 2$	5.59±0.68	6.66±0.34	3.96±1.58	7.26±0.29	1.77±1.98	0.50±0.30
$k = 3$	5.72±0.69	6.82±0.37	4.08±1.62	7.44±0.32	1.72±2.04	0.50±0.29
$k = 4$	5.65±0.66	6.70±0.34	4.05±1.60	7.28±0.29	1.74±2.03	0.50±0.29
$k = 5$	5.65±0.67	6.71±0.35	4.05±1.60	7.30±0.30	1.71±2.03	0.49±0.29
$k = 6$	5.64±0.67	6.71±0.35	4.04±1.60	7.31±0.30	1.69±2.02	0.51±0.29
$k = 7$	5.64±0.68	6.73±0.36	4.02±1.59	7.34±0.32	1.65±2.00	0.51±0.29
$k = 8$	5.62±0.67	6.68±0.35	4.03±1.59	7.27±0.30	1.68±2.01	0.50±0.29
$k = 9$	5.65±0.66	6.70±0.34	4.05±1.60	7.29±0.29	1.73±2.03	0.50±0.29
RANDU	5.61±0.65	6.64±0.33	4.04±1.59	7.21±0.29	1.77±2.04	0.50±0.29
/dev/random	5.65±0.69	6.77±0.38	4.03±1.60	7.39±0.34	1.60±1.99	0.50±0.29
ANU	5.61±0.67	6.68±0.36	4.02±1.59	7.28±0.31	1.67±2.00	0.50±0.29

Source: By the author.

network. As such, after this modification we suggest to investigate surges of unusual high correlation where such correlation is not of short-term and/or expected.

Next improvement is what we call the *Correlation Network Projection*. Alves and Bruno employed a radius to induce correlations between points and an empirical approach which is an impediment to the induction of scale-free network features, since the radius imposes a scale. The CNP does not use a radius but certain statistical moments that are independent of scale, computed over a DTW adjacency matrix built after application of the all-pairs DTW with a window size W onto the orbit points. It works much like the matrix profile, but instead of the vector with minimal distances like in the matrix profile, we keep the full DTW matrix. We are justified in the use of the DTW measure in virtue of its discrimination ability as seen on Table 2.2.1.5. Additional preliminary results are presented in the Appendix.

We perform the CNP on the original k-logistic map orbit instead of the diffused orbit for the sake of preserving the original dynamics. The decay for the probability of observing a given sequence of symbols is usually exponential. Therefore, in order to use a window with low probability of collisions when the orbit is small ($m \geq 30$), we chose to apply a similarity measure, which does not require exact matching between sequences of symbols. The purpose of computing the DTW between non-intersecting windows, like in the matrix profile, is to extract as much information as possible from the orbit, considering each network maps – in the sense of ensembles – to exactly one orbit. It is like a single state which then turns into a complete ensemble, with its contained windows and their sequences of values as the new states.

One possible physical meaning of DTW, depending on the measure employed, could be to calculate how much energy is needed for state A to jump onto state B, assuming the process is reversible. However, we pay attention that were the aimed goal to perform comparisons of microstates as symbol sequences independently of the value of the actual symbol s_i, save for $s_i = s_j, i \neq j$, a better fit would be to use a family of algorithms like those of Longest Common Subsequence. Furthermore, DTW is not ideal to investigate issues related with the multiscale behavior of nonlinear systems. Instead, we choose the DTW for its robust performance on the time scale and that its output is distributed obeying a Tracy-Widom-like distribution. We justify choosing the value of 30 for window size on the basis of the probabilistic argument that the probability, considering the IEEE-754 floating-point double-precision, that any two distinct regions of a sequence of 30 draws from random variables are exactly the same and subsequently, have a time warping distance of exactly zero, is significantly small and lies below the threshold of 5×10^{-958}

The tails of the Tracy-Widom distribution are able to indicate certain statistical features of the random processes and phase transitions that deviate from the center of the distribution, as it is seen in experiments (157). As the Tracy-Widom distribution does not have a straightforward analytical form, a simple and conservative starting point for our analysis is to induce graphs onto the DTW adjacency matrix by means of the usual standard deviations. In our experiment we apply 1σ, 2σ and 3σ below and above the mean.

Our approach is to induce a network comprised only of outlying edges and project it as a spatial network, and we have thus a cue as for the differences between networks. Complex networks analysis of the structure of dynamical systems has been met with success (198). Applying this rationale to a PRNG or true RNG, we then attempt to verify their fitness by the means of a distribution that, in the case of LIS and, we assume, also DTW, converges to its asymptotic form when the inputs are merely random noise and should present deviations when the input is not perfectly random.

Ideally, we want the orbits and also the windows to be impossibly large. In turn, we would have incredibly informative networks but computational constraints prevent us from doing so. In practice, we attained networks of about 2,000 nodes which led to several days of processing time under 8-core/16-thread clusters. Shrinking the networks to 500 nodes, we note a remarkable decline in terms of accuracy during preliminary tests, as shown in Figures 39 and 40.

$< -3\sigma$ and $> 3\sigma$ CNP with 2,000 nodes have shown very small networks, sometimes without any edges. $< -1\sigma$, $> 1\sigma$ and $> 2\sigma$ networks with 2,000 nodes possess an exceedingly high number of edges, which barred us from proceeding due to computational constraints. The only remaining candidate were the $< -2\sigma$ CNP.

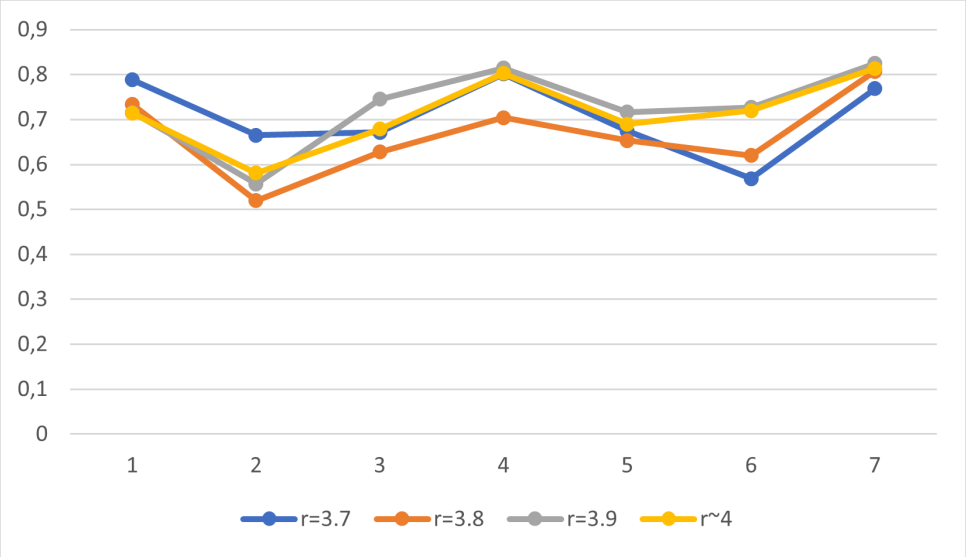

Figure 39 – Ratio of accuracy between 500-node and 2000-node networks, $k \in \{0, 1, 2, 3, 4\}$.
Source: By the author.

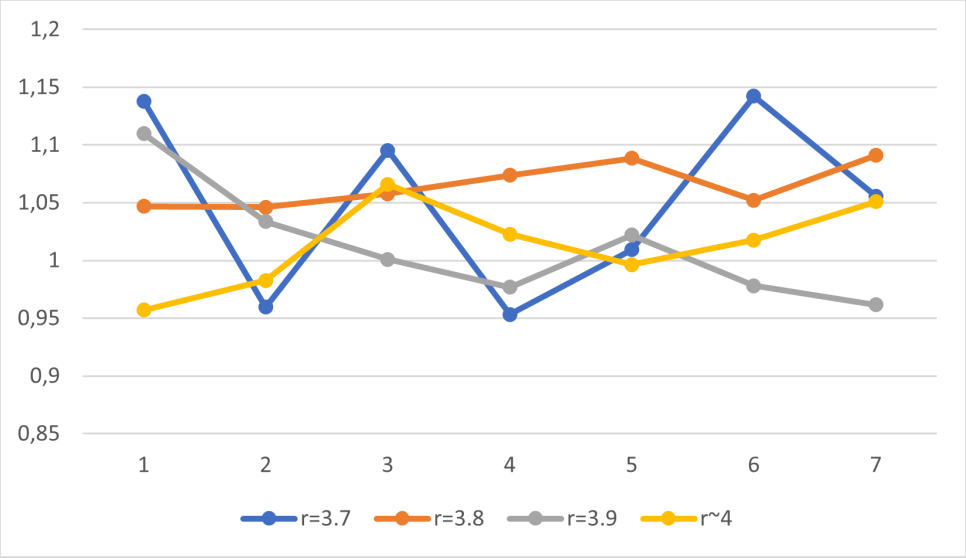

Figure 40 – Ratio of accuracy between 500-node and 2000-node networks, $k \in \{5, 6, 7, 8, 9\}$.
Source: By the author.

Furthermore, we use the RADAR algorithm to spot the outlying nodes and it is combined with computational geometric methods such as the Delaunay Triangulation. An improvement here over the approach used in (12) is that while the preceding work allowed for an unique visualization for each network only, by using RADAR in combination with computational geometric methods we allow instead for a selection of the outlying nodes induced by the outlying edges and, in this manner, we generate several distinct visualizations of the same orbit. In other words, the exact same network now can produce several geometries, depending on the parameters used.

3 RESULTS

We present results for the topological matrix, multi-tap LFSR, heat diffusion, correlation network projection, and anomaly network projection. We ran our tests in double-precision floating point conformant to the IEEE-754 standard *or* arbitrary precision decimal arithmetic up to 1,000 digits. We made use of software packages R (199), Octave (200), Mathematica (201), Weka (202), LIBSVM (203), JGraphT (204), NetworkX (205) and Gephi (206).

For the topological matrix, we built its data structure as a dense matrix with dimensions of $10^5 \times 10^5$ – 10 billion elements total. That is, we compute 10^5 different parametrizations of the k-logistic map with $r \sim 4$ save for the small perturbations – < 0.001 – added to the system, and the orbits' size is always equal to 10^5. We allow for several thousand transient iterations of the k-logistic map before doing any actual computation. Then, we compute a window with the frequency distributions of the top-n points. This window has sizes $\in \{1,000, 5,000, 10,000, 20,000\}$.

For verifying the robustness of the PRNG, statistical tests are applied via NIST SP 800-22 Rev. 1a and SP 800-90B (71, 207), TestU01 version 1.2.3 of the University of Montréal, Canada (208) and PractRand pre-release version 0.95 by Chris Doty-Humphrey (209) suites. The implementation of the SP 800-22 suite Rev. 1a available on the site of the NIST presents flaws as instability and output presenting wrong results for the tests, for this reason for this work it was employed an alternative implementation in Python in place of official implementation. The NIST results are condensed in the Figure 9. The orbits studied have 10 million bytes for NIST, 480 million bytes for TestU01 and 1 trillion bytes for PractRand. NIST and PractRand received as inputs base-2 maps $k \in \{0, 5, 10, 15, 20, 25, 30\}$, instead of the decimal map. As the orbits differ only up to a simple change of numeric base, the principles studied in the base-2 k-logistic map are precisely the same we investigate using the base-10 k-logistic map, which we use in all other tests. The complete set of NIST results is presented in the Appendix. TestU01's SmallCrush test received IEEE-754 floating-point data each converted from one 8-byte stream.

For the heat equation applied on the k-logistic map, we used a $\Delta t = 0.1$ and sufficient boundary conditions in order to conserve the energy of the system. Orbits of the k-logistic maps are sets with 2,000 points each. 10 distinct diffused orbits were subject to all-pairs DTW computation, that is, a 10×10 matrix with its element $M_{i,j}$ as the DTW distance of the pair i, j and then their mean and standard deviation were recorded.

For the baseline networks, we projected the networks onto the Cartesian plane

using a radius $r = 0.12$, vertical factor of $y = 1.0$ and a horizontal factor of $x = 0.005$. PCA plots were drawn taking into account the components with highest variances and, therefore, the highest weight and significance. To generate the violin plots we followed the procedure of Alves and Bruno (12), partitioning the space into 11 horizontal stripes or bands.

For building the $\boldsymbol{X}$ matrix of attributes for use with RADAR, we choose as attributes x and y coordinates of the nodes, indices Δ between the point and its nearest neighbor in the matrix profile, mean Spearman correlation between windows, variance of the Spearman correlation between windows, mean DTW distance between windows, variance of the DTW distance between windows, number of neighbors within radii $= \{0.03, 0.06, 0.12\}$ and estimate of density for radii $= \{0.01, 0.02, 0.04, 0.08\}$. Structural tests on graphs whose DTW values $\in \{> 1\sigma, > 2\sigma, < -1\sigma\}$ would not complete, due to an exceedingly large number of edges, in the order of over 290K. We present results with smaller network sizes in place of the larger networks in the Annex. The projected networks were used for the Delaunay Triangulation plots after application of the RADAR algorithm. We use 3 samples for each k-logistic map parametrization.

Transformation of networks into feature vectors via LLNA, LLNA-BP and LLNA-DTEP performed as specified on their respective references. Rules used for LLNA, LLNA-BP and LLNA-DTEP were B135678/S03456 and B0157/S457 due to their strong performance on synthetic networks. All LLNAs ran for 500 iterations and the first 20 transient iterations were thrown out. Structural measurements relied on a six-features histogram: comprising of the average hierachical degrees levels 1, 2 and 3, the average path length, average transitivity and degree assortativity. Statistics from Gephi include unweighted, undirected network diameter, mean clustering coefficient, modularity, average path length, mean degree and statistical inference community detection (206). Classification was performed via SVM 100 times for every test and mean accuracy plus standard deviation are reported in percentages. Classes were split in two sets. The first comprises of classes $k \in \{0, 1, 2, 3, 4\}$ and the other of classes $k \in \{5, 6, 7, 8, 9\}$. SVM was preferred over other alternatives due to its learning consistency guarrantees with a convex optimization algorithm.

All the LLNA implementations and DTW distance calculations were coded in Java by the author, to ensure a sane and parametrically consistent comparison between the diverse applied methods. RADAR was coded by the author in Python. The matrix profile codes makes extensive use of the package SCAMP (210).

- Application of 8 threshold values for 8 different monochrome realizations.
- Morphological transformations into spatial, weighted, graphs.
- Topological transformations into unweighted, undirected graphs.

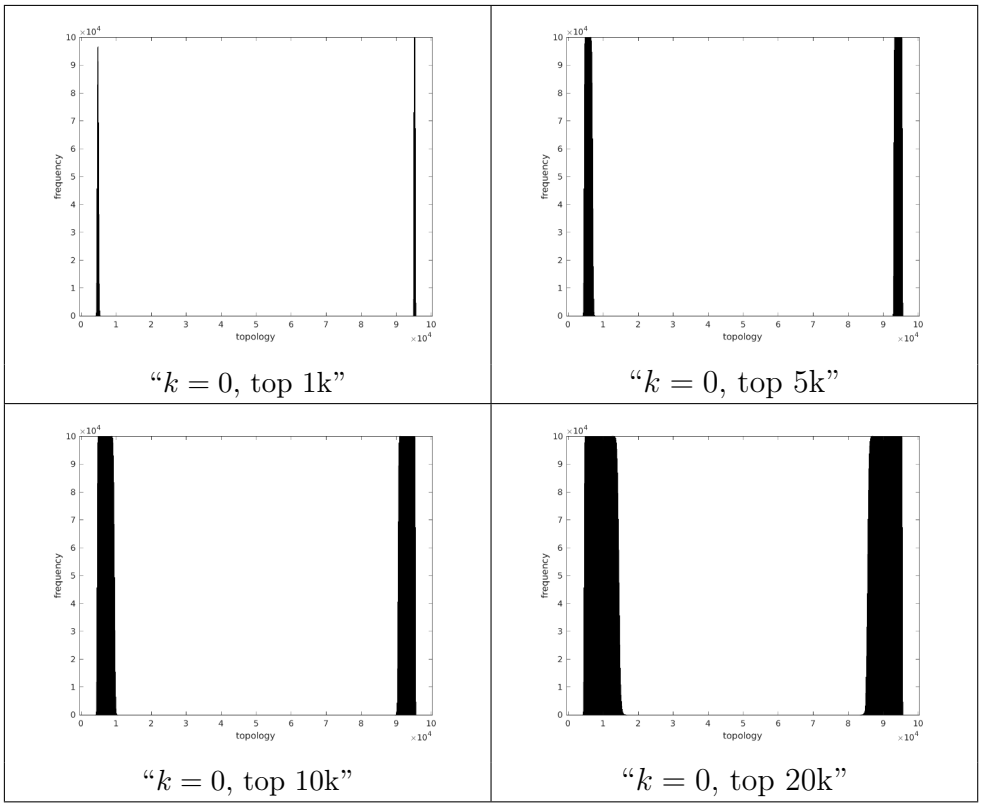

Figure 41 – Histograms of topological $10^5 \times 10^5$ matrices for the k-logistic map with $k = 0$ and $r \sim 4.0$.
Source: By the author.

Default visualizations were performed by Mathematica for unweighted, undirected graphs. It was computationally doable to visualize the $\{> 1\sigma, > 2\sigma, < -1\sigma\}$ graphs beside the $< -2\sigma$ counterparts.

Eventually we compare the k-logistic map, $k \in [0, 9]$, against the quantum random numbers deployed by the Australian National University $(211, 212)$ and also the random numbers generated by the /dev/random Linux device.

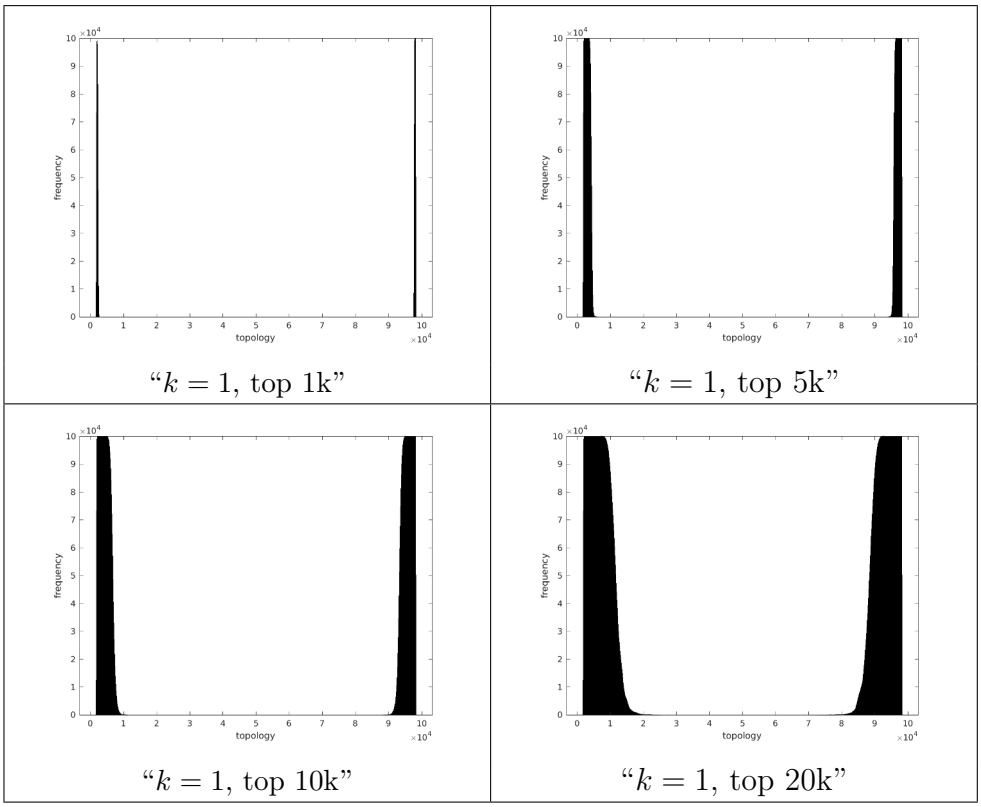

Figure 42 – Histograms of topological $10^5 \times 10^5$ matrices for the k-logistic map with $k = 1$ and $r \sim 4.0$.
Source: By the author.

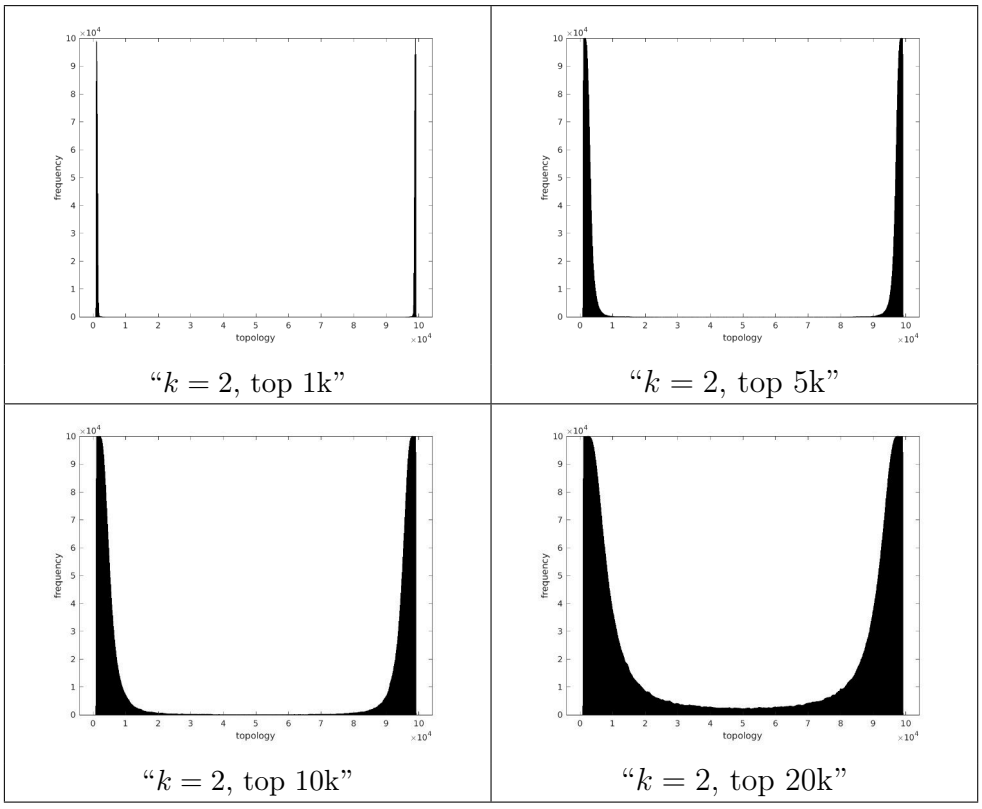

Figure 43 – Histograms of topological $10^5 \times 10^5$ matrices for the k-logistic map with $k = 2$ and $r \sim 4.0$.
Source: By the author.

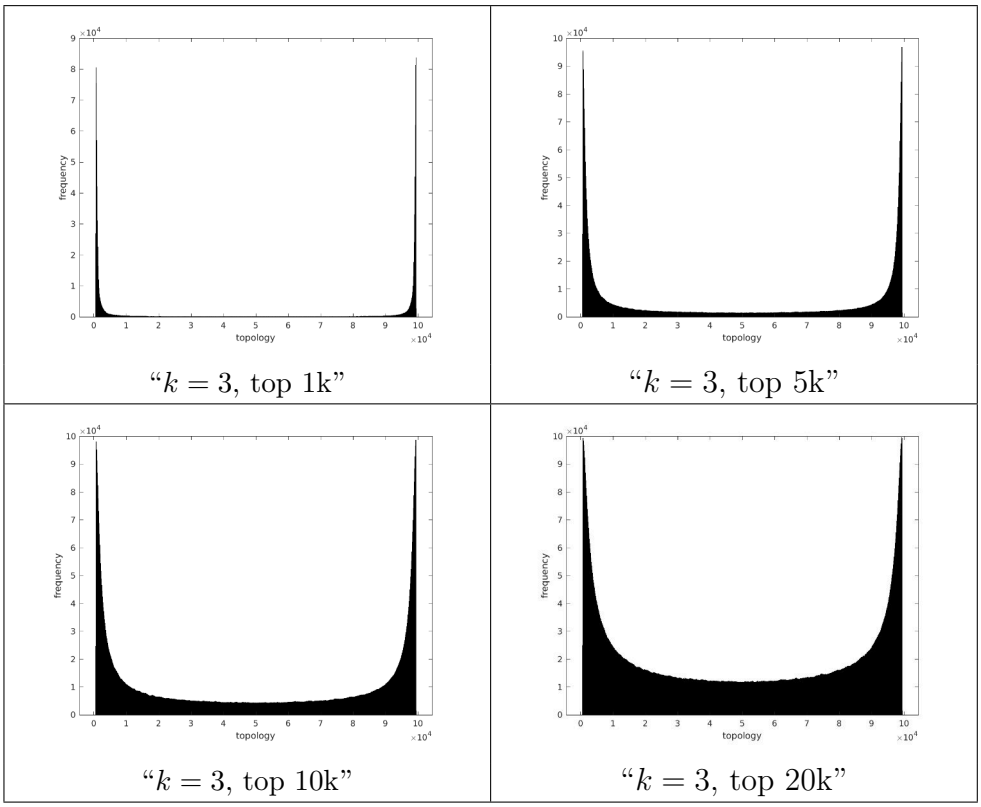

Figure 44 – Histograms of topological $10^5 \times 10^5$ matrices for the k-logistic map with $k = 3$ and $r \sim 4.0$.
Source: By the author.

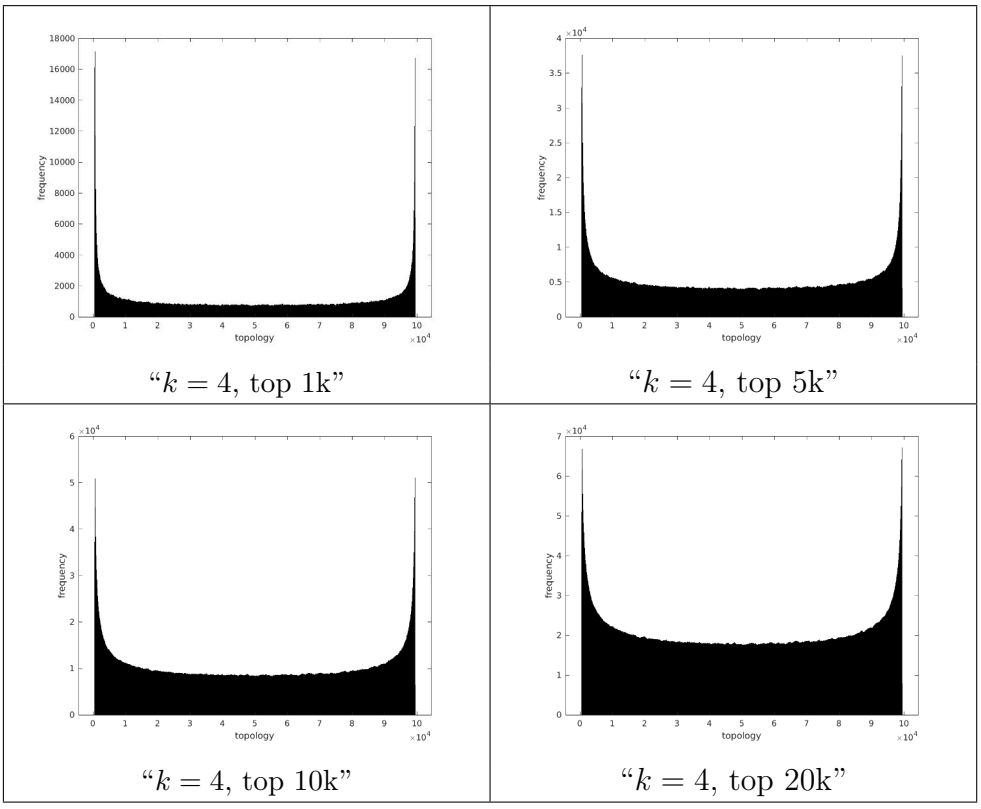

Figure 45 – Histograms of topological $10^5 \times 10^5$ matrices for the k-logistic map with $k = 4$ and $r \sim 4.0$.
Source: By the author.

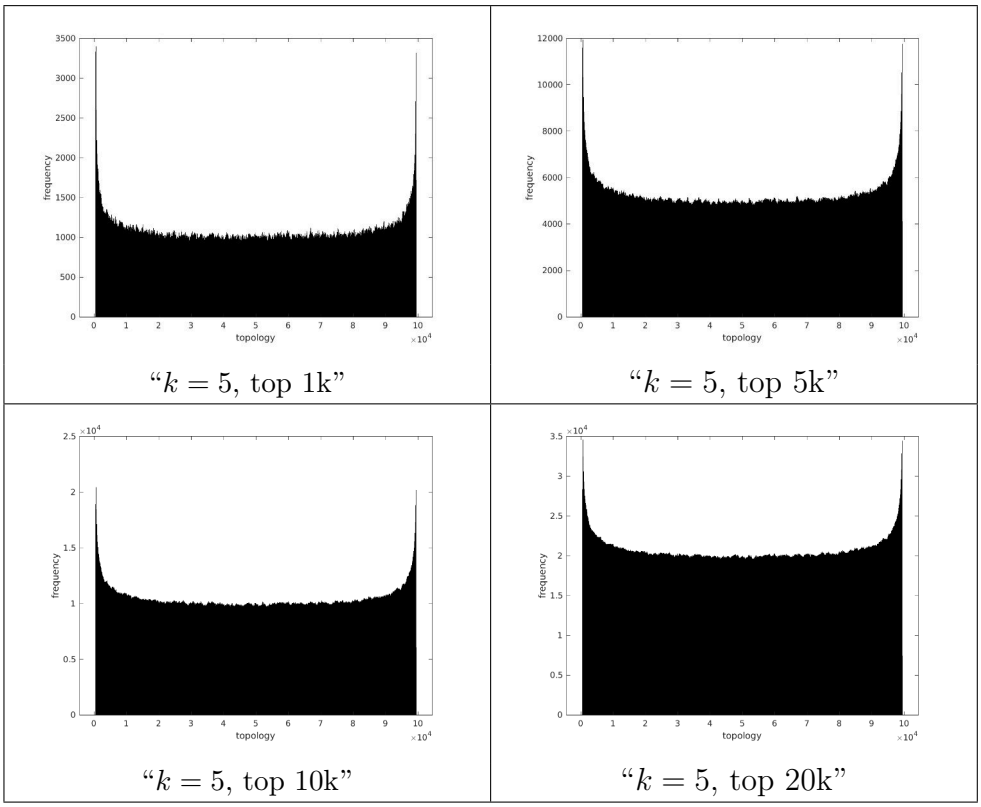

Figure 46 – Histograms of topological $10^5 \times 10^5$ matrices for the k-logistic map with $k = 5$ and $r \sim 4.0$.
Source: By the author.

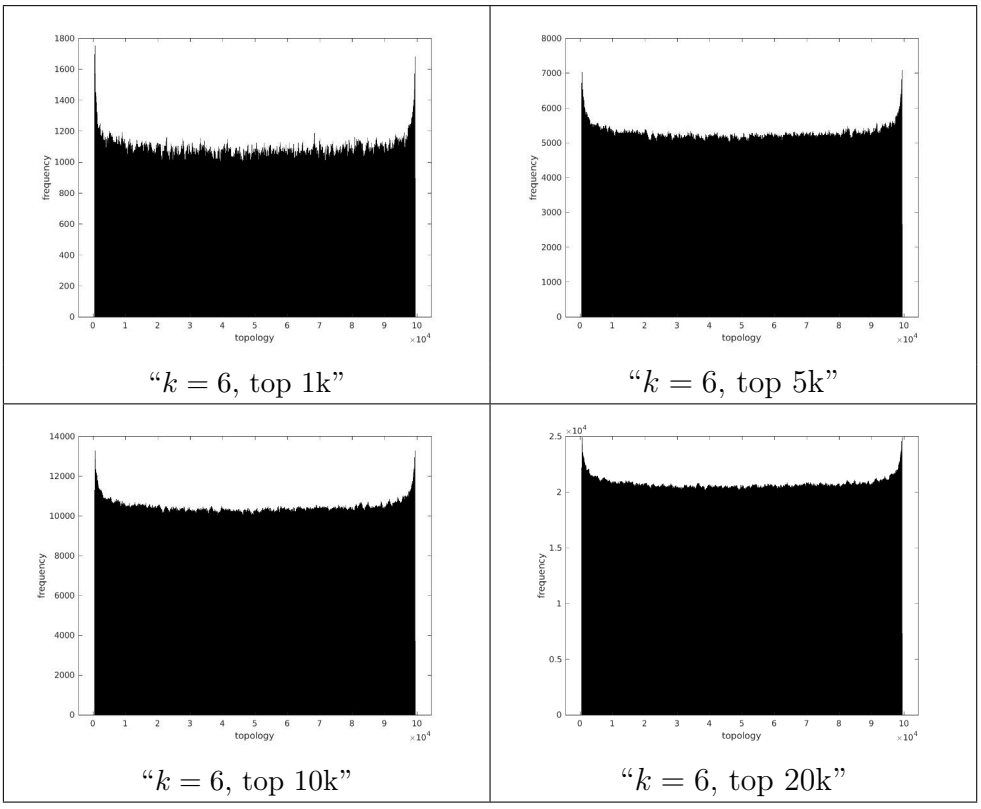

Figure 47 – Histograms of topological $10^5 \times 10^5$ matrices for the k-logistic map with $k = 6$ and $r \sim 4.0$.
Source: By the author.

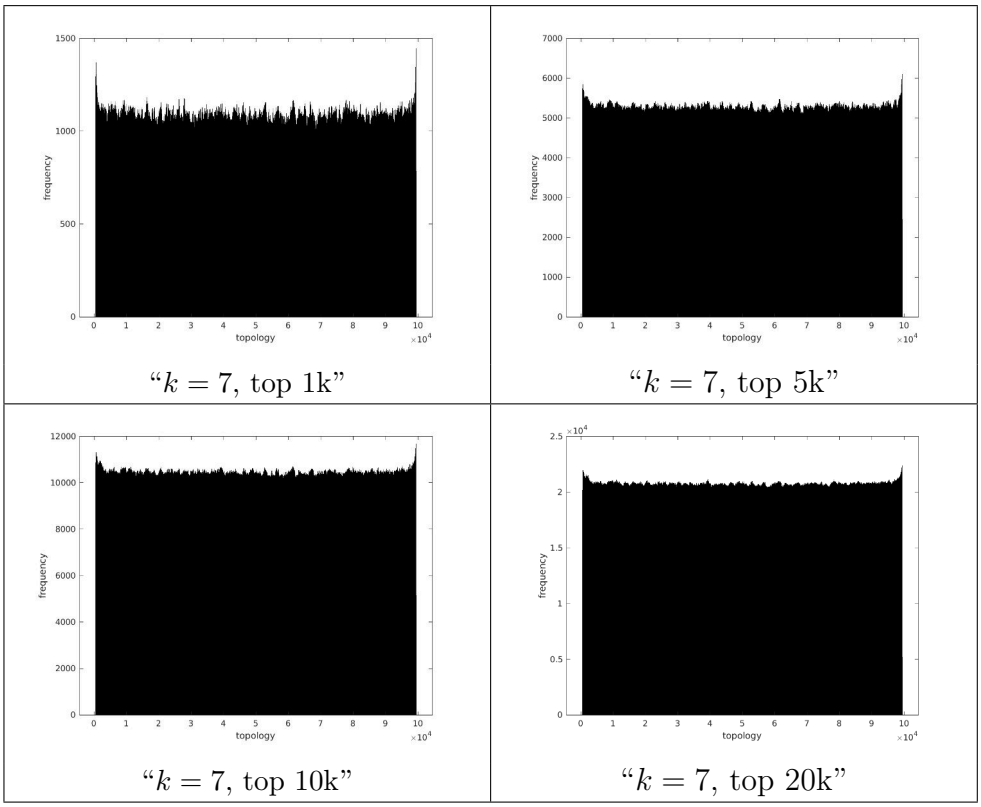

Figure 48 – Histograms of topological $10^5 \times 10^5$ matrices for the k-logistic map with $k = 7$ and $r \sim 4.0$.
Source: By the author.

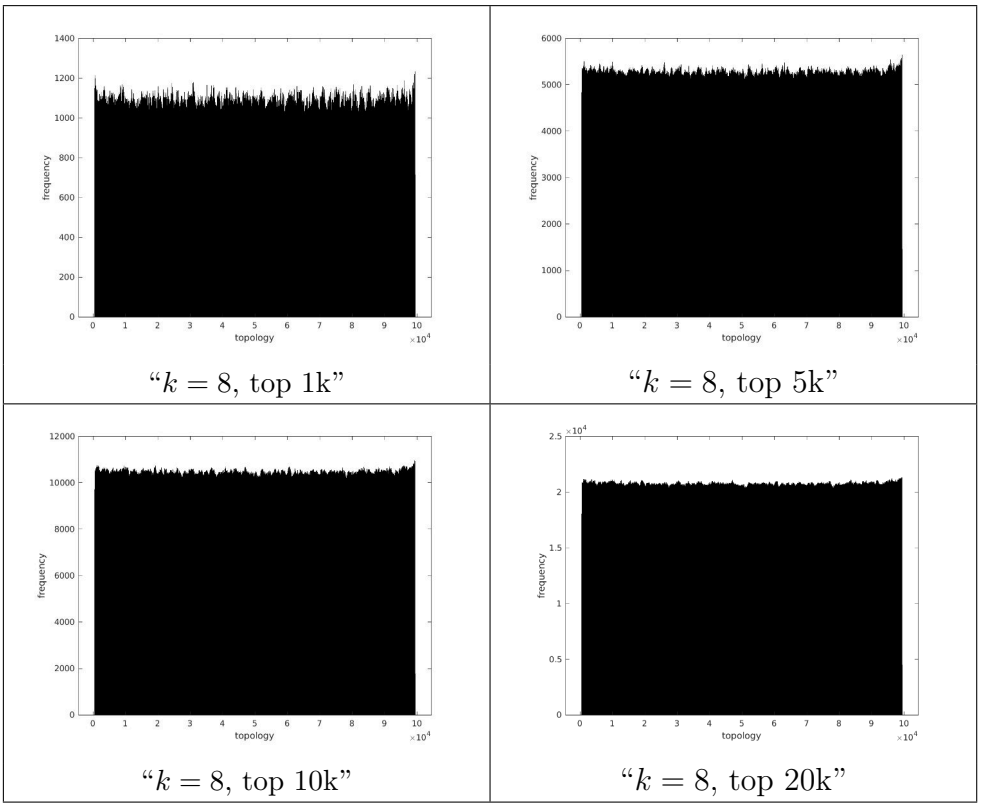

Figure 49 – Histograms of topological $10^5 \times 10^5$ matrices for the k-logistic map with $k = 8$ and $r \sim 4.0$.
Source: By the author.

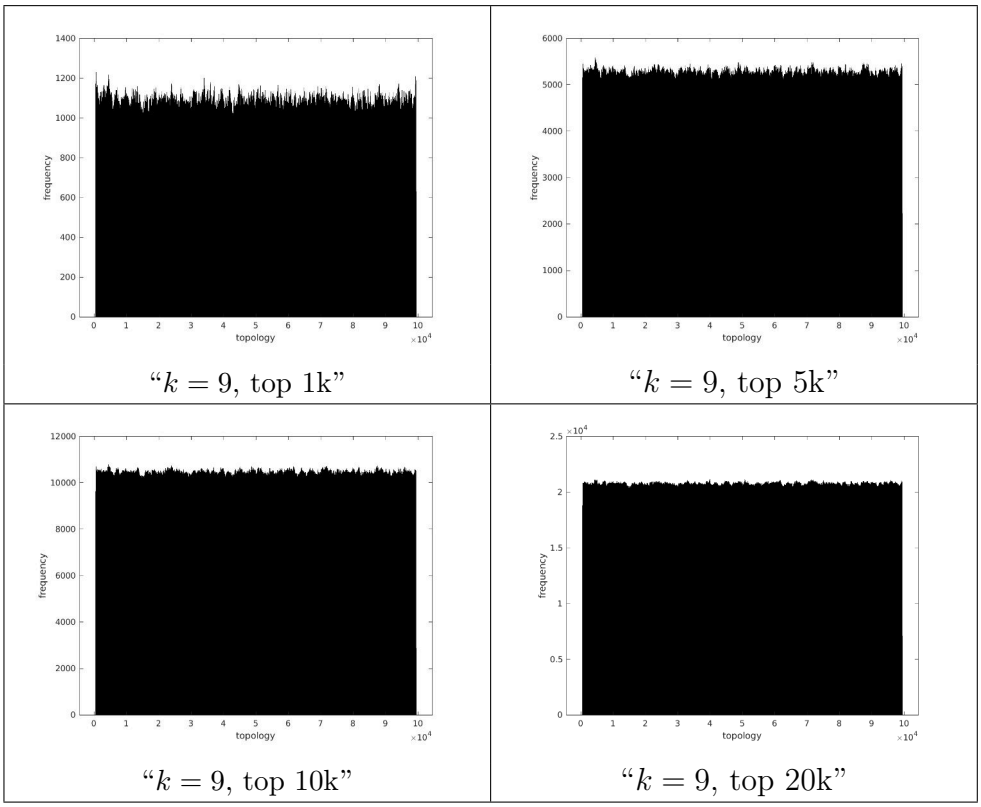

Figure 50 – Histograms of topological $10^5 \times 10^5$ matrices for the k-logistic map with $k = 9$ and $r \sim 4.0$.
Source: By the author.

Table 3 – Failures for Smallcrush RNG tests for the k-logistic map with $k = 0$ (base 2) and $r \sim 4.0$.

test #	test	baseline	x8	LFSR	x8 LFSR
1	BirthdaySpacings	*	*		
2	Collision	*	*		
3	Gap	*	*	*	
4	SimpPoker	*	*		
5	CouponCollector	*	*		
6	MaxOft	*	*		
6	MaxOft AD	*	*		*
7	WeightDistrib	*	*	*	*
9	HammingIndep	*	*	*	*
10	RandomWalk1 H	*	*	*	*
10	RandomWalk1 M	*	*	*	*
10	RandomWalk1 J	*	*	*	*
10	RandomWalk1 R	*	*	*	
10	RandomWalk1 C	*	*		

Source: By the author.

Table 4 – Failures for Smallcrush RNG tests for the k-logistic map with $k = 5$ (base 2) and $r \sim 4.0$.

test #	test	baseline	x8	LFSR	x8 LFSR
1	BirthdaySpacings	*	*		
2	Collision	*	*		
3	Gap	*	*	*	
4	SimpPoker	*	*		
5	CouponCollector	*	*		
6	MaxOft	*	*		
6	MaxOft AD	*	*		*
7	WeightDistrib	*	*	*	
9	HammingIndep	*	*	*	*
10	RandomWalk1 H	*	*	*	*
10	RandomWalk1 M	*	*	*	*
10	RandomWalk1 J	*	*	*	*
10	RandomWalk1 R	*	*		
10	RandomWalk1 C	*	*		

Source: By the author.

Table 5 – Failures for Smallcrush RNG tests for the k-logistic map with $k = 10$ (base 2) and $r \sim 4.0$.

test #	test	baseline	x8	LFSR	x8 LFSR
1	BirthdaySpacings	*			
2	Collision	*	*		
3	Gap	*	*		
4	SimpPoker		*		
5	CouponCollector	*	*		
6	MaxOft	*	*		
6	MaxOft AD	*	*	*	*
7	WeightDistrib		*	*	*
9	HammingIndep	*		*	*
10	RandomWalk1 H	*	*	*	*
10	RandomWalk1 M	*	*	*	*
10	RandomWalk1 J	*	*	*	*
10	RandomWalk1 R	*			
10	RandomWalk1 C	*			

Source: By the author.

Table 6 – Failures for Smallcrush RNG tests for the k-logistic map with $k = 15$ (base 2) and $r \sim 4.0$.

test #	test	baseline	x8	LFSR	x8 LFSR
1	BirthdaySpacings	*			
2	Collision	*	*		
3	Gap	*			
4	SimpPoker				
5	CouponCollector	*	*		
6	MaxOft	*			
6	MaxOft AD	*	*		
7	WeightDistrib				
9	HammingIndep				
10	RandomWalk1 H		*		
10	RandomWalk1 M				
10	RandomWalk1 J				
10	RandomWalk1 R	*			
10	RandomWalk1 C	*			

Source: By the author.

Table 7 – Failures for Smallcrush RNG tests for the k-logistic map with $k = 20$ (base 2) and $r \sim 4.0$.

test #	test	baseline	x8	LFSR	x8 LFSR
1	BirthdaySpacings	*			
2	Collision				
3	Gap	*	*		
4	SimpPoker				
5	CouponCollector	*	*		
6	MaxOft	*			
6	MaxOft AD				
7	WeightDistrib		*		
9	HammingIndep				
10	RandomWalk1 H				
10	RandomWalk1 M				
10	RandomWalk1 J				
10	RandomWalk1 R				
10	RandomWalk1 C				

Source: By the author.

Table 8 – Failures for Smallcrush RNG tests for the k-logistic map with $k = 25$ (base 2) and $r \sim 4.0$.

test #	test	baseline	x8	LFSR	x8 LFSR
1	BirthdaySpacings				
2	Collision				
3	Gap	*	*		
4	SimpPoker				
5	CouponCollector	*	*		
6	MaxOft	*			
6	MaxOft AD				
7	WeightDistrib				
9	HammingIndep				
10	RandomWalk1 H				
10	RandomWalk1 M				
10	RandomWalk1 J				
10	RandomWalk1 R				
10	RandomWalk1 C				

Source: By the author.

Table 9 – Failures for Smallcrush RNG tests for the k-logistic map with $k = 30$ (base 2) and $r \sim 4.0$.

test #	test	baseline	x8	LFSR	x8 LFSR
1	BirthdaySpacings				
2	Collision				
3	Gap	*	*		
4	SimpPoker				
5	CouponCollector	*	*		
6	MaxOft	*			
6	MaxOft AD				
7	WeightDistrib		*		
9	HammingIndep				
10	RandomWalk1 H				
10	RandomWalk1 M				
10	RandomWalk1 J				
10	RandomWalk1 R				
10	RandomWalk1 C				

Source: By the author.

Table 10 – # failures for PractRand RNG tests for the k-logistic map (base 2) and $r \sim 4.0$.

k	baseline	x8	LFSR	x8 LFSR
0	107	147	199	96
5	111	158	212	97
10	125	187	223	95
15	125	202	251	96
20	121	201	252	97
25	125	200	245	96
30	127	205	252	95

Source: By the author.

Table 11 – Assessed minimal entropy for the k-logistic map (base 2) and $r \sim 4.0$. Minimal entropy for the vanilla LFSR at maximal 32-bit period is 0.74.

k	baseline	x8	LFSR	x8 LFSR
0	0,66	3,72	7,47	7,47
5	0,77	6,28	7,47	7,47
10	1,62	7,32	7,47	7,47
15	1,75	7,47	7,53	5,97
20	2,74	7,47	7,47	7,47
25	3,50	7,47	7,43	7,47
30	6,49	7,56	7,47	7,47

Source: By the author.

Table 12 – # failed SP 800-22 Rev. 1 NIST tests for the k-logistic map (base 2) and $r \sim 4.0$.

k	baseline	x8	LFSR	x8 LFSR
k=0	12	11	6	7
k=5	11	10	6	8
k=10	10	7	6	7
k=15	5	2	4	2
k=20	0	0	0	0
k=25	0	0	0	1
k=30	0	0	0	0

Source: By the author.

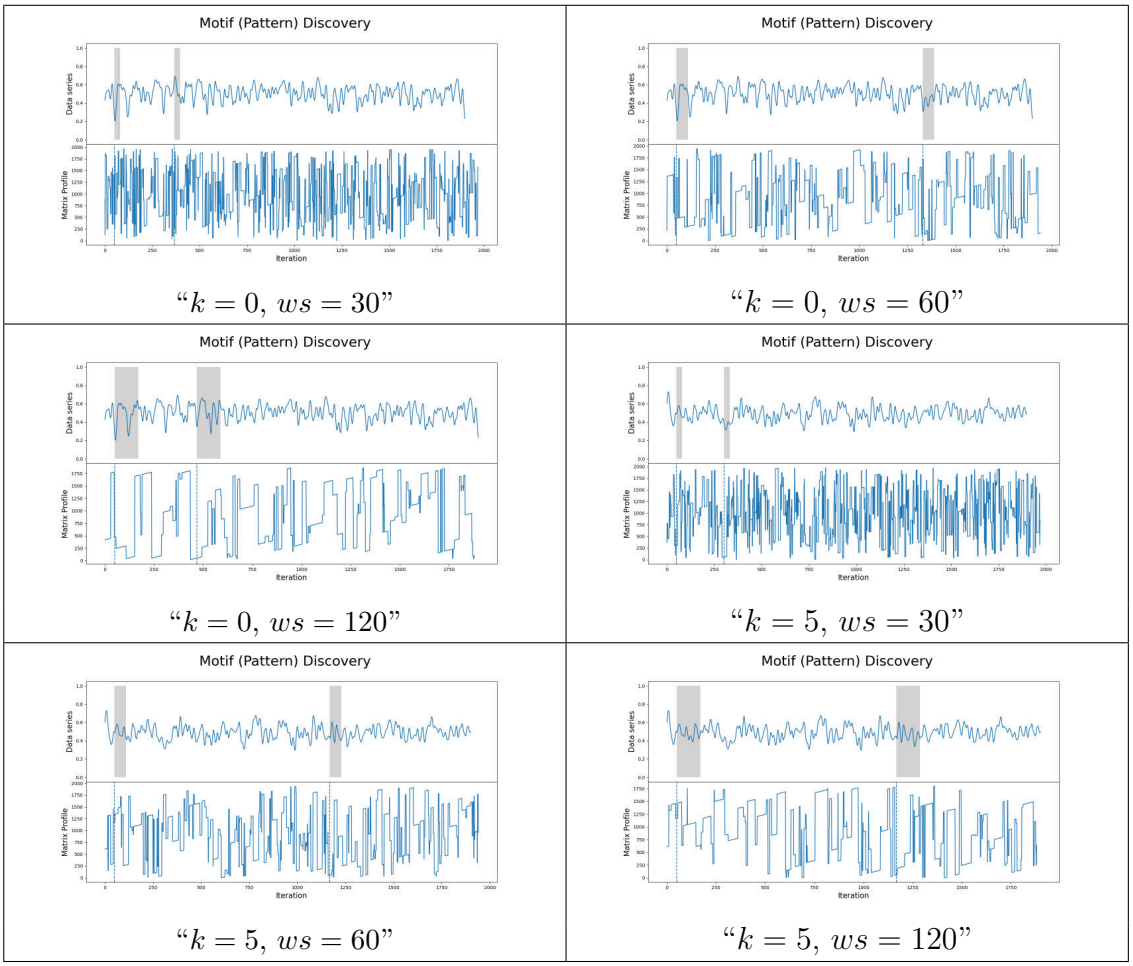

Figure 51 – Motif extraction with the matrix profile and different window sizes for the k-logistic map with $r \sim 4.0$ after diffusion.
Source: By the author.

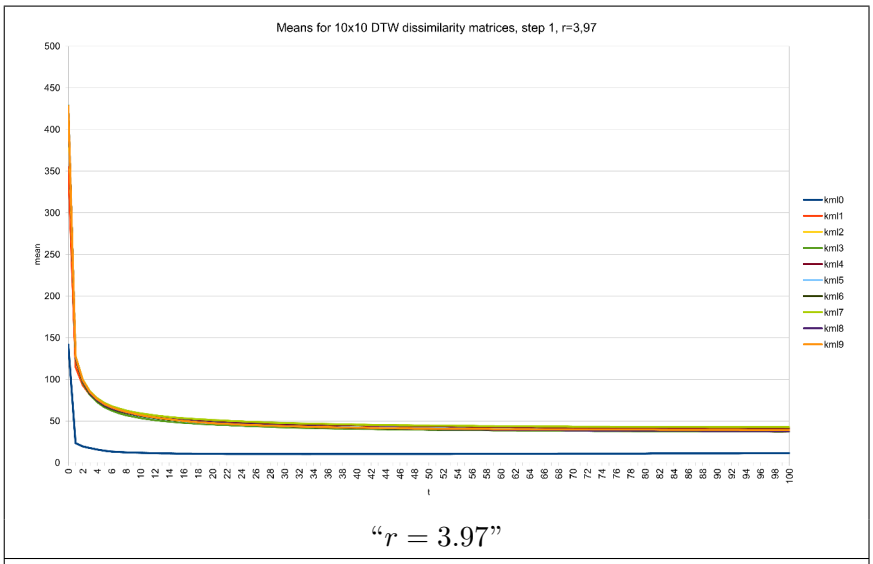

Figure 52 – Means for 10×10 DTW dissimilarity matrix and different diffusion intensities for the k-logistic map, diffusion time = 1.
Source: By the author.

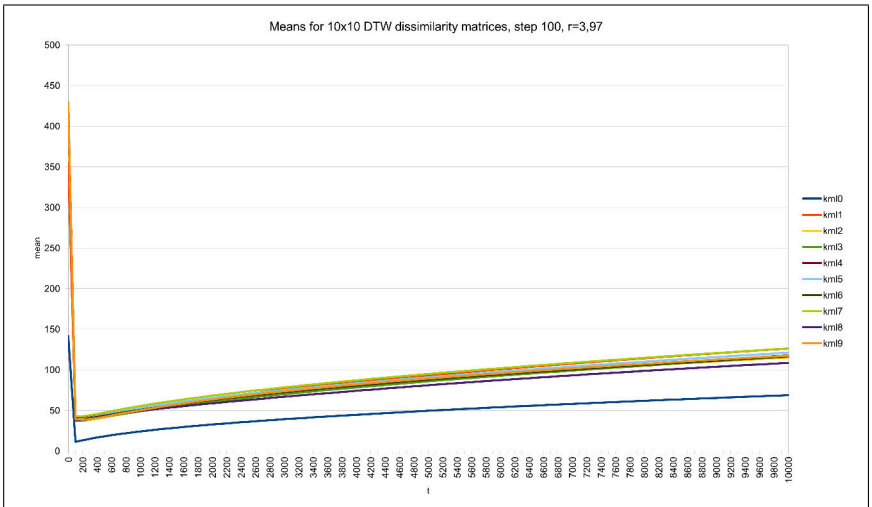

“$r = 3.97$, 100-pass”

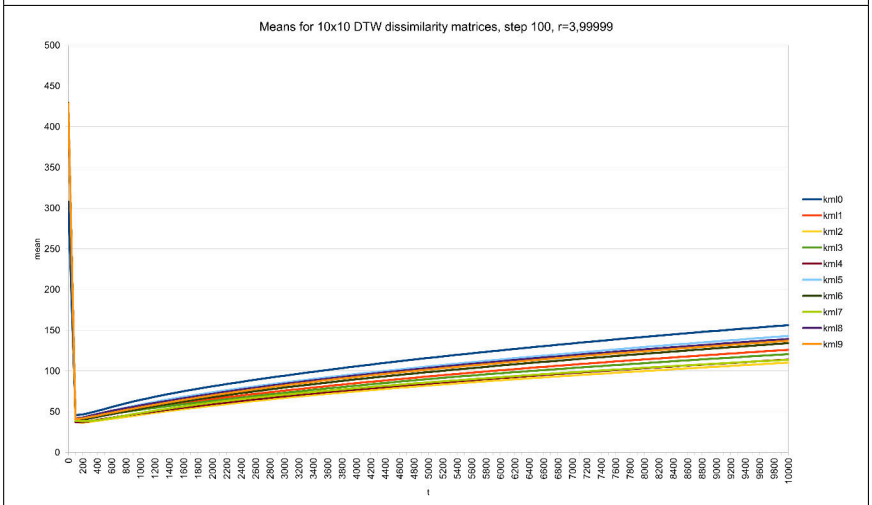

“$r \sim 4.0$, 100-pass”

Figure 53 – Means for 10×10 DTW dissimilarity matrix and different diffusion intensities for the k-logistic map, diffusion time = 100.
Source: By the author.

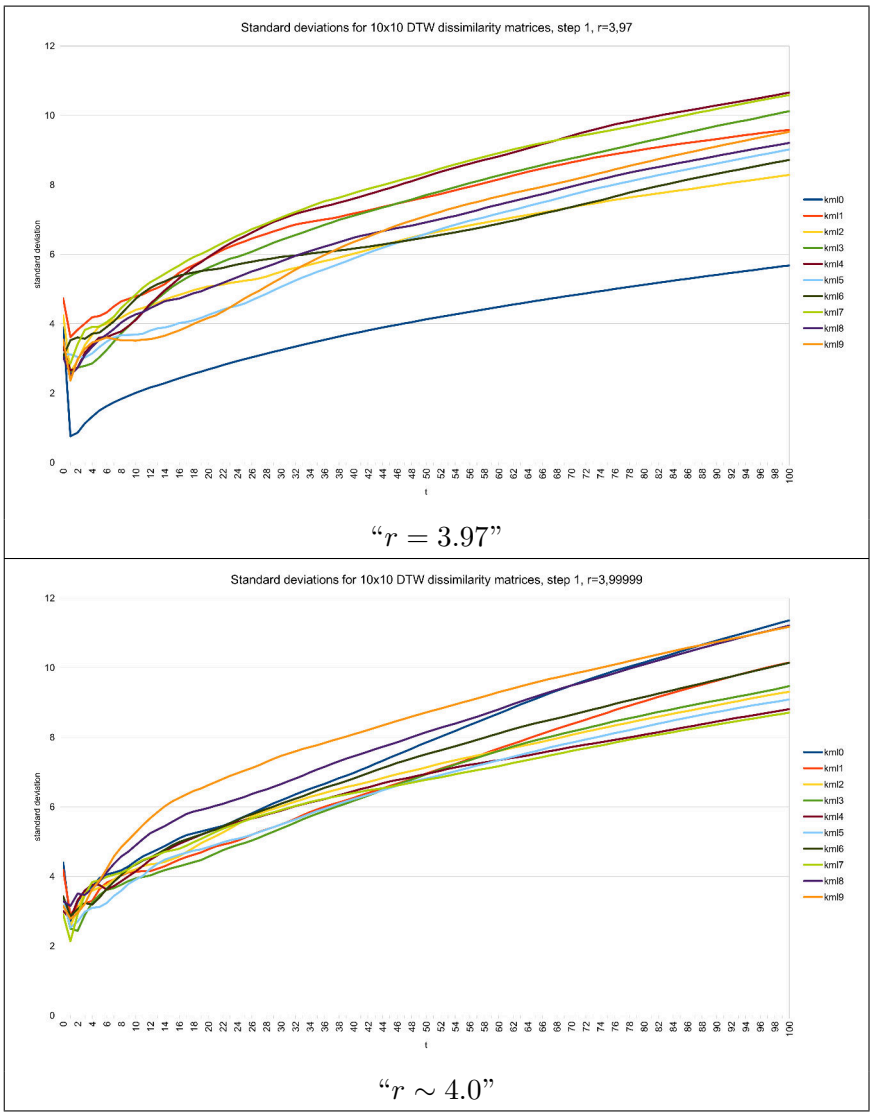

Figure 54 – Standard deviations for 10×10 DTW dissimilarity matrix and different diffusion intensities for the k-logistic map, one pass diffusion.
Source: By the author.

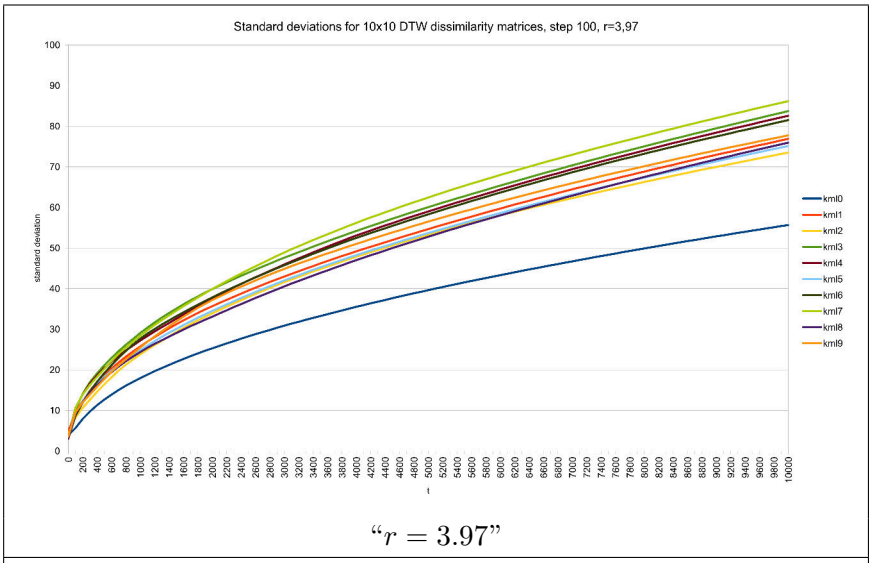

“$r = 3.97$”

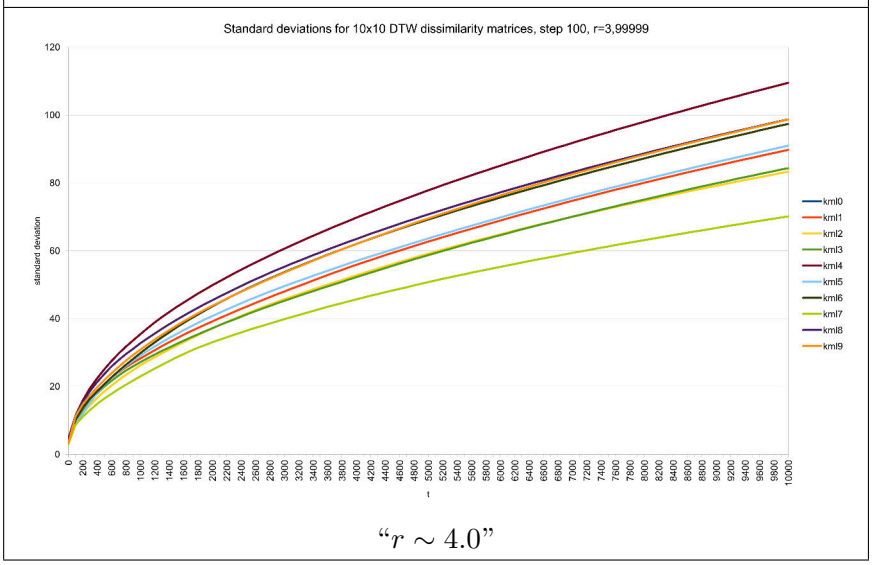

“$r \sim 4.0$”

Figure 55 – Standard deviations for 10×10 DTW dissimilarity matrix and different diffusion intensities for the k-logistic map, one hundred passes diffusion.
Source: By the author.

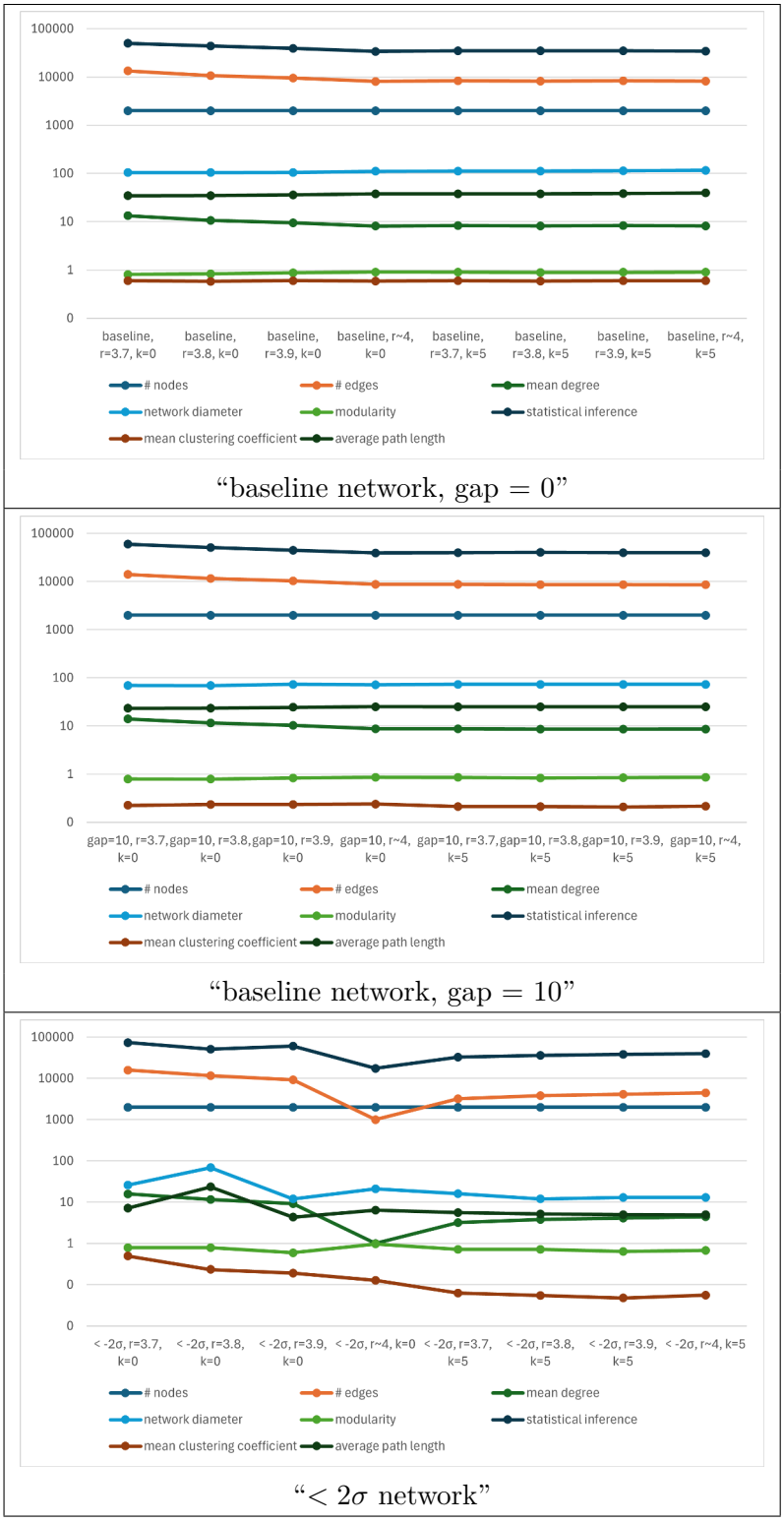

Figure 56 – Network statistics for baseline and $< 2\sigma$ networks.
Source: By the author.

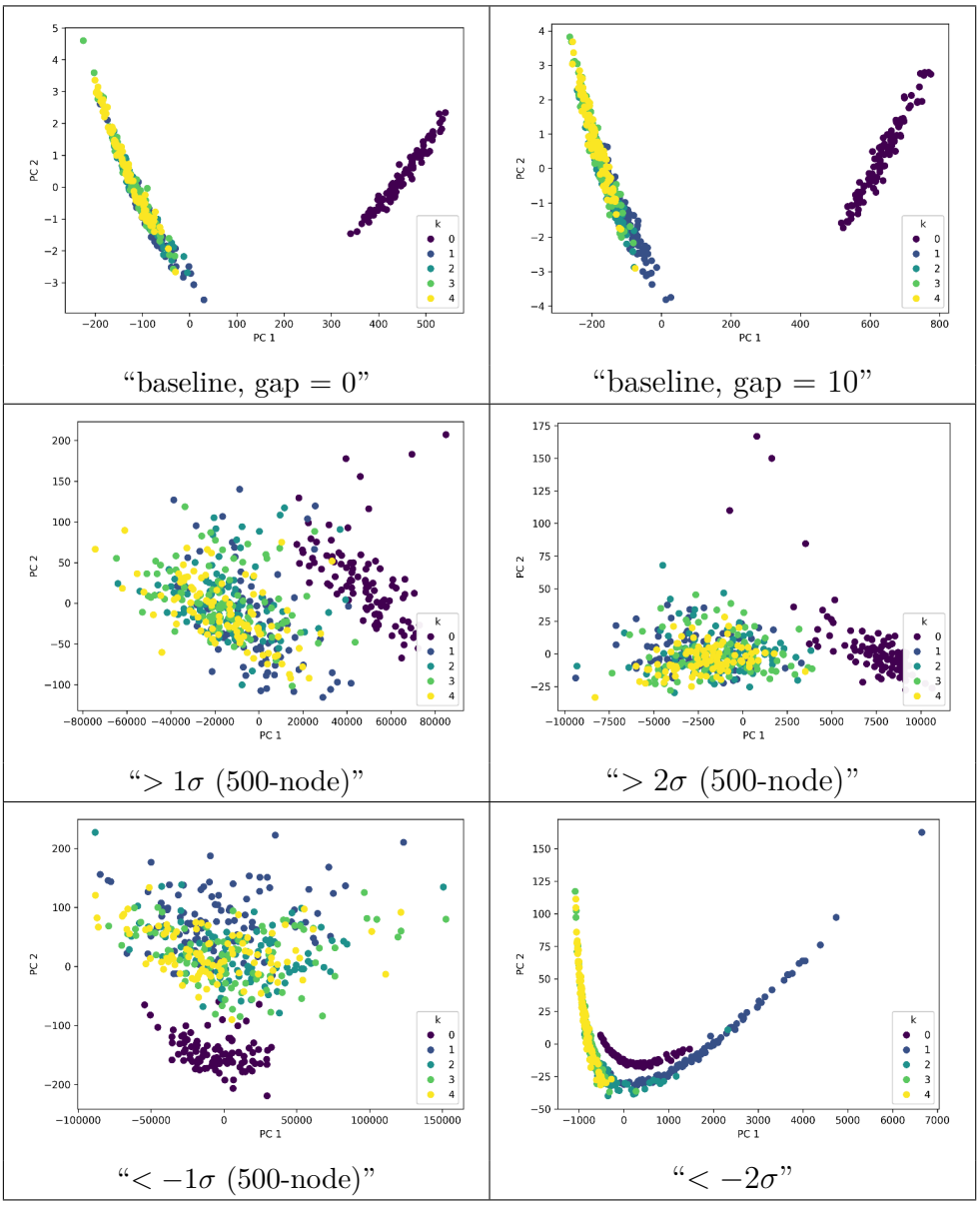

“baseline, gap = 0” “baseline, gap = 10”

“$> 1\sigma$ (500-node)” “$> 2\sigma$ (500-node)”

“$< -1\sigma$ (500-node)” “$< -2\sigma$”

Figure 57 – PCA projection for structural features of k-logistic map networks, $k \in \{0, 1, 2, 3, 4\}$, $r = 3.9$.
Source: By the author.

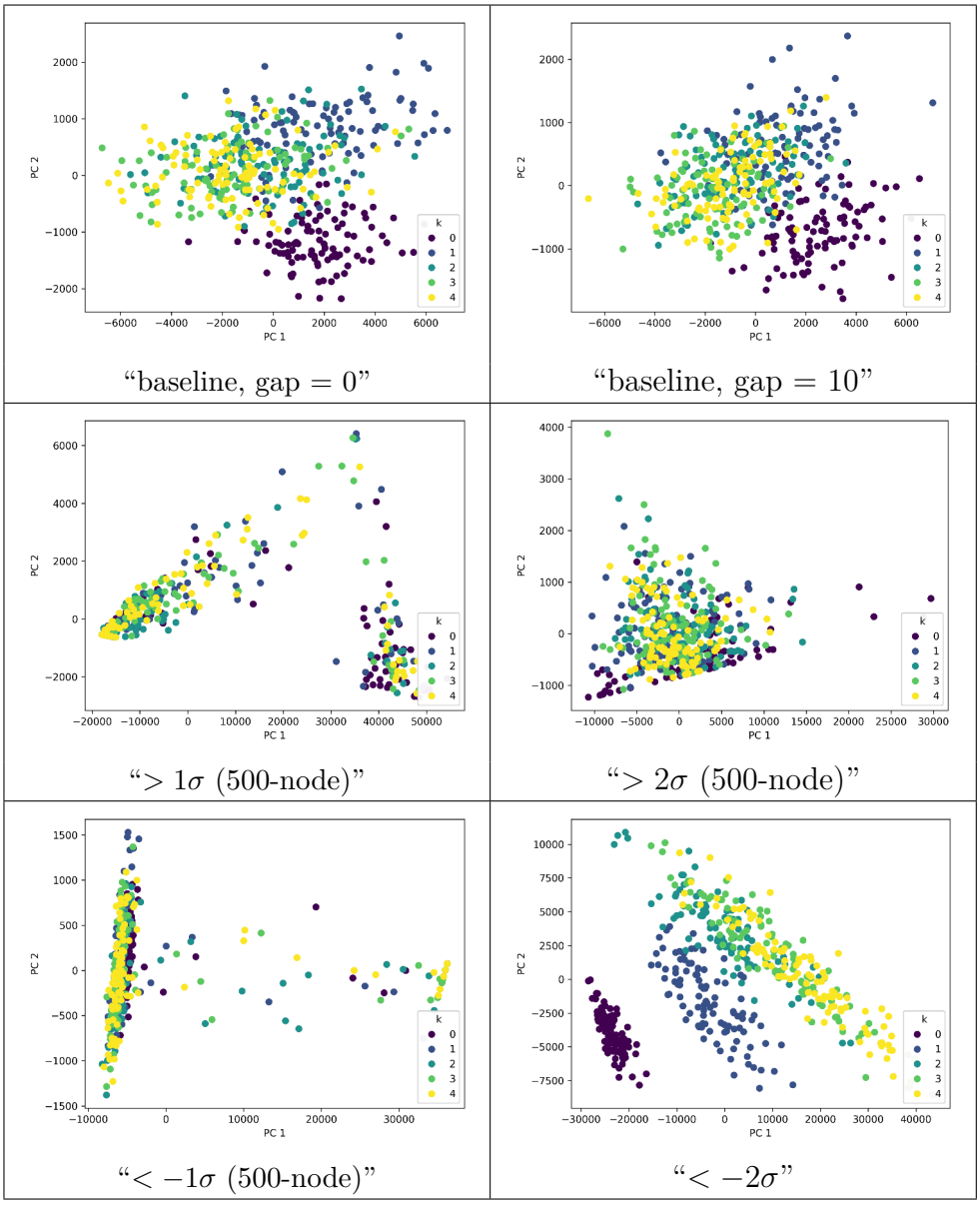

Figure 58 – PCA projection for rule B135678/S03456 LLNA features of k-logistic map networks, $k \in \{0, 1, 2, 3, 4\}$, $r = 3.9$.
Source: By the author.

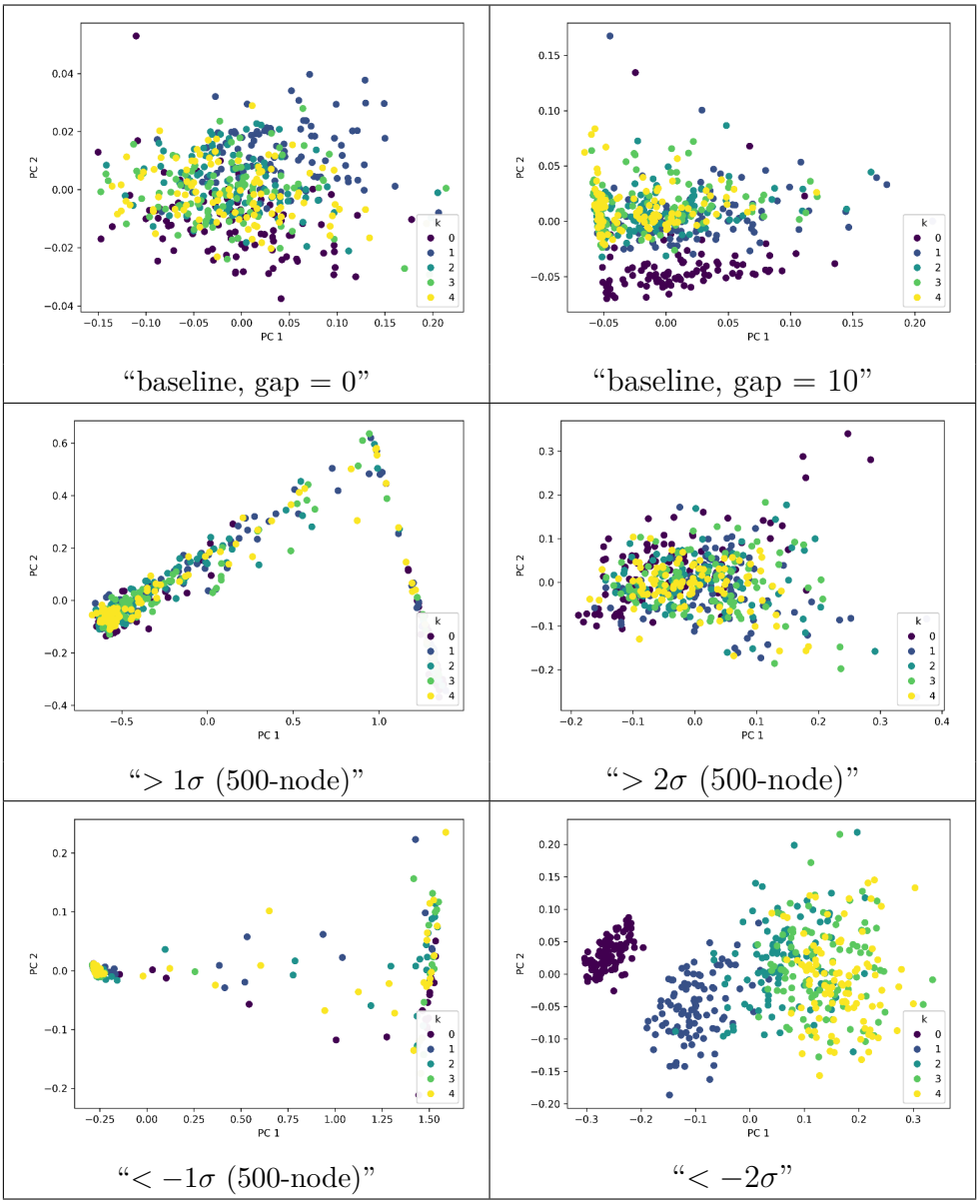

“baseline, gap = 0” “baseline, gap = 10”

“$> 1\sigma$ (500-node)” “$> 2\sigma$ (500-node)”

“$< -1\sigma$ (500-node)” “$< -2\sigma$”

Figure 59 – PCA projection for rule B135678/S03456 LLNA-BP features of k-logistic map networks, $k \in \{0, 1, 2, 3, 4\}$, $r = 3.9$.
Source: By the author.

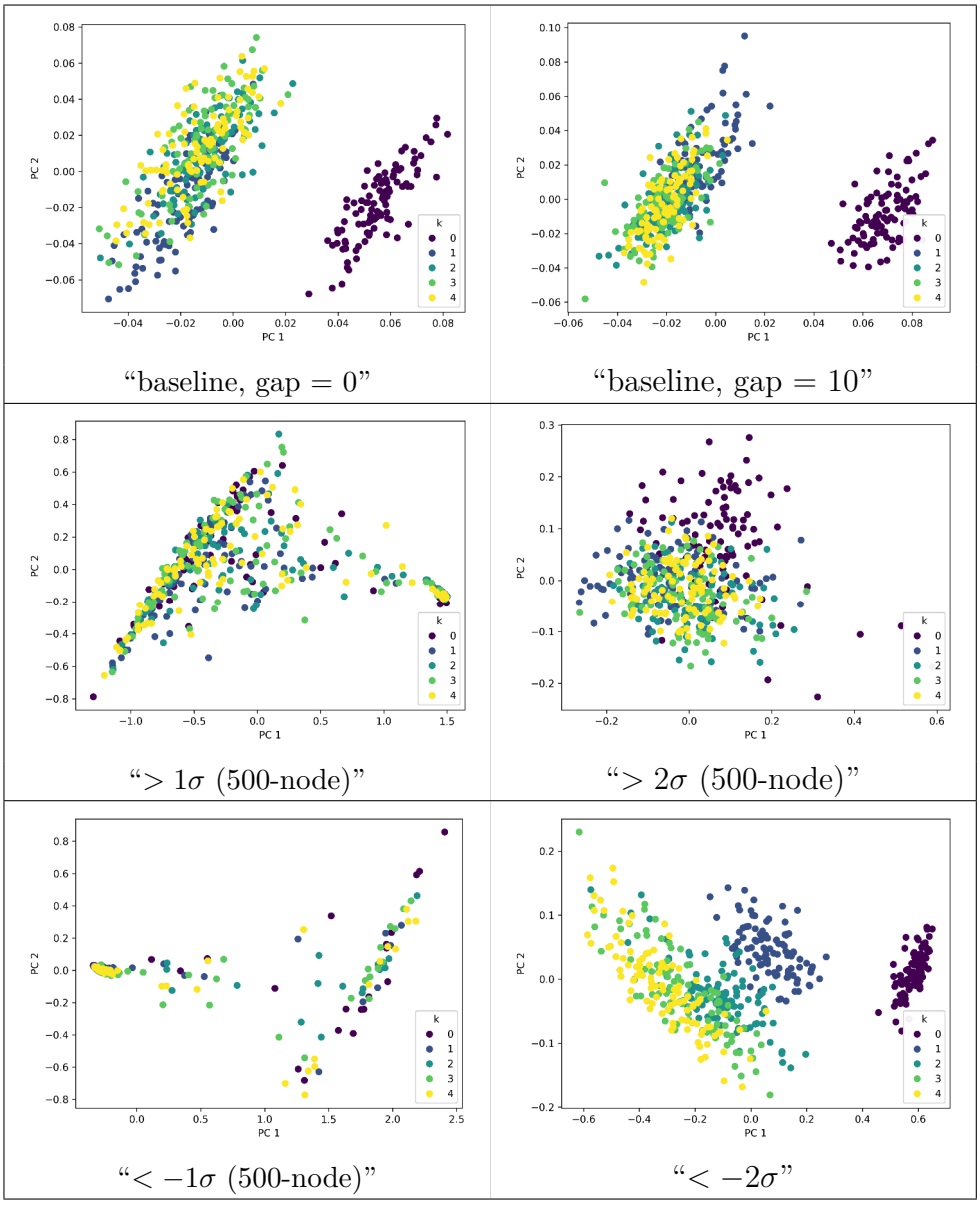

Figure 60 – PCA projection for rule B135678/S03456 LLNA-DTEP features of k-logistic map networks, $k \in \{0, 1, 2, 3, 4\}$, $r = 3.9$.
Source: By the author.

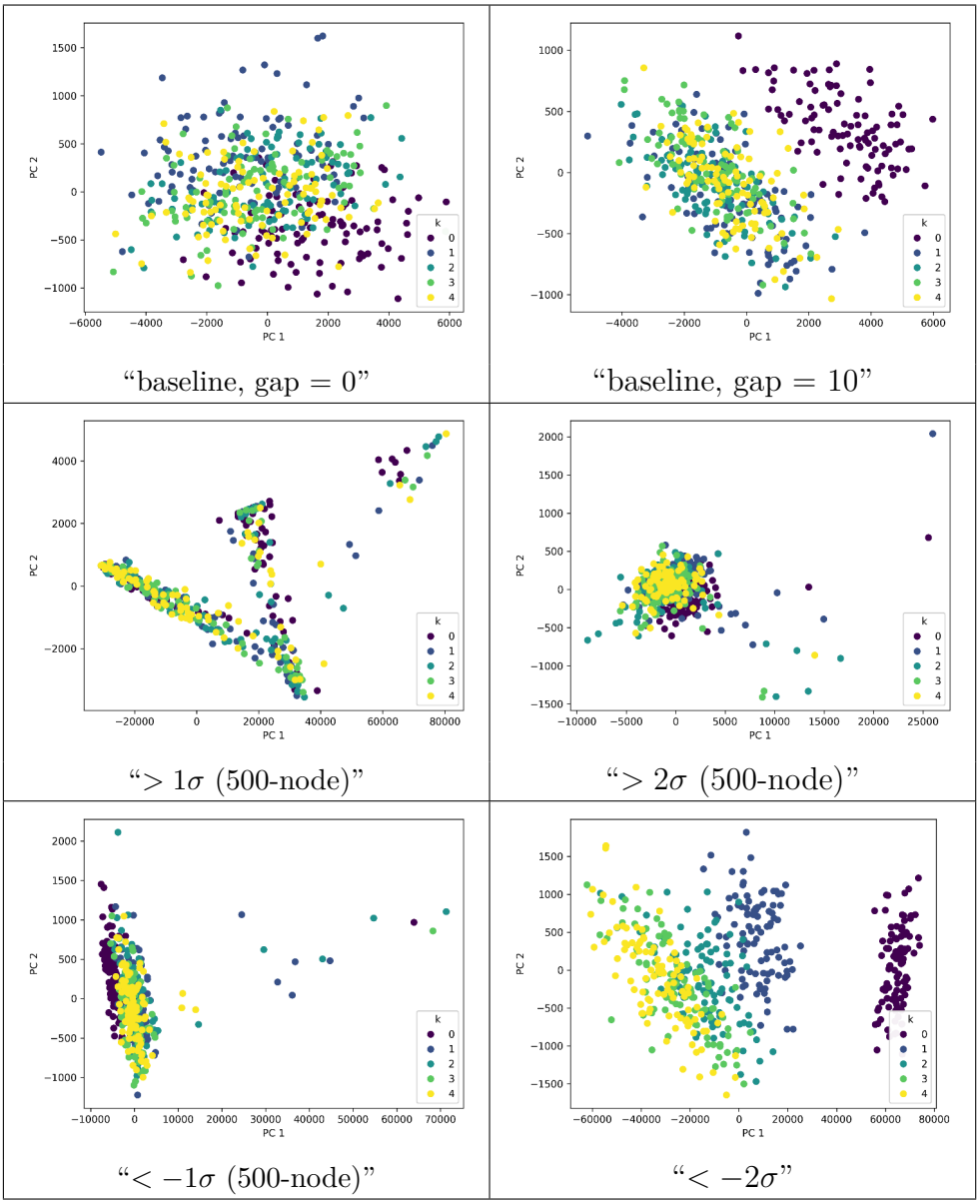

Figure 61 – PCA projection for rule B0157/S457 LLNA features of k-logistic map networks, $k \in \{0, 1, 2, 3, 4\}$, $r = 3.9$.
Source: By the author.

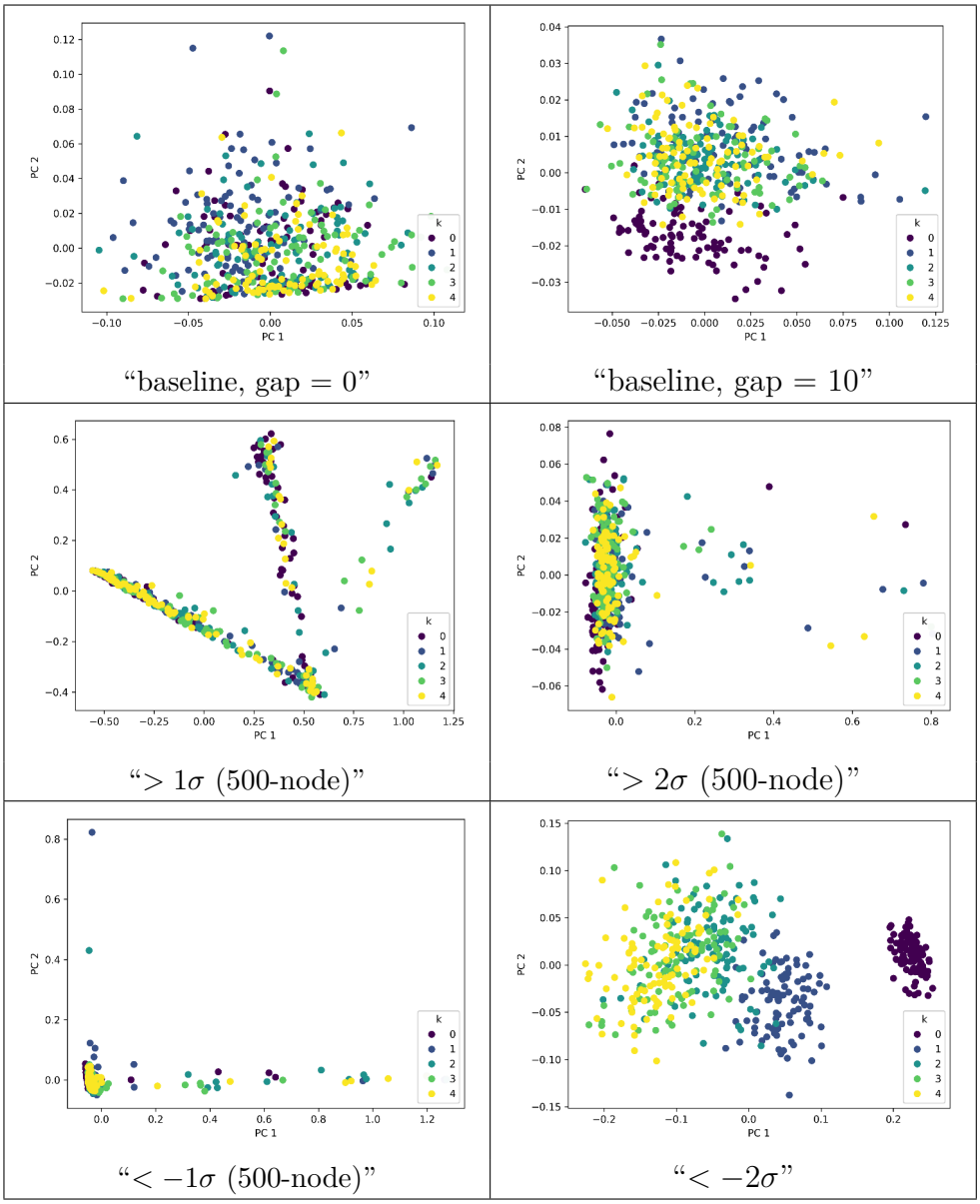

Figure 62 – PCA projection for rule B0157/S457 LLNA-BP features of k-logistic map networks, $k \in \{0, 1, 2, 3, 4\}$, $r = 3.9$.
Source: By the author.

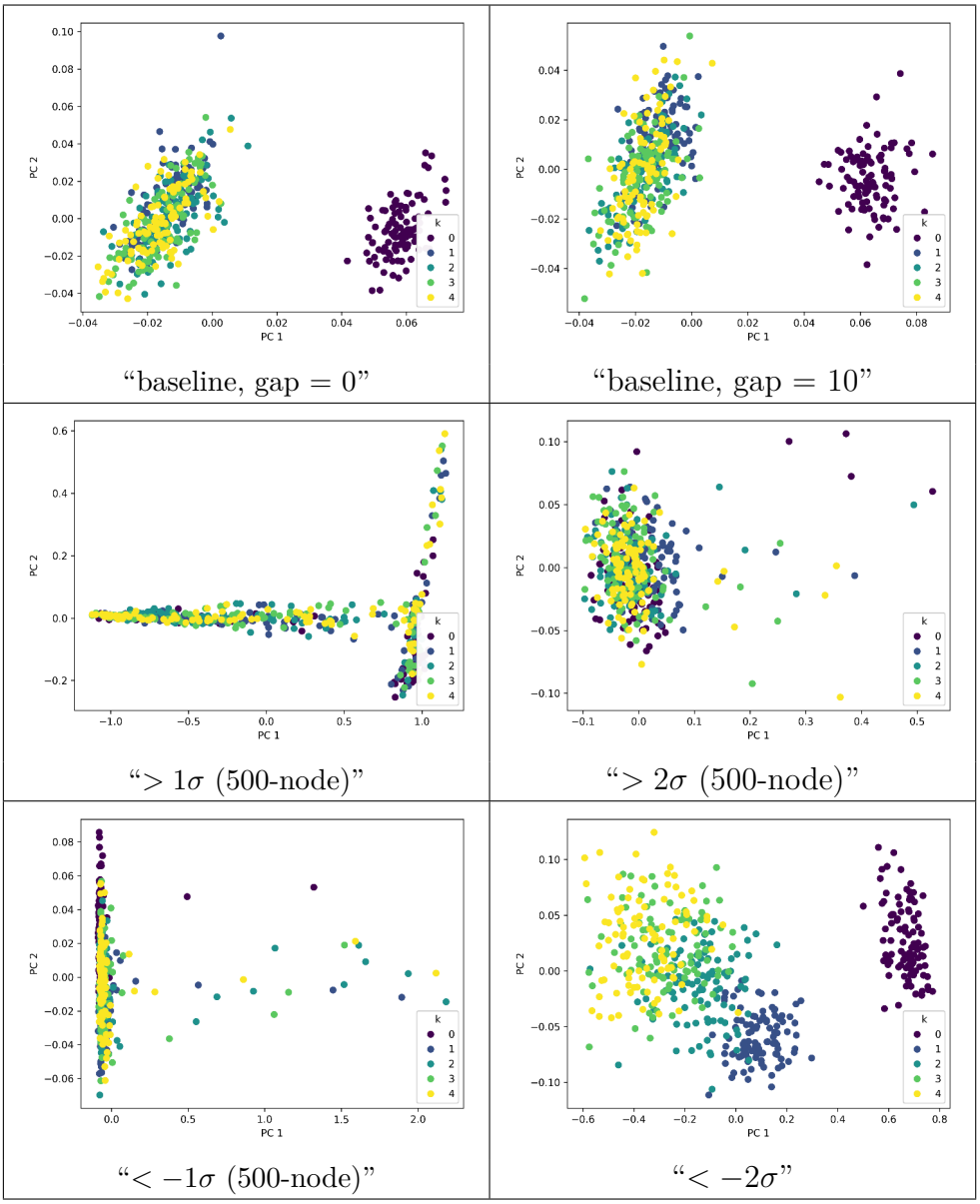

Figure 63 – PCA projection for rule B0157/S457 LLNA-DTEP features of k-logistic map networks, $k \in \{0, 1, 2, 3, 4\}$, $r = 3.9$.
Source: By the author.

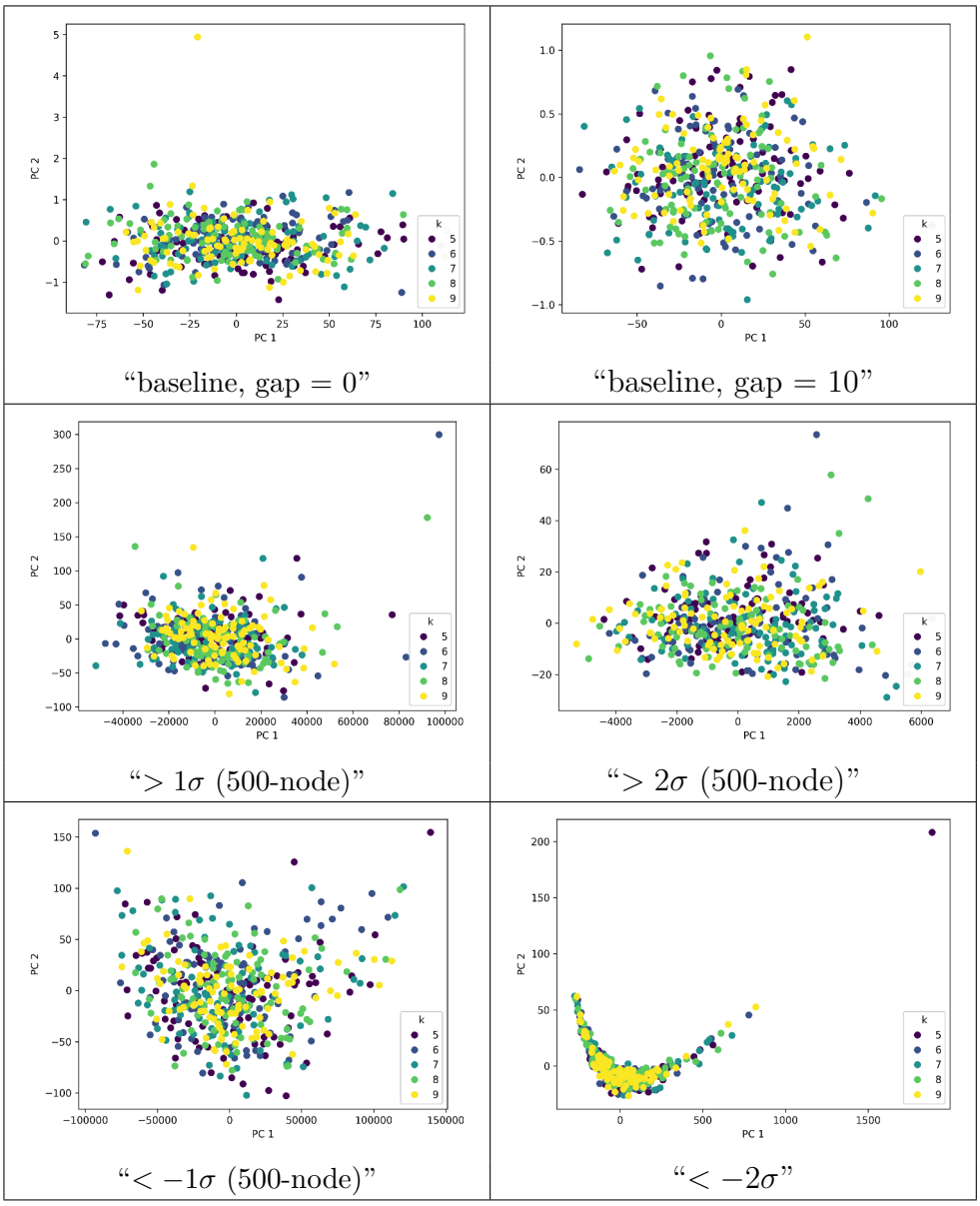

Figure 64 – PCA projection for structural features of k-logistic map networks, $k \in \{5, 6, 7, 8, 9\}$, $r = 3.9$.
Source: By the author.

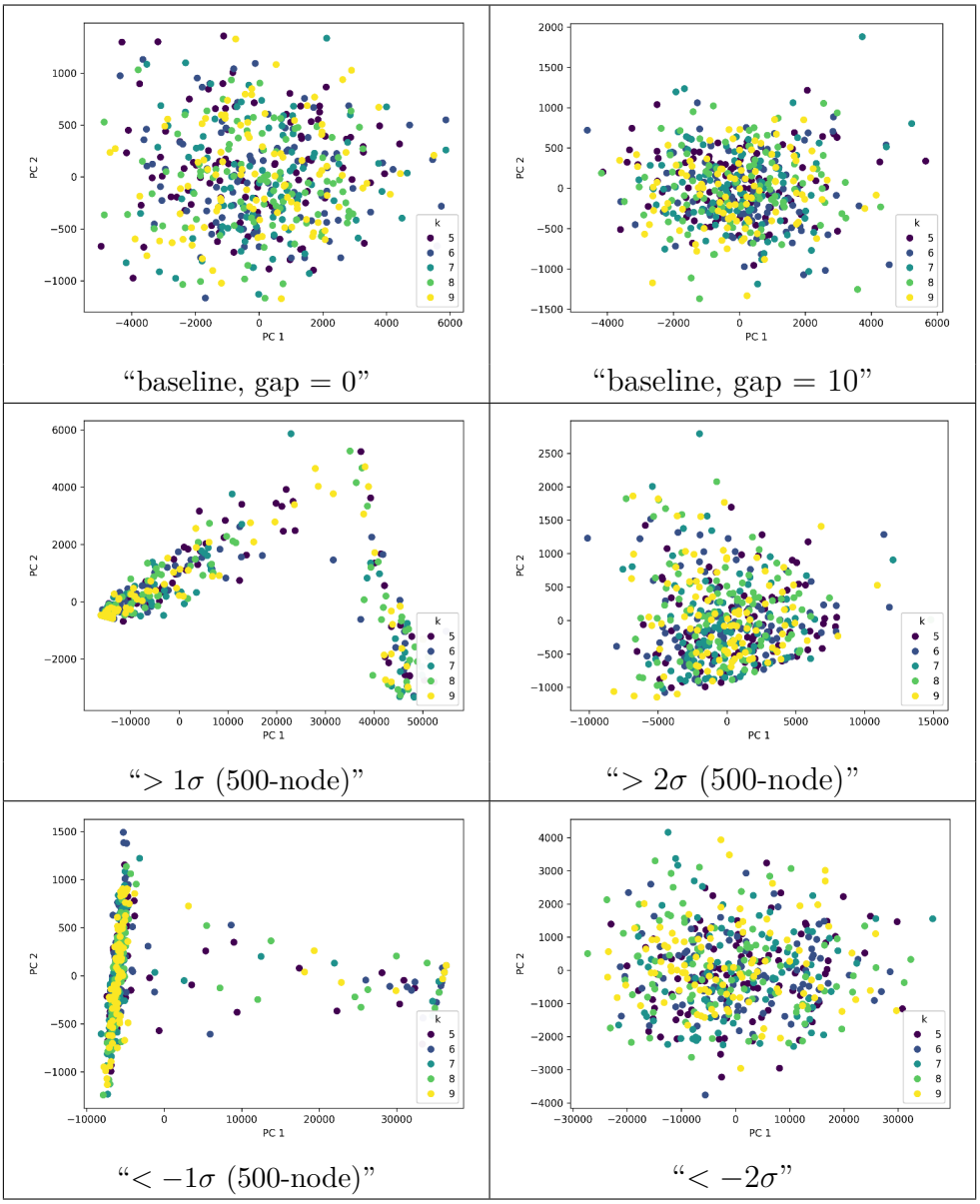

Figure 65 – PCA projection for rule B135678/S03456 LLNA features of k-logistic map networks, $k \in \{5, 6, 7, 8, 9\}$, $r = 3.9$.
Source: By the author.

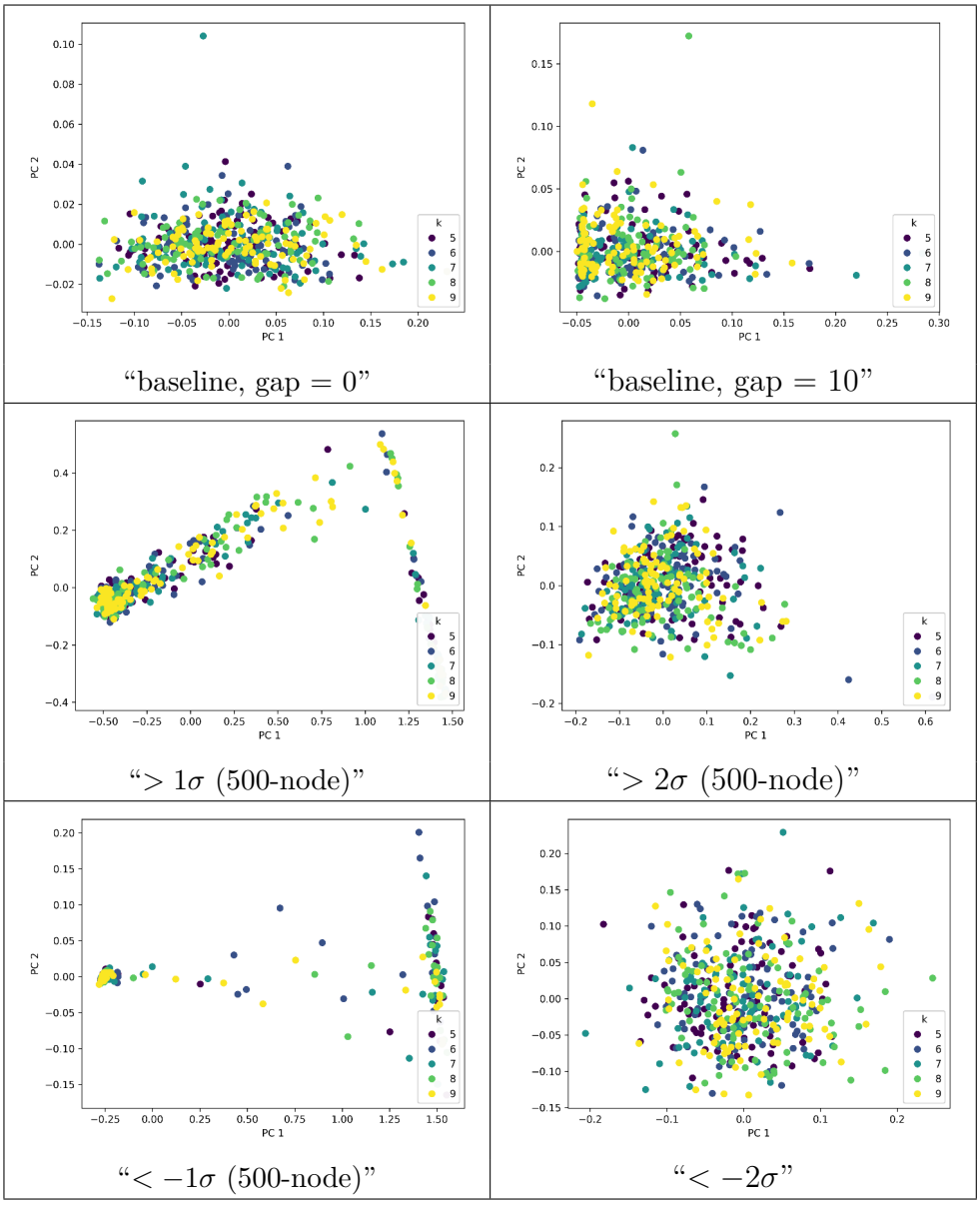

“baseline, gap = 0” “baseline, gap = 10”

“$> 1\sigma$ (500-node)” “$> 2\sigma$ (500-node)”

“$< -1\sigma$ (500-node)” “$< -2\sigma$”

Figure 66 – PCA projection for rule B135678/S03456 LLNA-BP features of k-logistic map networks, $k \in \{5, 6, 7, 8, 9\}$, $r = 3.9$.
Source: By the author.

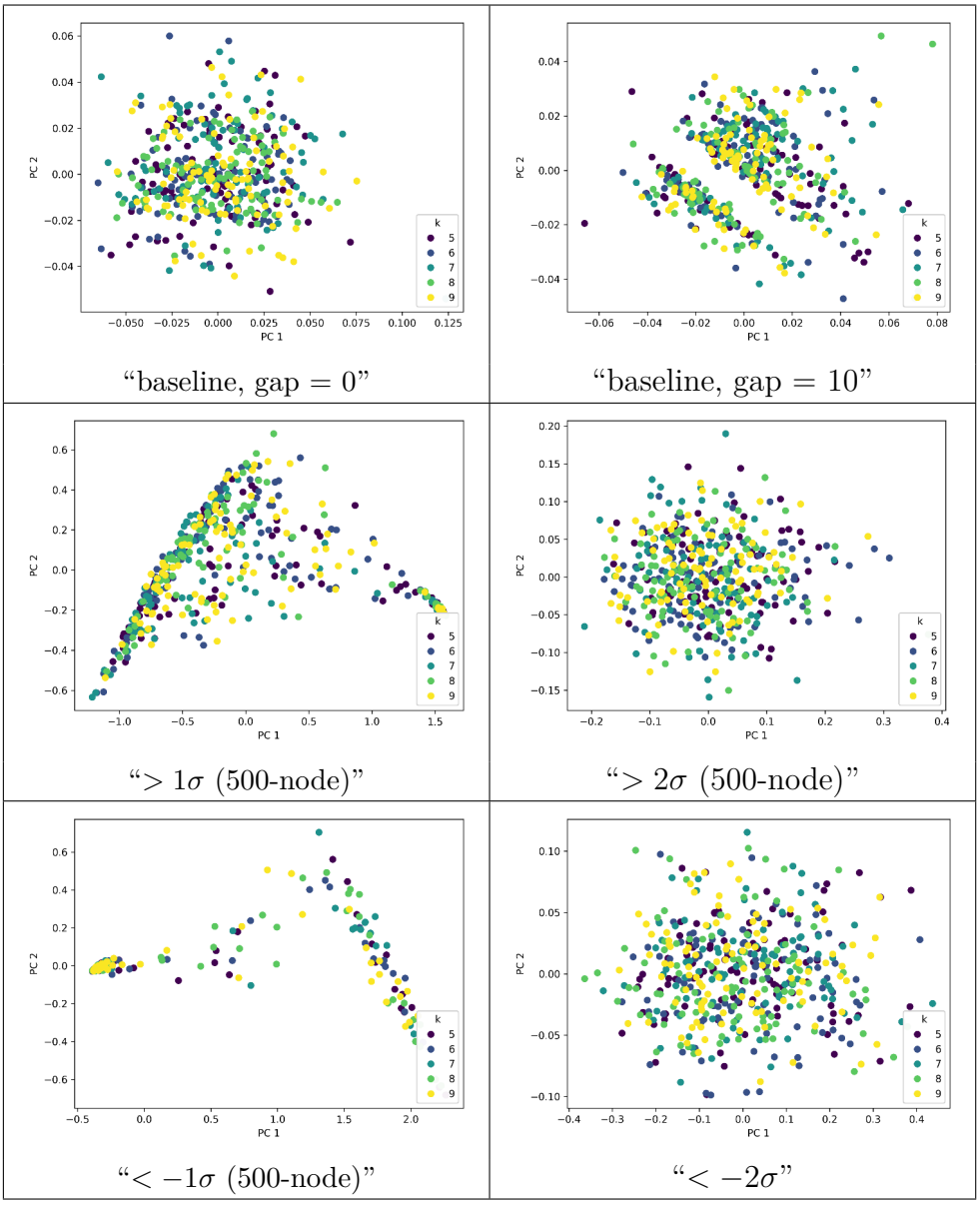

"baseline, gap = 0" "baseline, gap = 10"

"$> 1\sigma$ (500-node)" "$> 2\sigma$ (500-node)"

"$< -1\sigma$ (500-node)" "$< -2\sigma$"

Figure 67 – PCA projection for rule B135678/S03456 LLNA-DTEP features of k-logistic map networks, $k \in \{5, 6, 7, 8, 9\}$, $r = 3.9$.
Source: By the author.

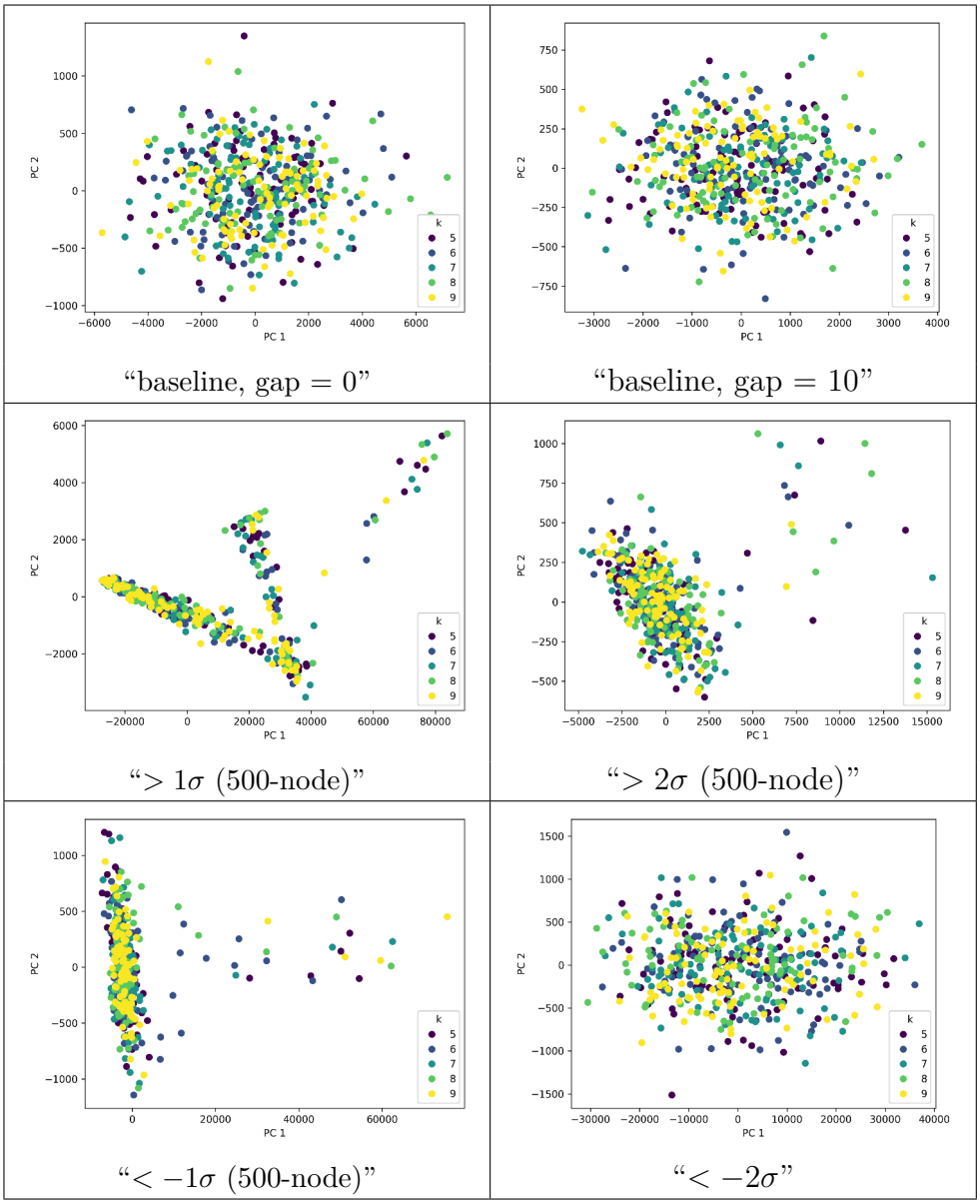

Figure 68 – PCA projection for rule B0157/S457 LLNA features of k-logistic map networks, $k \in \{5, 6, 7, 8, 9\}$, $r = 3.9$.
Source: By the author.

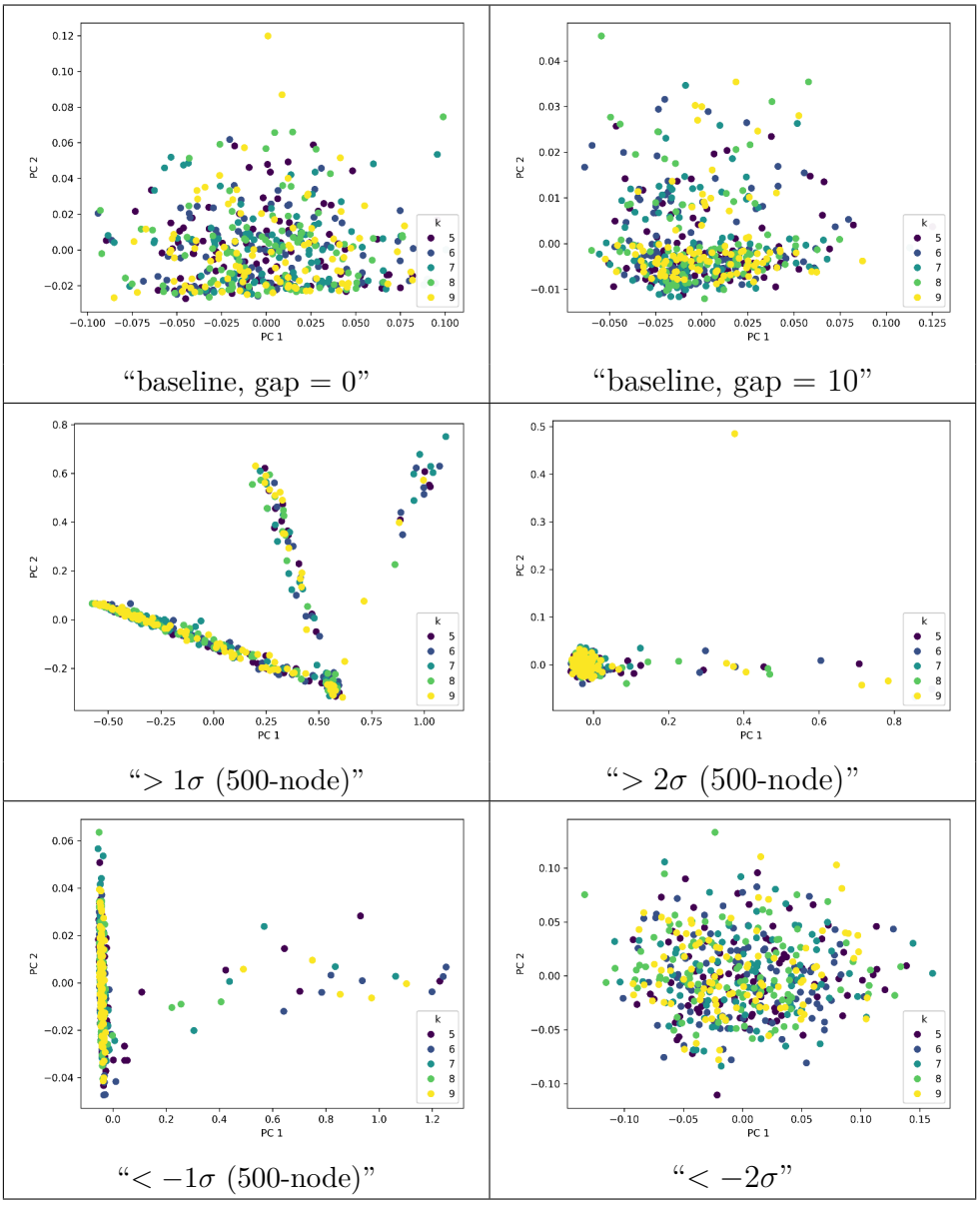

Figure 69 – PCA projection for rule B0157/S457 LLNA-BP features of k-logistic map networks, $k \in \{5, 6, 7, 8, 9\}$, $r = 3.9$.
Source: By the author.

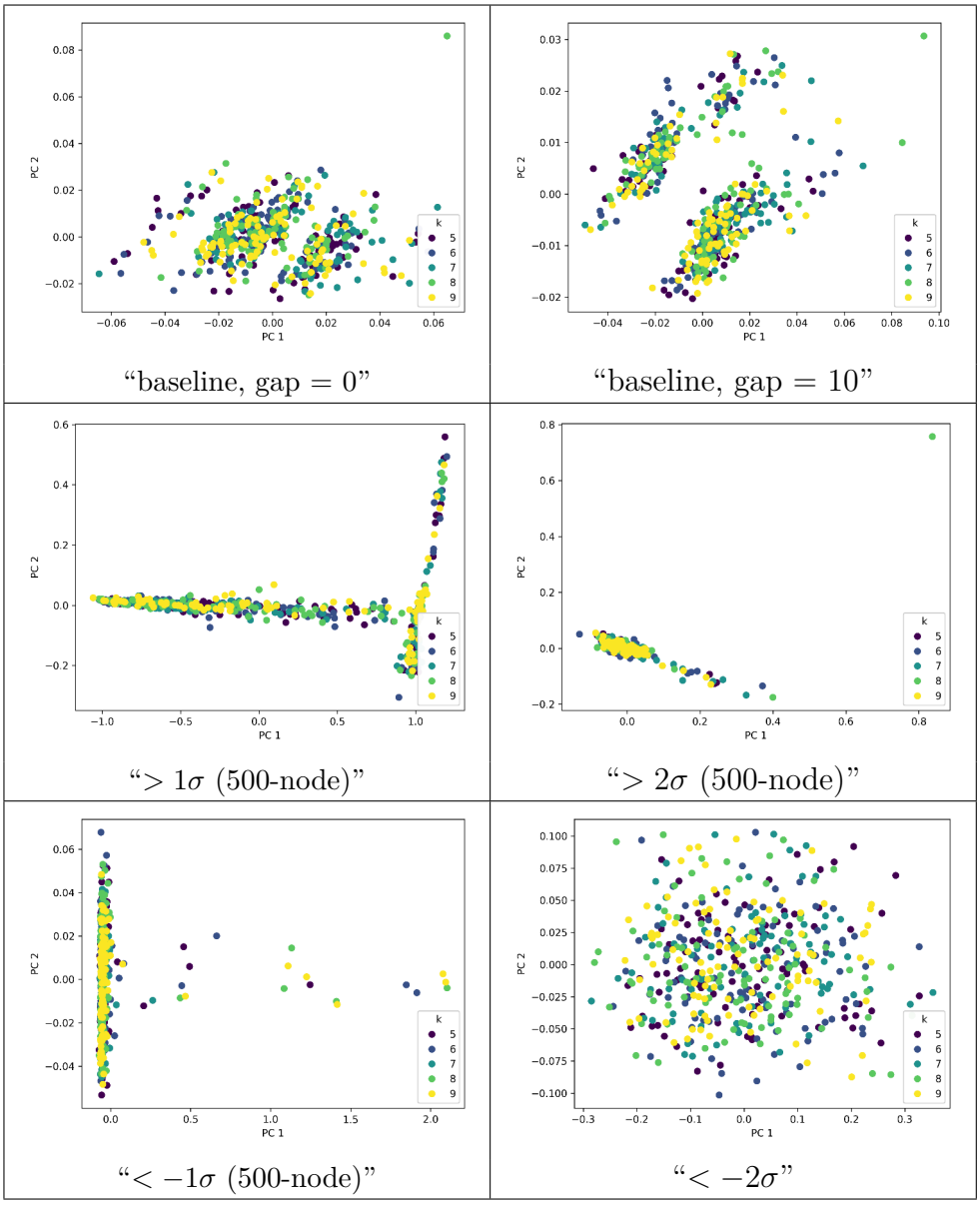

Figure 70 – PCA projection for rule B0157/S457 LLNA-DTEP features of k-logistic map networks, $k \in \{5, 6, 7, 8, 9\}$, $r = 3.9$.
Source: By the author.

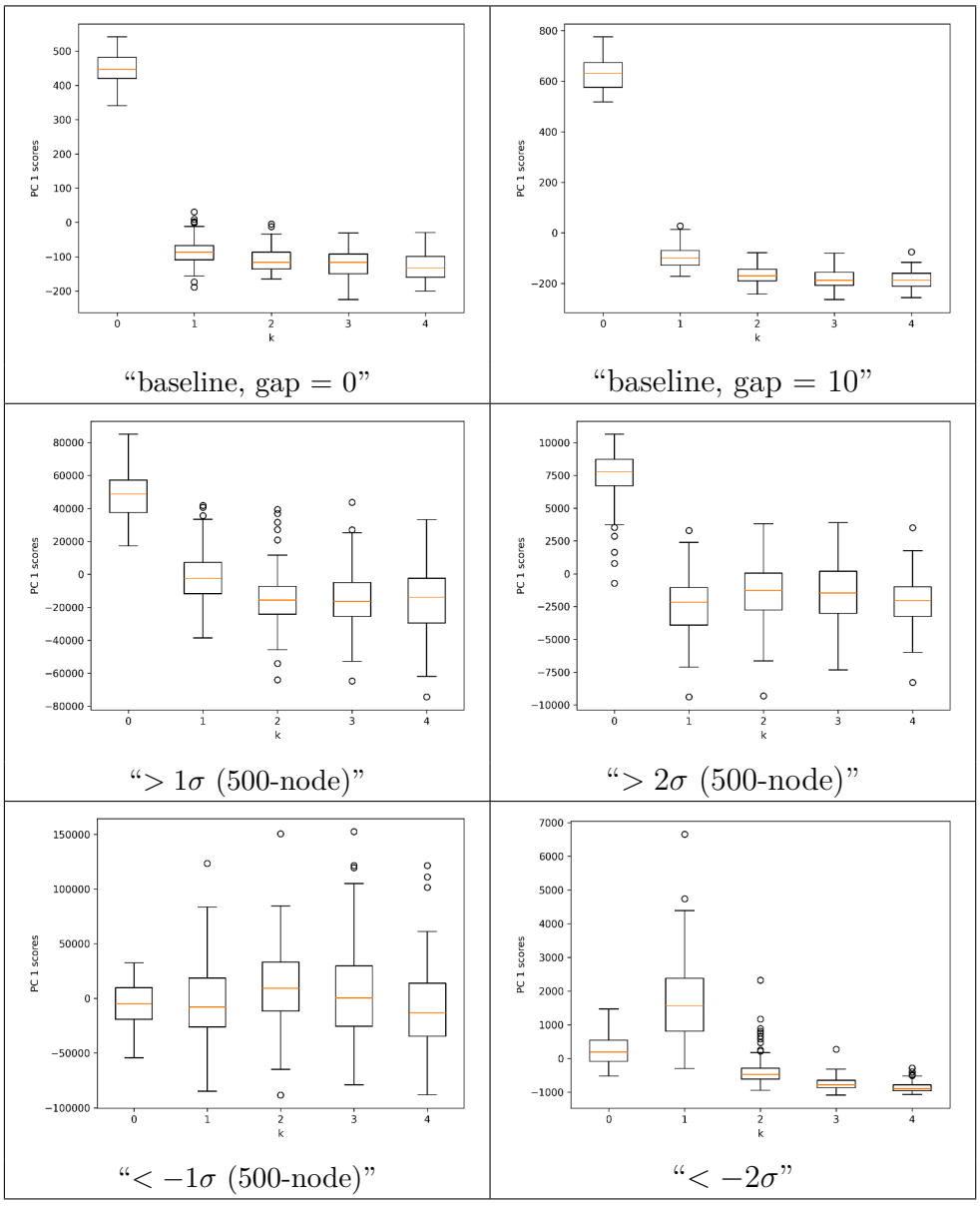

Figure 71 – Boxplot of principal component for structural features of k-logistic map networks, $k \in \{0, 1, 2, 3, 4\}$, $r = 3.9$.
Source: By the author.

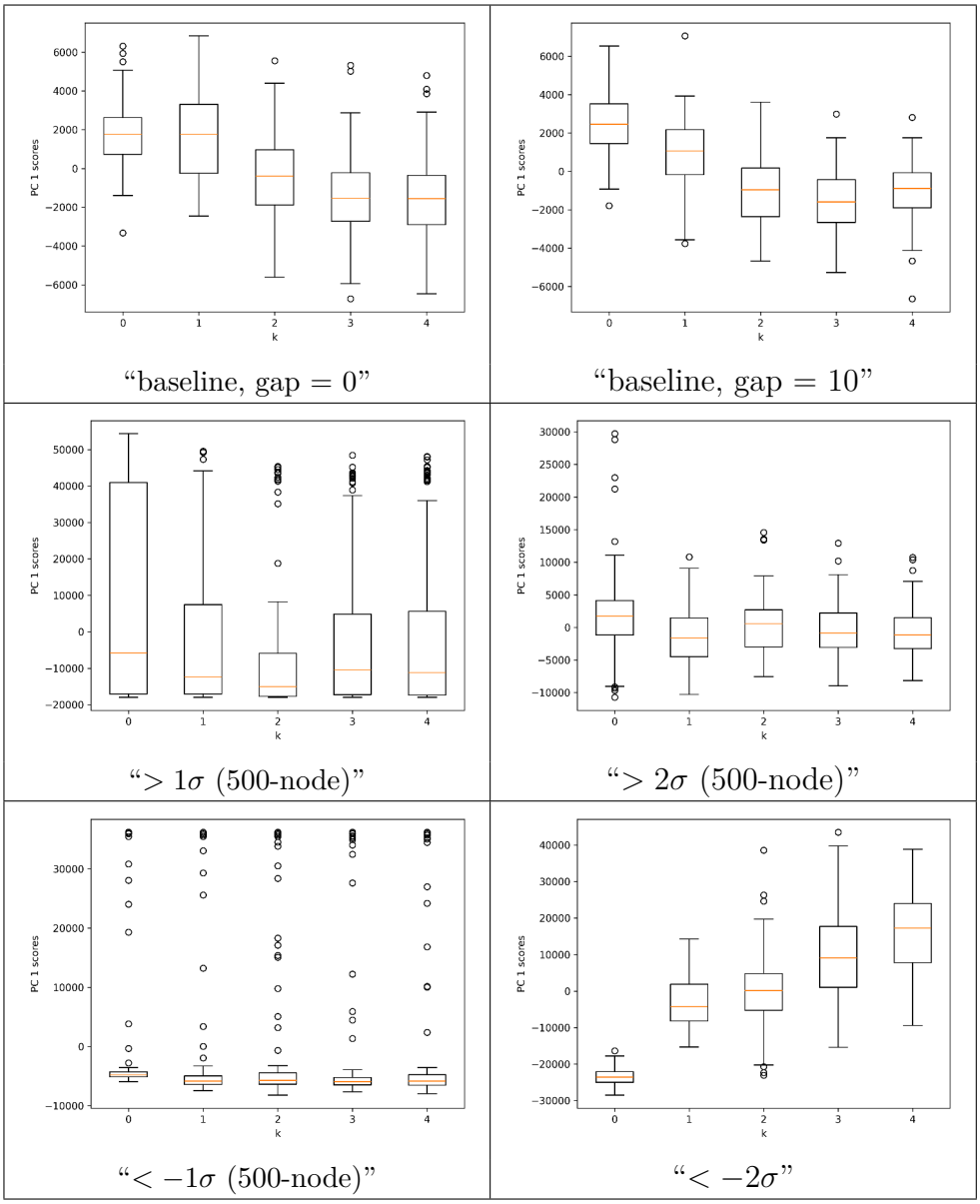

Figure 72 – Boxplot of principal component for rule B135678/S03456 LLNA features of k-logistic map networks, $k \in \{0, 1, 2, 3, 4\}$, $r = 3.9$.
Source: By the author.

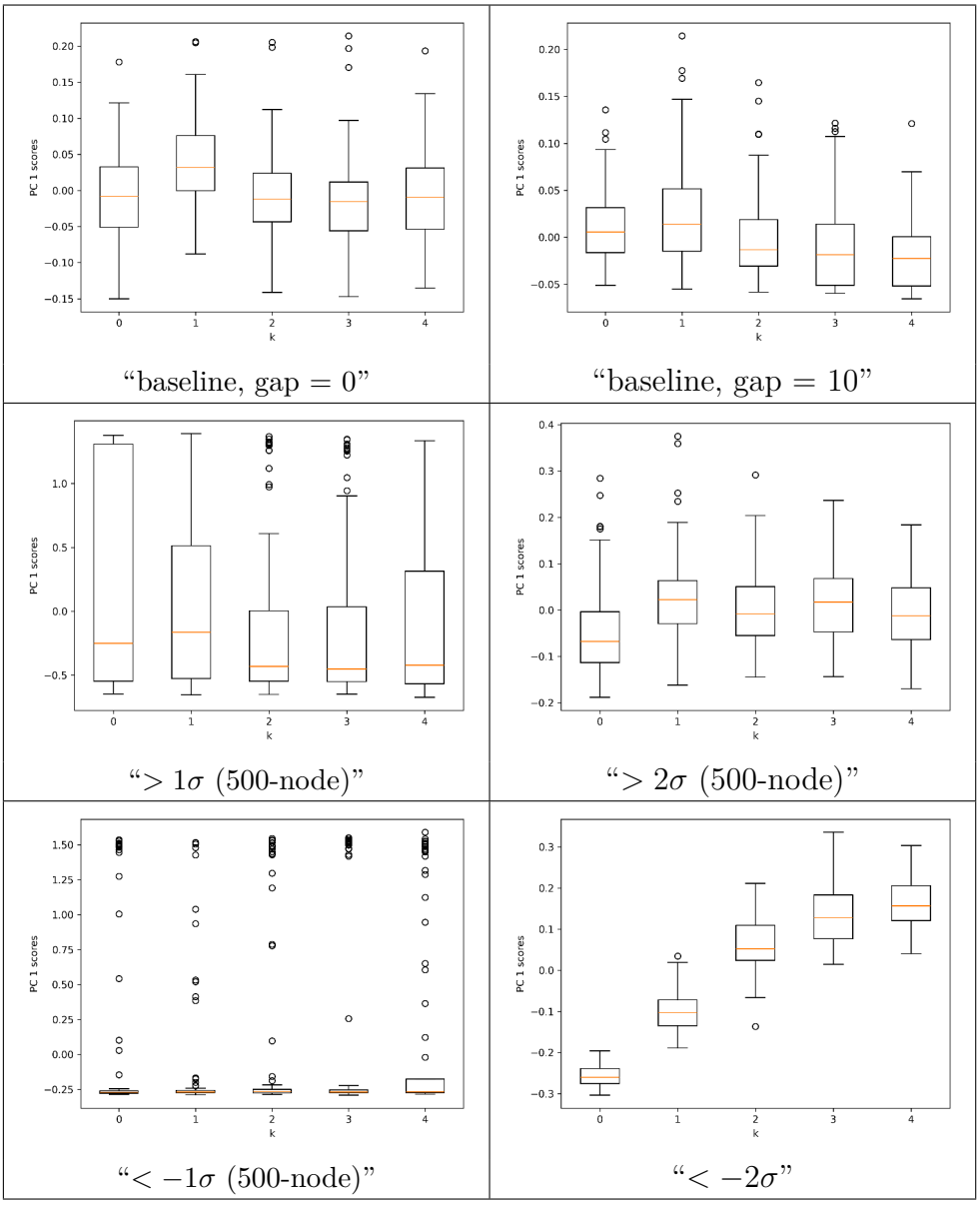

Figure 73 – Boxplot of principal component for rule B135678/S03456 LLNA-BP features of k-logistic map networks, $k \in \{0, 1, 2, 3, 4\}$, $r = 3.9$.
Source: By the author.

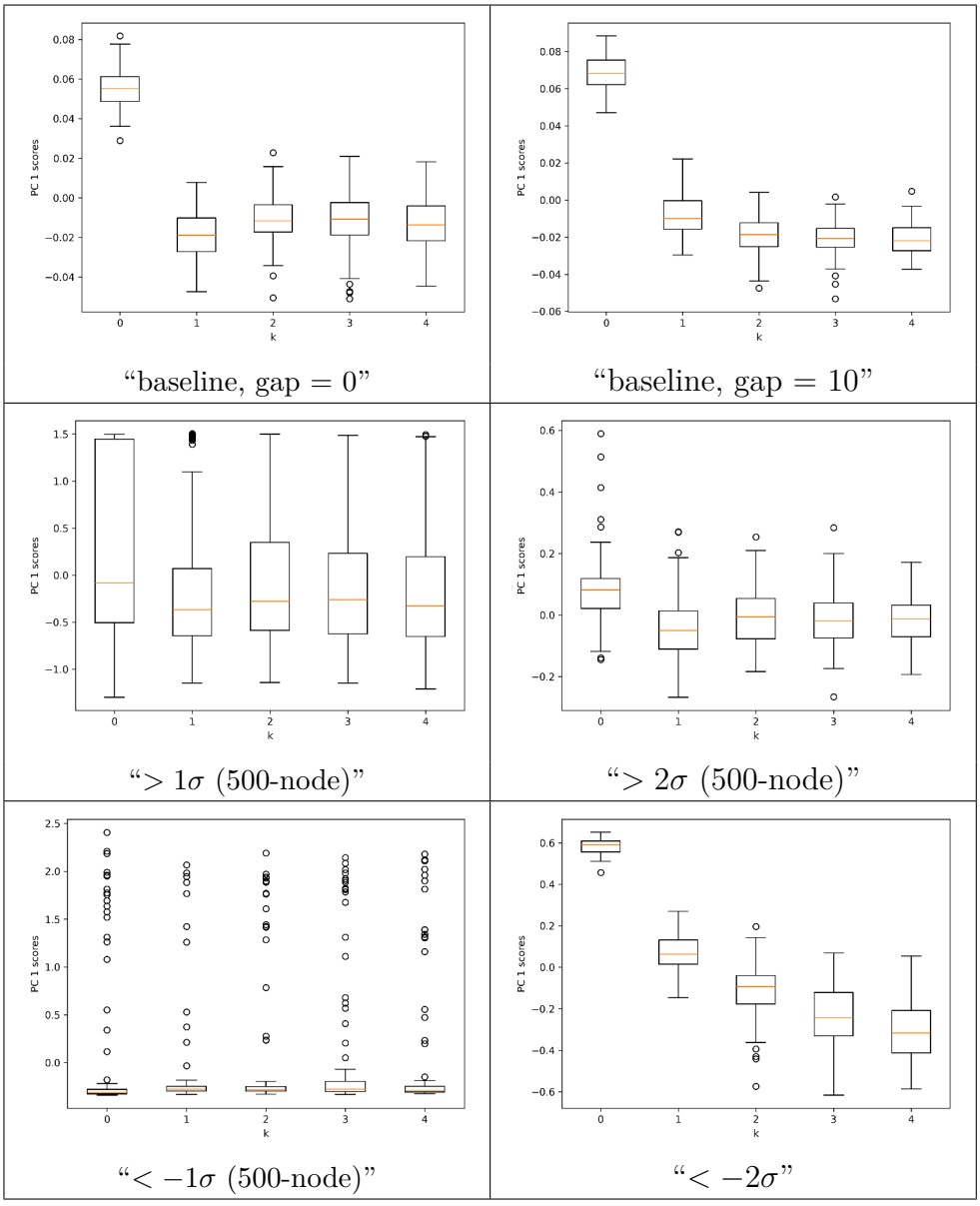

Figure 74 – Boxplot of principal component for rule B135678/S03456 LLNA-DTEP features of k-logistic map networks, $k \in \{0, 1, 2, 3, 4\}$, $r = 3.9$.
Source: By the author.

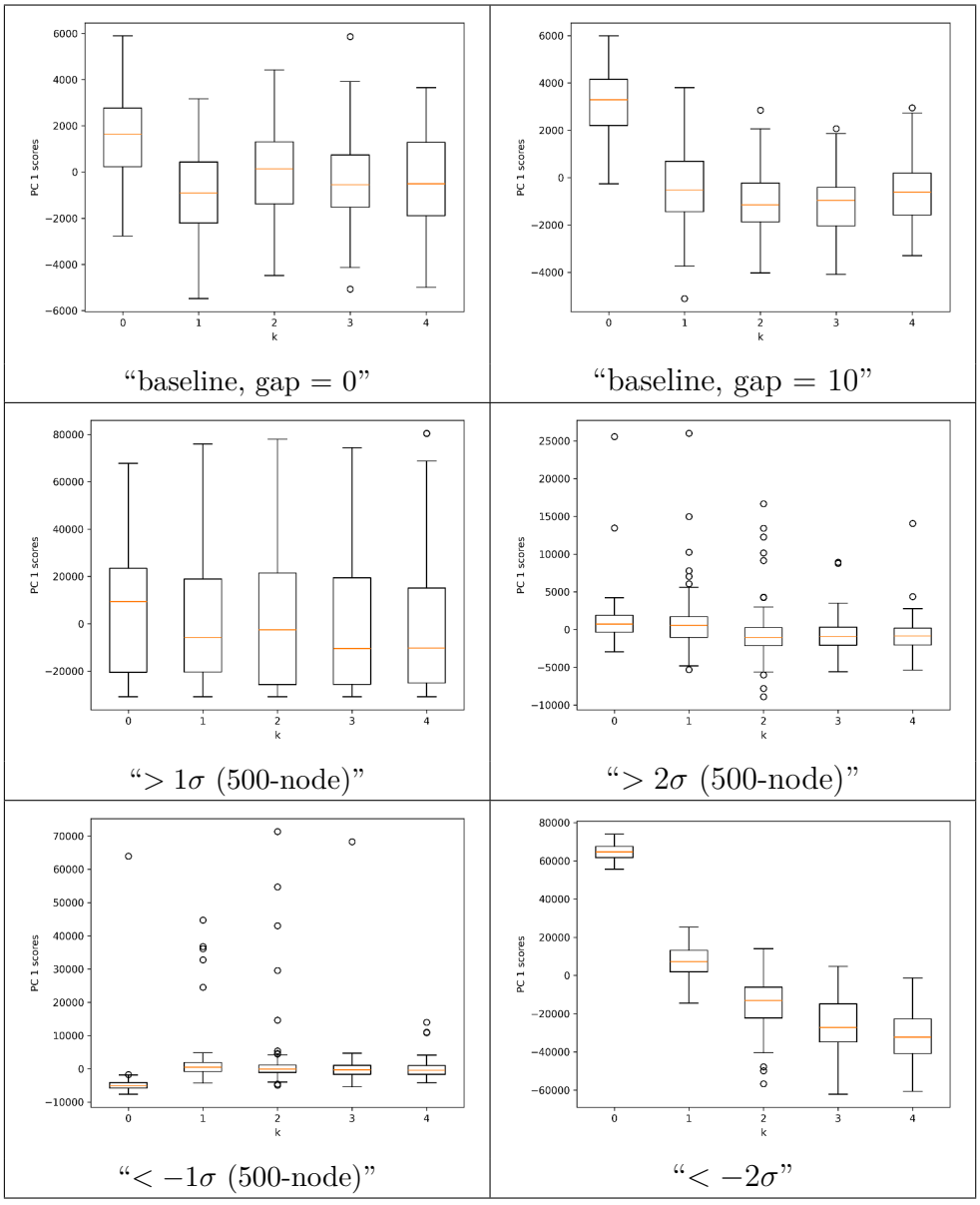

Figure 75 – Boxplot of principal component for rule B0157/S457 LLNA features of k-logistic map networks, $k \in \{0, 1, 2, 3, 4\}$, $r = 3.9$.
Source: By the author.

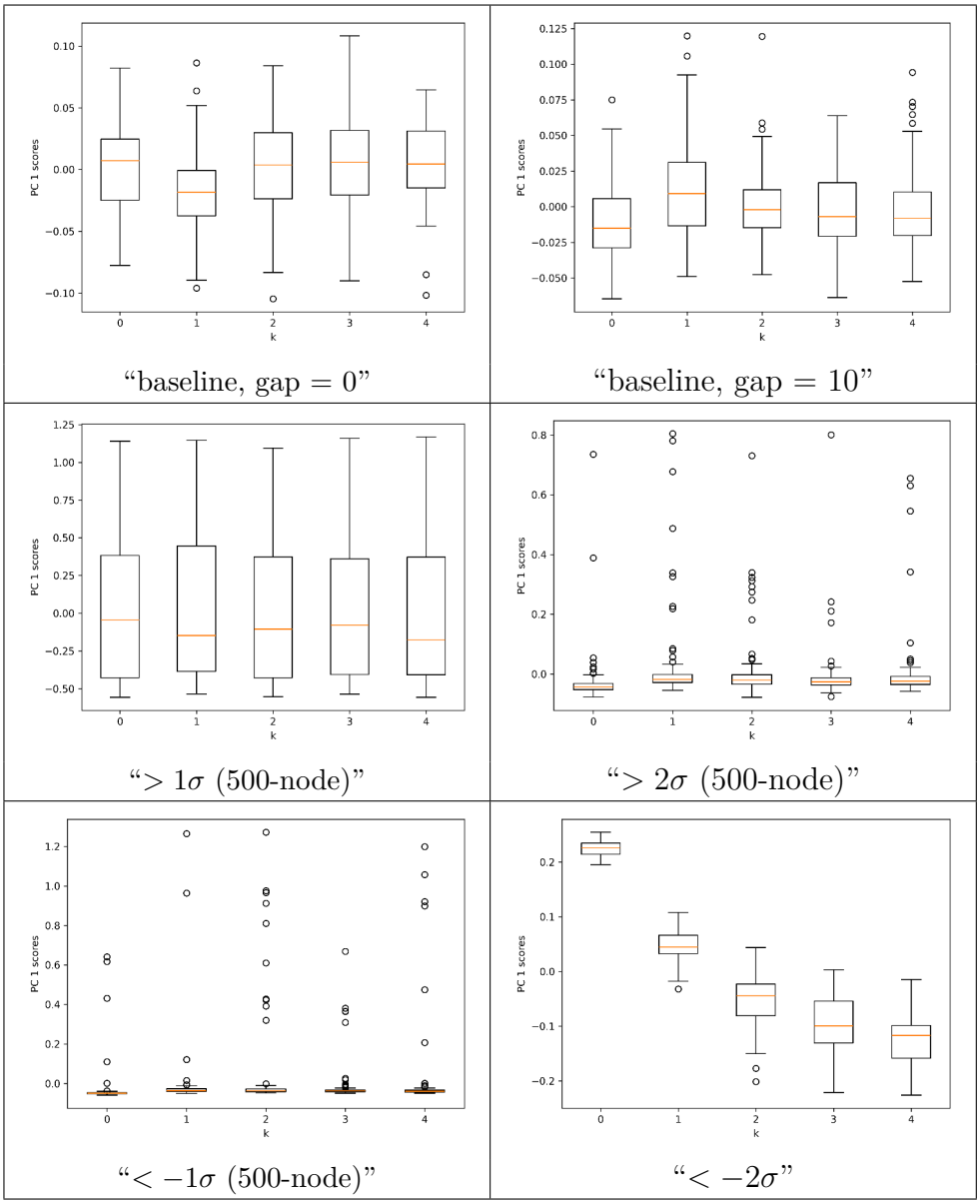

Figure 76 – Boxplot of principal component for rule B0157/S457 LLNA-BP features of k-logistic map networks, $k \in \{0, 1, 2, 3, 4\}$, $r = 3.9$.
Source: By the author.

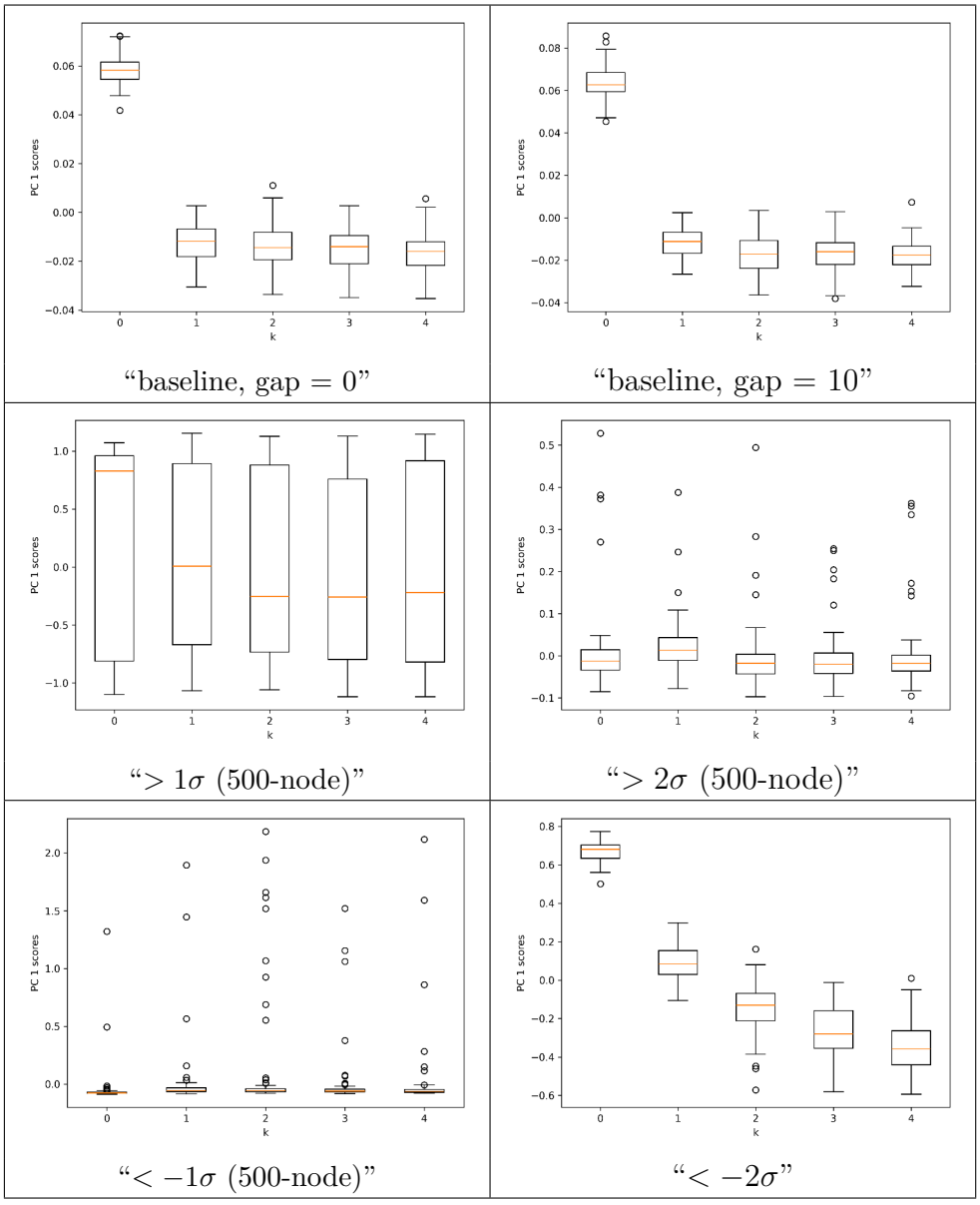

Figure 77 – Boxplot of principal component for rule B0157/S457 LLNA-DTEP features of k-logistic map networks, $k \in \{0, 1, 2, 3, 4\}$, $r = 3.9$.
Source: By the author.

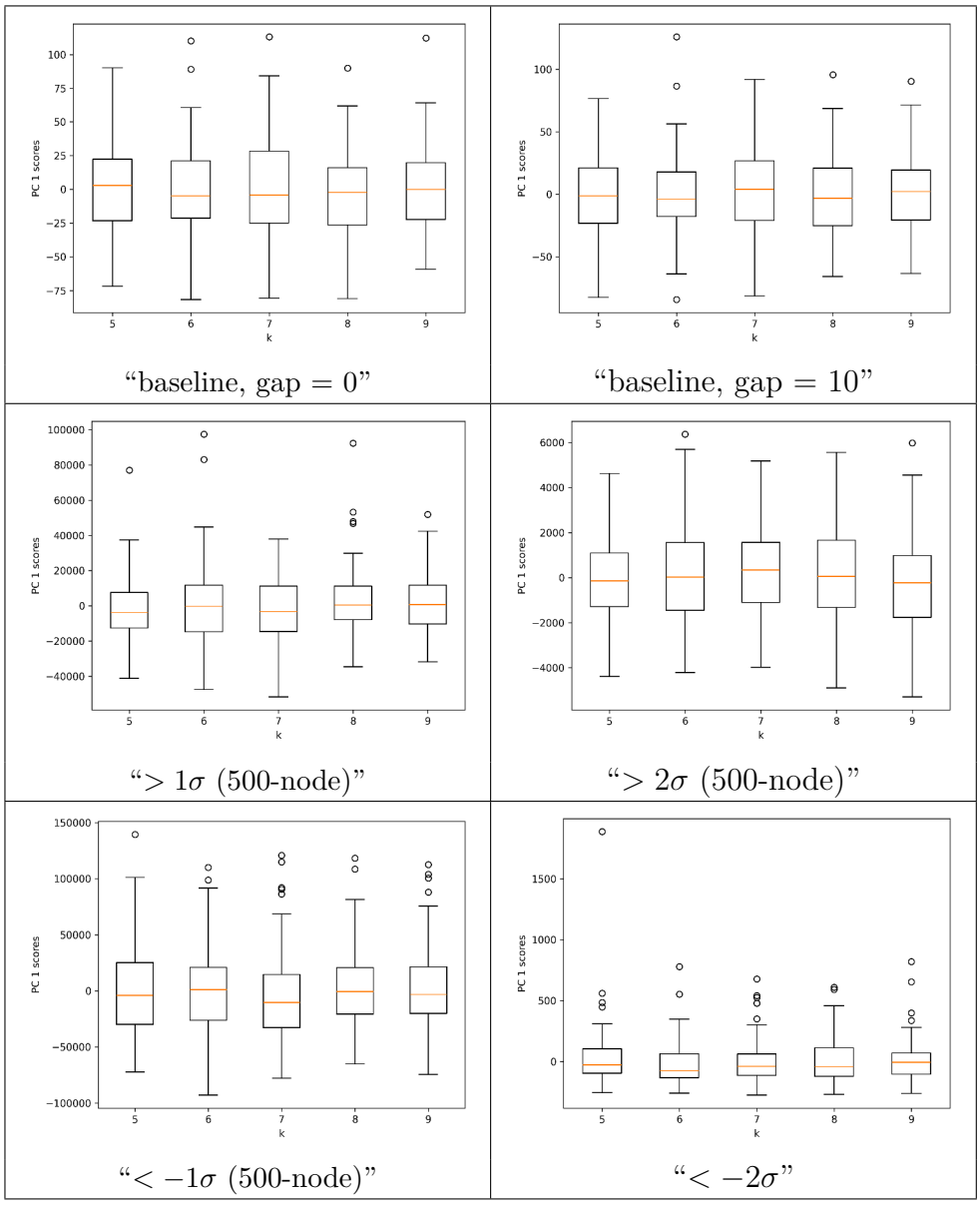

Figure 78 – Boxplot of principal component for structural features of k-logistic map networks, $k \in \{5, 6, 7, 8, 9\}$, $r = 3.9$.
Source: By the author.

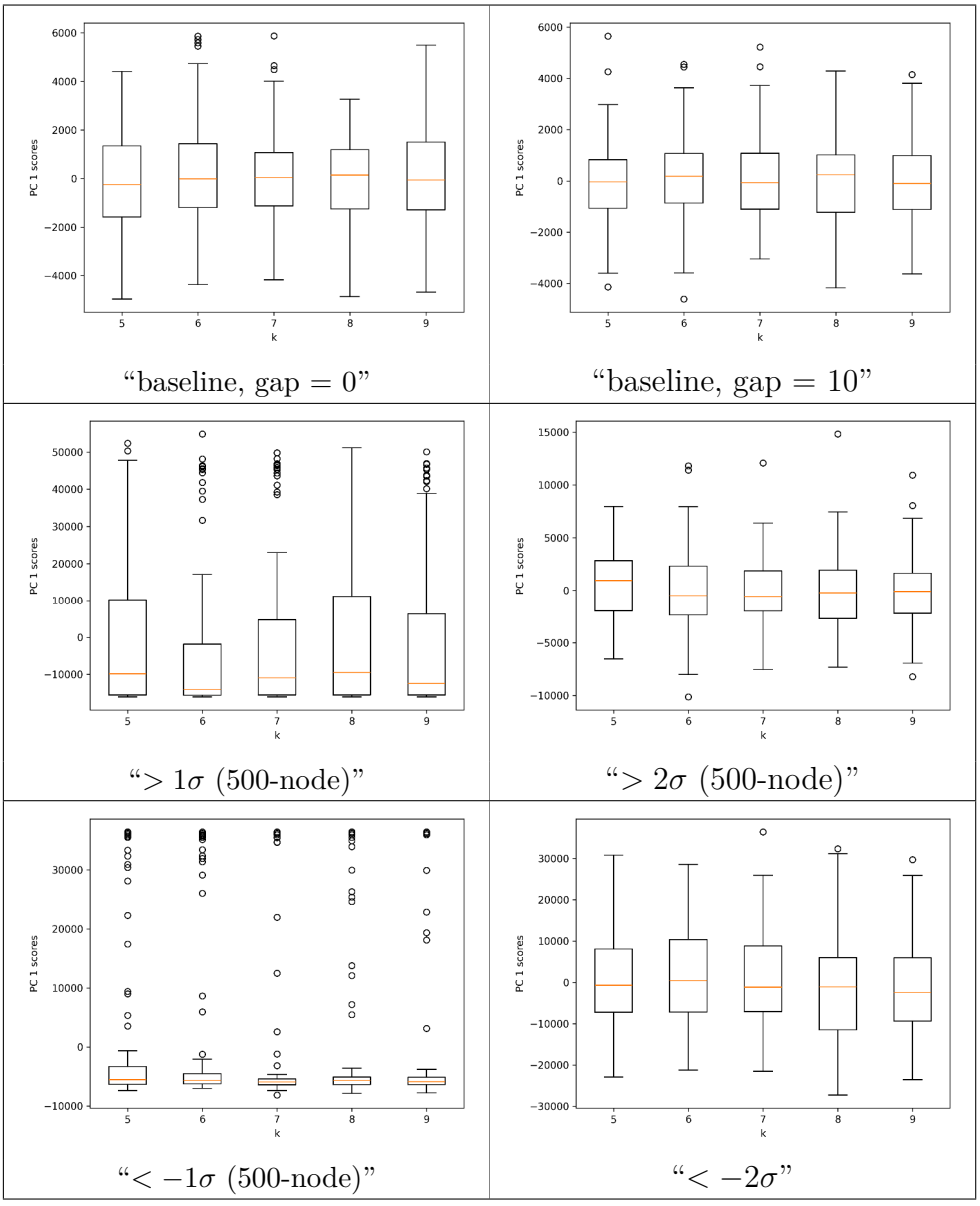

Figure 79 – Boxplot of principal component for rule B135678/S03456 LLNA features of k-logistic map networks, $k \in \{5, 6, 7, 8, 9\}$, $r = 3.9$.
Source: By the author.

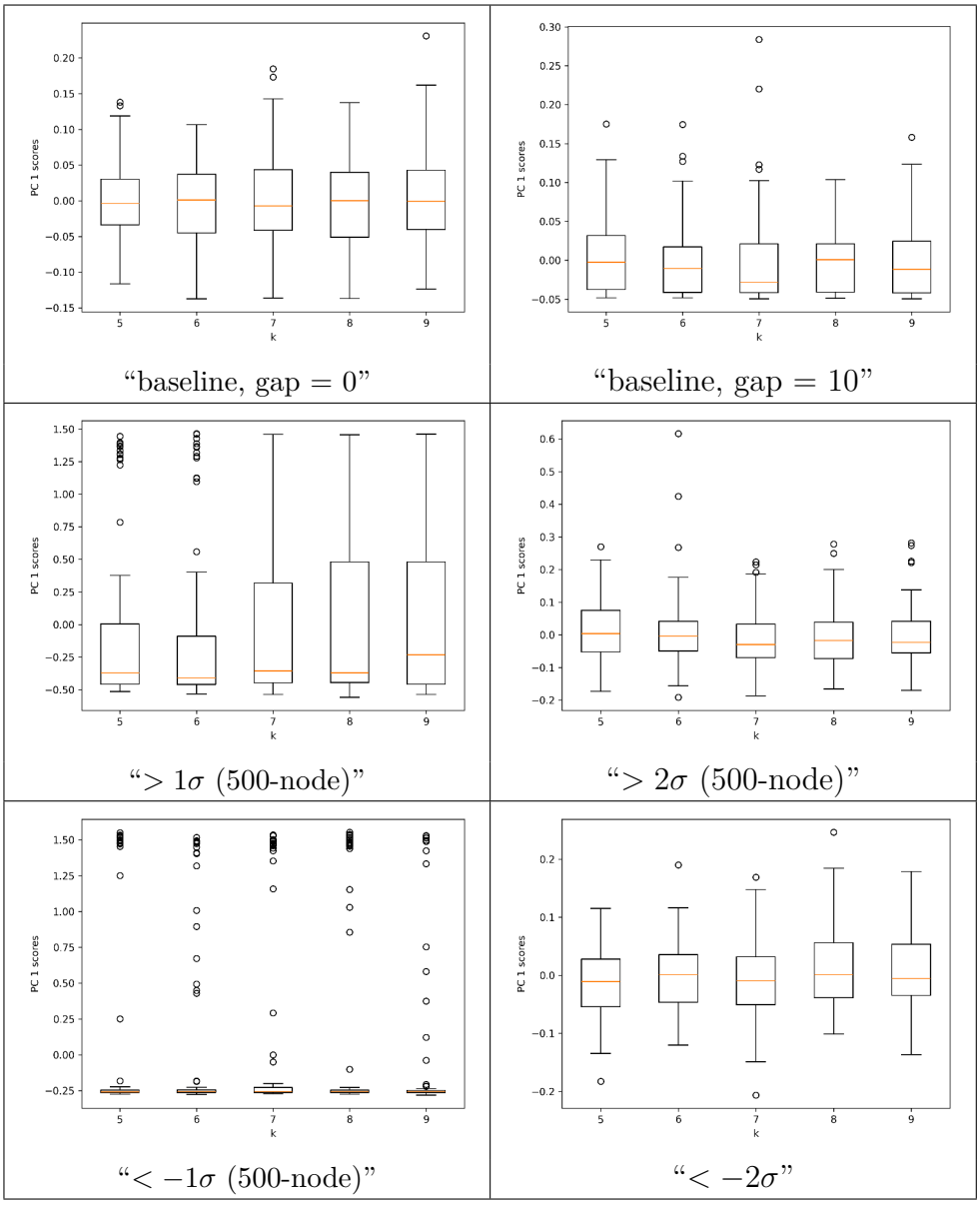

Figure 80 – Boxplot of principal component for rule B135678/S03456 LLNA-BP features of k-logistic map networks, $k \in \{5, 6, 7, 8, 9\}$, $r = 3.9$.
Source: By the author.

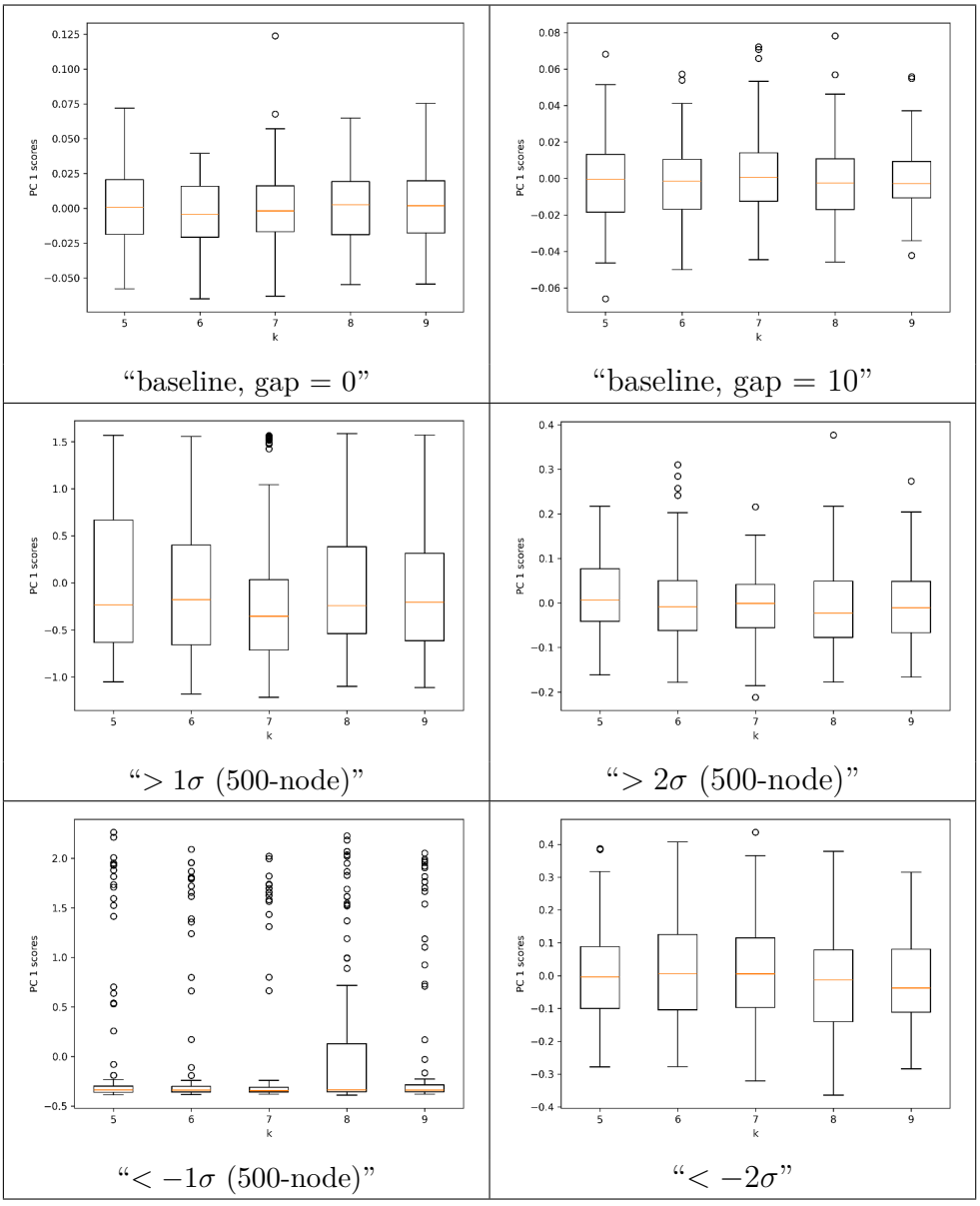

Figure 81 – Boxplot of principal component for rule B135678/S03456 LLNA-DTEP features of k-logistic map networks, $k \in \{5, 6, 7, 8, 9\}$, $r = 3.9$.
Source: By the author.

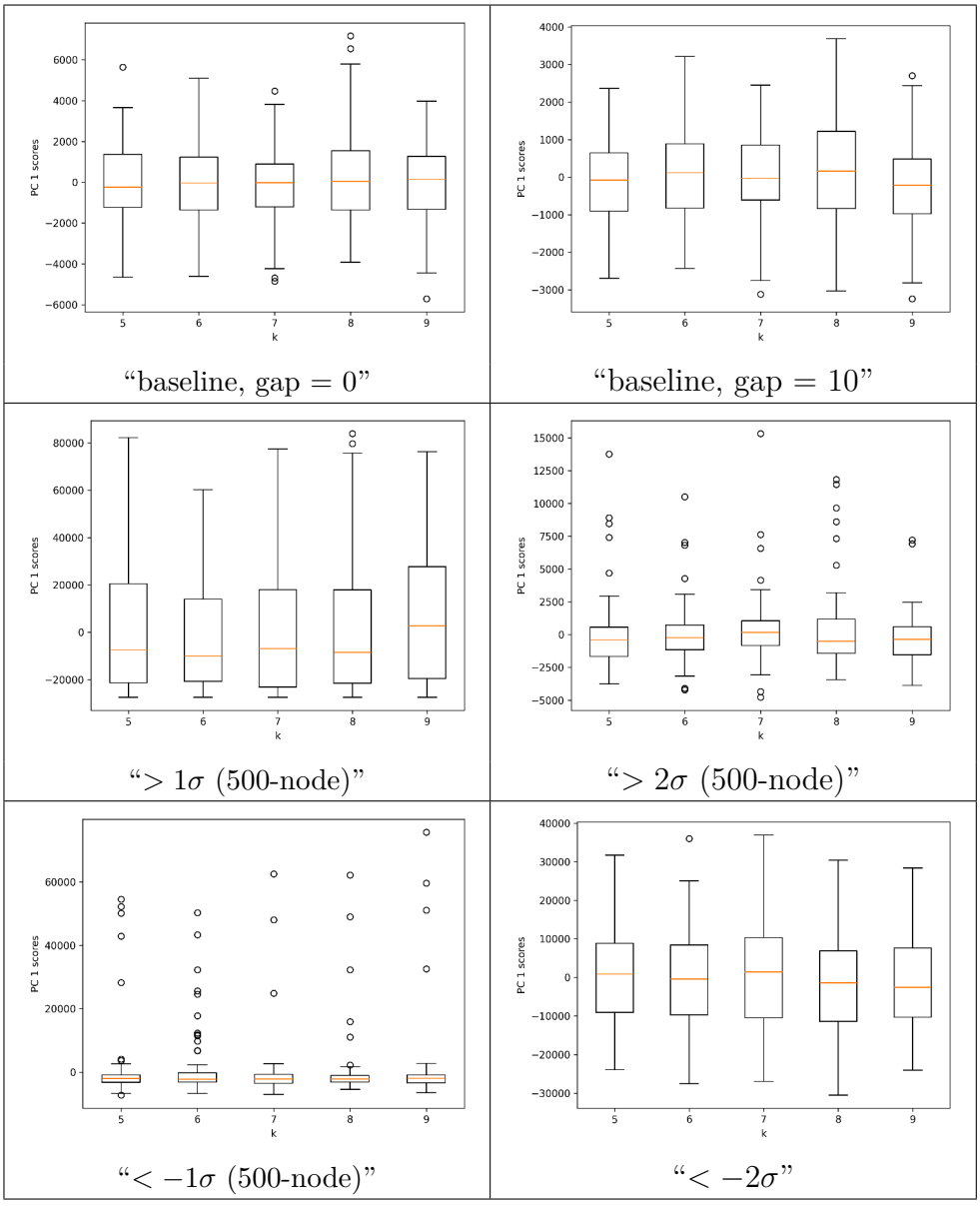

Figure 82 – Boxplot of principal component for rule B0157/S457 LLNA features of k-logistic map networks, $k \in \{5, 6, 7, 8, 9\}$, $r = 3.9$.
Source: By the author.

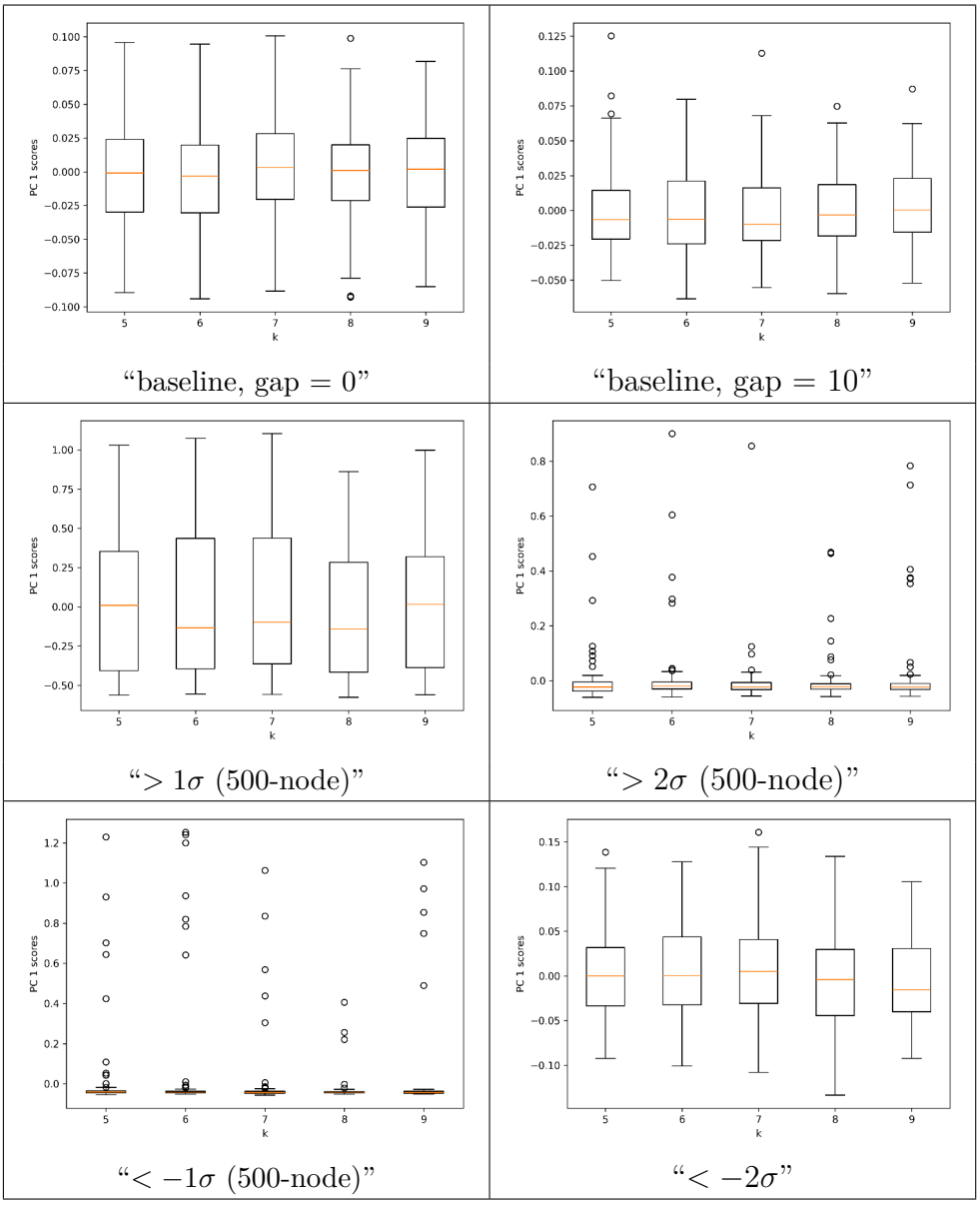

Figure 83 – Boxplot of principal component for rule B0157/S457 LLNA-BP features of k-logistic map networks, $k \in \{5, 6, 7, 8, 9\}$, $r = 3.9$.
Source: By the author.

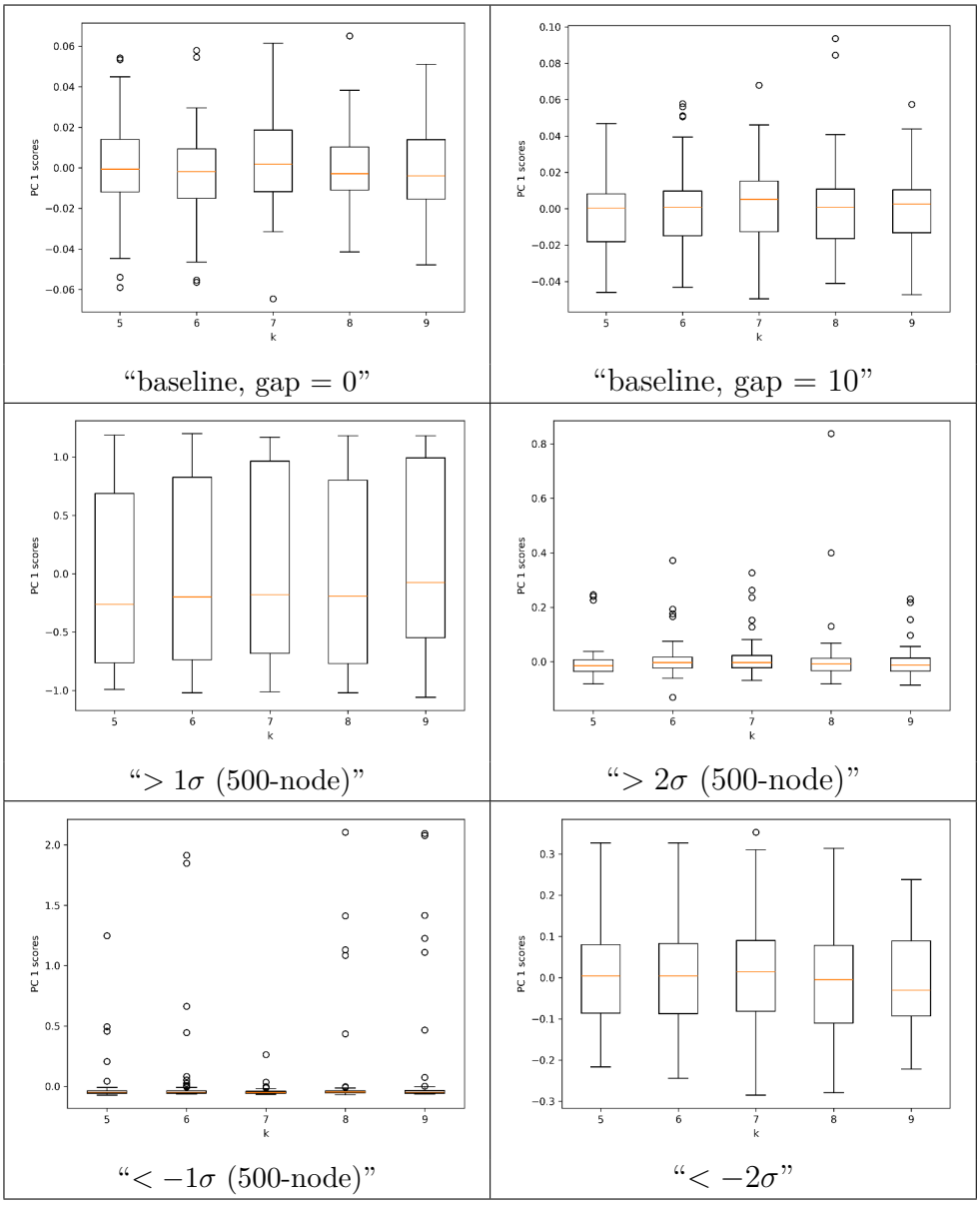

Figure 84 – Boxplot of principal component for rule B0157/S457 LLNA-DTEP features of k-logistic map networks, $k \in \{5, 6, 7, 8, 9\}$, $r = 3.9$.
Source: By the author.

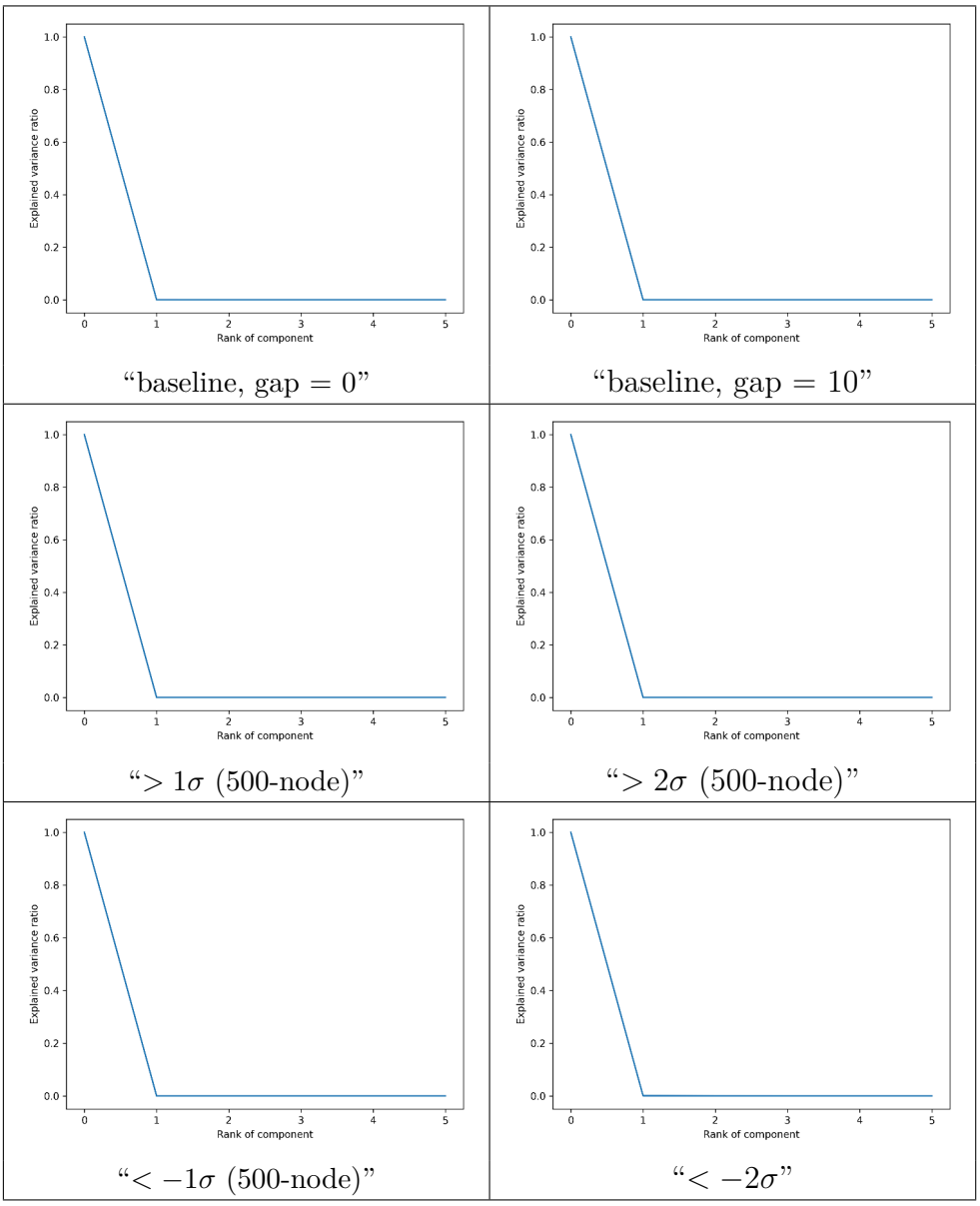

Figure 85 – PCA variance ratio for structural features of k-logistic map networks, $k \in \{0, 1, 2, 3, 4\}$, $r = 3.9$.
Source: By the author.

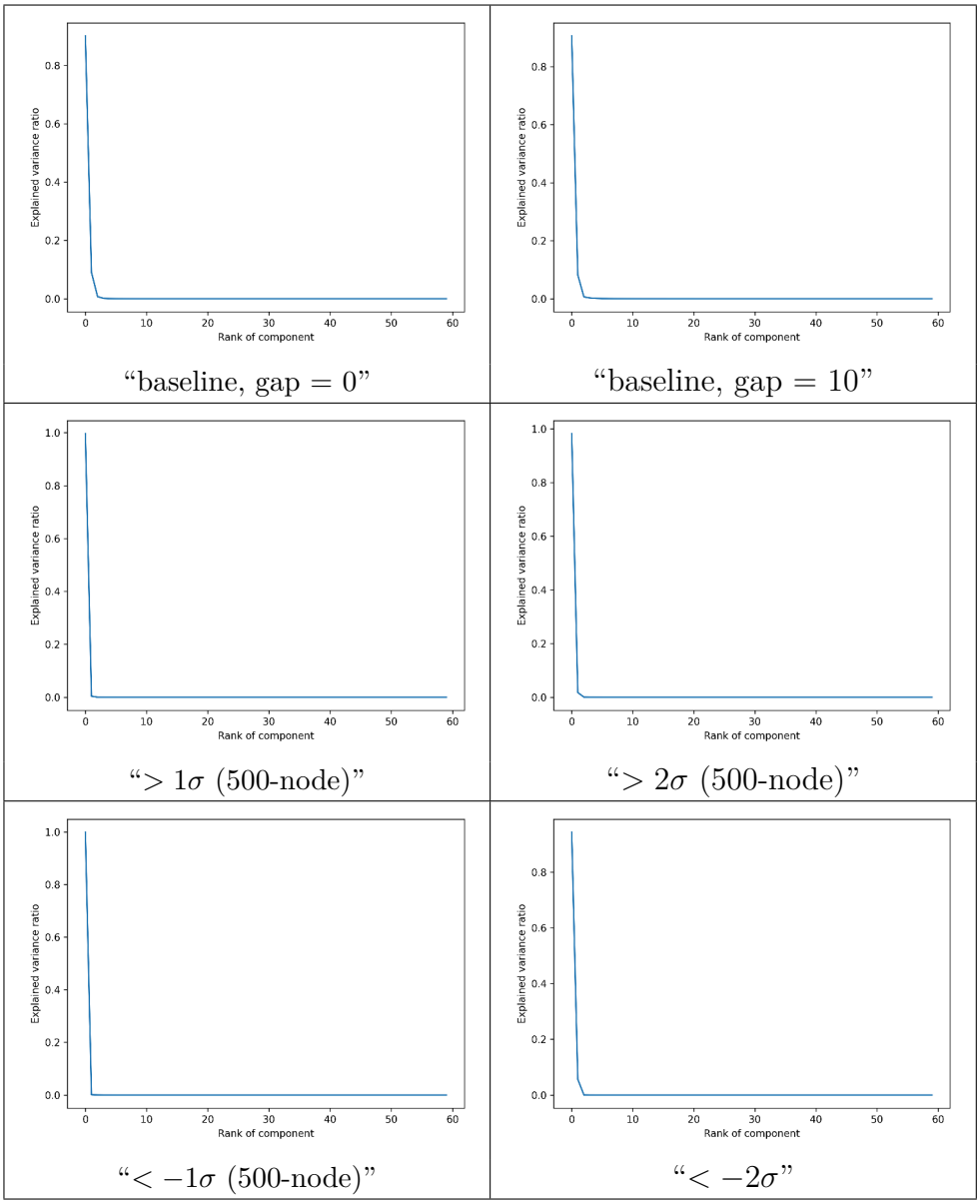

Figure 86 – PCA variance ratio for rule B135678/S03456 LLNA features of k-logistic map networks, $k \in \{0, 1, 2, 3, 4\}$, $r = 3.9$.
Source: By the author.

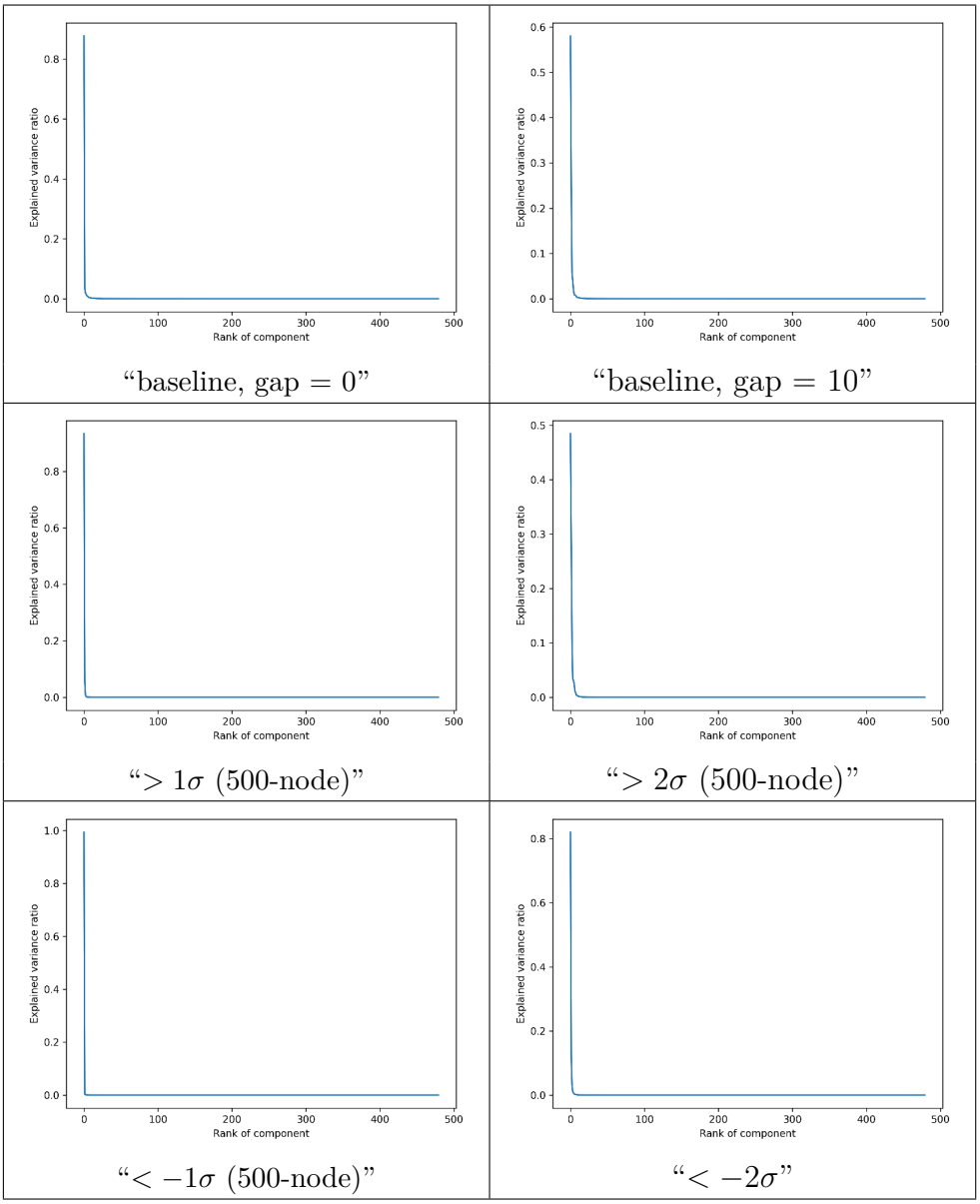

Figure 87 – PCA variance ratio for rule B135678/S03456 LLNA-BP features of k-logistic map networks, $k \in \{0, 1, 2, 3, 4\}$, $r = 3.9$.
Source: By the author.

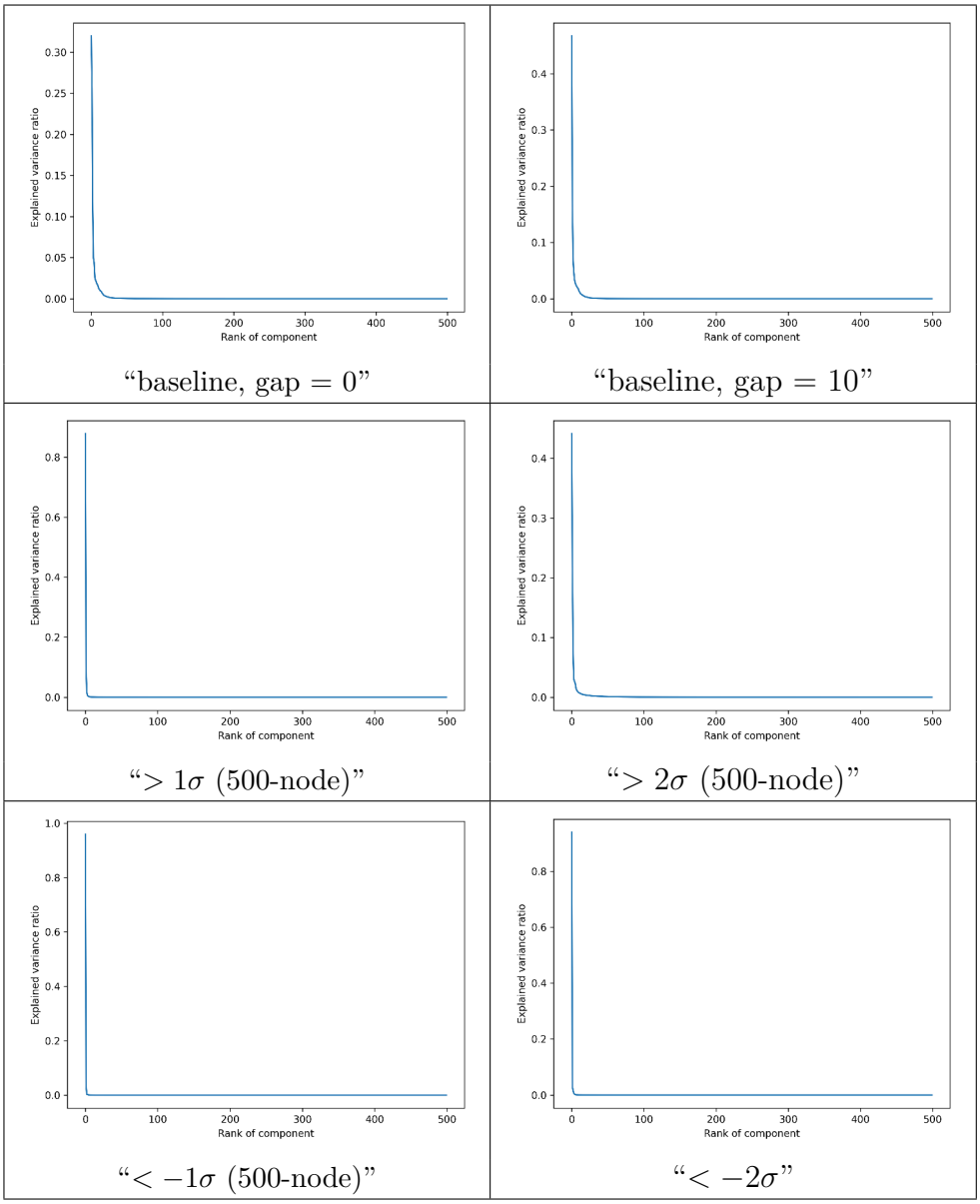

Figure 88 – PCA variance ratio for rule B135678/S03456 LLNA-DTEP features of k-logistic map networks, $k \in \{0, 1, 2, 3, 4\}$, $r = 3.9$.
Source: By the author.

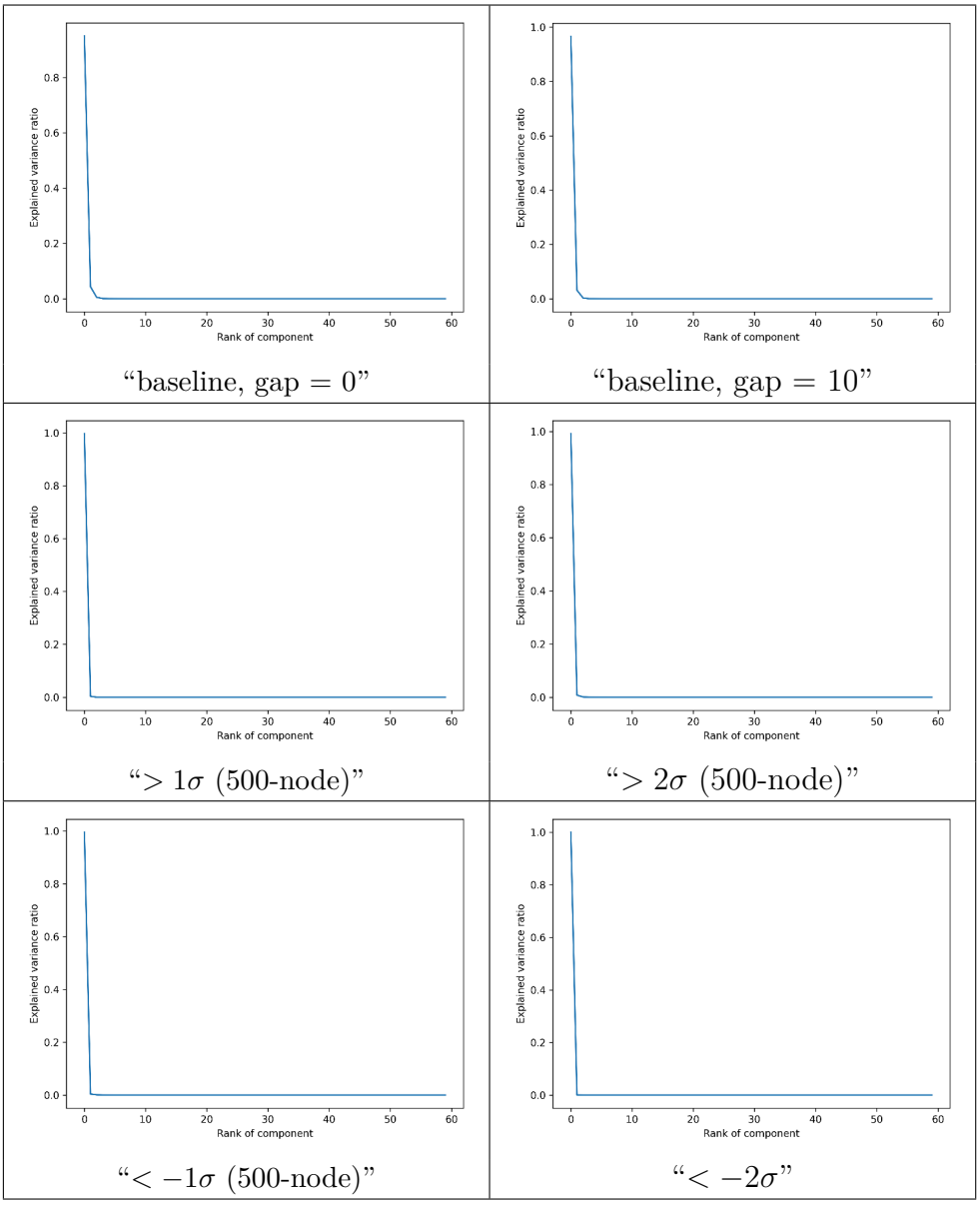

Figure 89 – PCA variance ratio for rule B0157/S457 LLNA features of k-logistic map networks, $k \in \{0, 1, 2, 3, 4\}$, $r = 3.9$.
Source: By the author.

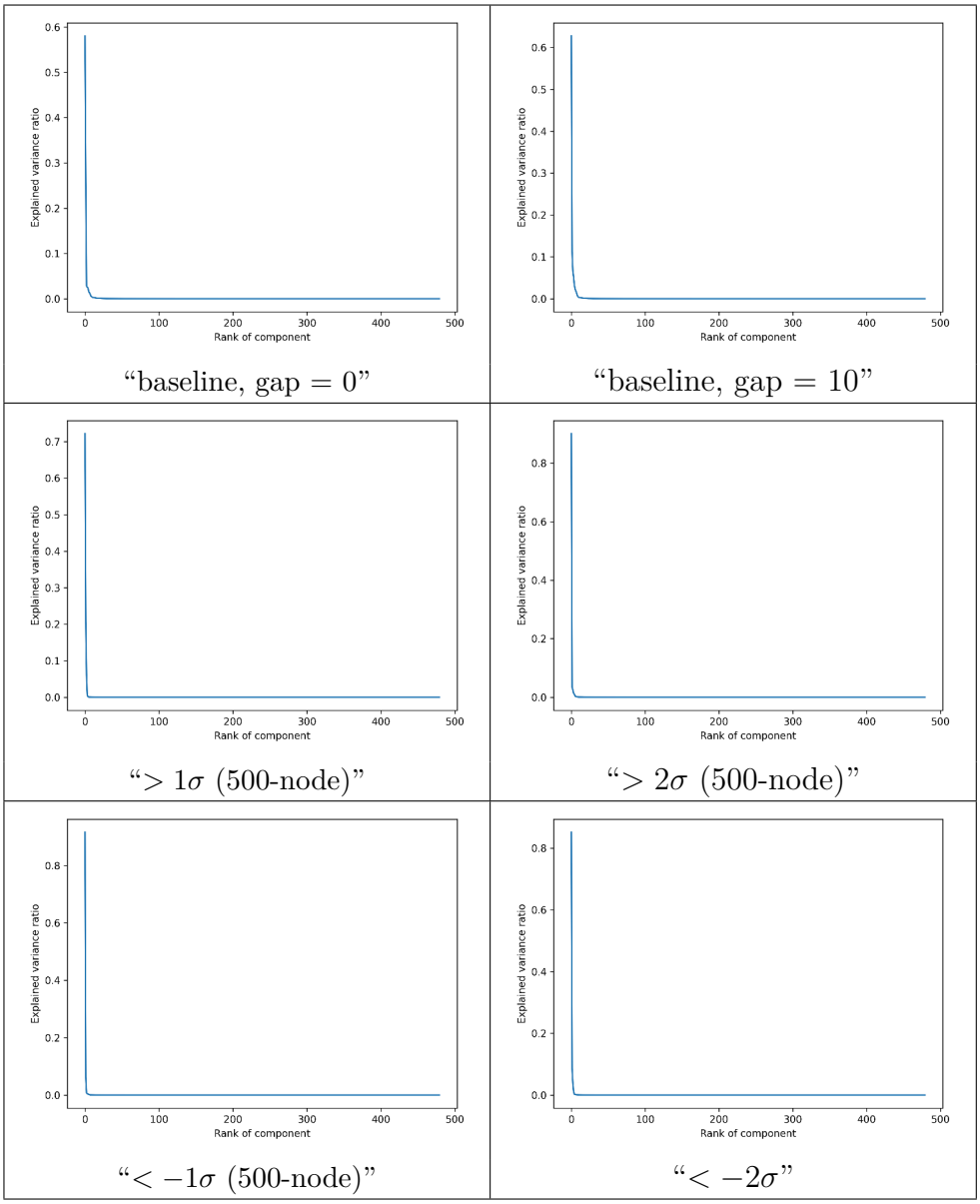

Figure 90 – PCA variance ratio for rule B0157/S457 LLNA-BP features of k-logistic map networks, $k \in \{0, 1, 2, 3, 4\}$, $r = 3.9$.
Source: By the author.

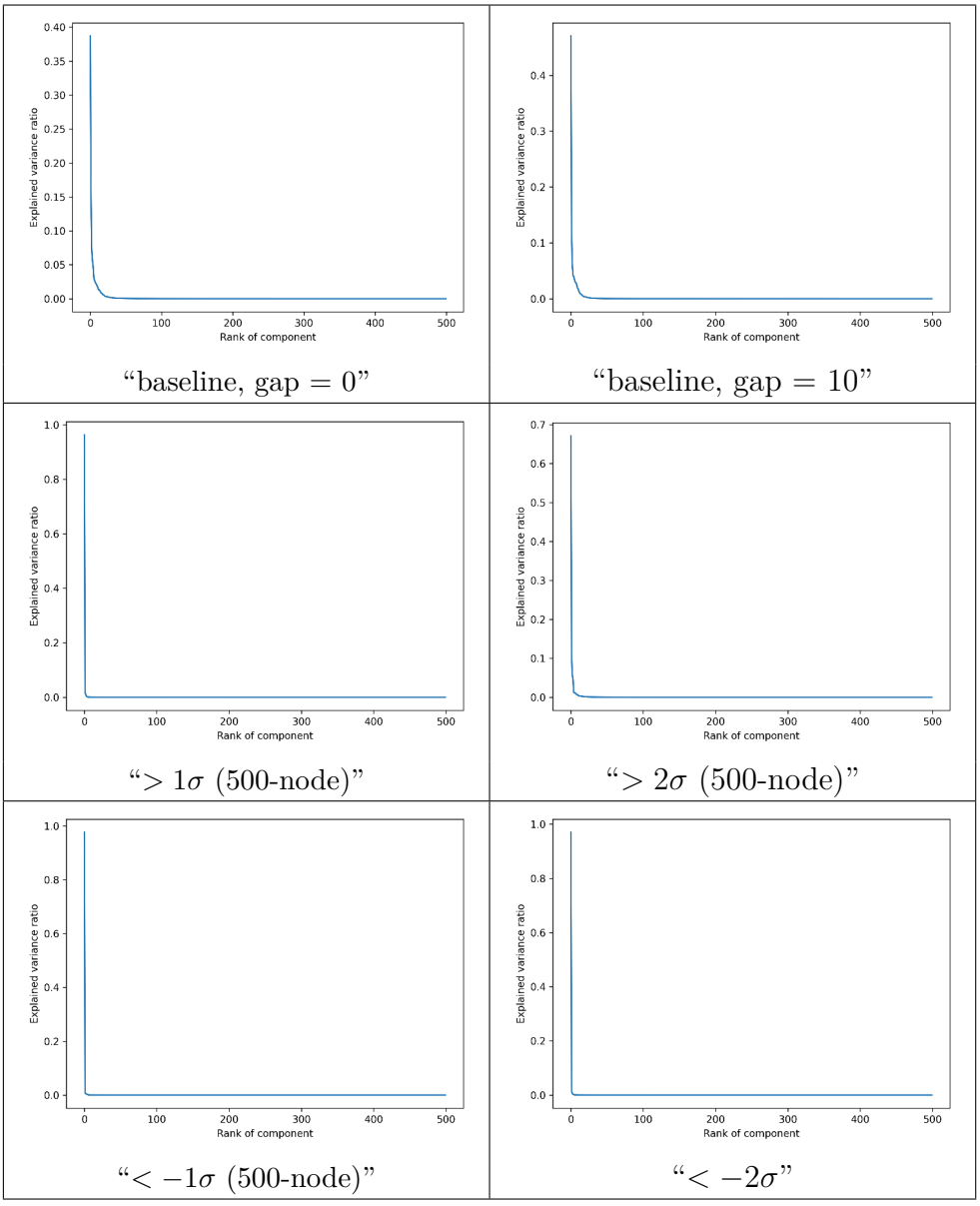

Figure 91 – PCA variance ratio for rule B0157/S457 LLNA-DTEP features of k-logistic map networks, $k \in \{0, 1, 2, 3, 4\}$, $r = 3.9$.
Source: By the author.

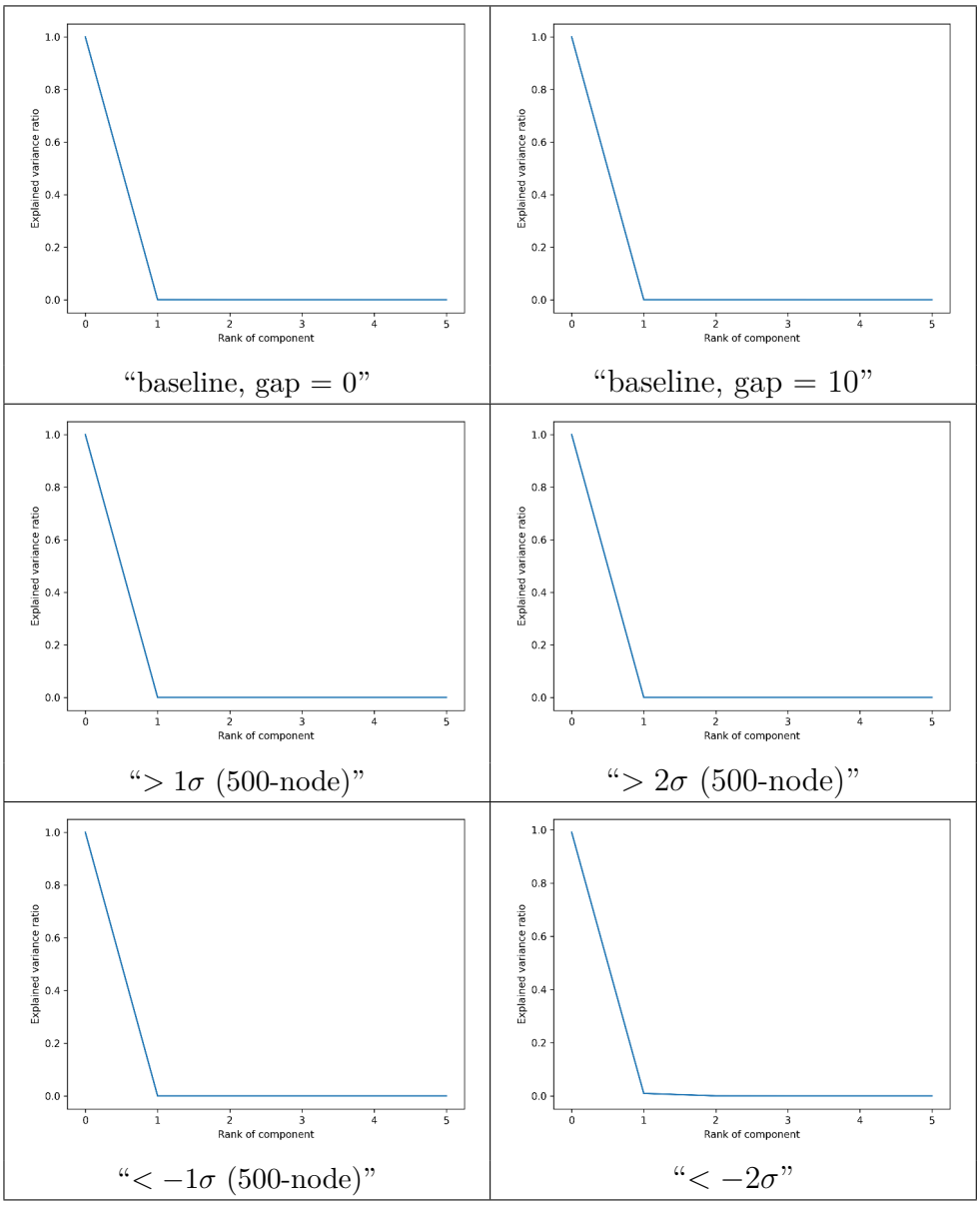

Figure 92 – PCA variance ratio for structural features of k-logistic map networks, $k \in \{5, 6, 7, 8, 9\}$, $r = 3.9$.
Source: By the author.

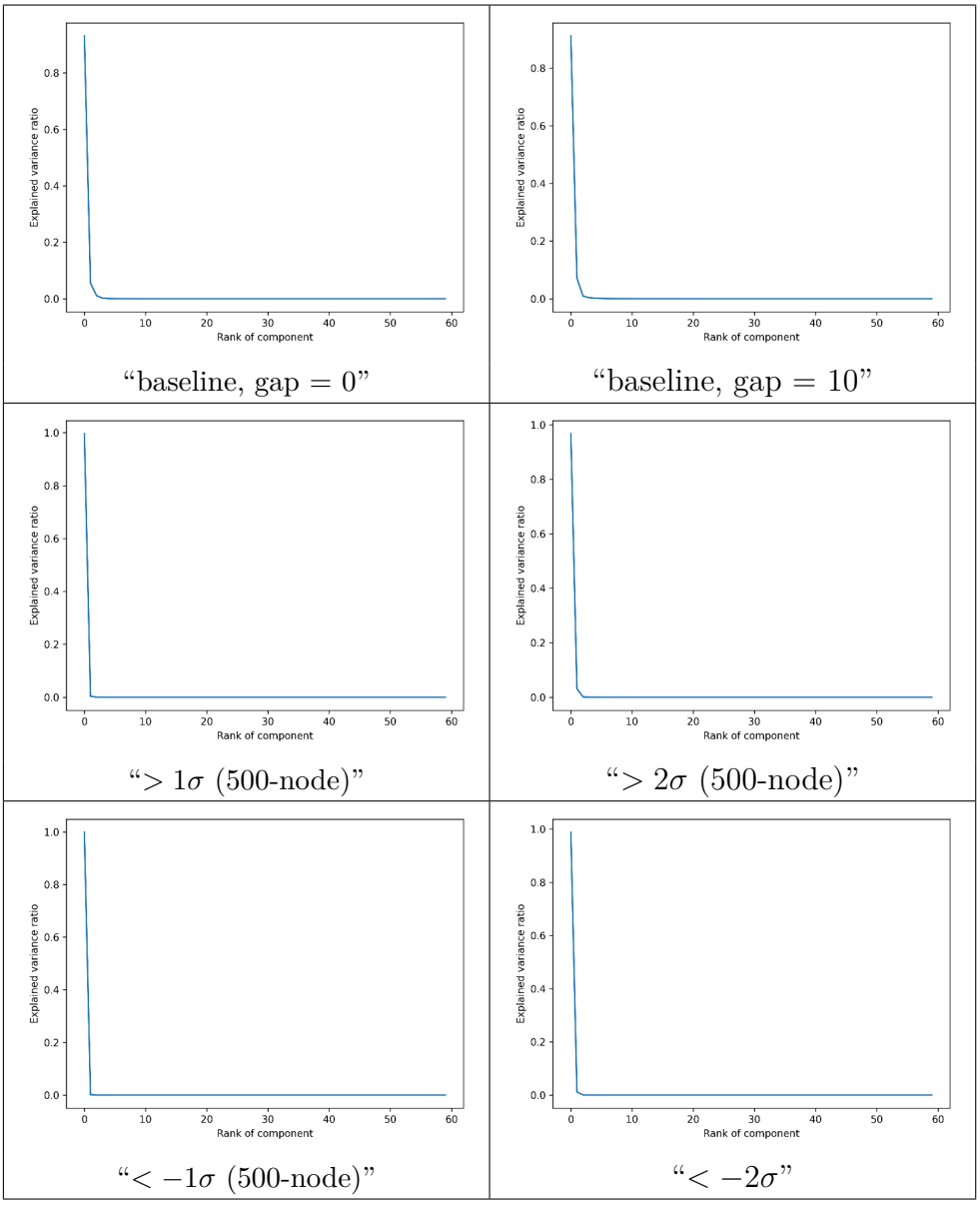

Figure 93 – PCA variance ratio for rule B135678/S03456 LLNA features of k-logistic map networks, $k \in \{5, 6, 7, 8, 9\}$, $r = 3.9$.
Source: By the author.

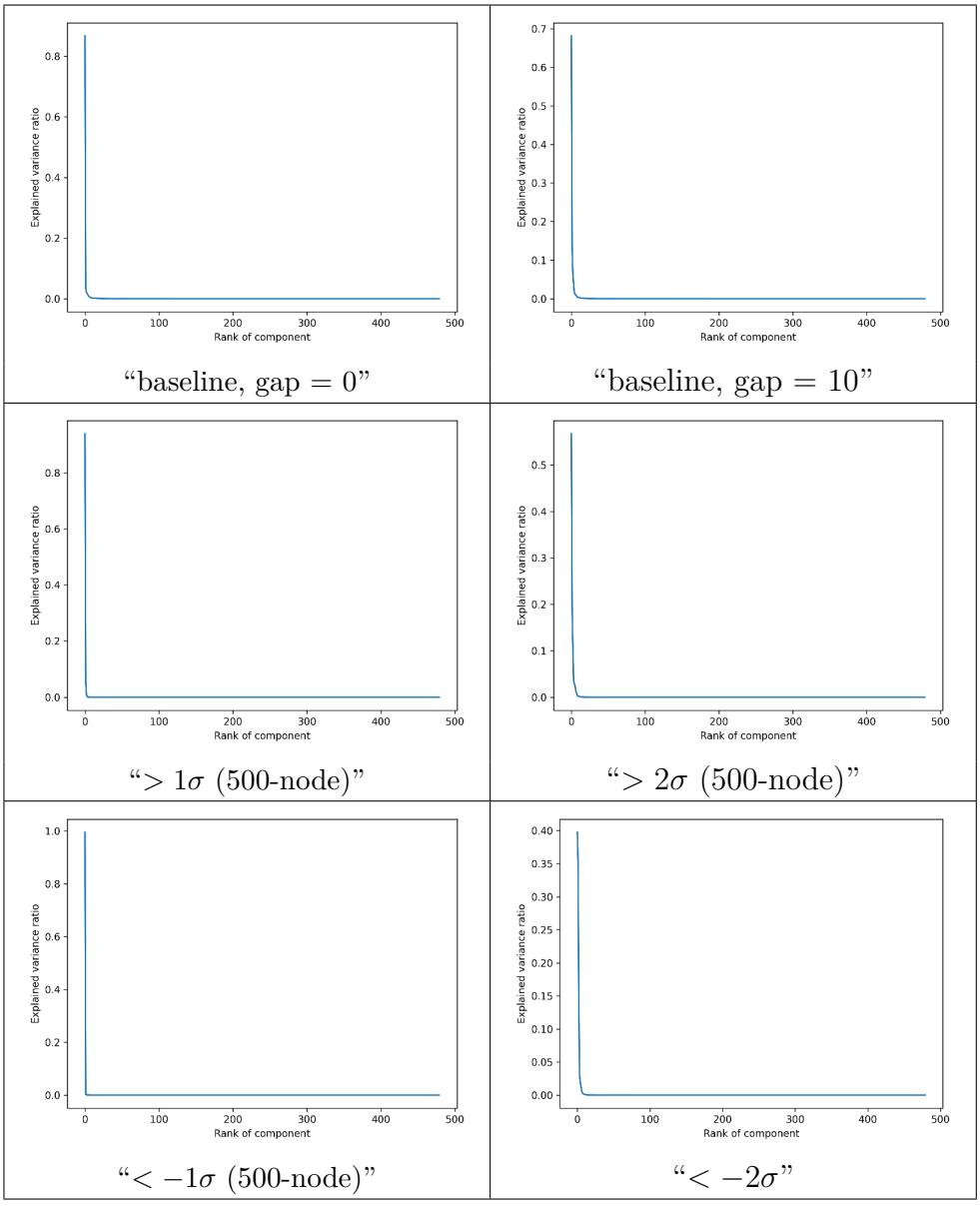

Figure 94 – PCA variance ratio for rule B135678/S03456 LLNA-BP features of k-logistic map networks, $k \in \{5, 6, 7, 8, 9\}$, $r = 3.9$.
Source: By the author.

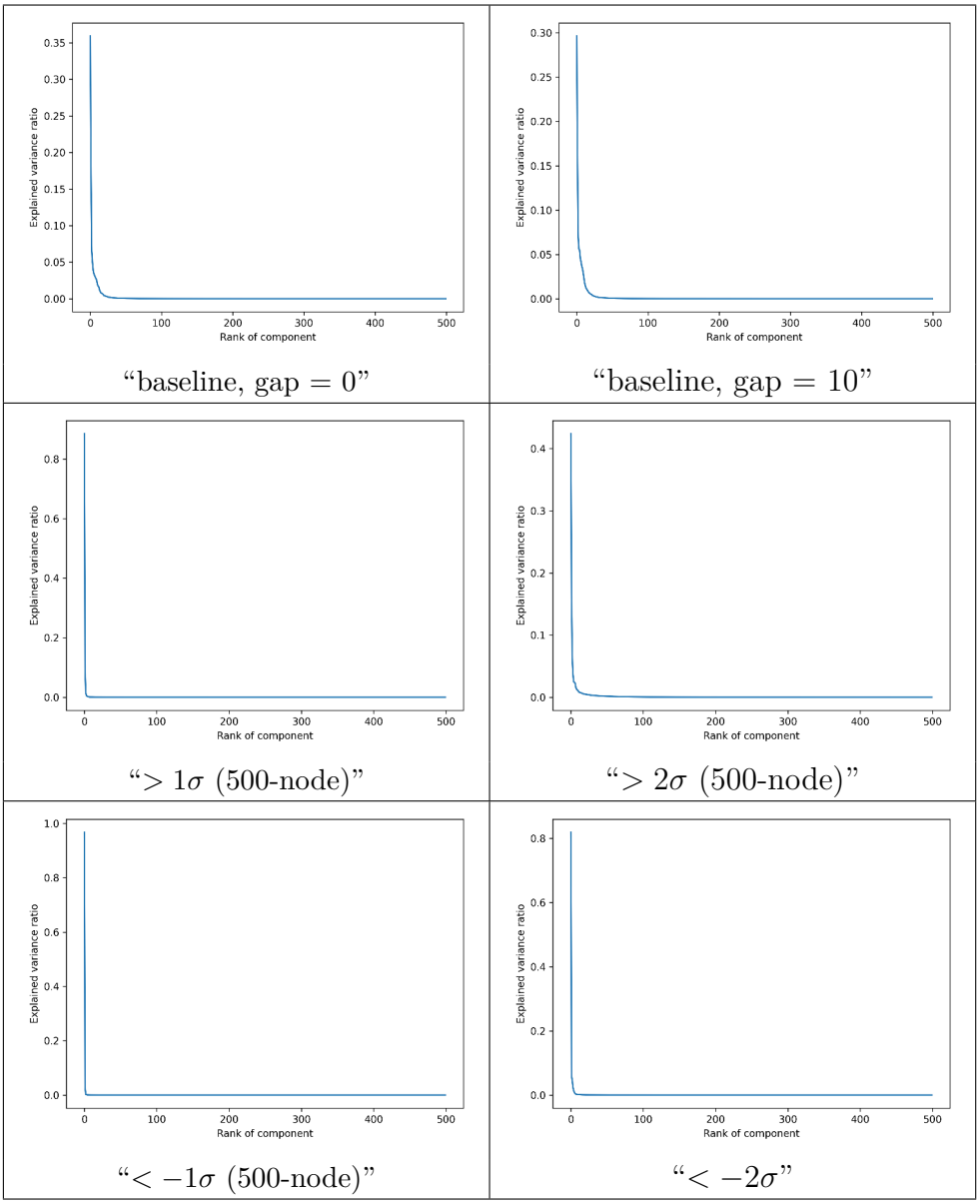

Figure 95 – PCA variance ratio for rule B135678/S03456 LLNA-DTEP features of k-logistic map networks, $k \in \{5, 6, 7, 8, 9\}$, $r = 3.9$.
Source: By the author.

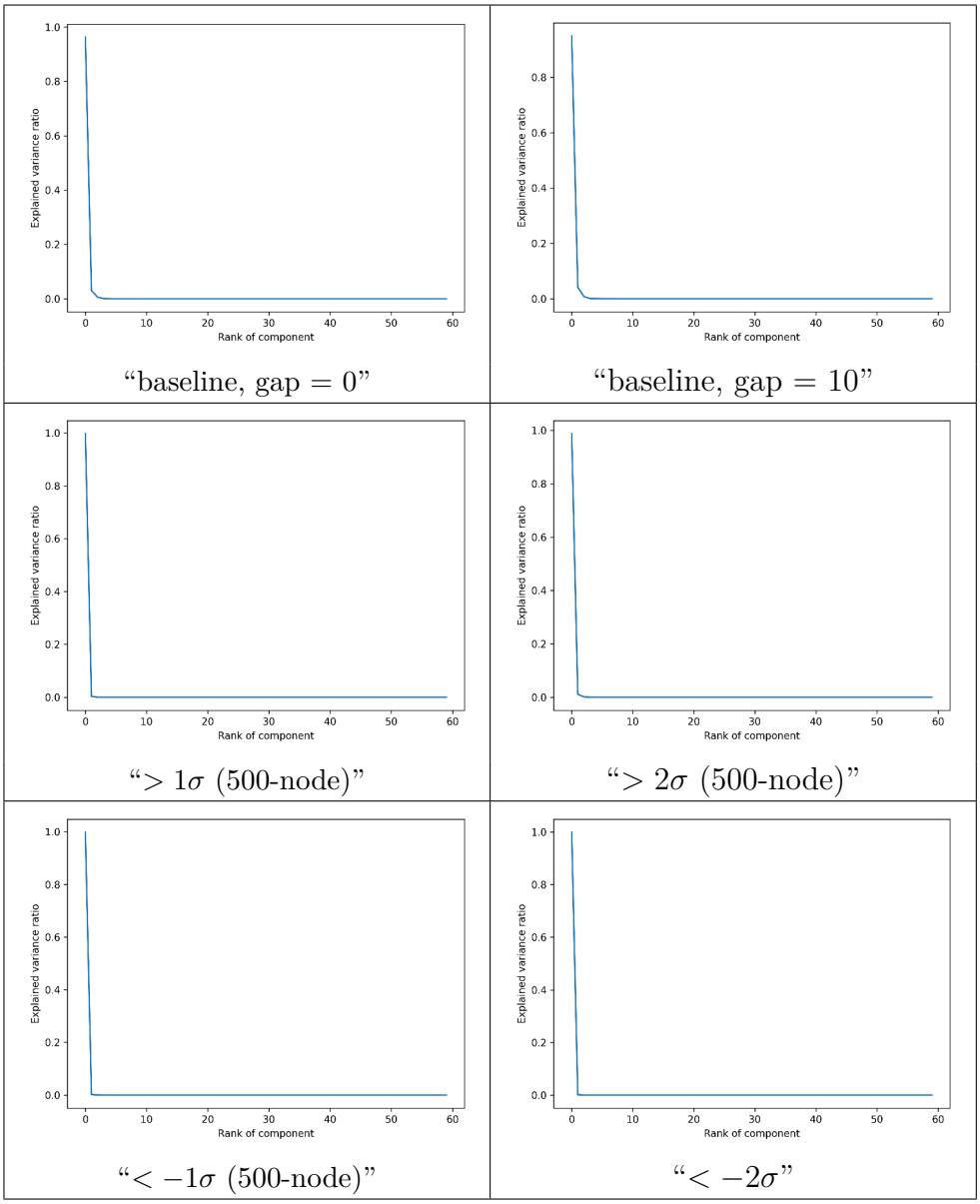

Figure 96 – PCA variance ratio for rule B0157/S457 LLNA features of k-logistic map networks, $k \in \{5, 6, 7, 8, 9\}$, $r = 3.9$.
Source: By the author.

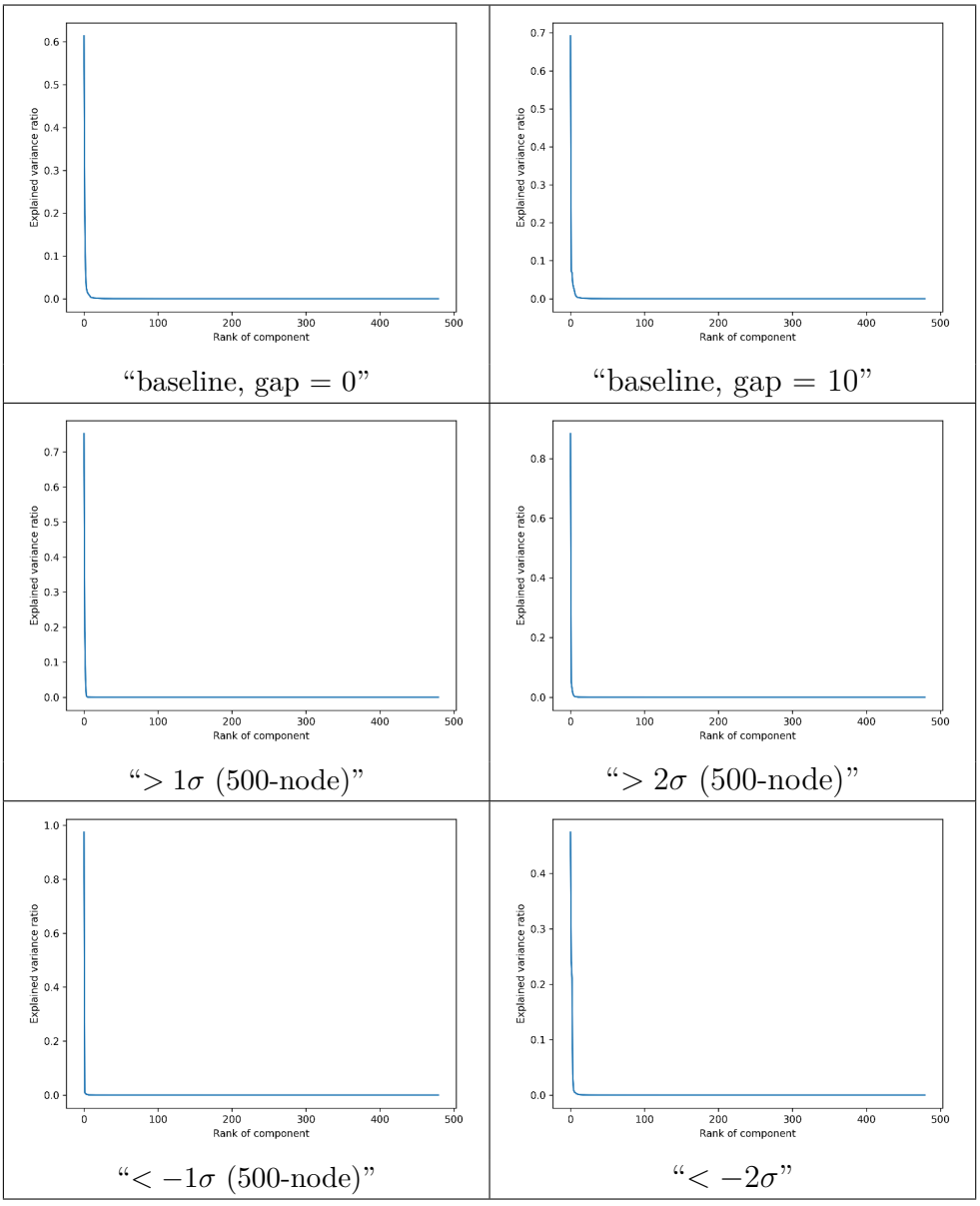

Figure 97 – PCA variance ratio for rule B0157/S457 LLNA-BP features of k-logistic map networks, $k \in \{5, 6, 7, 8, 9\}$, $r = 3.9$.
Source: By the author.

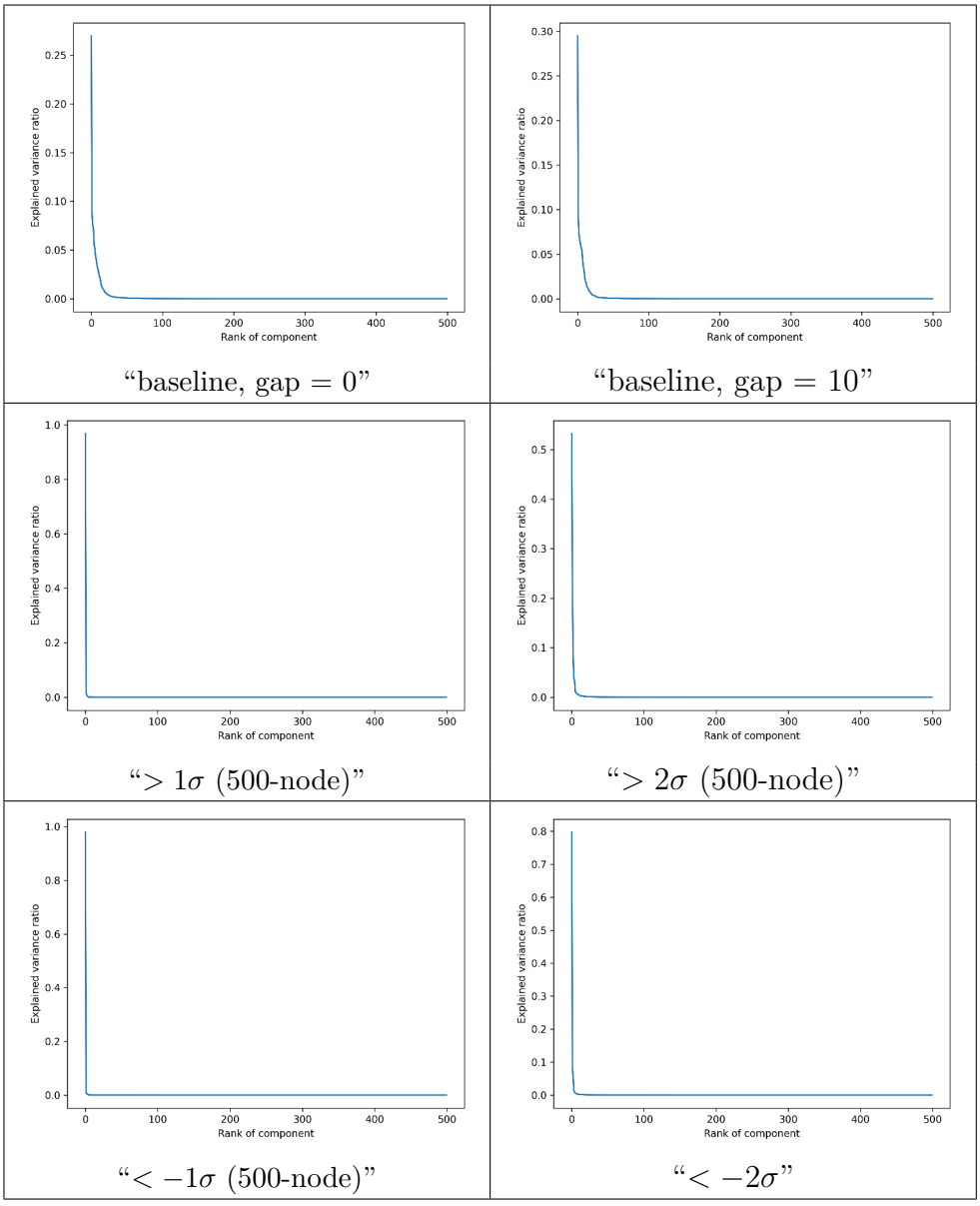

Figure 98 – PCA variance ratio for rule B0157/S457 LLNA-DTEP features of k-logistic map networks, $k \in \{5, 6, 7, 8, 9\}$, $r = 3.9$.
Source: By the author.

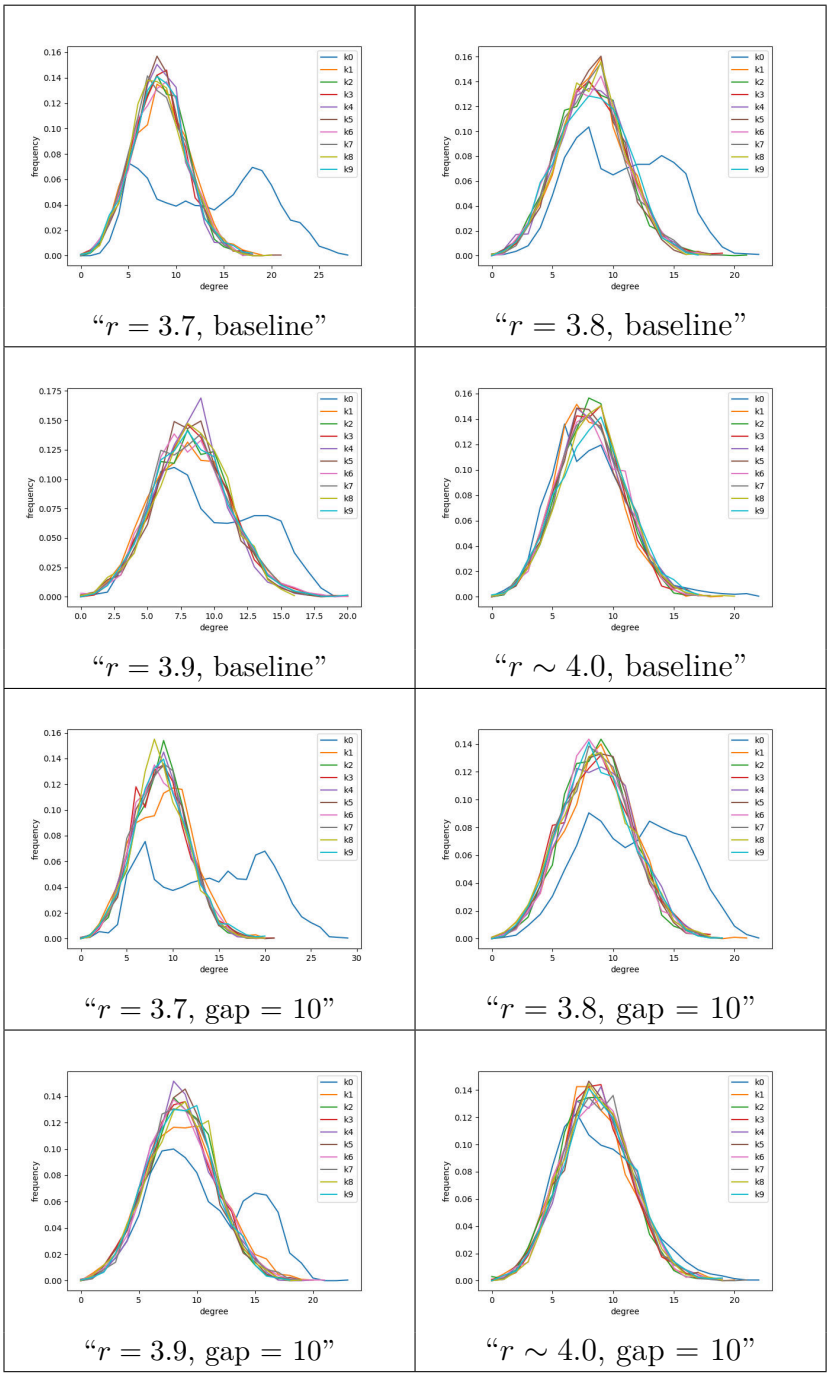

Figure 99 – Degree distribution for the k-logistic map, baseline networks and with gap $= 10$.
Source: By the author.

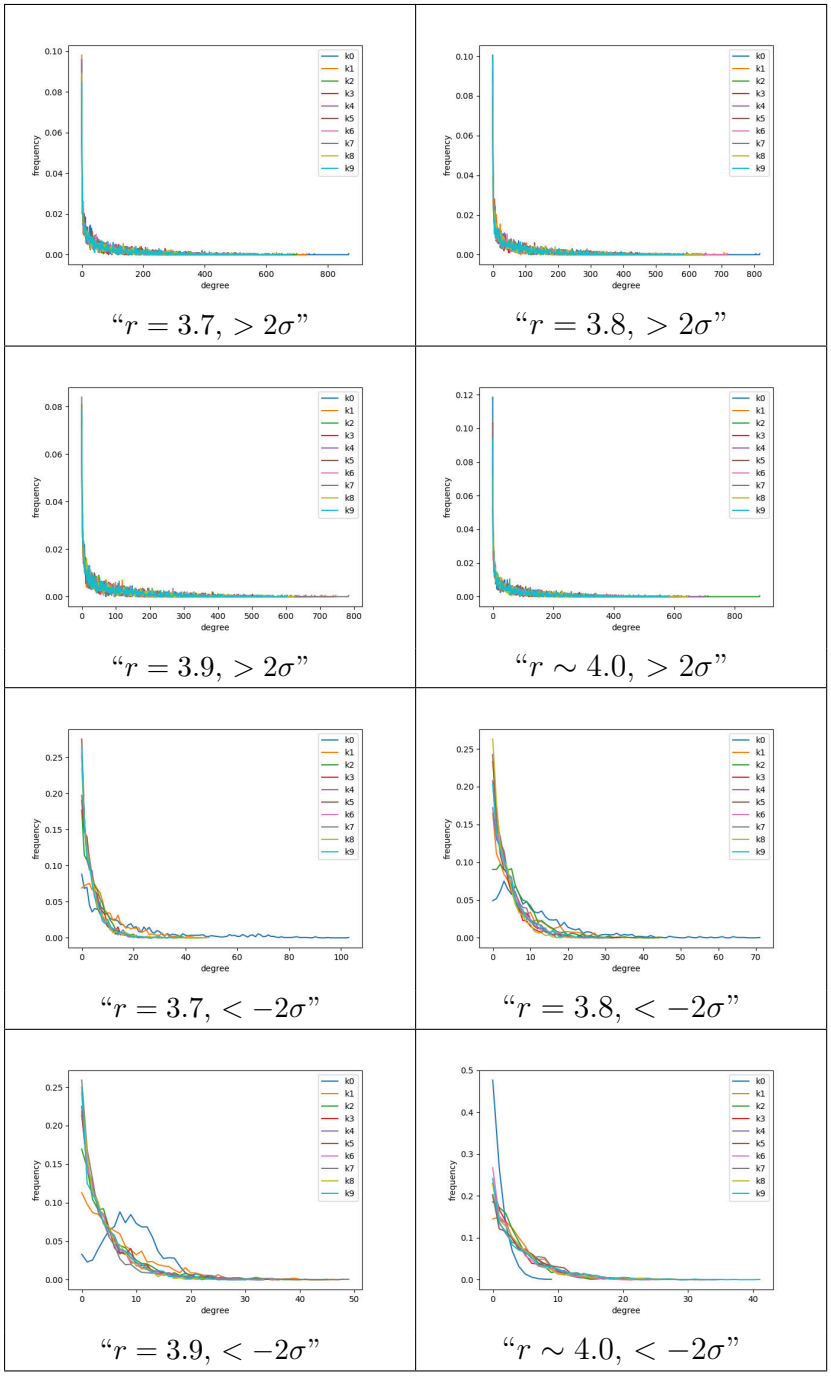

Figure 100 – Degree distribution for k-logistic map CNP.
Source: By the author.

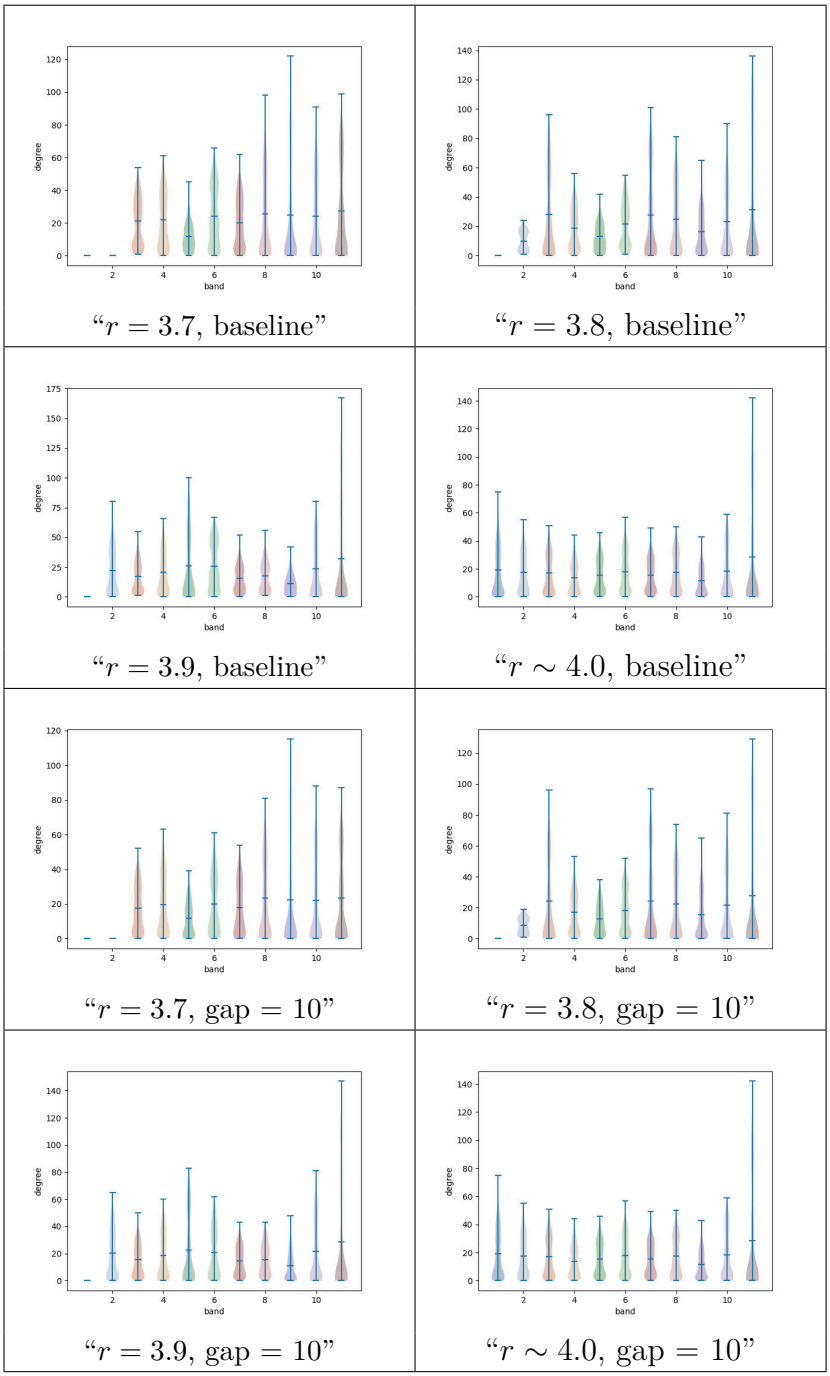

Figure 101 – Violin plots for k-logistic map with $k = 0$, baseline networks and with gap $= 10$.
Source: By the author.

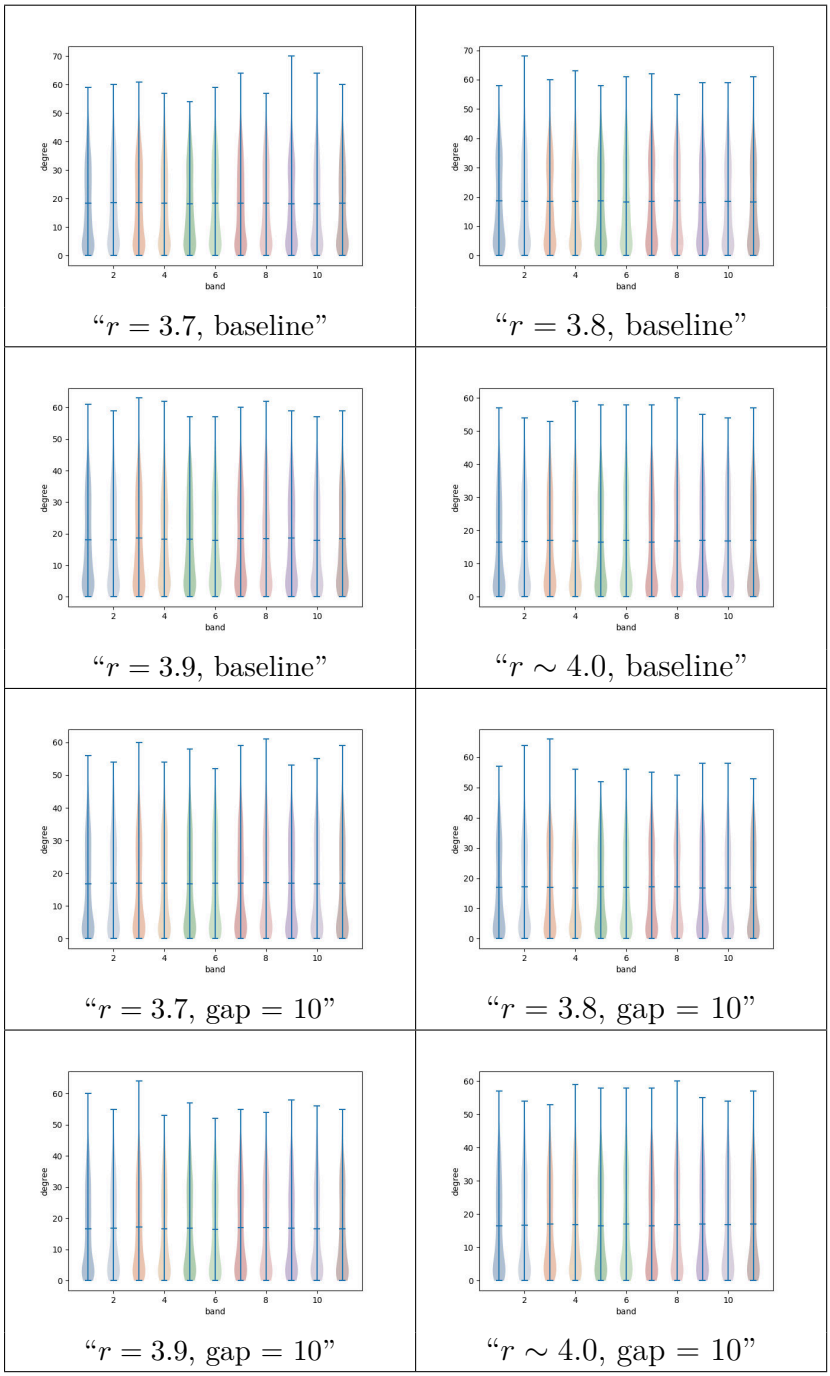

Figure 102 – Violin plots for k-logistic map with $k = 5$, baseline networks with gap $= 0$ and gap $= 10$.
Source: By the author.

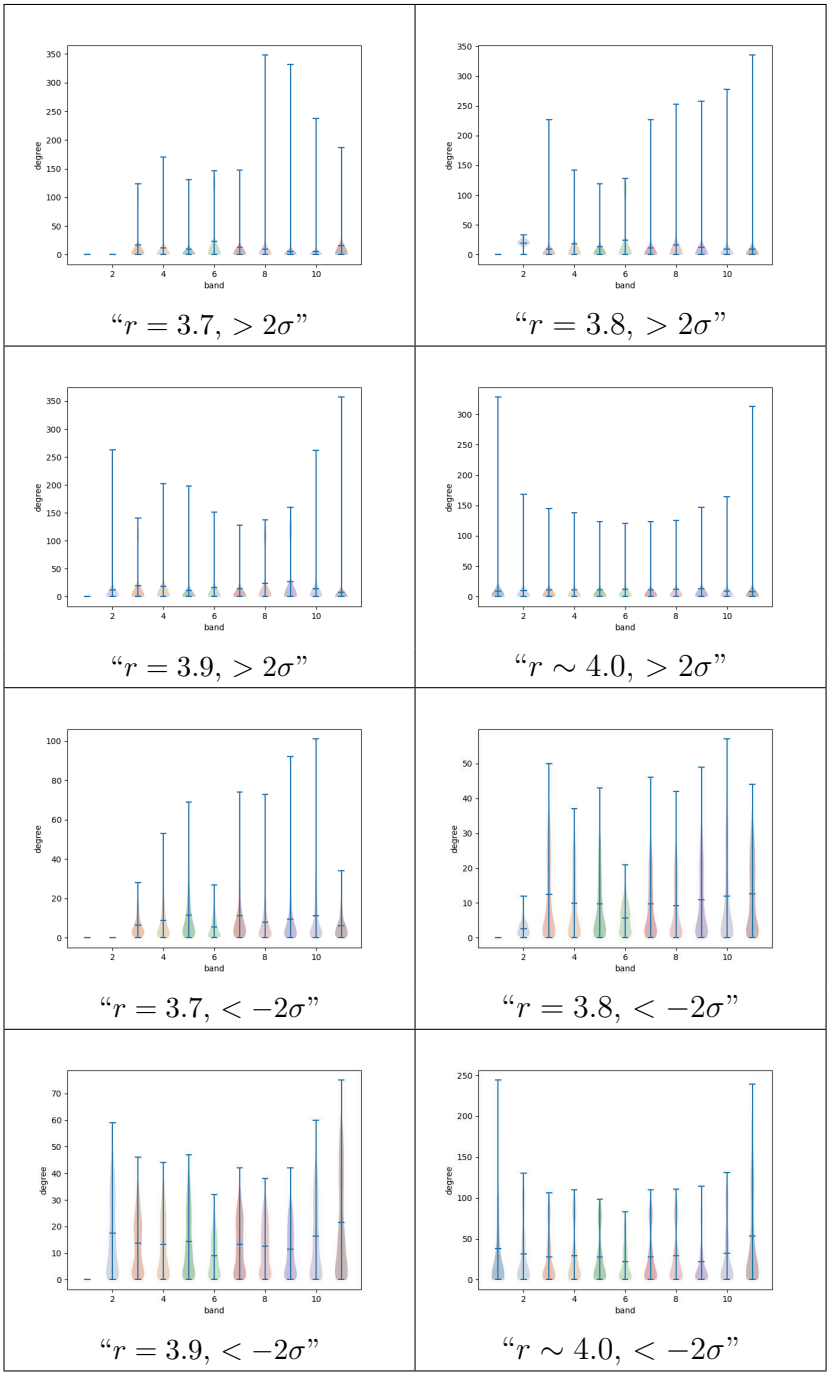

Figure 103 – Violin plots for k-logistic map CNP with $k = 0$.
Source: By the author.

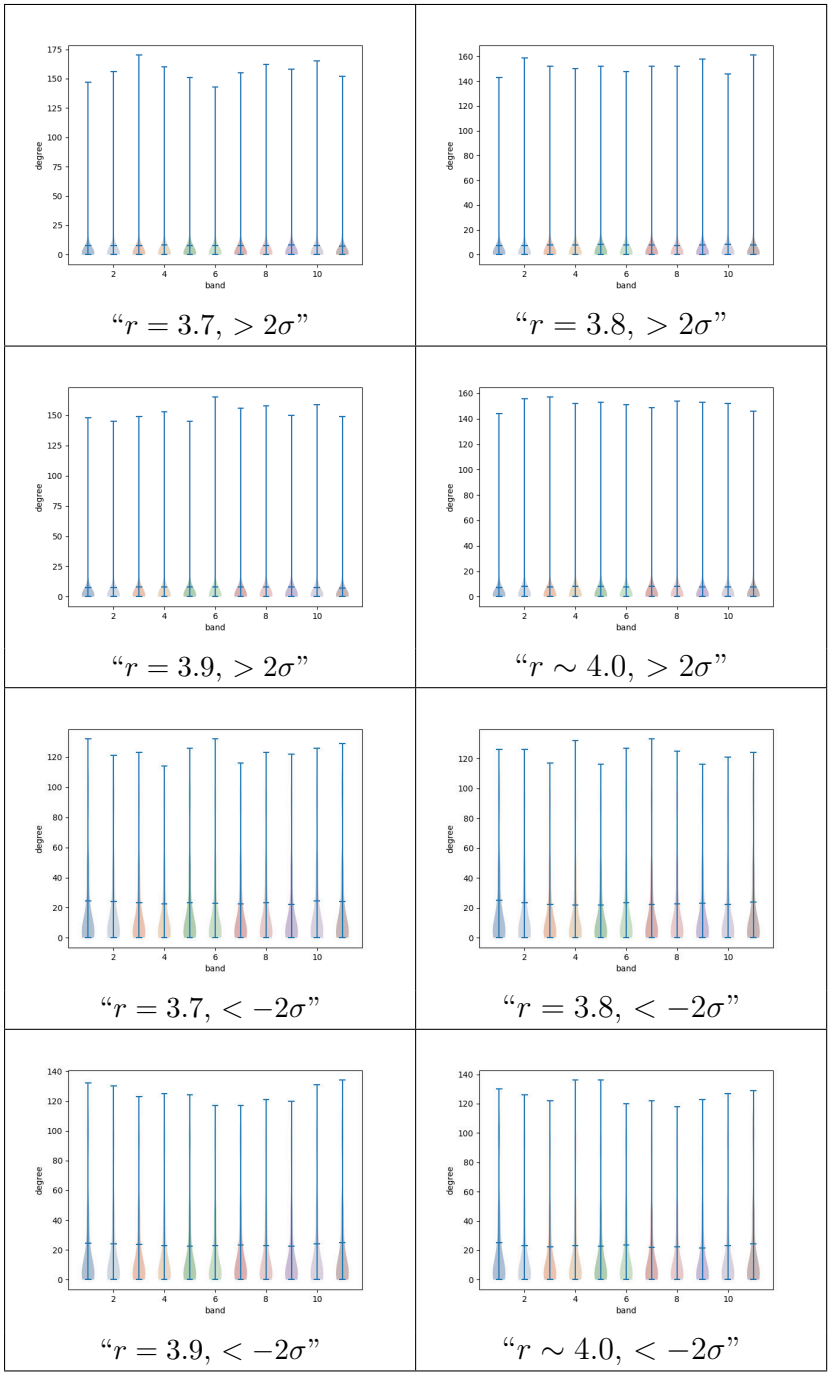

Figure 104 – Violin plots for k-logistic map CNP with $k = 5$.
Source: By the author.

Table 13 – Results for network classification, k-logistic map CNP with $k = \{0, 1, 2, 3, 4\}$ and $r = 3.7$.

	baseline	gap = 10	$< -2\sigma$
Structural measurements	69.95±0.60	68.82±0.59	**71.04**±0.70
LLNA B135678/S03456	58.39±1.80	56.04±1.59	**72.48**±1.41
LLNA-BP B135678/S03456	37.72±1.53	28.94±3.85	**68.66**±0.91
LLNA-DTEP B135678/S03456	61.13±1.10	60.77±1.12	**69.87**±0.49
LLNA B0157/S457	53.01±1.38	52.28±1.67	**73.11**±1.18
LLNA-BP B0157/S457	42.13±1.32	40.66±1.48	**70.04**±1.23
LLNA-DTEP B0157/S457	58.06±1.14	61.09±1.05	**70.39**±0.53

Source: By the author.

Table 14 – Results for network classification, k-logistic map CNP with $k \in \{0, 1, 2, 3, 4\}$ and $r = 3.8$.

	baseline	gap = 10	$< -2\sigma$
Structural measurements	60.03±0.82	65.64±0.69	**71.34**±0.73
LLNA B135678/S03456	55.30±1.63	53.29±1.92	**73.35**±1.73
LLNA-BP B135678/S03456	31.89±1.20	33.32±2.57	**71.84**±1.08
LLNA-DTEP B135678/S03456	53.55±1.19	56.20±1.24	**72.00**±0.95
LLNA B0157/S457	54.85±1.61	55.75±1.64	**72.52**±1.50
LLNA-BP B0157/S457	31.99±1.19	35.25±1.24	**72.22**±0.81
LLNA-DTEP B0157/S457	53.41±0.87	55.78±1.19	**63.84**±0.71

Source: By the author.

Table 15 – Results for network classification, k-logistic map CNP with $k \in \{0, 1, 2, 3, 4\}$ and $r = 3.9$.

	baseline	gap = 10	$< -2\sigma$
Structural measurements	59.82±0.61	64.51±0.89	**73.55**±0.68
LLNA B135678/S03456	53.01±1.63	54.53±1.80	**69.55**±1.68
LLNA-BP B135678/S03456	31.75±1.60	39.87±1.64	**68.37**±0.76
LLNA-DTEP B135678/S03456	51.60±1.34	52.65±1.46	**67.19**±0.52
LLNA B0157/S457	43.21±1.68	49.02±1.57	**72.19**±1.44
LLNA-BP B0157/S457	30.33±1.16	37.21±1.59	**68.65**±0.55
LLNA-DTEP B0157/S457	53.67±1.22	54.39±1.04	**66.36**±0.37

Source: By the author.

Table 16 – Results for network classification, k-logistic map CNP with $k \in \{0, 1, 2, 3, 4\}$ and $r \sim 4.0$.

	baseline	gap = 10	$< -2\sigma$
Structural measurements	**64.20**±0.67	62.90±0.73	53.23±0.82
LLNA B135678/S03456	47.12±1.56	45.15±1.85	**52.31**±1.92
LLNA-BP B135678/S03456	28.29±3.05	23.49±1.36	**50.12**±1.04
LLNA-DTEP B135678/S03456	57.85±1.40	**58.18**±1.22	46.20±0.84
LLNA B0157/S457	47.90±1.88	47.84±1.90	**51.01**±1.47
LLNA-BP B0157/S457	33.41±2.72	34.67±1.71	**46.57**±1.04
LLNA-DTEP B0157/S457	**59.88**±1.28	58.89±1.04	46.02±0.88

Source: By the author.

Table 17 – Results for network classification, k-logistic map CNP with $k \in \{5, 6, 7, 8, 9\}$ and $r = 3.7$.

	baseline	gap = 10	$< -2\sigma$
Structural measurements	**23.89**±1.14	19.52±0.86	19.79±1.00
LLNA B135678/S03456	**20.76**±1.75	19.17±1.73	19.26±1.88
LLNA-BP B135678/S03456	20.67±1.22	20.82±1.11	**21.43**±1.40
LLNA-DTEP B135678/S03456	**20.63**±1.46	20.51±1.28	19.44±1.04
LLNA B0157/S457	**20.17**±1.80	19.67±1.77	19.09±1.69
LLNA-BP B0157/S457	21.38±1.24	**22.97**±1.11	22.27±1.28
LLNA-DTEP B0157/S457	**22.27**±1.23	22.03±0.99	20.80±1.22

Source: By the author.

Table 18 – Results for network classification, k-logistic map CNP with $k \in \{5, 6, 7, 8, 9\}$ and $r = 3.8$.

	baseline	gap = 10	$< -2\sigma$
Structural measurements	16.81±1.17	17.58±1.14	**22.73**±1.00
LLNA B135678/S03456	19.49±2.04	**20.81**±1.86	20.69±1.94
LLNA-BP B135678/S03456	20.56±1.18	**22.16**±1.01	21.39±1.35
LLNA-DTEP B135678/S03456	21.80±1.42	18.40±1.49	**22.78**±0.91
LLNA B0157/S457	19.73±1.75	20.32±1.88	**21.79**±1.64
LLNA-BP B0157/S457	20.65±1.24	18.96±1.21	**21.01**±1.15
LLNA-DTEP B0157/S457	18.91±1.15	18.17±1.05	**22.90**±0.55

Source: By the author.

Table 19 – Results for network classification, k-logistic map CNP with $k \in \{5, 6, 7, 8, 9\}$ and $r = 3.9$.

	baseline	gap = 10	$< -2\sigma$
Structural measurements	21.12±1.12	21.31±1.14	**21.93**±1.13
LLNA B135678/S03456	**20.58**±1.79	20.37±1.94	20.24±2.05
LLNA-BP B135678/S03456	17.82±1.33	19.43±1.44	**21.31**±1.38
LLNA-DTEP B135678/S03456	**20.39**±1.33	18.56±1.34	19.60±1.09
LLNA B0157/S457	**21.26**±1.71	20.84±1.72	19.84±1.62
LLNA-BP B0157/S457	19.68±1.46	18.64±1.33	**20.62**±1.36
LLNA-DTEP B0157/S457	**21.00**±1.31	20.97±0.98	20.04±1.19

Source: By the author.

Table 20 – Results for network classification, k-logistic map CNP with $k \in \{5, 6, 7, 8, 9\}$ and $r \sim 4.0$.

	baseline	gap = 10	$< -2\sigma$
Structural measurements	17.81±1.24	17.68±1.22	**20.88**±1.02
LLNA B135678/S03456	**19.82**±1.86	19.14±1.57	19.73±1.74
LLNA-BP B135678/S03456	18.60±1.04	20.34±1.19	**21.59**±1.19
LLNA-DTEP B135678/S03456	18.11±1.40	18.44±1.52	**21.72**±1.13
LLNA B0157/S457	19.60±1.79	19.56±1.77	**20.45**±1.77
LLNA-BP B0157/S457	19.43±1.36	**20.96**±1.22	20.74±1.32
LLNA-DTEP B0157/S457	18.82±1.32	18.36±1.31	**21.71**±1.10

Source: By the author.

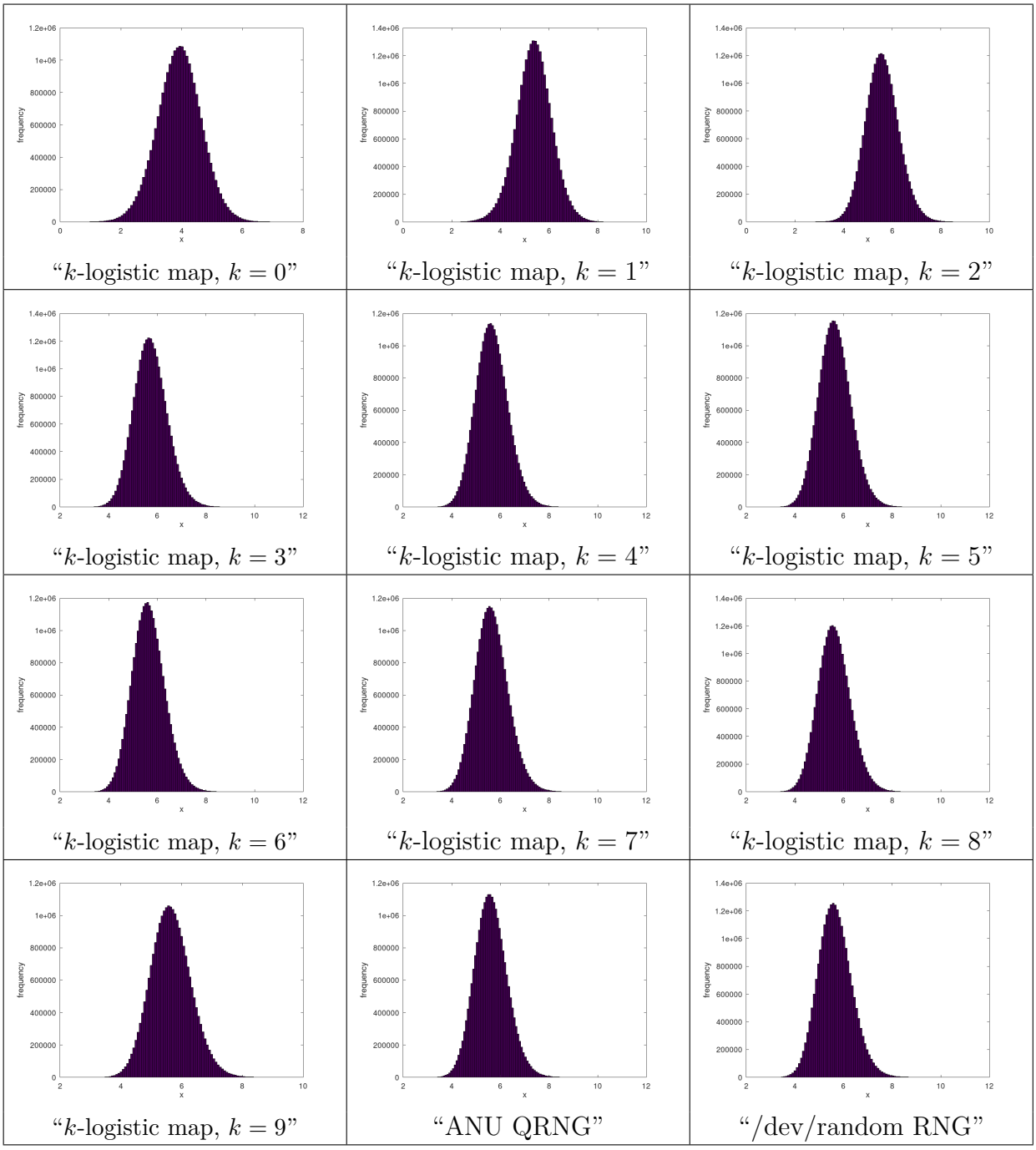

Figure 105 – Histograms displaying the Tracy-Widom-like distribution for the distribution of nonzero DTW values for the adjacency matrix. $r = 3.9$ for k-logistic map values.
Source: By the author.

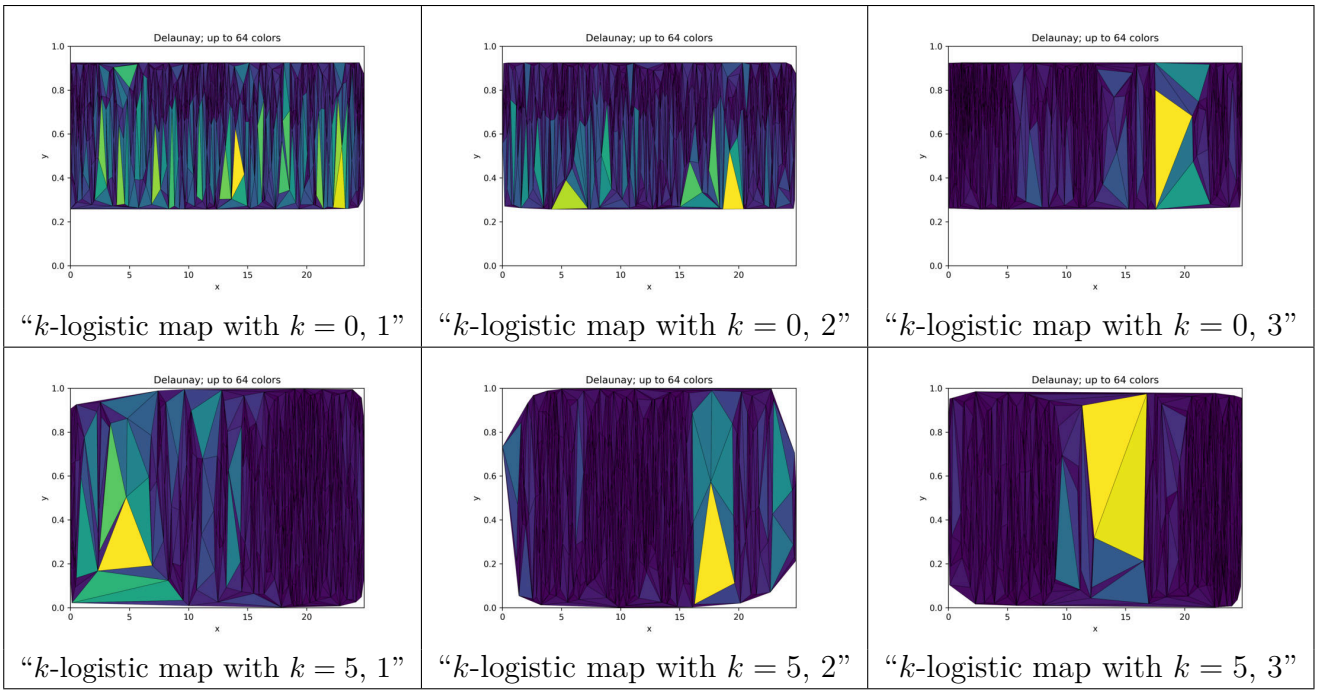

Figure 106 – Delaunay triangulations of baseline complex networks for networks with 5,000 vertices, k-logistic map CNP with $k = 0$ and $k = 5$, $r = 3.7$.
Source: By the author.

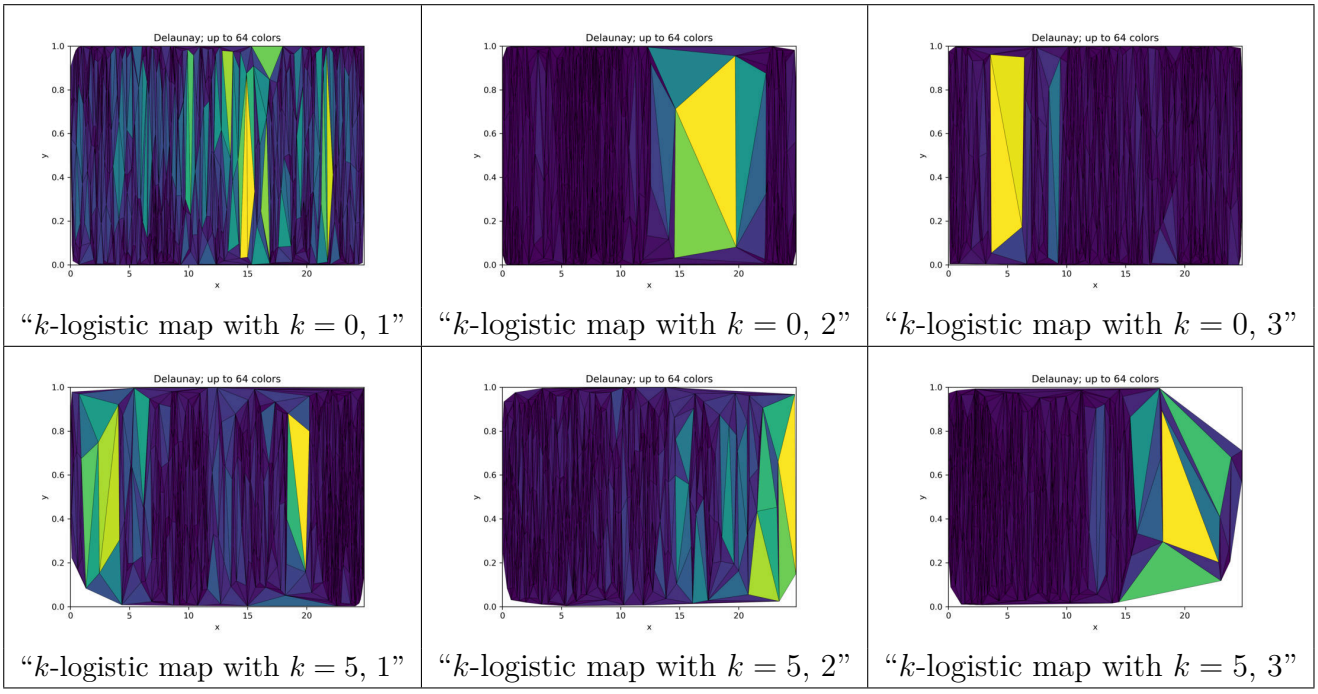

Figure 107 – Delaunay triangulations of baseline complex networks for networks with 5,000 vertices, k-logistic map CNP with $k = 0$ and $k = 5$, $r = 3.99999$.
Source: By the author.

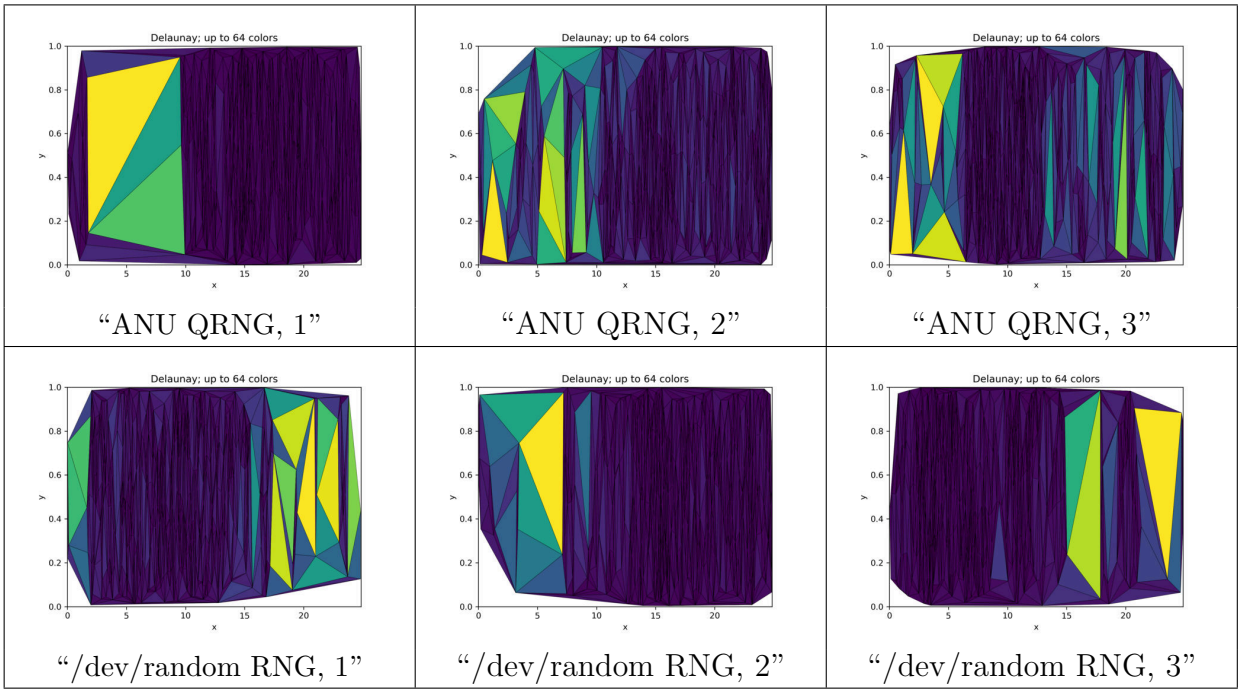

Figure 108 – Delaunay triangulations of baseline complex networks for networks with 5,000 vertices. ANU Quantum and Linux /dev/random RNGs CNP.
Source: By the author.

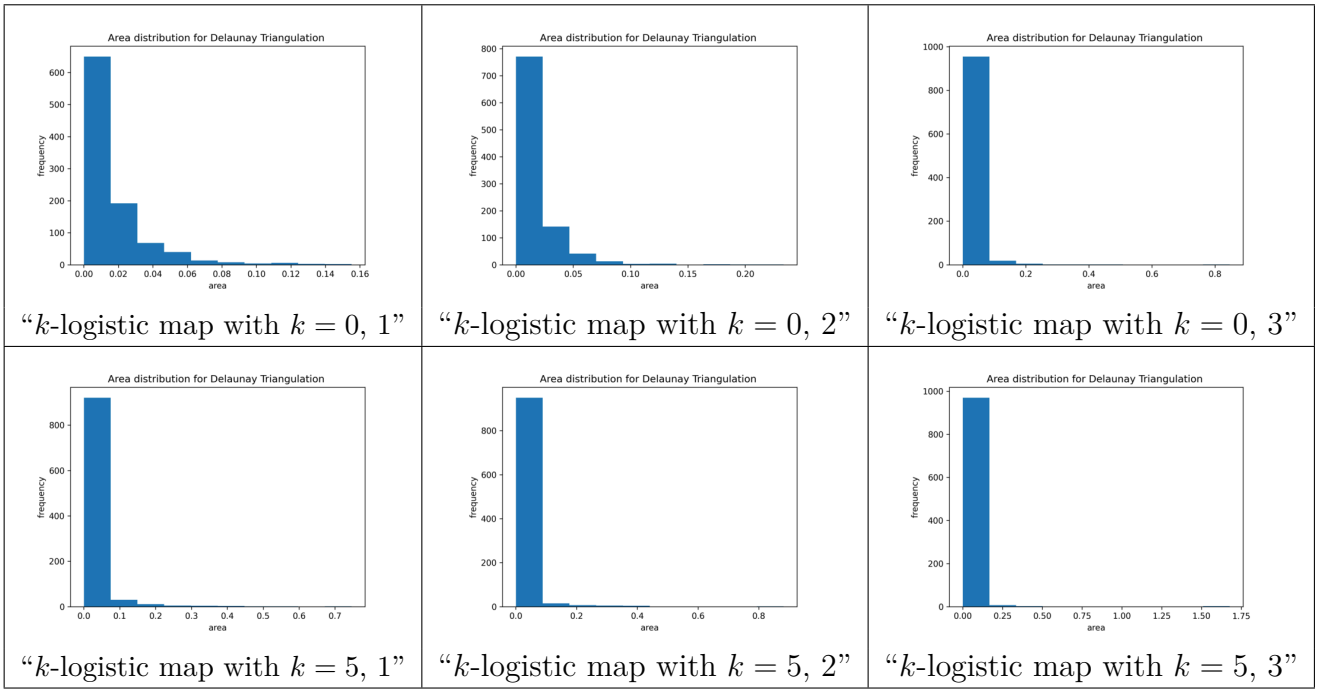

Figure 109 – Histograms for area distribution of Delaunay triangulations of baseline complex networks for networks with 5,000 vertices, k-logistic map CNP with $k = 0$ and $k = 5$, $r = 3.7$.
Source: By the author.

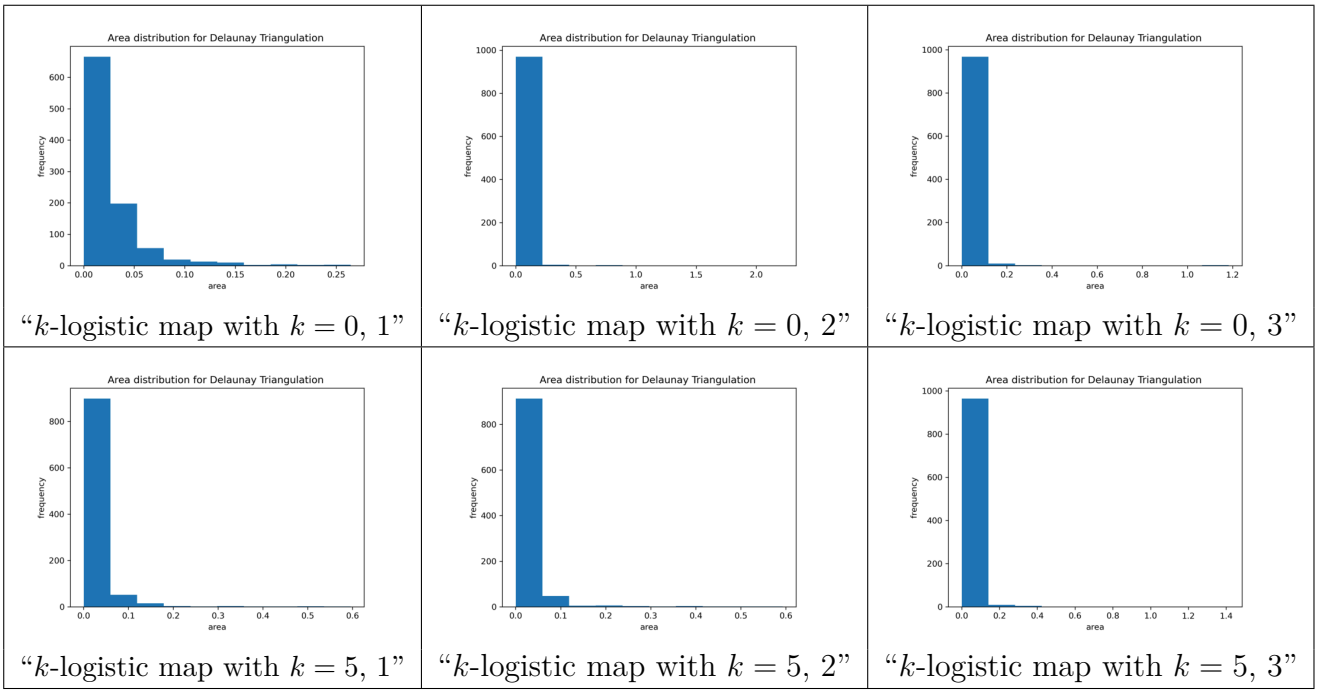

Figure 110 – Histograms for area distribution of Delaunay triangulations of baseline complex networks for networks with 5,000 vertices, k-logistic map CNP with $k = 0$ and $k = 5$, $r = 3.99999$.
Source: By the author.

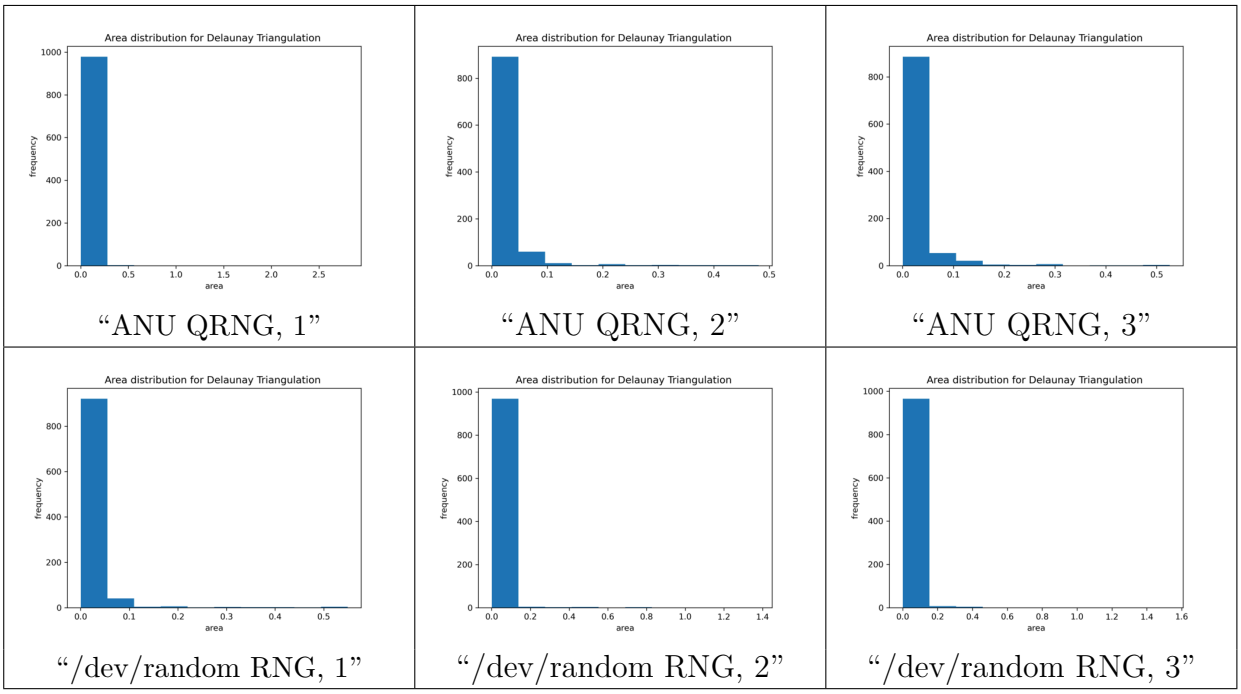

Figure 111 – Histograms for area distribution of Delaunay triangulations of baseline complex networks for networks with 5,000 vertices. ANU Quantum and Linux /dev/random RNGs CNP.
Source: By the author.

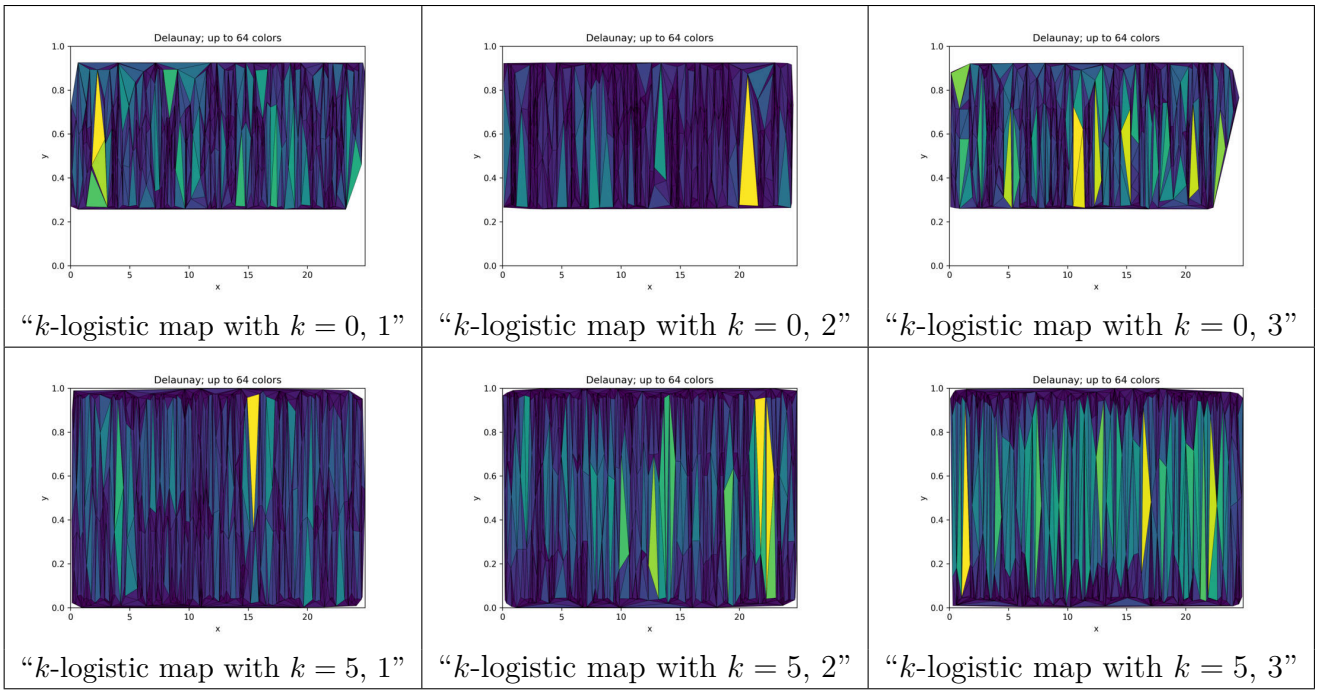

“k-logistic map with $k = 0$, 1” “k-logistic map with $k = 0$, 2” “k-logistic map with $k = 0$, 3”

“k-logistic map with $k = 5$, 1” “k-logistic map with $k = 5$, 2” “k-logistic map with $k = 5$, 3”

Figure 112 – Delaunay triangulations of $> 1\sigma$ complex networks for networks with 5,000 vertices, k-logistic map CNP with $k = 0$ and $k = 5$, $r = 3.7$.
Source: By the author.

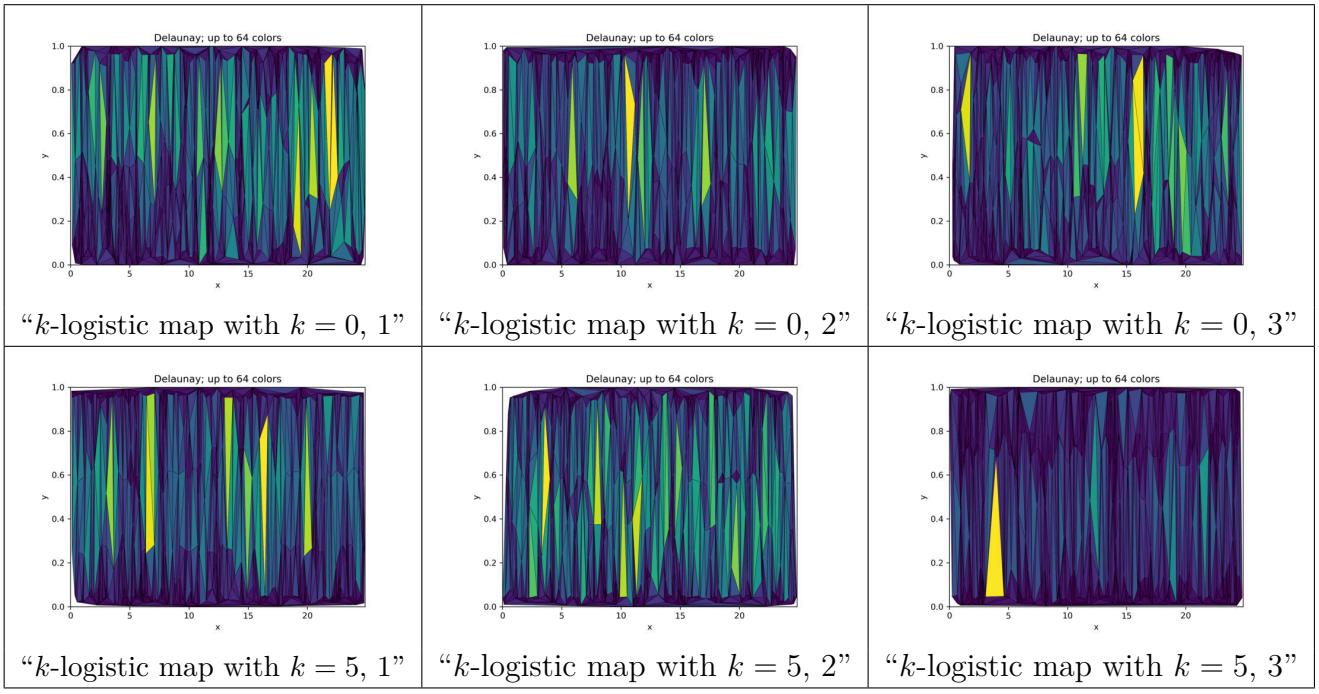

“k-logistic map with $k = 0$, 1” “k-logistic map with $k = 0$, 2” “k-logistic map with $k = 0$, 3”

“k-logistic map with $k = 5$, 1” “k-logistic map with $k = 5$, 2” “k-logistic map with $k = 5$, 3”

Figure 113 – Delaunay triangulations of $> 1\sigma$ complex networks for networks with 5,000 vertices, k-logistic map CNP with $k = 0$ and $k = 5$, $r = 3.99999$.
Source: By the author.

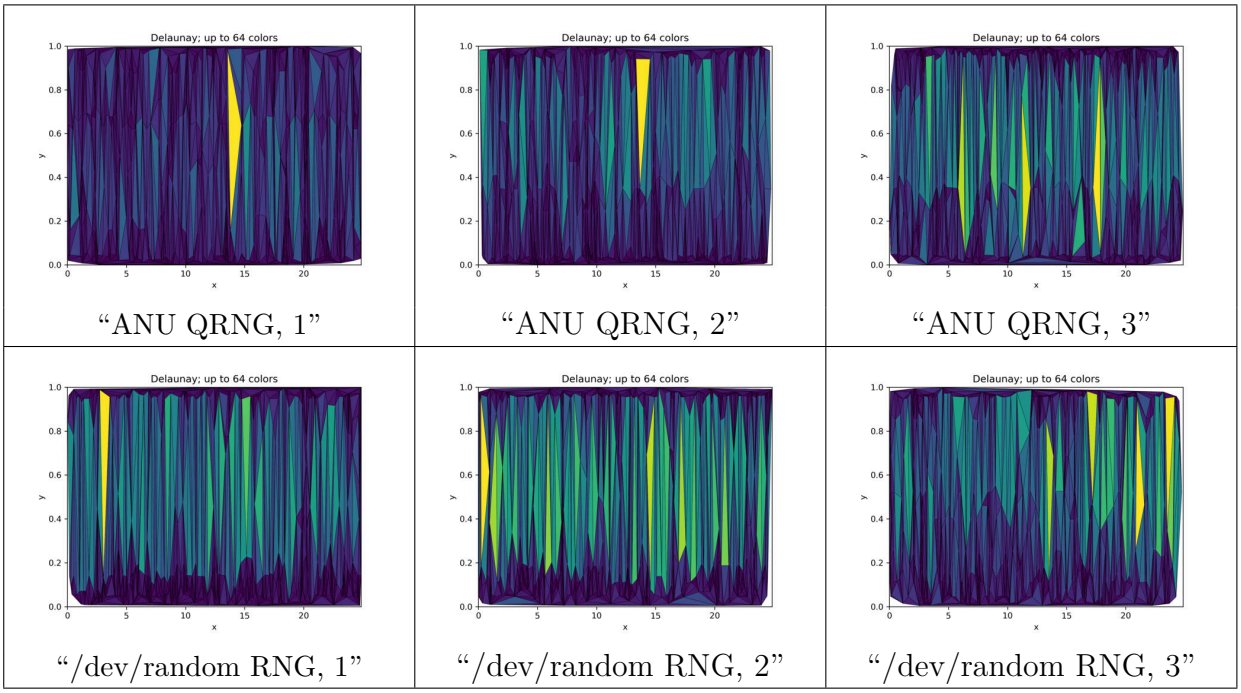

Figure 114 – Delaunay triangulations of $> 1\sigma$ complex networks for networks with 5,000 vertices. ANU Quantum and Linux /dev/random RNGs CNP.
Source: By the author.

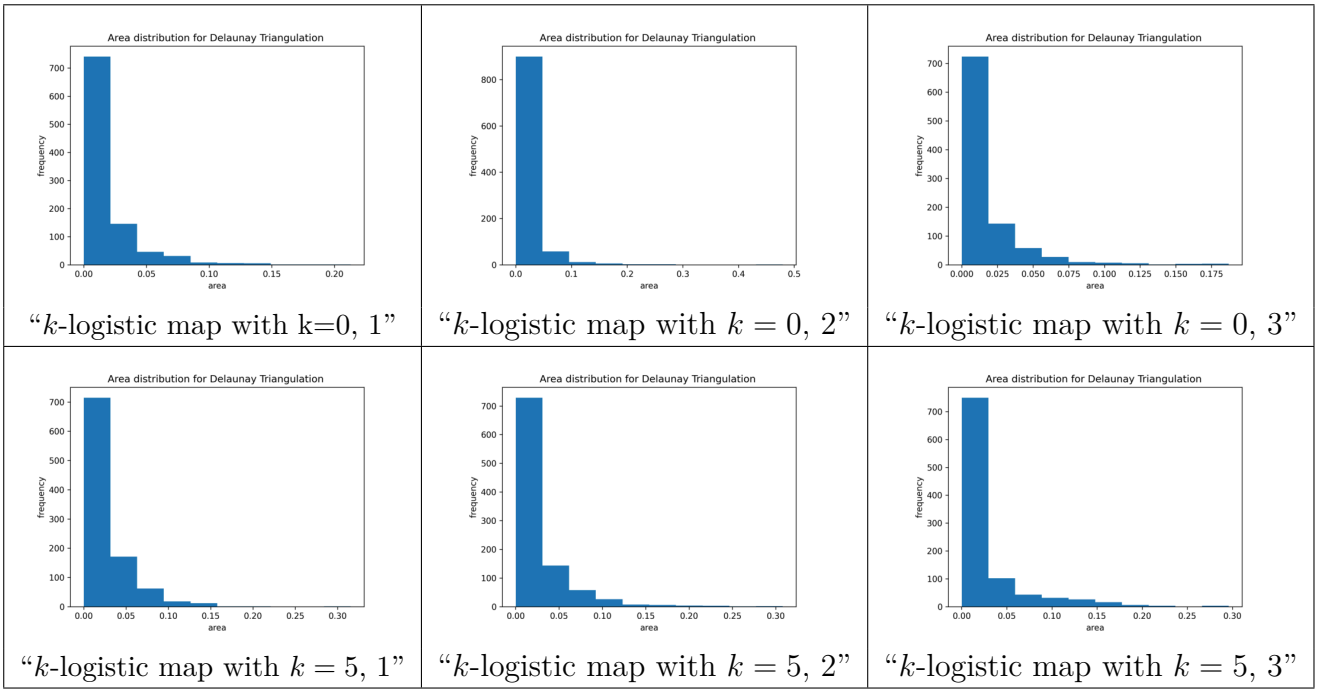

Figure 115 – Histograms for area distribution of Delaunay triangulations of $> 1\sigma$ complex networks for networks with 5,000 vertices, k-logistic map CNP with $k = 0$ and $k = 5$, $r = 3.7$.
Source: By the author.

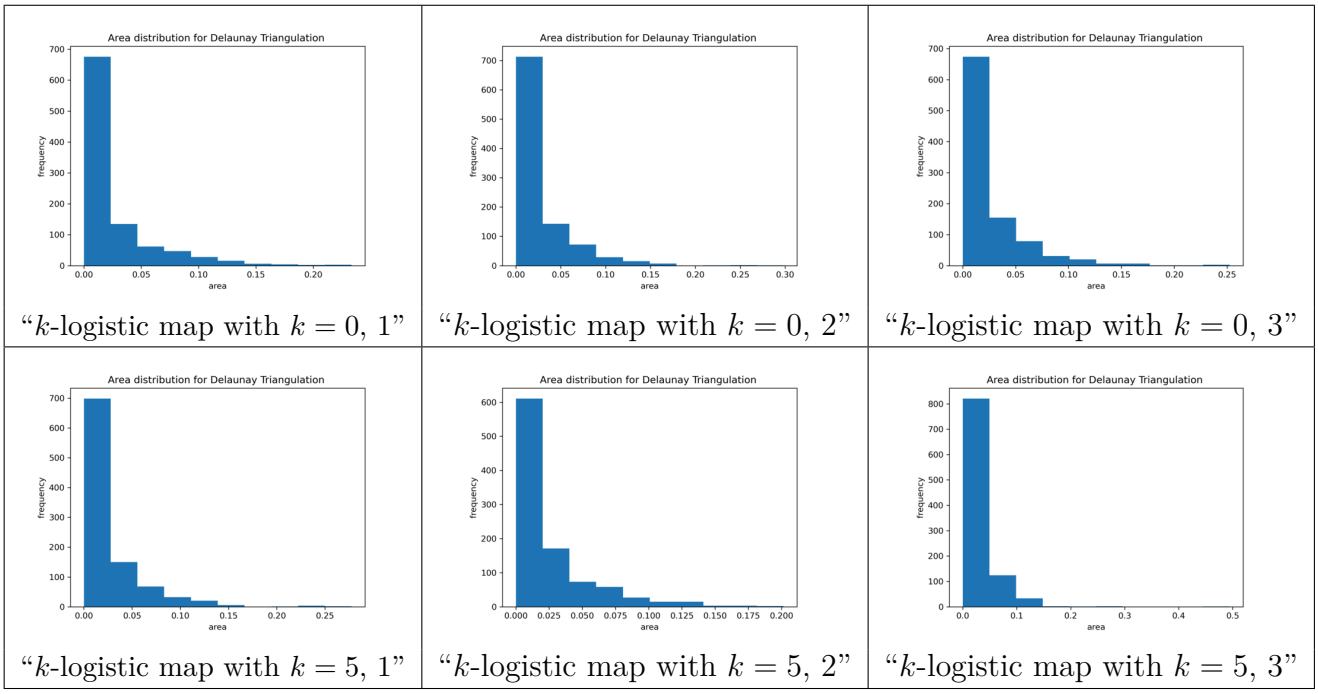

Figure 116 – Histograms for area distribution of Delaunay triangulations of $> 1\sigma$ complex networks for networks with 5,000 vertices, k-logistic map CNP with $k = 0$ and $k = 5$, $r = 3.99999$.
Source: By the author.

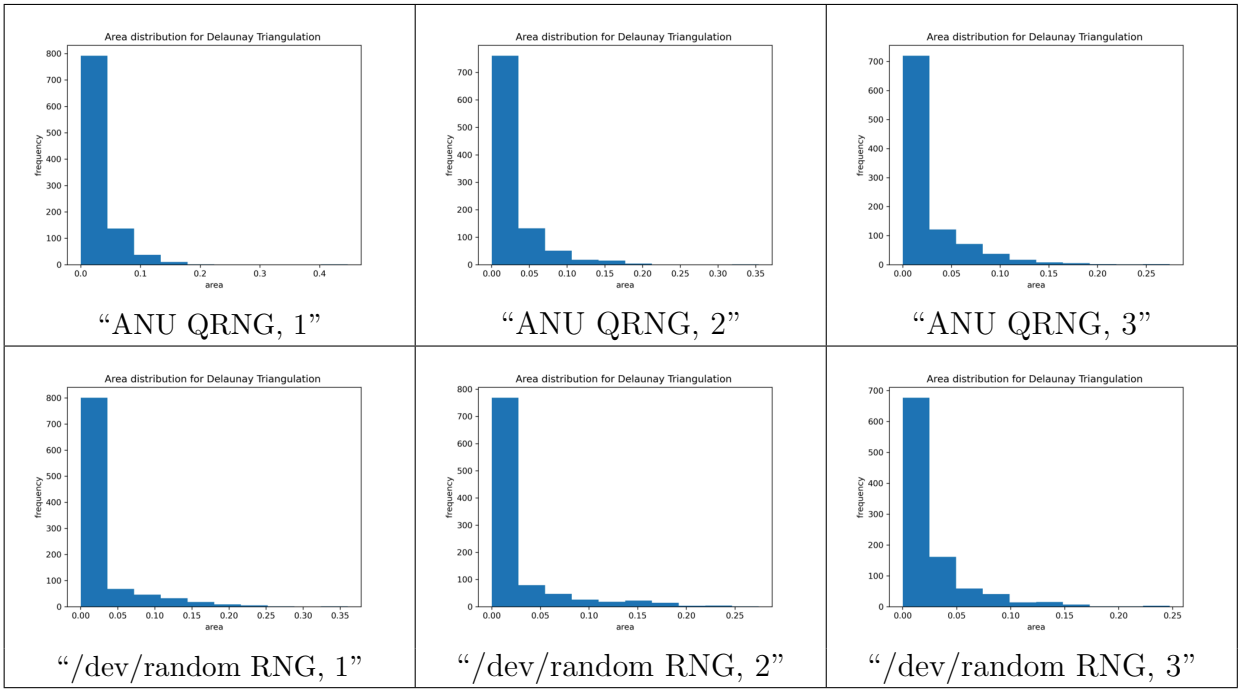

Figure 117 – Histograms for area distribution of Delaunay triangulations of $> 1\sigma$ complex networks for networks with 5,000 vertices. ANU Quantum and Linux /dev/random RNGs CNP.
Source: By the author.

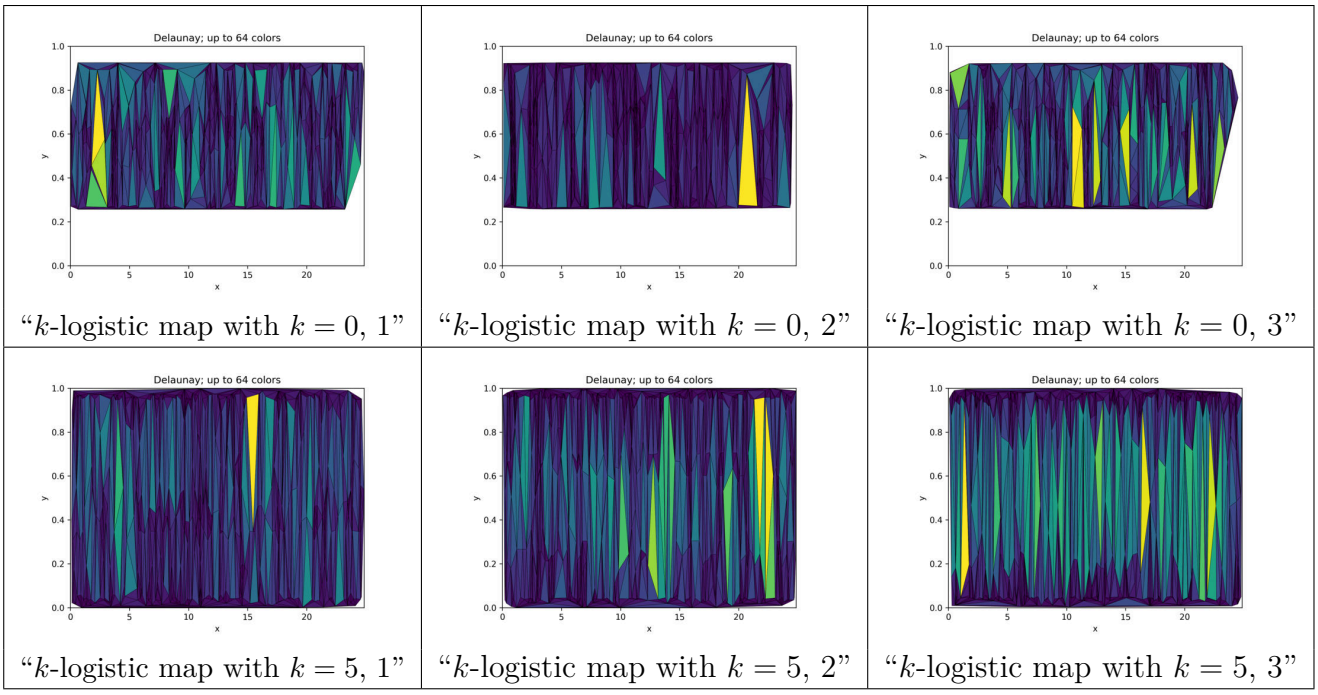

“k-logistic map with $k = 0$, 1” “k-logistic map with $k = 0$, 2” “k-logistic map with $k = 0$, 3”

“k-logistic map with $k = 5$, 1” “k-logistic map with $k = 5$, 2” “k-logistic map with $k = 5$, 3”

Figure 118 – Delaunay triangulations of $> 2\sigma$ complex networks for networks with 5,000 vertices, k-logistic map CNP with $k = 0$ and $k = 5$, $r = 3.7$.
Source: By the author.

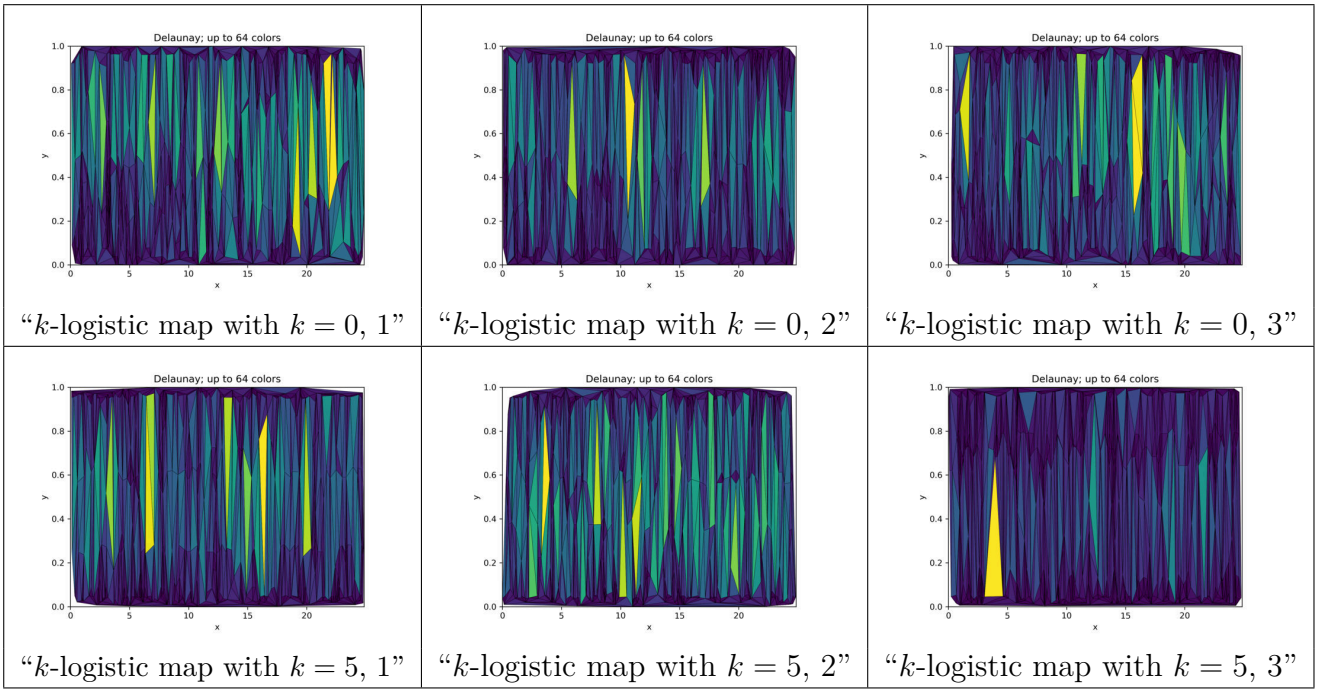

“k-logistic map with $k = 0$, 1” “k-logistic map with $k = 0$, 2” “k-logistic map with $k = 0$, 3”

“k-logistic map with $k = 5$, 1” “k-logistic map with $k = 5$, 2” “k-logistic map with $k = 5$, 3”

Figure 119 – Delaunay triangulations of $> 2\sigma$ complex networks for networks with 5,000 vertices, k-logistic map CNP from $k = 0$ and $k = 5$, $r = 3.99999$.
Source: By the author.

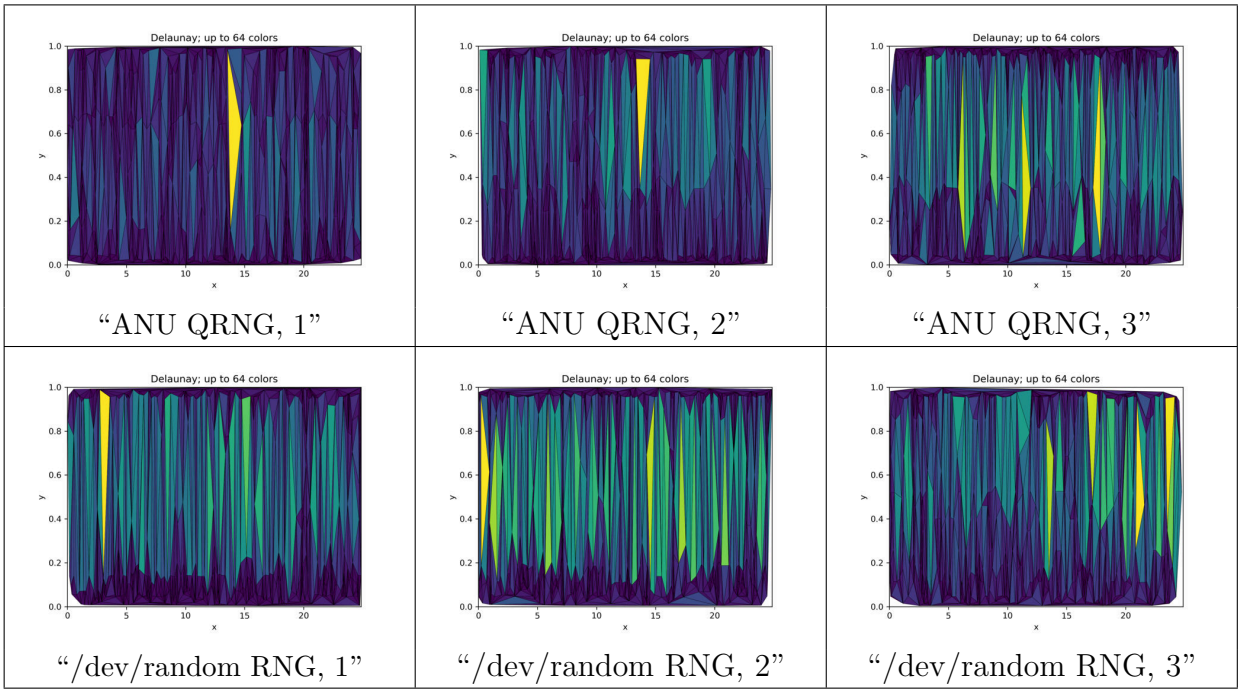

Figure 120 – Delaunay triangulations of $> 2\sigma$ complex networks for networks with 5,000 vertices. ANU Quantum and Linux /dev/random RNGs CNP.
Source: By the author.

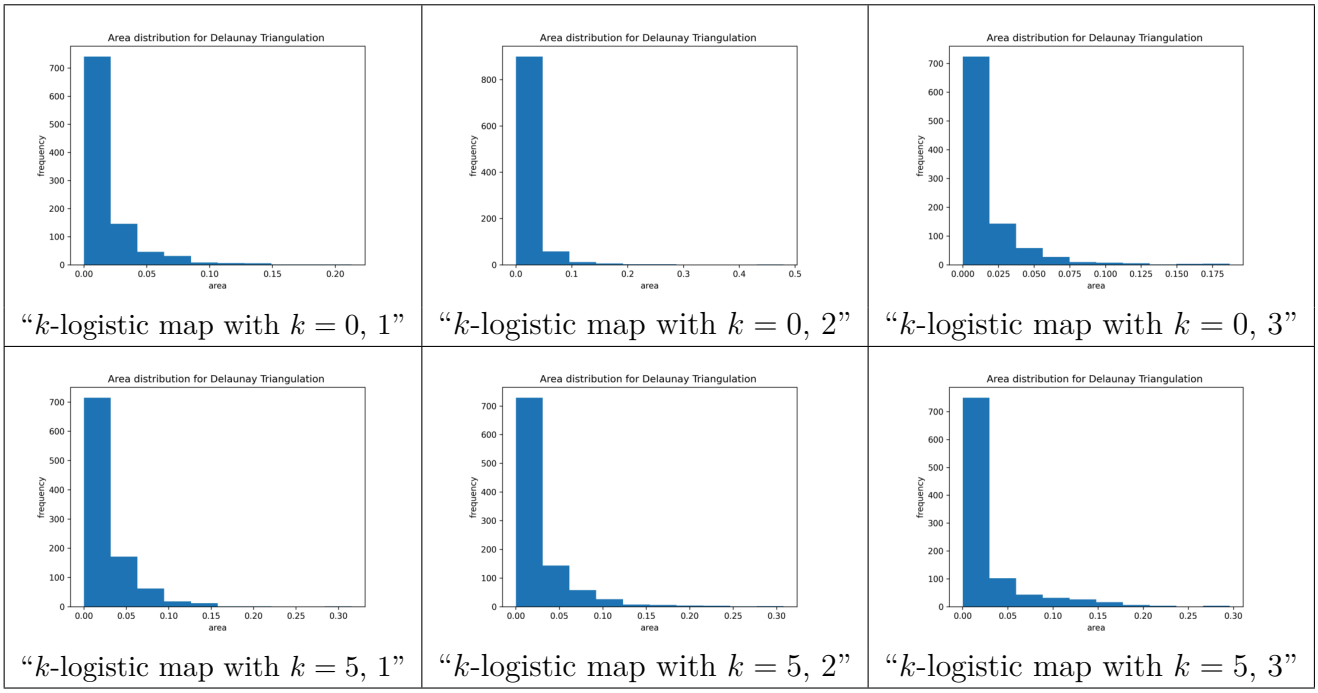

Figure 121 – Histograms for area distribution of Delaunay triangulations of $> 2\sigma$ complex networks for networks with 5,000 vertices, k-logistic map CNP with $k = 0$ and $k = 5$, $r = 3.7$.
Source: By the author.

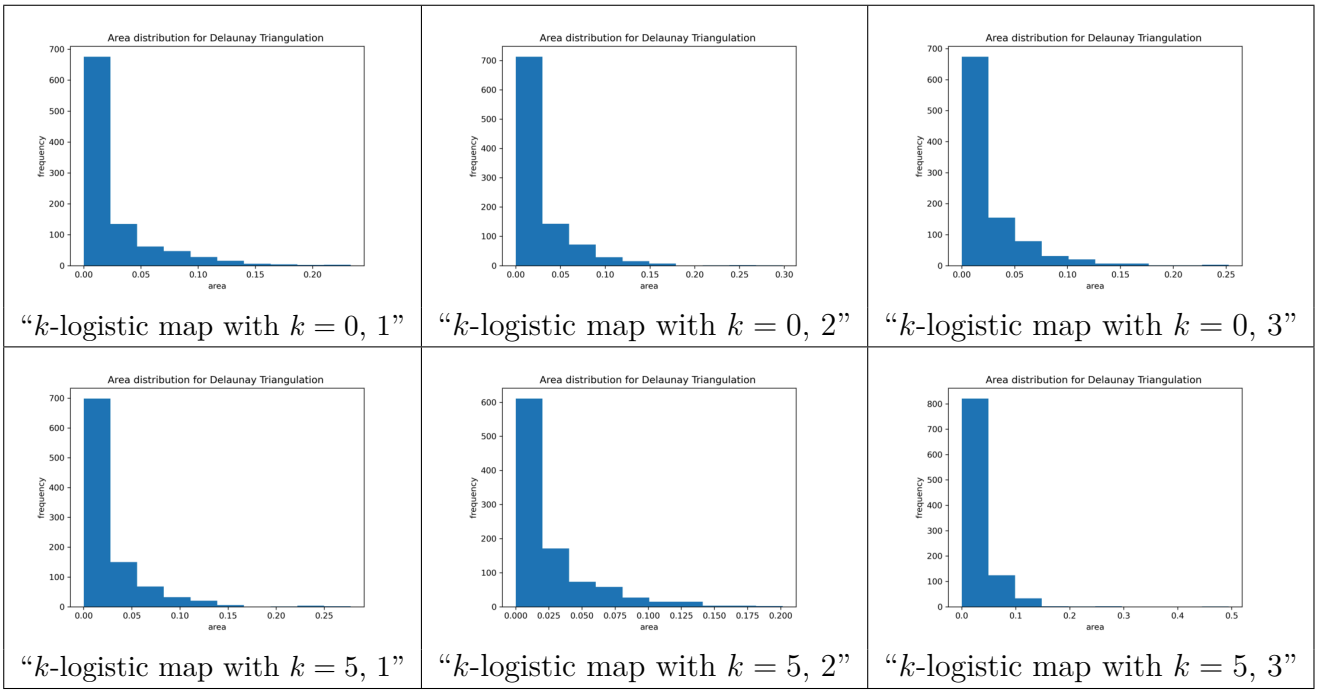

“k-logistic map with $k = 0$, 1” “k-logistic map with $k = 0$, 2” “k-logistic map with $k = 0$, 3”

“k-logistic map with $k = 5$, 1” “k-logistic map with $k = 5$, 2” “k-logistic map with $k = 5$, 3”

Figure 122 – Histograms for area distribution of Delaunay triangulations of $> 2\sigma$ complex networks for networks with 5,000 vertices, k-logistic map CNP with $k = 0$ and $k = 5$, $r = 3.99999$.
Source: By the author.

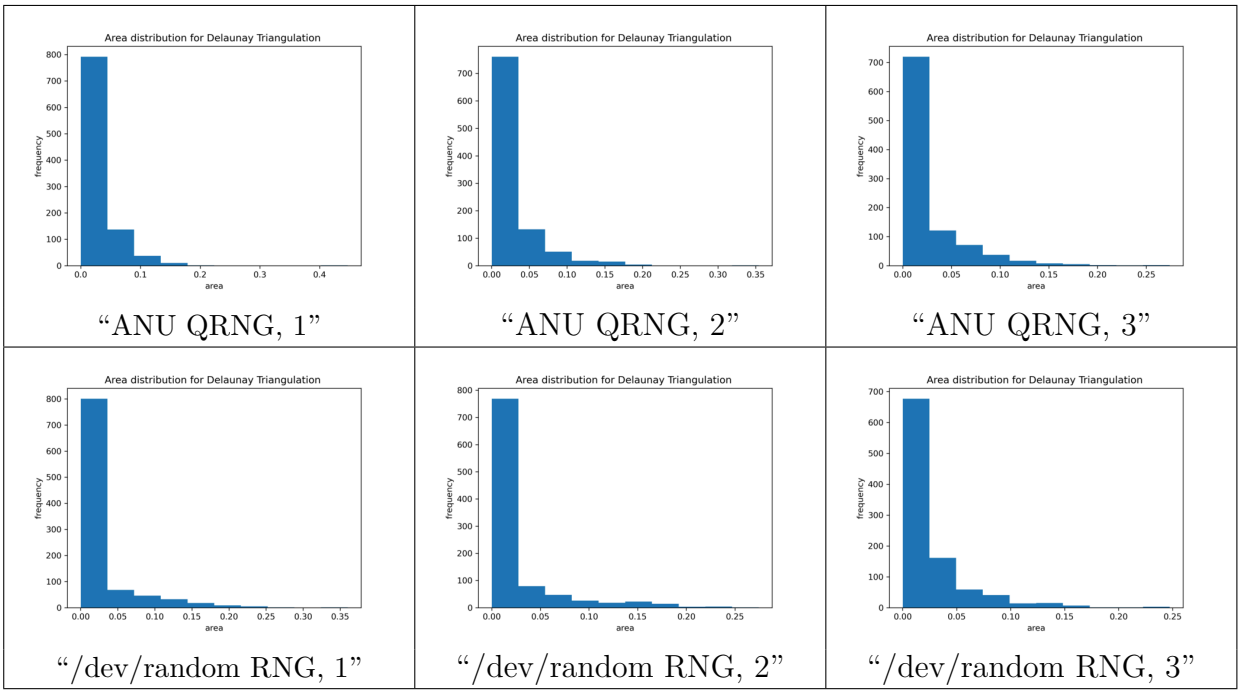

“ANU QRNG, 1” “ANU QRNG, 2” “ANU QRNG, 3”

“/dev/random RNG, 1” “/dev/random RNG, 2” “/dev/random RNG, 3”

Figure 123 – Histograms for area distribution of Delaunay triangulations of $> 2\sigma$ complex networks for networks with 5,000 vertices. ANU Quantum and Linux /dev/random RNGs CNP.
Source: By the author.

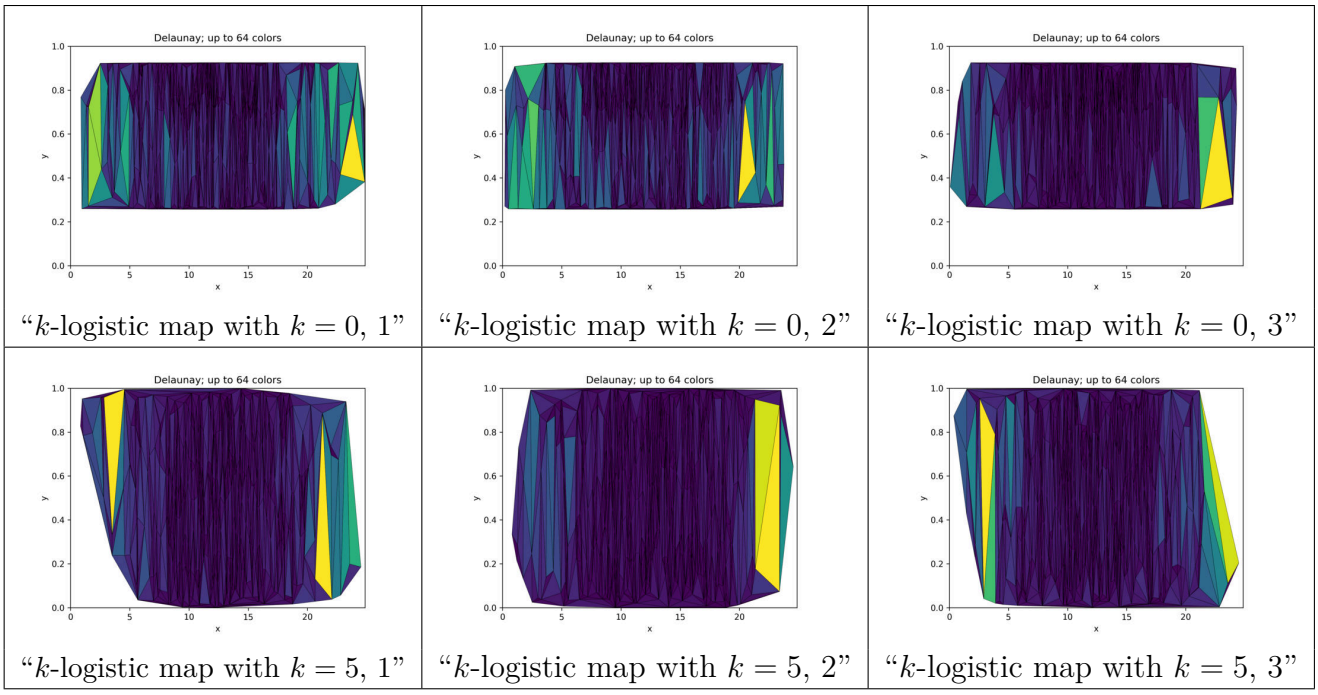

Figure 124 – Delaunay triangulations of $< -1\sigma$ complex networks for networks with 5,000 vertices, k-logistic map CNP with $k = 0$ and $k = 5$, $r = 3.7$.
Source: By the author.

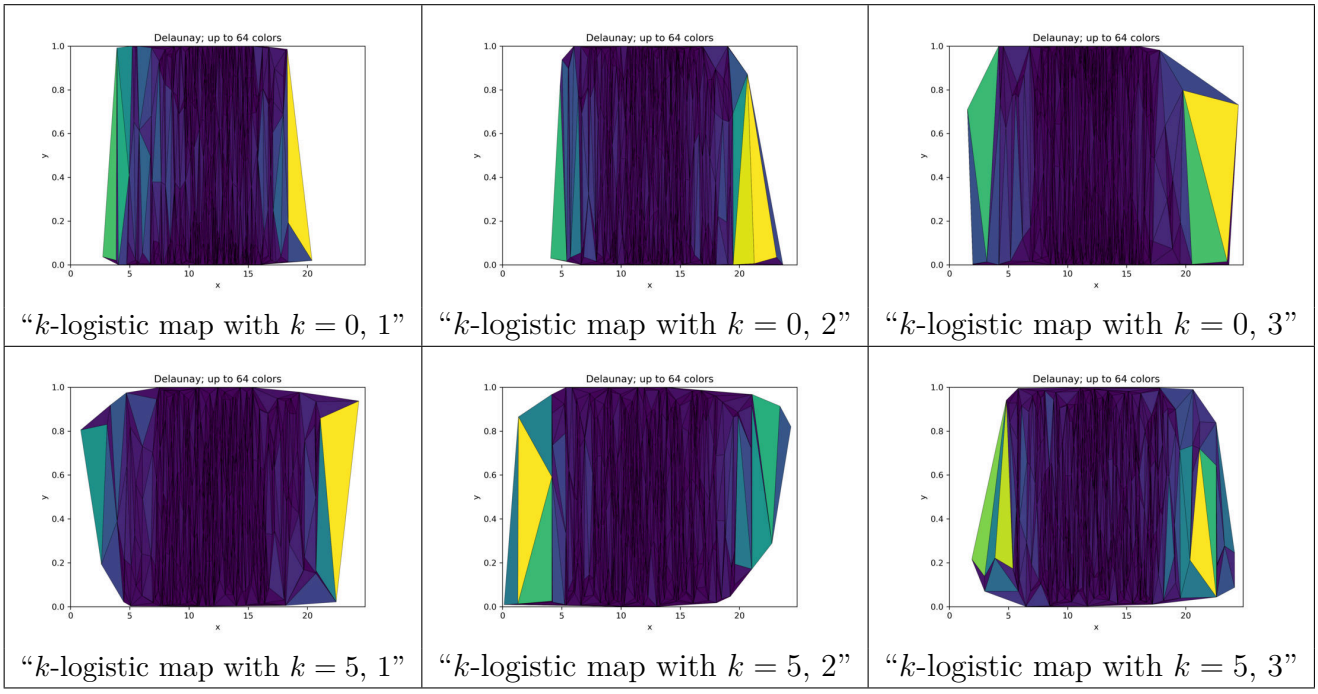

Figure 125 – Delaunay triangulations of $< -1\sigma$ complex networks for networks with 5,000 vertices, k-logistic map CNP with $k = 0$ and $k = 5$, $r = 3.99999$.
Source: By the author.

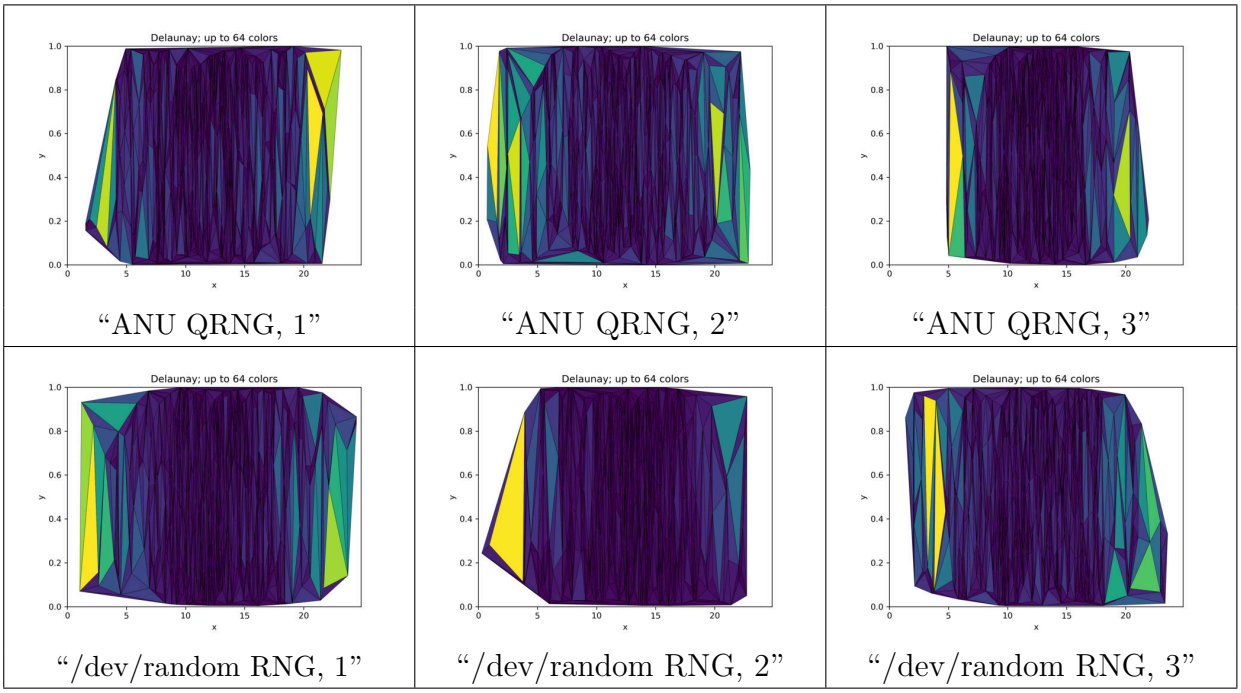

Figure 126 – Delaunay triangulations of $< -1\sigma$ complex networks for networks with 5,000 vertices. ANU Quantum and Linux /dev/random RNGs CNP.
Source: By the author.

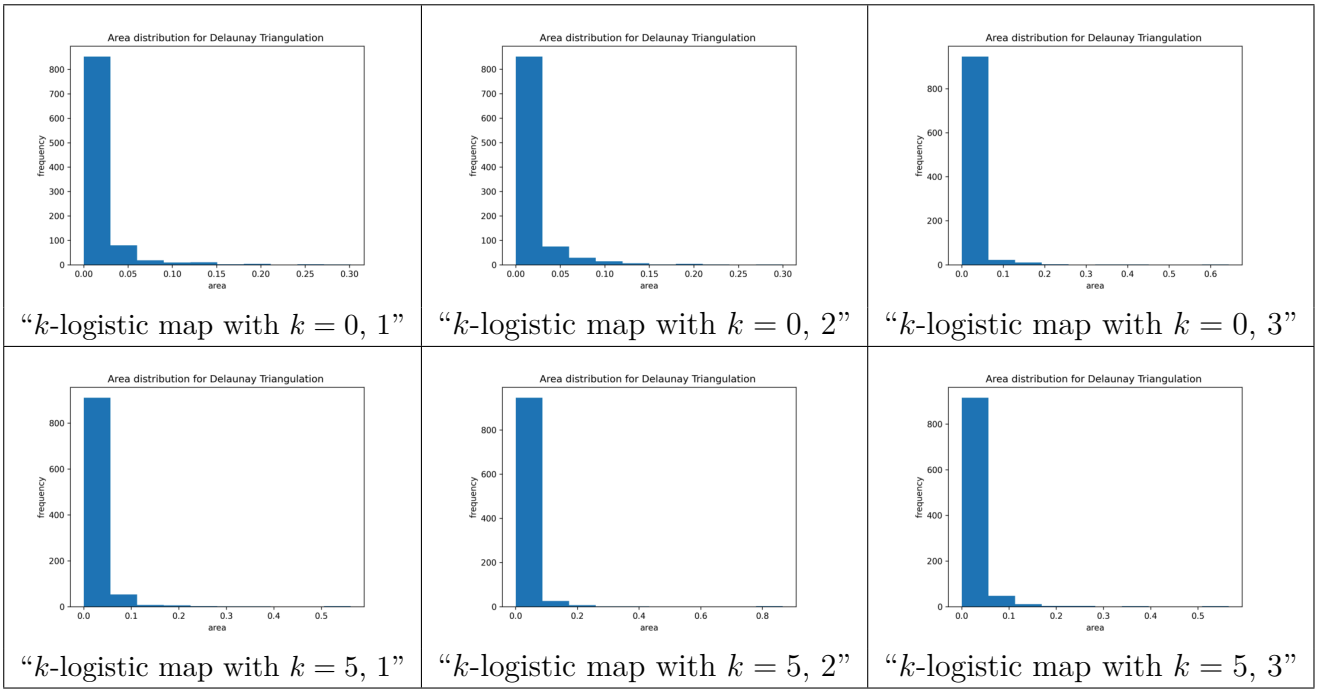

Figure 127 – Histograms for area distribution of Delaunay triangulations of $< -1\sigma$ complex networks for networks with 5,000 vertices, k-logistic map CNP with $k = 0$ and $k = 5$, $r = 3.7$.
Source: By the author.

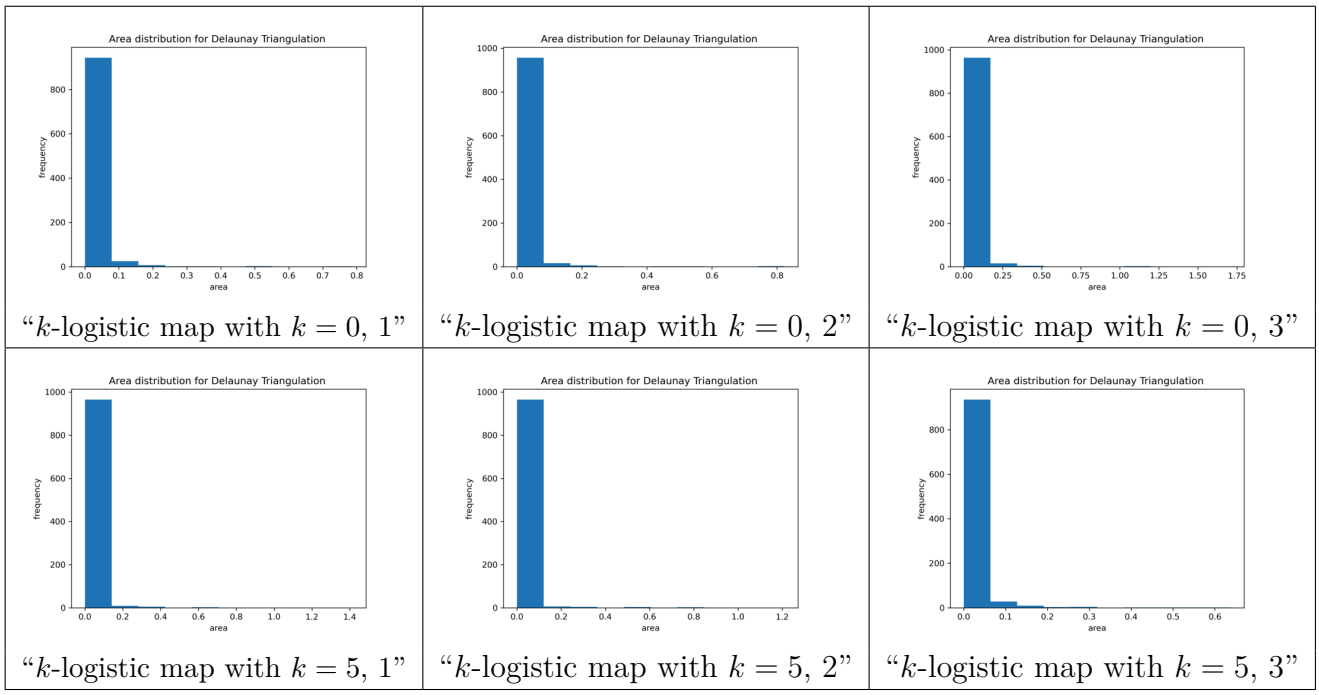

Figure 128 – Histograms for area distribution of Delaunay triangulations of $< -1\sigma$ complex networks for networks with 5,000 vertices, k-logistic map CNP with $k = 0$ and $k = 5$, $r = 3.99999$.
Source: By the author.

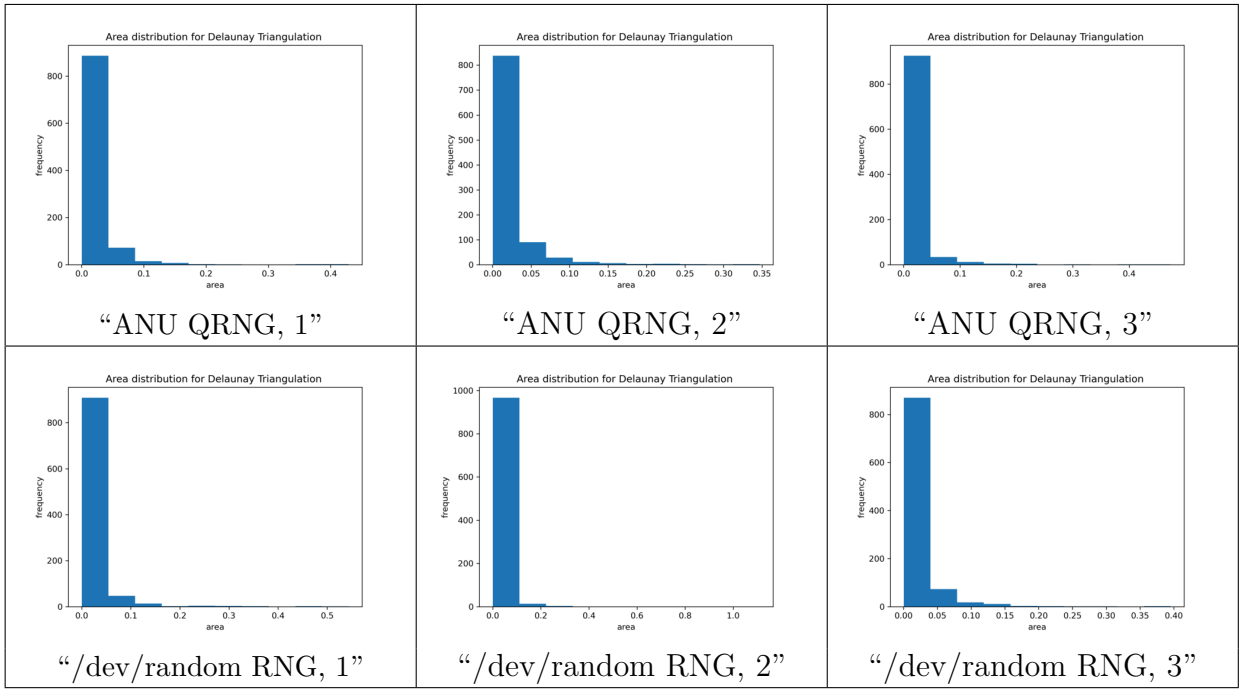

Figure 129 – Histograms for area distribution of Delaunay triangulations of $< -1\sigma$ complex networks for networks with 5,000 vertices. ANU Quantum and Linux /dev/random RNGs CNP.
Source: By the author.

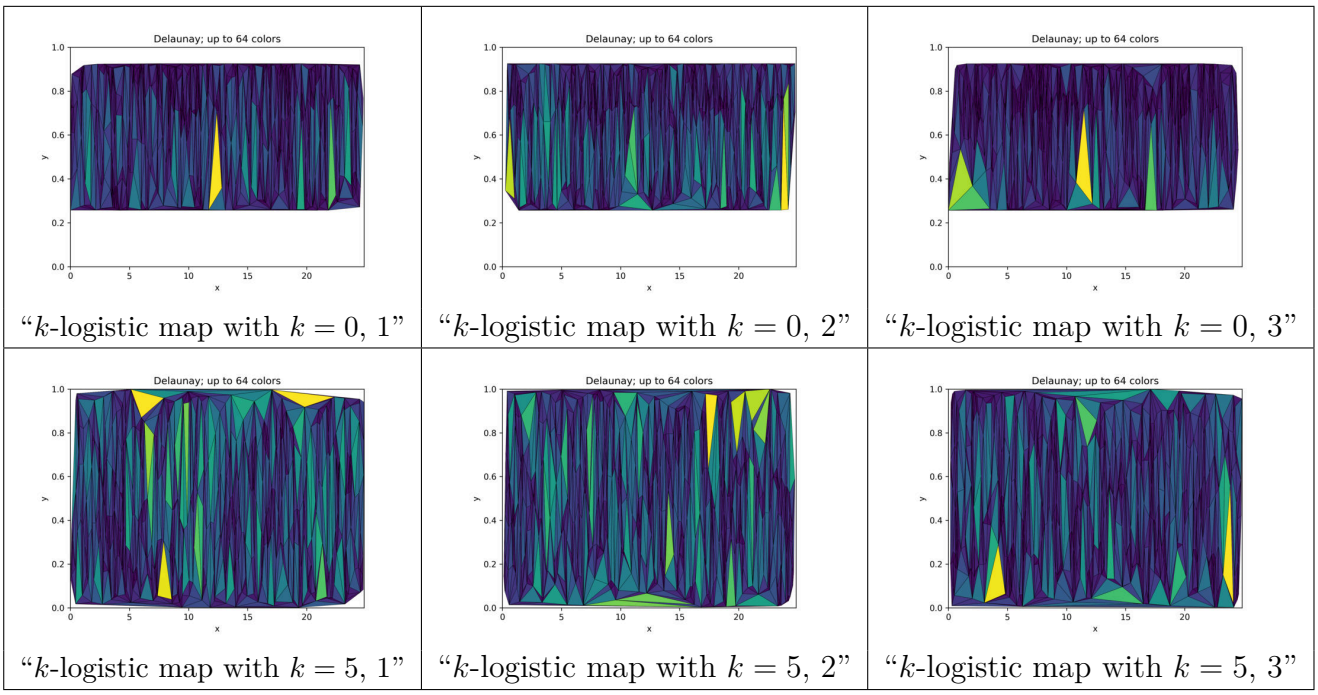

Figure 130 – Delaunay triangulations of $< -2\sigma$ complex networks for networks with 5,000 vertices, k-logistic map CNP with $k = 0$ and $k = 5$, $r = 3.7$.
Source: By the author.

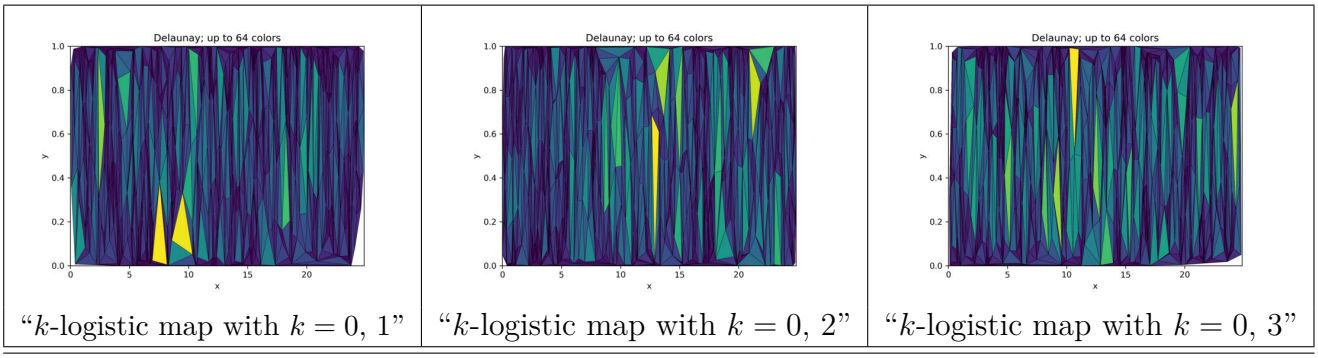

Figure 131 – Delaunay triangulations of $< -2\sigma$ complex networks for networks with 5,000 vertices, k-logistic map CNP with $k = 0$ and $k = 5$, $r = 3.99999$.
Source: By the author.

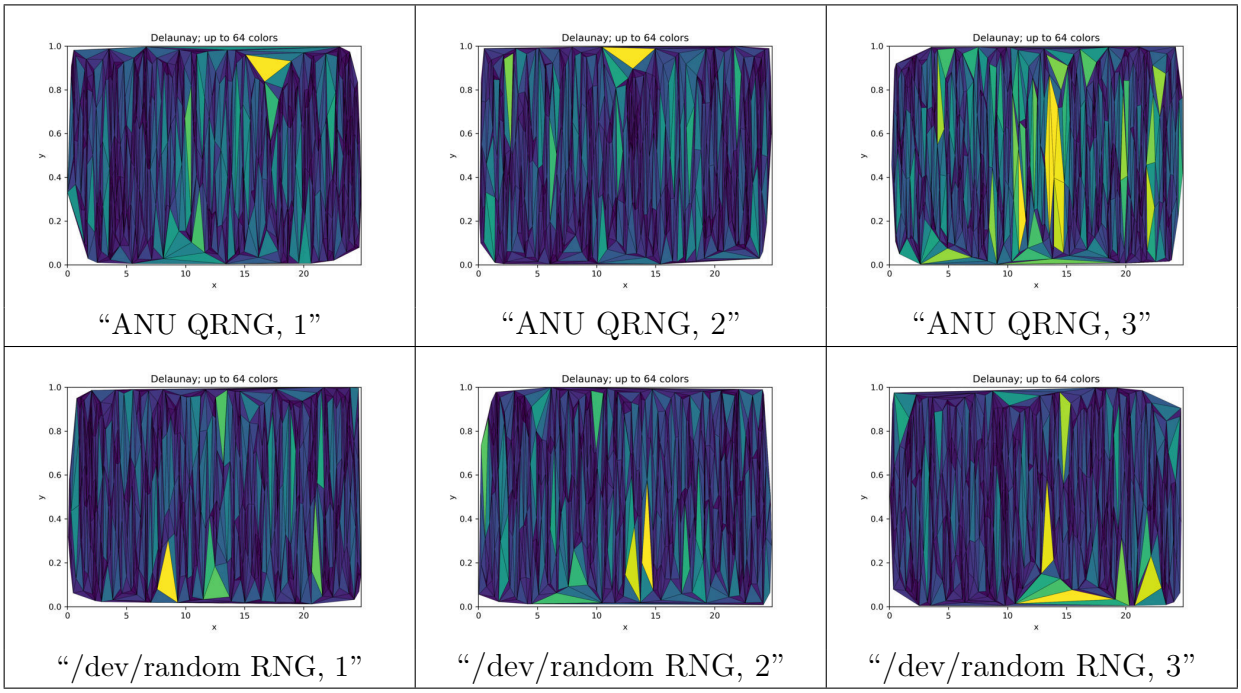

Figure 132 – Delaunay triangulations of $< -2\sigma$ complex networks for networks with 5,000 vertices. ANU Quantum and Linux /dev/random RNGs CNP.
Source: By the author.

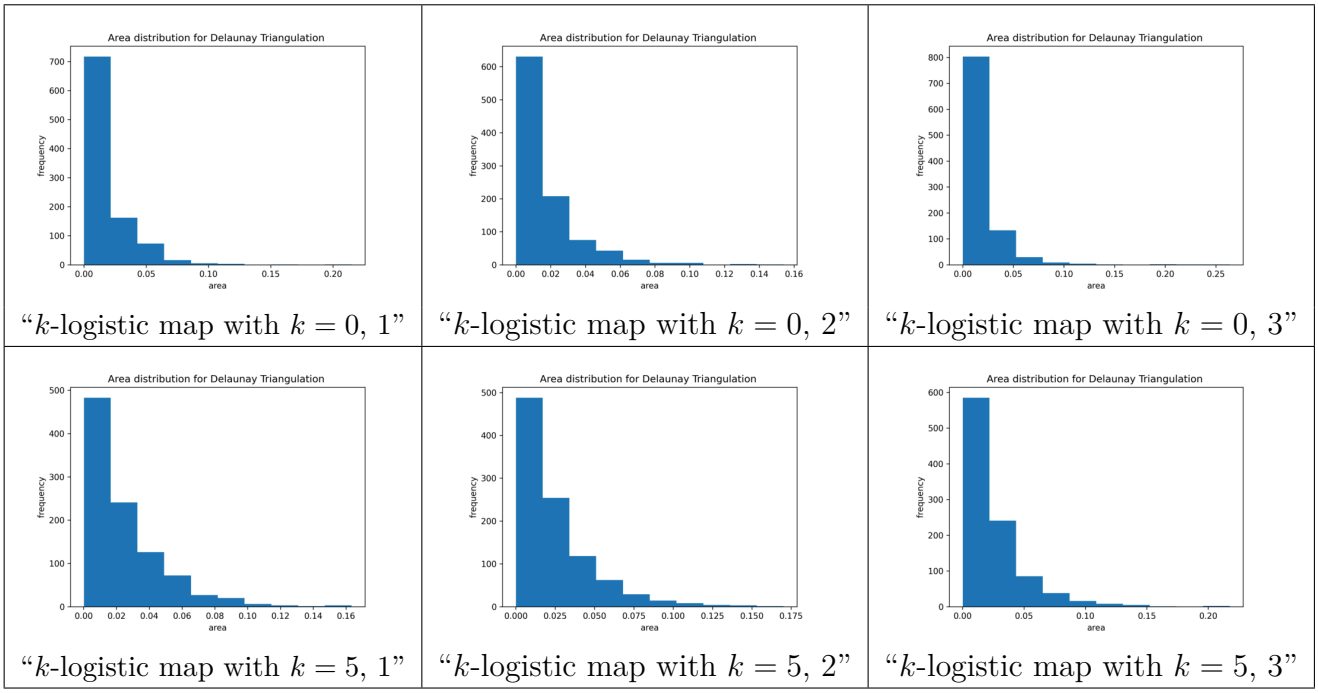

Figure 133 – Histograms for area distribution of Delaunay triangulations of $< -2\sigma$ complex networks for networks with 5,000 vertices, k-logistic map CNP with $k = 0$ and $k = 4$, $r = 3.7$.
Source: By the author.

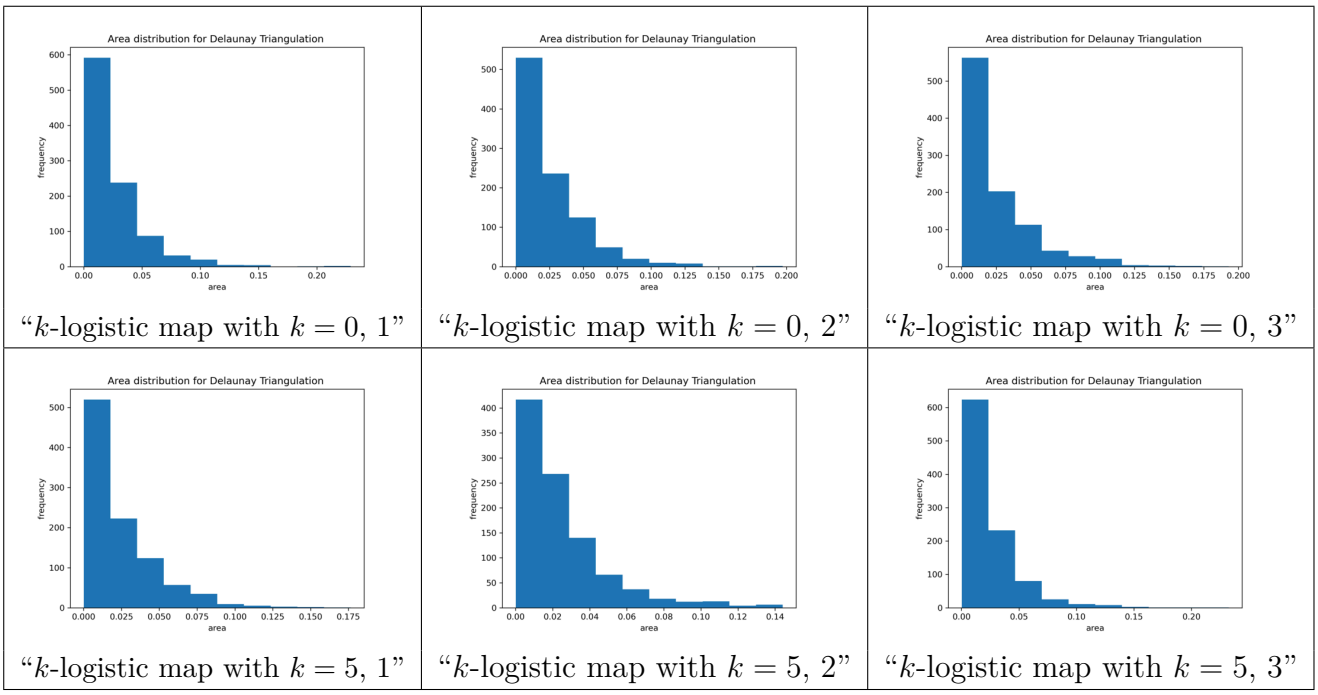

Figure 134 – Histograms for area distribution of Delaunay triangulations of $< -2\sigma$ complex networks for networks with 5,000 vertices, k-logistic map CNP with $k = 0$ and $k = 5$, $r = 3.99999$.
Source: By the author.

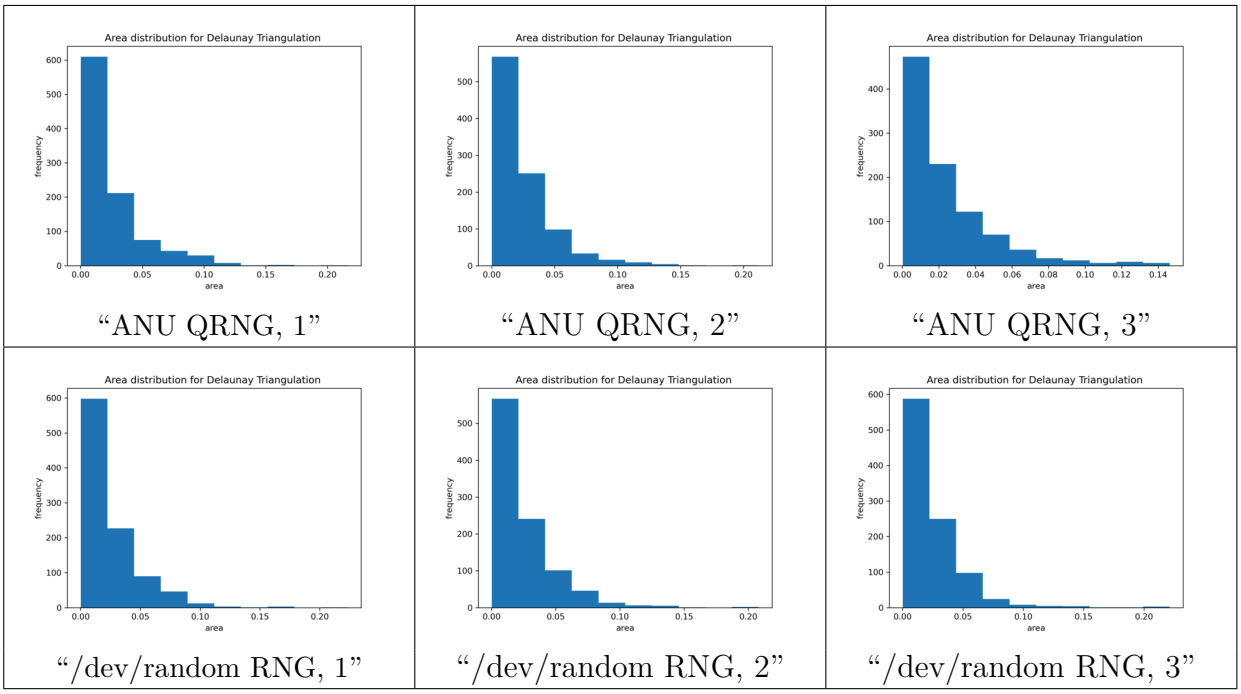

Figure 135 – Histograms for area distribution of Delaunay triangulations of $< -2\sigma$ complex networks for networks with 5,000 vertices. ANU Quantum and Linux /dev/random RNGs CNP.
Source: By the author.

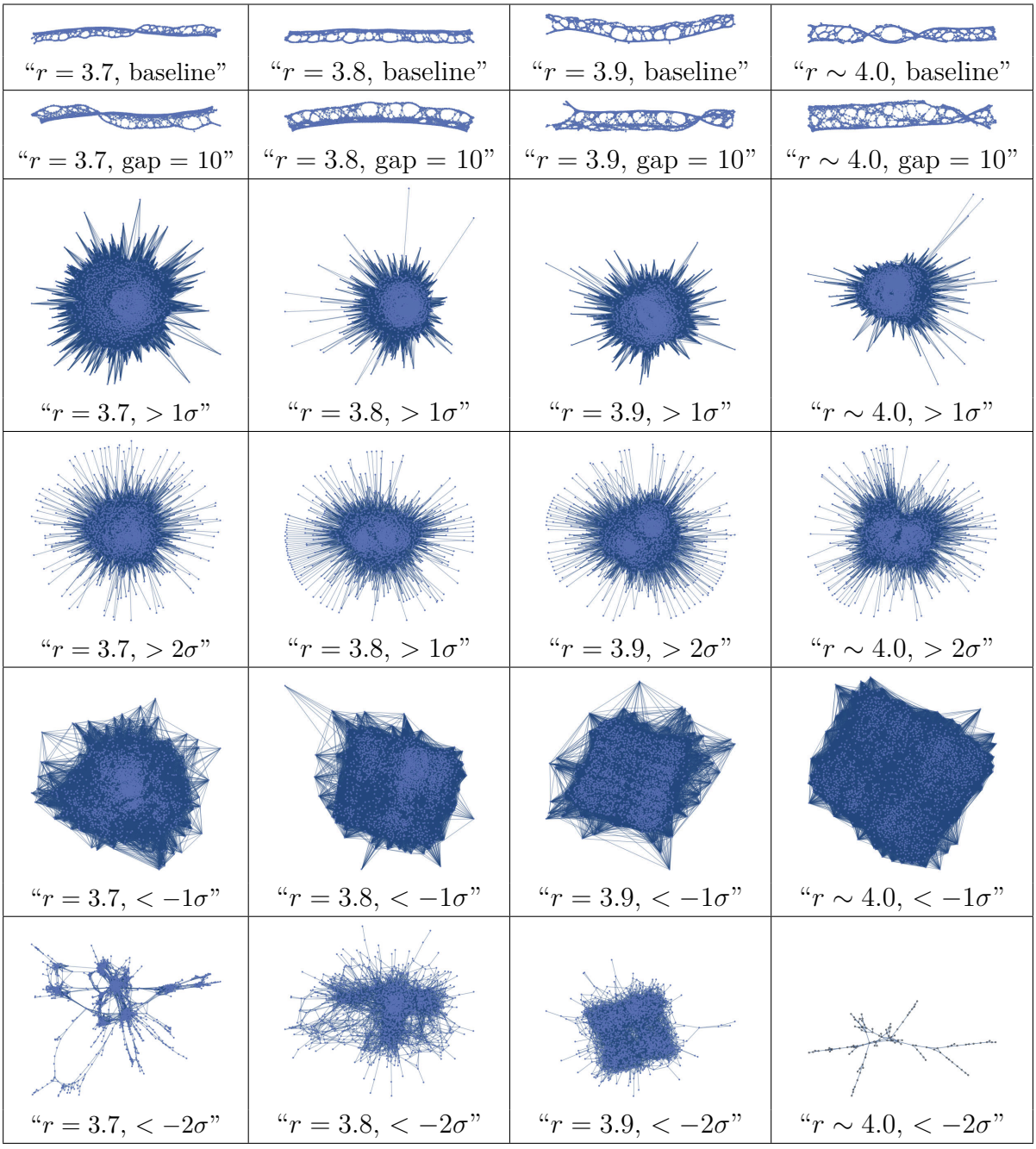

Figure 136 – Network structure for the k-logistic map CNP with $k = 0$.
Source: By the author.

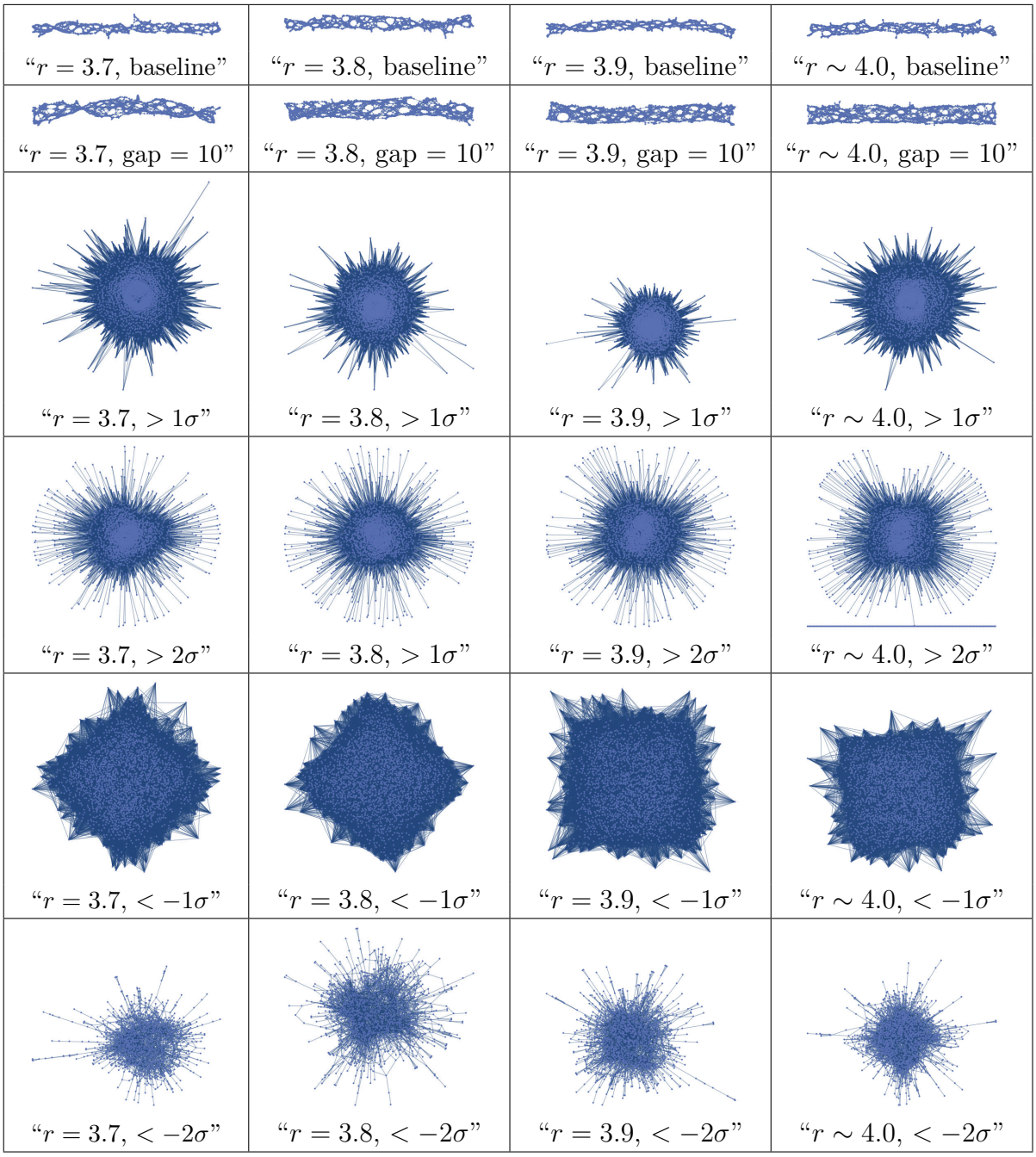

Figure 137 – Network structure for the k-logistic map CNP with $k = 5$.
Source: By the author.

4 DISCUSSION

Judging from the results shown on Tables 3 to 3, the LFSR, despite its celebrated properties, does in fact show subpar entropy when compared to the k-logistic map. Even the vanilla logistic map – k-logistic map with k set to zero – presents comparable results under the test suite of our choice. On the other side, the composition of the k-logistic map and the LFSR or of a non-linear funcion and a linear function harnessed the strengths of both. From $k = 0$ to $k = 30$ (base 2), the entropy property and randomness are enhanced as the value of k increases, and the combination of LFSR's scrambling and nonlinearity enhances it further. The minimum entropy and randomness tests assessed that the gains from those modifications were consistent, just as the PractRand and SmallCrush tests. Using multi source k-logistic maps increased entropy less markedly than the composition of the k-logistic map and the LFSR. Both the ANU and /dev/random generators – not shown – passed all tests with flying colors.

In the results shown on Figure 51, the human eye easily recognizes the newfound motifs via the MP algorithm. For the results in Figures 54 to 55, under the value of $r = 3.97$ – that is not far off from $r = 4!$ – the k-logistic map with $k = 0$ shows intriguing distinct behavior compared to the other parametrizations. Figure 56 pinpoints the variations in network measures according to the parametrization used.

Seen on Figures 57 to 70, the kind of correlation between the two largest-variance PCA components changes dramatically according to the projection technique for generating networks, varying from the apparently uncorrelated to interesting spatial symmetries. Boxplots on Figures 71 to 84 also show substantial variations between the networks. Figures 99 and 100 on degree distributions show striking difference between the baseline network and the $< -2\sigma$ network, pointing to power law or exponential distributions for the CNP and normal-like distributions for the baseline networks. The degree distributions of $< -2\sigma$ CNP show that these networks possess also the scale-free property, beyond the small-world property of complex networks. The violin plots on Figures 101 to 104 also show substantial degree distribution differences.

On the results of representation networks for the k-logistic map in Tables 3 to 3, the $< -2\sigma$ CNP surpassed the baseline transformation of the k-logistic map into complex networks, and accuracy is especially noteworthy when the CNP and LLNA are employed together, when the classes $k \in \{0, 1, 2, 3, 4\}$. We stress that CNP has been designed to privilege long-range correlations – which truly are signs of chaotic behavior of a system – in detriment of the relatively uninformative short-range correlations. The best result for the classification task with baseline networks occurs when $r = 3.7$ and from there on their returns are diminished as $r \sim 4$. We know from bifurcation theory that, as $r \sim 4$,

the system becomes more and more chaotic. We interpret from this result that when short-range correlations in the object are privileged in the representation, it does have the side effect of masking the long-range correlations associated with chaos. With the classes $k \in \{5, 6, 7, 8, 9\}$, which are much closer to pure noise, the classifier meets a much harder work and thus this specific set of results is a mixed bag.

On Figure 105 we witness the convergence of the distribution of the DTW distances $d > 0$ to the Tracy-Widom distribution. Remind that when building the CNP we peek data at one tail of the distribution, and as the Tracy-Widom distribution is assymmetric, we end up with two distinct complex network structures. Data at the tails of the distribution are associated with phase transition phenomena in the literature (157). We did not perform further numerical experiments to check if the CNP indeed follows the Tracy-Widom distribution at is tails or deviate from it, which might reveal more interesting details on the k-logistic map dynamics.

5 CONCLUSION

This work was crafted with the vision of improving the current state-of-the-art and, to an extent, to also present new directions for investigations in the field of cryptanalysis and academic research in dynamical systems. We have verified that the projection or transformation of a chaotic orbit harnessing its topological aspects, and then to apply trivial statistical tests, can give satisfactory results. We have also verified that principles of thermodynamics formalism and random matrix theory both form a sound base that, when combined with proven approaches in the field of computer science, algorithms and data mining, provide a a refreshing and compelling view of the k-logistic map and also of a handful of RNGs. The simple heat diffusion allows for previously inaccessible time series concepts and methods. From those time series concepts and methods we then develop our next solution that exploits in a new way the inherent characteristics of random variables. With the purpose of maximizing success in extracting meaning from chaotic orbits, we propose a combination of heuristics, techniques and projections, combining thus the strengths and expertise developed over the timespan of years of research on several fields of knowledge.

A natural step is the concentration of efforts on experiments upon other dynamical systems and competitor PRNGs, for the purpose of depthening our study of patterns and our tests for numerical sequences with applications in cryptography. A desirable improvement is to achieve hefty reductions in computation time, which would allow the proposed CNP to extract even more information off the chaotic orbits. The topological matrix is fruit of an algorithm and implementation that is able to deal with dense matrices of over $10^5 \times 10^5$ elements and it is a doable alternative in situations and under constraints where the CNP cannot be applied at all. An obvious and very desirable improvement for the usage of the CNP is to harness finer-grained deltas for the values of the σ (standard deviation) and to have a peek at subtler details of the generated networks as the configuration parameters are changed. The degree distributions for the CNP also deserve to be more closely studied. The PCA for the feature vectors of networks manifest intriguing categories of correlations between the major principal components that deserve to be studied in-depth.

REFERENCES

1 HöRNFELDT, B. Longterm decline in numbers of cyclic voles in boreal sweden: analysis and presentation of hypotheses. **Oikos**, v. 107, n. 2, p. 376–392, 2004.

2 FRANK, K. T. *et al.* Transient dynamics of an altered large marine ecosystem. **Nature**, v. 477, n. 7362, p. 86–89, 2011.

3 LUDWIG, D.; JONES, D. D.; HOLLING, C. S. Qualitative analysis of insect outbreak systems: the spruce budworm and forest. **The Journal of animal ecology**, v. 47, n. 1, p. 315–332, 1978.

4 MOROZOV, A. Y.; BANERJEE, M.; PETROVSKII, S. V. Long-term transients and complex dynamics of a stage-structured population with time delay and the allee effect. **Journal of Theoretical Biology**, v. 396, p. 116–124, 2016.

5 HASTINGS, A. *et al.* Transient phenomena in ecology. **Science**, v. 361, n. 6406, 2018.

6 WOLF, A. *et al.* Determining lyapunov exponents from a time series. **Physica D: nonlinear phenomena**, v. 16, n. 3, p. 285–317, 1985.

7 FARMER, J. D.; SIDOROWICH, J. J. Optimal shadowing and noise reduction. **Physica D: nonlinear phenomena**, v. 47, n. 3, p. 373–392, 1991. ISSN 01672789.

8 MACHICAO, J.; BRUNO, O. M. Improving the pseudo-randomness properties of chaotic maps using deep-zoom. **Chaos**, v. 27, n. 5, p. 053116, 2017.

9 SPROTT, J. C. **Chaos Data Analyzer**. Accessible at: 22 Mar. 2024. Available at: https://sprott.physics.wisc.edu/CDA.HTM.

10 MILGRAM, S. The small world problem. **Psychology Today**, n. 2, p. 60–67, 1967.

11 WOLFRAM MATHWORLD. Elementary Cellular Automaton. Accessible at: 22 Mar. 2024. Available at: https://mathworld.wolfram.com/ElementaryCellularAutomaton.html.

12 ALVES, M. L. **Classification of pseudo-random number generators by complex networks and computational geometry**. 2019. Dissertation (Master of Science) – Instituto de Ciências Matemáticas e de Computação, Universidade de São Paulo, São Carlos, 2019., 2019.

13 OESTREICHER, C. A history of chaos theory. **Dialogues in Clinical Neuroscience**, v. 9, n. 3, p. 279–289, 2007.

14 PALIS, J.; MELO, W. **Geometric theory of dynamical systems: an introduction**. New York: Springer, 1982. ISBN 978-1-4612-5703-5.

15 MELO, W.; STRIEN, S. **One-Dimensional Dynamics**. Berlin, Heidelberg: Springer, 1993. ISBN 978-3-642-78043-1.

16 PATHAK, J. *et al.* Using machine learning to replicate chaotic attractors and calculate lyapunov exponents from data. **Chaos**, v. 27, n. 12, p. 121102, 2017.

17 PATHAK, J. *et al.* Model-free prediction of large spatiotemporally chaotic systems from data: A reservoir computing approach. **Physical Review Letters**, v. 120, n. 2, p. 024102, 2018.

18 RAJAGOPALAN, V. *et al.* Pattern identification in dynamical systems via symbolic time series analysis. **Pattern Recognition**, v. 40, n. 11, p. 2897–2907, 2007. ISSN 00313203.

19 ROGERS, T. L.; JOHNSON, B. J.; MUNCH, S. B. Chaos is not rare in natural ecosystems. **Nature Ecology & Evolution**, v. 6, n. 8, p. 1105–1111, 2022. ISSN 2397-334X.

20 DENNIS, E. B. *et al.* Integrated modelling of insect population dynamics at two temporal scales. **Ecological Modelling**, v. 441, p. 109408, 2021. ISSN 03043800.

21 GARCIA, A. G. *et al.* Ecological modelling of insect movement in cropping systems. **Neotropical Entomology**, v. 50, n. 3, p. 321–334, 2021.

22 ASHWIN, P.; CAMP, C. D.; HEYDT, A. S. von der. Chaotic and non-chaotic response to quasiperiodic forcing: limits to predictability of ice ages paced by milankovitch forcing. **Dynamics and Statistics of the Climate System**, v. 3, n. 1, 2018. ISSN 2059-6987.

23 WOLFRAM, S. Statistical mechanics of cellular automata. *In*: WOLFRAM, S. (ed.). **Cellular automata and complexity**. Boca Raton: CRC Press, 2018. p. 3–69. ISBN 9780429494093.

24 TANTARDINI, M. *et al.* Comparing methods for comparing networks. **Scientific Reports**, v. 9, n. 1, p. 17557, 2019.

25 PETROVSKII, S. V.; LI, B.-L. **Exactly solvable models of biological invasion**. Boca Raton: Chapman and Hall/CRC, 2005. ISBN 9780429141430.

26 RUELLE, D.; TAKENS, F. On the nature of turbulence. **Communications in Mathematical Physics**, v. 20, n. 3, p. 167–192, 1971. ISSN 0010-3616.

27 VOLTERRA, V. Variations and fluctuations of the number of individuals in animal species living together. **ICES Journal of Marine Science**, v. 3, n. 1, p. 3–51, 1928.

28 MALCHOW, H. **Spatiotemporal patterns in ecology and epidemiology: theory, models, and simulation**. Boca Raton: Chapman and Hall/CRC, 2007. ISBN 9780429178214.

29 LONGTIN, A.; BULSARA, A.; MOSS, F. Time-interval sequences in bistable systems and the noise-induced transmission of information by sensory neurons. **Physical Review Letters**, v. 67, n. 5, p. 656–659, 1991.

30 STANKOVSKI, T. *et al.* Coupling functions: Universal insights into dynamical interaction mechanisms. **Reviews of Modern Physics**, v. 89, n. 4, p. 045001, 2017. ISSN 0034-6861.

31 CLAESEN, M.; MOOR, B. D. Hyperparameter search in machine learning. abs/1502.02127, 2015. Accessible at: 22 Mar. 2024. Available at: http://arxiv.org/abs/1502.02127.

32 HANAN, J. *et al.* Simulation of insect movement with respect to plant architecture and morphogenesis. **Computers and Electronics in Agriculture**, v. 35, n. 2-3, p. 255–269, 2002. ISSN 01681699.

33 MAZZI, D.; DORN, S. Movement of insect pests in agricultural landscapes. **The Annals of Applied Biology**, v. 160, n. 2, p. 97–113, 2012. ISSN 00034746.

34 MOORCROFT, P. R. Mechanistic approaches to understanding and predicting mammalian space use: recent advances, future directions. **Journal of Mammalogy**, v. 93, n. 4, p. 903–916, 2012. ISSN 0022-2372.

35 TILLES, P. F. C.; PETROVSKII, S. V.; NATTI, P. L. A random acceleration model of individual animal movement allowing for diffusive, superdiffusive and superballistic regimes. **Scientific Reports**, v. 7, n. 1, p. 14364, 2017.

36 BULSARA, A. R.; GAMMAITONI, L. Tuning in to noise. **Physics Today**, v. 49, n. 3, p. 39–45, 1996. ISSN 0031-9228.

37 STROGATZ, S. Synchronization: A universal concept in nonlinear sciences synchronization: A universal concept in nonlinear sciences , arkady pikovsky , michael rosenblum , and jürgen kurths cambridge u. press, new york, 2001. $100.00 (411 pp.). ISBN 0-521-59285-2. **Physics Today**, v. 56, n. 1, p. 47–47, 2003. ISSN 0031-9228.

38 McDonnell, M. D.; ABBOTT, D. What is stochastic resonance? definitions, misconceptions, debates, and its relevance to biology. **PLoS Computational Biology**, v. 5, n. 5, p. e1000348, 2009.

39 LI, T.-Y.; YORKE, J. A. Period three implies chaos. **The American Mathematical Monthly**, v. 82, n. 10, p. 985–992, 1975. ISSN 0002-9890.

40 MAY, R. M. Simple mathematical models with very complicated dynamics. **Nature**, v. 261, n. 5560, p. 459–467, 1976.

41 FEIGENBAUM, M. J. Quantitative universality for a class of nonlinear transformations. **Journal of Statistical Physics**, v. 19, n. 1, p. 25–52, 1978. ISSN 0022-4715.

42 GLEICK, J. **Chaos: Making a New Science**. First edition. New York: Penguin Books, 1988. 352 p. ISBN 978-0-14-009250-9.

43 BECHHOEFER, J. The birth of period 3, revisited. **Mathematics Magazine**, v. 69, n. 2, p. 115–118, 1996. ISSN 0025-570X.

44 PERSOHN, K.; POVINELLI, R. Analyzing logistic map pseudorandom number generators for periodicity induced by finite precision floating-point representation. **Chaos, Solitons & Fractals**, v. 45, n. 3, p. 238–245, 2012. ISSN 09600779.

45 STROGATZ, S. H. **Nonlinear Dynamics and chaos: with applications to physics, biology, chemistry, and engineering**. Boca Raton: CRC Press, 2018. ISBN 9780429492563.

46 BROCK, W. Distinguishing random and deterministic systems: Abridged version. **Journal of Economic Theory**, v. 40, n. 1, p. 168–195, 1986. ISSN 00220531.

47 COLLET, P.; ECKMANN, J.-P. **Iterated maps on the interval as dynamical systems**. Boston: Birkhäuser Boston, 2009. ISBN 978-0-8176-4927-2.

48 ALLIGOOD, K. T.; SAUER, T. D.; YORKE, J. A. **Chaos**. New York: Springer-Verlag, 1996. ISBN 0-387-94677-2.

49 SMITH, P. **Explaining Chaos**. Cambridge: Cambridge University Press, 1998. ISBN 9780511554544.

50 LORENZ, E. N. Deterministic nonperiodic flow. **Journal of the Atmospheric Sciences**, v. 20, n. 2, p. 130–141, 1963. ISSN 0022-4928.

51 FEIGENBAUM, M. J. The transition to aperiodic behavior in turbulent systems. **Communications in Mathematical Physics**, v. 77, n. 1, p. 65–86, 1980. ISSN 0010-3616.

52 TéL, T.; GRUIZ, M. **Chaotic dynamics: an introduction based on classical mechanics**. [*S.l.: s.n.*]: Cambridge University Press, 2006. ISBN 9780511803277.

53 OTT, E.; GREBOGI, C.; YORKE, J. Controlling chaos. **Physical Review Letters**, v. 64, n. 11, p. 1196–1199, 1990.

54 DITTO, W. L.; PECORA, L. M. Mastering chaos. **Scientific American**, v. 269, n. 2, p. 78–84, 1993.

55 DIAMOND, P.; KLOEDEN, P.; POKROVSKII, A. Collapsing effects in computation of dynamical systems. *In*: JUDD, K. *et al.* (ed.). **Control and Chaos**. Boston, MA: Birkhäuser, 1996. p. 60–90. ISBN 978-1-4612-2446-4.

56 PYRAGAS, K. Continuous control of chaos by self-controlling feedback. *In*: **Controlling Chaos**. [*S.l.: s.n.*]: Elsevier, 1996. p. 118–123. ISBN 9780123968401.

57 FRADKOV, A. L.; POGROMSKY, A. Y. **Introduction to control of oscillations and chaos**. Singapore: WORLD SCIENTIFIC, 1998. v. 35. (World scientific series on nonlinear science series A, v. 35). ISBN 978-981-02-3069-2.

58 GONZáLEZ-MIRANDA, J. M. **Synchronization and control of chaos: an introduction for scientists and engineers**. Singapore: PUBLISHED BY IMPERIAL COLLEGE PRESS AND DISTRIBUTED BY WORLD SCIENTIFIC PUBLISHING CO., 2004. ISBN 978-1-86094-488-8.

59 KRAKOWSKI, K. **Triangulation, Modelling and Controlling Dynamical Systems: Theory and Applications**. Saarbrucken: VDM Verlag Dr. Müller, 2009. 104 p. ISBN 978-3639119701.

60 MONTEIRO, S.; BICHO, E. Attractor dynamics approach to formation control: theory and application. **Autonomous Robots**, v. 29, n. 3-4, p. 331–355, 2010. ISSN 0929-5593.

61 FRADKOV, A. L. **Cybernetical Physics**. Berlin, Heidelberg: Springer, 2007. ISBN 978-3-540-46275-0.

62 TAKENS, F. Detecting strange attractors in turbulence. *In*: RAND, D.; YOUNG, L.-S. (ed.). **Dynamical systems and turbulence, Warwick 1980**. Berlin, Heidelberg: Springer, 1981, (Lecture notes in mathematics, v. 898). p. 366–381. ISBN 978-3-540-11171-9.

63 BROER, H.; TAKENS, F. **Dynamical systems and chaos**. New York: Springer, 2011. v. 172. (Applied Mathematical Sciences, v. 172). ISSN 0066-5452. ISBN 978-1-4419-6869-2.

64 BAPTISTA, M. Cryptography with chaos. **Physics Letters A**, v. 240, n. 1-2, p. 50–54, 1998. ISSN 03759601.

65 ÁLVAREZ, G. *et al.* Cryptanalysis of an ergodic chaotic cipher. **Physics Letters A**, v. 311, n. 2-3, p. 172–179, 2003. ISSN 03759601.

66 ALVAREZ, G.; LI, S. Some basic cryptographic requirements for chaos-based cryptosystems. **International Journal of Bifurcation and Chaos**, v. 16, n. 08, p. 2129–2151, 2006. ISSN 0218-1274.

67 KOCAREV, L.; LIAN, S.; KACPRZYK, J. (ed.). **Chaos-Based Cryptography: theory, algorithms and applications**. Berlin, Heidelberg: Springer, 2011. v. 354. (Studies in computational intelligence, v. 354). ISSN 1860-949X. ISBN 978-3-642-20541-5.

68 MACHICAO, J. *et al.* A dynamical systems approach to the discrimination of the modes of operation of cryptographic systems. **Communications in Nonlinear Science and Numerical Simulation**, v. 29, n. 1-3, p. 102–115, 2015. ISSN 10075704.

69 MACHICAO, J. *et al.* Exploiting ergodicity of the logistic map using deep-zoom to improve security of chaos-based cryptosystems. **International Journal of Modern Physics C**, v. 30, n. 05, p. 1950033, 2019. ISSN 0129-1831.

70 MACHICAO, J.; BRUNO, O. M.; BAPTISTA, M. S. Zooming into chaos as a pathway for the creation of a fast, light and reliable cryptosystem. **Nonlinear Dynamics**, v. 104, n. 1, p. 753–764, 2021. ISSN 0924-090X.

71 BASSHAM, L. E. *et al.* **A statistical test suite for random and pseudorandom number generators for cryptographic applications**. 0. ed. Gaithersburg, MD, 2010.

72 STIPČEVIĆ, M.; KOÇ, Ç. K. True random number generators. *In*: KOÇ, Ç. K. (ed.). **Open problems in mathematics and computational science**. Cham: Springer International Publishing, 2014. p. 275–315. ISBN 978-3-319-10682-3.

73 HERRERO-COLLANTES, M.; GARCIA-ESCARTIN, J. C. Quantum random number generators. **Reviews of Modern Physics**, v. 89, n. 1, p. 015004, 2017. ISSN 0034-6861.

74 VAZIRANI, U.; VIDICK, T. Certifiable quantum dice: Or, true random number generation secure against quantum adversaries. *In*: ANNUAL ACM SYMPOSIUM ON THEORY OF COMPUTING, 44., New York, NY, USA. **Proceedings [...]**. New York: ACM, 2012. p. 61–76. ISBN 9781450312455.

75 TASHIAN, C. **A Brief History of Random Numbers**. Accessible at: 12 Mar. 2024. Available at: https://tashian.com/articles/a-brief-history-of-random-numbers/.

76 MIRANDA, G. H. B.; MACHICAO, J.; BRUNO, O. M. Exploring spatio-temporal dynamics of cellular automata for pattern recognition in networks. **Scientific Reports**, v. 6, n. 1, p. 37329, 2016.

77 RIBAS, L. C.; MACHICAO, J.; BRUNO, O. M. Life-like network automata descriptor based on binary patterns for network classification. **Information Sciences**, v. 515, p. 156–168, 2020. ISSN 00200255.

78 ZIELINSKI, K. M. *et al.* A network classification method based on density time evolution patterns extracted from network automata. **Pattern Recognition**, v. 146, p. 109946, 2024. ISSN 00313203.

79 BARTO, F. *et al.* Fair coins tend to land on the same side they started: Evidence from 350,757 flips. **arXiv**, 2023. Available at: https://arxiv.org/abs/2310.04153.

80 NEUMANN, J. von. Various techniques used in connection with random digits. Accessible at: 23 Jan. 2024. Available at: https://mcnp.lanl.gov/pdf_files/InBook_Computing_1961_Neumann_JohnVonNeumannCollectedWorks_VariousTechniquesUsedinConnectionwithRandomDigits.pdf.

81 KNUTH, D. **Art of computer programming: seminumerical algorithms, volume 2**. 3. ed. Reading, Mass: Addison-Wesley Professional, 1997. 784 p. ISBN 0-201-89684-2.

82 GENTLE, J. E. **Random number generation and Monte Carlo methods**. New York: Springer, 1998. (Statistics and Computing). ISSN 1431-8784. ISBN 978-1-4757-2960-3.

83 SIDHPURWALA, H. **A brief history of cryptography**. 2023. Accessible at: 10 Mar. 2024. Available at: https://www.redhat.com/en/blog/brief-history-cryptography.

84 DIFFIE, W.; HELLMAN, M. New directions in cryptography. **IEEE Transactions on Information Theory**, v. 22, n. 6, p. 644–654, 1976. ISSN 0018-9448.

85 DELFS, H.; KNEBL, H. **Introduction to cryptography: principles and applications**. 3rd ed. 2015. ed. New York: Springer, 2015. 528 p. ISBN 978-3662479735.

86 PETITCOLAS, F. A. P. Kerckhoffs'principle. *In*: TILBORG, H. C. A. van; JAJODIA, S. (ed.). **Encyclopedia of Cryptography and Security**. Boston, MA: Springer, 2011. p. 675–675. ISBN 978-1-4419-5905-8.

87 HAMMEL, S. M.; YORKE, J. A.; GREBOGI, C. Numerical orbits of chaotic processes represent true orbits. **Bulletin of the American Mathematical Society**, v. 19, n. 2, p. 465–469, 1988. ISSN 0273-0979.

88 DIAMOND, P.; KLOEDEN, P.; POKROVSKII, A. **Shadowing and approximation dynamical systems**. Accessible at: 14 Mar. 2024. Available at: https://projecteuclid.org/proceedings/proceedings-of-the-centre-for-mathematics-and-its-applications/Miniconferences-on-Analysis-and-Applications/Chapter/Shadowing-and-approximation-dynamical-systems/pcma/1416323439.

89 MANDELBROT, B. B. **Fractals and scaling in finance**. New York: Springer, 1997. ISBN 978-1-4419-3119-1.

90 PAGLIARI, C.; MATTOSCIO, N. The logistic map: an AI tool for economists investigating complexity and suggesting policy decisions. *In*: BUCCIARELLI, E.; CHEN, S.-H.; CORCHADO, J. M. (ed.). **Decision economics. designs, models, and techniques for boundedly rational decisions**. Cham: Springer International Publishing, 2019, (Advances in intelligent systems and computing, v. 805). p. 18–27. ISBN 978-3-319-99697-4.

91 III, O. E. L. A computer-assisted proof of the feigenbaum conjectures. **Bulletin of the American Mathematical Society**, v. 6, n. 3, p. 427–435, 1982. ISSN 0273-0979.

92 LI, S. *et al.* On the security of a chaotic encryption scheme: problems with computerized chaos in finite computing precision. **Computer Physics Communications**, v. 153, n. 1, p. 52–58, 2003. ISSN 00104655.

93 WINN, T.; CALDER, P. Is this a pattern? **IEEE Software**, v. 19, n. 1, p. 59–66, 2002. ISSN 07407459.

94 WOODS, K. S. *et al.* Comparative evaluation of pattern recognition techniques for detection of microcalcifications in mammography. **International Journal of Pattern Recognition and Artificial Intelligence**, v. 07, n. 06, p. 1417–1436, 1993. ISSN 0218-0014.

95 COSTA, L. d. F. *et al.* Characterization of complex networks: A survey of measurements. **Advances in Physics**, v. 56, n. 1, p. 167–242, 2007. ISSN 0001-8732.

96 BACKES, A. R.; CASANOVA, D.; BRUNO, O. M. A complex network-based approach for boundary shape analysis. **Pattern Recognition**, v. 42, n. 1, p. 54–67, 2009. ISSN 00313203.

97 COSTA, L. d. F. *et al.* Analyzing and modeling real-world phenomena with complex networks: a survey of applications. **Advances in Physics**, v. 60, n. 3, p. 329–412, 2011. ISSN 0001-8732.

98 BACKES, A. R.; CASANOVA, D.; BRUNO, O. M. Texture analysis and classification: A complex network-based approach. **Information Sciences**, v. 219, p. 168–180, 2013. ISSN 00200255.

99 ERNáK, J. Digital generators of chaos. **Physics Letters A**, v. 214, n. 3-4, p. 151–160, 1996. ISSN 03759601.

100 GREBOGI, C.; OTT, E.; YORKE, J. Roundoff-induced periodicity and the correlation dimension of chaotic attractors. **Physical review A: general physics**, v. 38, n. 7, p. 3688–3692, 1988.

101 BECK, C. Scaling behavior of random maps. **Physics Letters A**, v. 136, n. 3, p. 121–125, 1989. ISSN 03759601.

102 CHRISTIAN, B. Digital machines iterating chaotic maps: roundoff induced periodicity. *In*: 13ř COLLOQUE SUR LE TRAITEMENT DU SIGNAL ET DES IMAGES. **Proceedings [...]**. Juan-les-Pins: GRETSI, Groupe d'Etudes du Traitement du Signal et des Images, 1991. p. p. 1257–1264.

103 MURILO, P. **Física em Computadores**. São Paulo: Livraria da Fìsica Editora, 2010. ISBN 9788578610814.

104 TANG, Q.-Y.; KANEKO, K. Long-range correlation in protein dynamics: Confirmation by structural data and normal mode analysis. **PLoS Computational Biology**, v. 16, n. 2, p. e1007670, 2020.

105 PENG, C. K. *et al.* Long-range correlations in nucleotide sequences. **Nature**, v. 356, n. 6365, p. 168–170, 1992.

106 SCHENKEL, A.; ZHANG, J.; ZHANG, Y.-C. Long range correlation in human writings. **Fractals**, v. 01, n. 01, p. 47–57, 1993. ISSN 0218-348X.

107 PENG, C.-K. *et al.* Long-range anticorrelations and non-gaussian behavior of the heartbeat. **Physical Review Letters**, v. 70, n. 9, p. 1343–1346, 1993.

108 OLIVEIRA, P. M. C. de. Studying DNA evolution through successive file editions. **Physica A: statistical mechanics and its applications**, v. 273, n. 1-2, p. 70–74, 1999. ISSN 03784371.

109 LIMA, A. R. de; PENNA, T. J. P.; OLIVEIRA, P. M. C. de. Monte carlo simulation of some dynamical aspects of drop formation. **International Journal of Modern Physics C**, v. 08, n. 05, p. 1073–1080, 1997. ISSN 0129-1831.

110 WEIMAR, J. R. Cellular automata for reaction-diffusion systems. **Parallel Computing**, v. 23, n. 11, p. 1699–1715, 1997. ISSN 01678191.

111 SONG, C.; HAVLIN, S.; MAKSE, H. A. Self-similarity of complex networks. **Nature**, v. 433, n. 7024, p. 392–395, 2005.

112 HARARY, F.; GUPTA, G. Dynamic graph models. **Mathematical and computer modelling**, v. 25, n. 7, p. 79–87, 1997. ISSN 08957177.

113 NEWMAN, M. **Networks: an introduction**. Oxford: Oxford University Press, 2010. ISBN 9780199206650.

114 RODRIGUES, F. A.; COSTA, L. d. F. **Caracterização, classificação e análise de redes complexas**. 2007. Thesis (Doctor of Science) Universidade de São Paulo, São Carlos, 2007 — Universidade de São Paulo, 2007.

115 BOLLOBAS, B. The evolution of random graphs. **Transactions of the American Mathematical Society**, v. 286, n. 1, p. 257, 1984. ISSN 00029947.

116 ERDS, P.; RéNYI, A. On random graphs. i. **Publicationes Mathematicae Debrecen**, v. 6, n. 3-4, p. 290–297, 2022. ISSN 00333883.

117 BARABáSI, A.-L. **Network Science**. Cambridge: Cambridge University Press, 2016. 475 p. ISBN 9781107076266.

118 BARABáSI, A.; ALBERT, R. Emergence of scaling in random networks. **Science**, v. 286, n. 5439, p. 509–512, 1999.

119 STROGATZ, S. H. Exploring complex networks. **Nature**, v. 410, p. 268–276, 2001.

120 COSTA, L. d. F. *et al.* A pattern recognition approach to complex networks. **Journal of Statistical Mechanics: Theory and Experiment**, v. 2010, n. 11, p. P11015, 2010. ISSN 1742-5468.

121 ESCUDERO, L. M. *et al.* Epithelial organisation revealed by a network of cellular contacts. **Nature Communications**, v. 2, p. 526, 2011.

122 SILVA, T. C.; ZHAO, L. Network construction techniques. *In*: **Machine learning in complex networks**. Cham: Springer International Publishing, 2016. p. 93–132. ISBN 978-3-319-17289-7.

123 GONçALVES, W. N.; MACHADO, B. B.; BRUNO, O. M. A complex network approach for dynamic texture recognition. **Neurocomputing**, v. 153, p. 211–220, 2015. ISSN 09252312.

124 TöNJES, R.; FIORE, C. E.; PEREIRA, T. Coherence resonance in influencer networks. **Nature Communications**, v. 12, n. 1, p. 72, 2021.

125 PISARCHIK, A. N. Coherence resonance in complex networks. *In*: 2021 5TH SCIENTIFIC SCHOOL DYNAMICS OF COMPLEX NETWORKS AND THEIR APPLICATIONS (DCNA). **Proceedings [...]**. Kaliningrad: IEEE, 2021. p. 151–154. ISBN 978-1-6654-4283-1.

126 MIRANDA, G. H. B. **Spatially explicit modeling on networks: understanding patterns & describing processes**. 2019. Ph. D. Thesis, 2019. Available at: https://teses.usp.br/teses/disponiveis/55/55134/tde-28082019-104837/en.php.

127 HOLLAND, P. W.; LEINHARDT, S. Transitivity in structural models of small groups. **Comparative Group Studies**, v. 2, n. 2, p. 107–124, 1971. ISSN 0010-4108.

128 WATTS, D. J.; STROGATZ, S. H. Collective dynamics of 'small-world' networks. **Nature**, v. 393, n. 6684, p. 440–442, 1998.

129 ZI-YOU, G.; KE-PING, L. Evolution of traffic flow with scale-free topology. **Chinese Physics Letters**, v. 22, n. 10, p. 2711–2714, 2005. ISSN 0256-307X.

130 BLASS, T. **The Man Who Shocked The World |Psychology Today**. 2002. Accessible at: 10 Mar. 2024. Available at: https://www.psychologytoday.com/intl/articles/200203/the-man-who-shocked-the-world.

131 BARTHéLEMY, M. Spatial networks. **Physics Reports**, v. 499, n. 1-3, p. 1–101, 2011. ISSN 03701573.

132 GODWIN, A. Paths through spatial networks. *In*: IEEE VISUALIZATION AND VISUAL ANALYTICS (VIS). **Proceedings [...]**. Virtual Conference: IEEE, 2022. p. 31–34. ISBN 978-1-6654-8812-9.

133 HAGGETT, P.; CHORLEY, R. J. **Network analysis in geography**. London: Edward Arnold London, 1969. (Explorations In Spatial Structure). ISBN 0713154594; 9780713154597; 0713157461; 9780713157468.

134 SPADON, G. *et al.* Detecting multi-scale distance-based inconsistencies in cities through complex-networks. **Journal of Computational Science**, v. 30, p. 209–222, 2019. ISSN 18777503.

135 IZHIKEVICH, E.; CONWAY, J.; SETH, A. Game of life. **Scholarpedia**, v. 10, n. 6, p. 1816, 2015. ISSN 1941-6016.

136 WOLFRAM, S. **A New Kind of Science**. 1. ed. Champaign, IL: Wolfram Media, Inc., 2002. 1192 p. ISBN 1-57955-008-8.

137 WEIMAR, J.; BOON, J. Class of cellular automata for reaction-diffusion systems. **Physical Review E, statistical physics, plasmas, fluids, and related interdisciplinary topics**, v. 49, n. 2, p. 1749–1752, 1994.

138 CORDEIRO, R. L. F.; FALOUTSOS, C.; JúNIOR, C. T. **Data mining in large sets of complex data**. London: Springer, 2013. (Springerbriefs in computer science). ISSN 2191-5768. ISBN 978-1-4471-4889-0.

139 WISHART, J. The generalised product moment distribution in samples from a normal multivariate population. **Biometrika**, v. 20A, n. 1/2, p. 32, 1928. ISSN 00063444.

140 WIGNER, E. P. Characteristic vectors of bordered matrices with infinite dimensions. **The Annals of Mathematics**, v. 62, n. 3, p. 548, 1955. ISSN 0003486X.

141 JAMES, A. T. Normal multivariate analysis and the orthogonal group. **The Annals of Mathematical Statistics**, v. 25, n. 1, p. 40–75, 1954. ISSN 0003-4851.

142 JAMES, A. T. The distribution of the latent roots of the covariance matrix. **The Annals of Mathematical Statistics**, v. 31, n. 1, p. 151–158, 1960. ISSN 0003-4851.

143 JAMES, A. T. Distributions of matrix variates and latent roots derived from normal samples. **The Annals of Mathematical Statistics**, v. 35, n. 2, p. 475–501, 1964. ISSN 0003-4851.

144 JOHNSTONE, I. M. On the distribution of the largest eigenvalue in principal components analysis. **The Annals of Statistics**, v. 29, n. 2, 2001. ISSN 0090-5364.

145 EDELMAN, A.; WANG, Y. **Random matrix theory and its innovative applications**. Accessible at: 24 Jan. 2024. Available at: http://dspace.mit.edu/handle/1721.1/115827.

146 DYSON, F. J. Statistical theory of the energy levels of complex systems. III. **Journal of Mathematical Physics**, v. 3, n. 1, p. 166–175, 1962. ISSN 0022-2488.

147 DYSON, F. J.; MEHTA, M. L. Statistical theory of the energy levels of complex systems. IV. **Journal of Mathematical Physics**, v. 4, n. 5, p. 701–712, 1963. ISSN 0022-2488.

148 MEHTA, M. L.; DYSON, F. J. Statistical theory of the energy levels of complex systems. v. **Journal of Mathematical Physics**, v. 4, n. 5, p. 713–719, 1963. ISSN 0022-2488.

149 TIMME, M.; WOLF, F.; GEISEL, T. Topological speed limits to network synchronization. **Physical Review Letters**, v. 92, n. 7, p. 074101, 2004.

150 BAIK, J.; AROUS, G. B.; PéCHé, S. Phase transition of the largest eigenvalue for nonnull complex sample covariance matrices. **The Annals of Probability**, v. 33, n. 5, p. 1643–1697, 2005. ISSN 0091-1798.

151 DEAN, D. S.; MAJUMDAR, S. N. Large deviations of extreme eigenvalues of random matrices. **Physical Review Letters**, v. 97, n. 16, p. 160201, 2006.

152 ERGüN, G. Random matrix theory. *In*: MEYERS, R. A. (ed.). **Encyclopedia of complexity and systems science**. New York: Springer, 2009. p. 7505–7520. ISBN 978-0-387-30440-3.

153 WIGNER, E. P. Characteristics vectors of bordered matrices with infinite dimensions II. **The Annals of Mathematics**, v. 65, n. 2, p. 203, 1957. ISSN 0003486X.

154 MAY, R. M. Will a large complex system be stable? **Nature**, v. 238, n. 5364, p. 413–414, 1972.

155 CARRO, E.; BENET, L.; CASTILLO, I. P. A smooth transition towards a tracywidom distribution for the largest eigenvalue of interacting k-body fermionic embedded gaussian ensembles. **Journal of Statistical Mechanics: theory and experiment**, v. 2023, n. 4, p. 043201, 2023. ISSN 1742-5468.

156 BöRJES, J.; SCHAWE, H.; HARTMANN, A. K. Large deviations of the length of the longest increasing subsequence of random permutations and random walks. **Physical Review E**, v. 99, n. 4-1, p. 042104, 2019.

157 MAJUMDAR, S. N.; SCHEHR, G. Top eigenvalue of a random matrix: large deviations and third order phase transition. **Journal of Statistical Mechanics: theory and experiment**, v. 2014, n. 1, p. P01012, 2014. ISSN 1742-5468.

158 SILVA, D. F. *et al.* Speeding up similarity search under dynamic time warping by pruning unpromising alignments. **Data Mining and Knowledge Discovery**, v. 32, n. 4, p. 988–1016, 2018. ISSN 1384-5810.

159 GUO, H. *et al.* CUDA-based parallelization of time-weighted dynamic time warping algorithm for time series analysis of remote sensing data. **Computers & Geosciences**, v. 164, p. 105122, 2022. ISSN 00983004.

160 RICCADONNA, S. *et al.* DTW-MIC coexpression networks from time-course data. **Plos One**, v. 11, n. 3, p. e0152648, 2016.

161 LINKE, A. C. *et al.* Dynamic time warping outperforms pearson correlation in detecting atypical functional connectivity in autism spectrum disorders. **Neuroimage**, v. 223, p. 117383, 2020.

162 GELER, Z. *et al.* Time-series classification with constrained DTW distance and inverse-square weighted k-NN. *In*: INTERNATIONAL CONFERENCE ON INnovations IN INTELLIGENT SysTems AND APPLICATIONS (INISTA). **Proceedings** [**...**]. Novi Sad: IEEE, 2020. p. 1–7. ISBN 978-1-7281-6799-2.

163 YEH, C.-C. M. *et al.* Matrix profile i: all pairs similarity joins for time series: a unifying view that includes motifs, discords and shapelets. *In*: IEEE 16TH INTERNATIONAL CONFERENCE ON DATA MINING (ICDM). **Proceedings** [**...**]. Barcelona: IEEE, 2016. p. 1317–1322. ISBN 978-1-5090-5473-2.

164 KEOGH, E. **UCR Matrix Profile Page**. Accessible at: 10 Mar. 2024. Available at: https://www.cs.ucr.edu/~eamonn/MatrixProfile.html.

165 HAWKINS, D. M. **Identification of Outliers**. Dordrecht: Springer, 1980. ISBN 978-94-015-3994-4.

166 KRIEGEL, H.-P.; HUBERT, M. S.; ZIMEK, A. Angle-based outlier detection in high-dimensional data. *In*: ACM SIGKDD INTERNATIONAL CONFERENCE ON KNOWLEDGE DISCOVERY AND DATA MINING - KDD 08, 14. **Proceedings** [**...**]. New York: ACM Press, 2008. p. 444. ISBN 9781605581934.

167 CHANDOLA, V.; BANERJEE, A.; KUMAR, V. Anomaly detection. **ACM Computing Surveys**, v. 41, n. 3, p. 1–58, 2009. ISSN 03600300.

168 ZIMEK, A.; SCHUBERT, E.; KRIEGEL, H.-P. A survey on unsupervised outlier detection in high-dimensional numerical data. **Statistical analysis and data mining**, v. 5, n. 5, p. 363–387, 2012. ISSN 19321864.

169 THIEL, M.; ROMANO, M. C.; KURTHS, J. Spurious structures in recurrence plots induced by embedding. **Nonlinear Dynamics**, v. 44, n. 1-4, p. 299–305, 2006. ISSN 0924-090X.

170 KRIEGEL, H.-P.; KRöGER, P.; ZIMEK, A. Clustering high-dimensional data: a survey on subspace clustering, pattern-based clustering, and correlation clustering. **ACM TKDD**, ACM, New York, v. 3, n. 1, p. 1–58, 2009. ISSN 1556-4681.

171 GHOTING, A.; PARTHASARATHY, S.; OTEY, M. E. Fast mining of distance-based outliers in high-dimensional datasets. **Data Mining and Knowledge Discovery**, v. 16, n. 3, p. 349–364, 2008. ISSN 1384-5810.

172 AGGARWAL, C. C.; YU, P. S. Outlier detection for high dimensional data. **ACM SIGMOD Record**, v. 30, n. 2, p. 37–46, 2001. ISSN 01635808.

173 HODGE, V. J.; AUSTIN, J. A survey of outlier detection methodologies. **Artificial Intelligence Review**, v. 22, n. 2, p. 85–126, 2004. ISSN 0269-2821.

174 AHMED, M.; MAHMOOD, A. N.; HU, J. A survey of network anomaly detection techniques. **Journal of Network and Computer Applications**, v. 60, p. 19–31, 2016. ISSN 10848045.

175 MULLER, E. *et al.* Outrank: ranking outliers in high dimensional data. *In*: IEEE 24TH INTERNATIONAL CONFERENCE ON DATA ENGINEERING WORKSHOP. **Proceedings** [**...**]. Cancun: IEEE, 2008. p. 600–603. ISBN 978-1-4244-2161-9.

176 BZDOK, D.; ALTMAN, N.; KRZYWINSKI, M. Statistics versus machine learning. **Nature Methods**, v. 15, n. 4, p. 233–234, 2018. ISSN 1548-7091.

177 FAN, J.; LI, R. Statistical challenges with high dimensionality: feature selection in knowledge discovery. *In*: SANZ-SOLé, M. *et al.* (ed.). **Proceedings of the international congress of mathematicians madrid, august 22-30, 2006**. Zuerich, Switzerland: European Mathematical Society Publishing House, 2007. p. 595–622. ISBN 978-3-03719-022-7.

178 JOHNSTONE, I. M.; TITTERINGTON, D. M. Statistical challenges of high-dimensional data. **Philosophical Transactions. Series A, Mathematical, Physical, and Engineering Sciences**, v. 367, n. 1906, p. 4237–4253, 2009.

179 FAN, J.; LI, R. [**math/0602133**] **Statistical Challenges with High Dimensionality: Feature Selection in Knowledge Discovery**. Accessible at: 28 Jan. 2019. Available at: https://arxiv.org/abs/math/0602133.

180 AGGARWAL, C. C. **Outlier Analysis**. Cham: Springer International Publishing, 2017. ISBN 978-3-319-47577-6.

181 JUNIOR, A. G. B.; CORDEIRO, R. L. F. Fast and scalable outlier detection with metric access methods. *In*: RODRIGUES, J. M. F. *et al.* (ed.). **Computational science ICCS 2019: 19th international conference, Faro, Portugal, June 12-14, 2019, Proceedings, Part II**. Cham: Springer International Publishing, 2019, (Lecture notes in computer science, v. 11537). p. 189–203. ISBN 978-3-030-22740-1.

182 MARQUES, H. O. *et al.* On the internal evaluation of unsupervised outlier detection. *In*: GUPTA, A.; RATHBUN, S. (ed.). **Proceedings [...]**. New York: ACM Press, 2015. p. 1–12. ISBN 9781450337090.

183 CAMPOS, G. O. *et al.* On the evaluation of unsupervised outlier detection: measures, datasets, and an empirical study. **Data Mining and Knowledge Discovery**, v. 30, n. 4, p. 891–927, 2016. ISSN 1384-5810.

184 TAMASSIA, R. Strategic directions in computational geometry. **ACM Computing Surveys**, v. 28, n. 4, p. 591–606, 1996. ISSN 0360-0300.

185 BOISSONNAT, J.-D.; CHAZAL, F.; YVINEC, M. **Computational Geometry and Topology for Data Analysis**. 2016.

186 LI, J. *et al.* Radar: residual analysis for anomaly detection in attributed networks. *In*: SIERRA, C. (ed.). **Proceedings [...]**. California: International Joint Conferences on Artificial Intelligence Organization, 2017. p. 2152–2158. ISBN 9780999241103.

187 TILBORG, H. C. A. van; JAJODIA, S. (ed.). **Encyclopedia of cryptography and security**. Boston, MA: Springer, 2011. ISBN 978-1-4419-5905-8.

188 BREUNIG, M. M. *et al.* Lof: Identifying density-based local outliers. *In*: 2000 ACM SIGMOD INTERNATIONAL CONFERENCE ON MANAGEMENT OF DATA - SIGMOD '00. **Proceedings [...]**. New York: ACM Press, 2000. p. 93–104. ISBN 1581132174.

189 PAPADIMITRIOU, S. *et al.* **LOCI: Fast Outlier Detection Using the Local Correlation Integral.** 2003. 315-326 p.

190 YAN, Y.; CAO, L.; RUNDENSTEINER, E. A. Scalable top-n local outlier detection. *In*: 23RD ACM SIGKDD INTERNATIONAL CONFERENCE ON KNOWLEDGE DISCOVERY AND DATA MINING - KDD '17. **Proceedings [...]**. New York: ACM Press, 2017. p. 1235–1244. ISBN 9781450348874.

191 MITSA, T. **Temporal Data Mining**. New York: Chapman and Hall/CRC, 2010. ISBN 9781420089776.

192 XU, X.; ZHANG, J.; SMALL, M. Superfamily phenomena and motifs of networks induced from time series. **Proceedings of the National Academy of Sciences of the United States of America**, v. 105, n. 50, p. 19601–19605, 2008.

193 SAKAI, Y.; INENAGA, S. A faster reduction of the dynamic time warping distance to the longest increasing subsequence length. **Algorithmica**, v. 84, n. 9, p. 2581–2596, 2022. ISSN 0178-4617.

194 BAIK, J. Limiting distribution of last passage percolation models. *In*: XIVTH INTERNATIONAL CONGRESS ON MATHEMATICAL PHYSICS. **Proceedings** [**...**]. Lisbon: World Scientific, 2006. p. 339–346.

195 HOFFMAN, C. **First Passage Percolation**. 2016. 1 - 52 p. Class notes.

196 HOU, L.; SMALL, M.; LAO, S. Dynamical systems induced on networks constructed from time series. **Entropy**, v. 17, n. 9, p. 6433–6446, 2015. ISSN 1099-4300.

197 LUCHESI, A. C. F. **Utilizando o aprendizado de máquina para análise de órbitas caóticas**. 2022. Dissertation (Master of Science) – Instituto de Física de São Carlos, Universidade de São Paulo, São Carlos, 2022., 2022.

198 GAO, Z.; JIN, N. Flow-pattern identification and nonlinear dynamics of gas-liquid two-phase flow in complex networks. **Physical Review E: statistical, nonlinear, and soft matter physics**, v. 79, n. 6 Pt 2, p. 066303, 2009.

199 R Core Team. **R: a language and environment for statistical computing**. Vienna, Austria, 2021.

200 EATON, J. W. *et al.* **GNU Octave version 6.3.0 manual: a high-level interactive language for numerical computations**. Madison, 2021.

201 INC., W. R. **Mathematica, Version 14.0**. Champaign, IL, 2024.

202 HALL, M. *et al.* The WEKA data mining software. **ACM SIGKDD Explorations Newsletter**, v. 11, n. 1, p. 10, 2009.

203 CHANG, C.-C.; LIN, C.-J. LIBSVM: A library for support vector machines. **ACM Transactions on Intelligent Systems and Technology**, v. 2, n. 3, p. 1–27, 2011. ISSN 21576904.

204 MICHAIL, D. *et al.* Jgrapht—a java library for graph data structures and algorithms. **ACM Transactions on Mathematical Software**, v. 46, n. 2, p. 1–29, 2020. ISSN 0098-3500.

205 HAGBERG, A.; SWART, P.; SCHULT, D. **Exploring network structure, dynamics, and function using NetworkX (Conference) |OSTI.GOV**. Accessible at: 11 Mar. 2024. Available at: https://www.osti.gov/biblio/960616.

206 BASTIAN, M.; HEYMANN, S.; JACOMY, M. **Gephi: An Open Source Software for Exploring and Manipulating Networks**. 2009.

207 TURAN, M. S. *et al.* **Recommendation for the entropy sources used for random bit generation**. Gaithersburg, MD, 2018.

208 L'ECUYER, P.; SIMARD, R. Testu01. **ACM Transactions on Mathematical Software**, v. 33, n. 4, p. 22–es, 2007. ISSN 00983500.

209 DOTY-HUMPHREY, C. **Practically Random - Browse Files at SourceForge.net**. Accessible at: 11 Mar. 2024. Available at: https://sourceforge.net/projects/pracrand/files/.

210 ZIMMERMAN, Z. *et al.* Matrix profile XIV: Scaling time series motif discovery with GPUs to break a quintillion pairwise comparisons a day and beyond. *In*: ACM SYMPOSIUM ON CLOUD COMPUTING - SoCC '19. **Proceedings [...]**. New York, New York, USA: ACM Press, 2019. p. 74–86. ISBN 9781450369732.

211 SYMUL, T.; ASSAD, S. M.; LAM, P. K. Real time demonstration of high bitrate quantum random number generation with coherent laser light. **Applied Physics Letters**, v. 98, n. 23, p. 231103, 2011. ISSN 0003-6951.

212 HAW, J. Y. *et al.* Maximization of extractable randomness in a quantum random-number generator. **Physical Review Applied**, v. 3, n. 5, p. 054004, 2015. ISSN 2331-7019.

213 BECK, C.; SCHOGL, F. **Thermodynamics of chaotic systems: an introduction**. Cambridge: Cambridge University Press, 1993. ISBN 9780511524585.

214 KAPLAN, J. L.; YORKE, J. A. Chaotic behavior of multidimensional difference equations. *In*: PEITGEN, H.-O.; WALTHER, H.-O. (ed.). **Functional differential equations and approximation of fixed points**. Berlin, Heidelberg: Springer, 1979, (Lecture notes in mathematics, v. 730). p. 204–227. ISBN 978-3-540-09518-7.

215 PALMERO, M. S. *et al.* Ensemble separation and stickiness influence in a driven stadium-like billiard: A lyapunov exponents analysis. **Communications in Nonlinear Science and Numerical Simulation**, v. 65, p. 248–259, 2018.

216 HILBORN, R. C. Quantifying chaos. *In*: **Chaos and Nonlinear Dynamics: an introduction for scientists and engineers**. Oxford: Oxford University PressOxford, 2000. p. 319–374. ISBN 0198507232.

217 KANTZ, H.; GRASSBERGER, P. Repellers, semi-attractors, and long-lived chaotic transients. **Physica D: nonlinear phenomena**, v. 17, n. 1, p. 75–86, 1985.

218 KADANOFF, L. P.; TANG, C. Escape from strange repellers. **Proceedings of the National Academy of Sciences of the United States of America**, v. 81, n. 4, p. 1276–1279, 1984.

APPENDIX

APPENDIX A – APÊNDICE(S)

A.0.0.1 Thermostatistics of multifractals

For physical systems, every of the regent probability distributions on every axis of a system adequately described by a multifractal is often unknown or indetermined. For the case of dynamical systems in a computer experiment, empirical data for probability distributions is generally readily available. It is commonplace for one to possess local information on system behavior where it is desirable to gain global and general knowledge but the converse might be true also, that is, one posseses relative frequencies for several probability distributions and would like to know further about locally concentrated tendencies on a certain scale and locally appliable formulae for the behavior of the system. Interestingly, there is a concept, the canonical distributions, that effectively links chaos theory and thermodynamics (213). These distributions assume the form of thermodynamic equilibrium distributions. When the system is off equilibrium, we tap into a particular piece of information. An ensemble comprises several realizations of the system, and help ascertain the true nature of the system.

In nonlinear dynamics, let events happen in a specific box contained in a grid of or a ball contained in a space, and

$$p_i = e^{-b_i},$$

be the observed relative frequencies of events or microstates i of a sample. Then we define normalized powers $(p_i)^\beta$ and the probability distributions

$$P_i = \frac{(p_i)^\beta}{\sum_{j=1}^{r}(p_j)^\beta}, \beta \in \mathbb{R}, p_j > 0.$$

Scaling β, the probabilities for the diverse events i are weighted accordingly, thus depthening the analysis. For our purposes it will be assumed that every nonlinear system under study always follows precisely every distribution P_i we assign as one of its distributions.

As for the analogy with statistical mechanics, let us define again the canonical distribution:

$$P_r = \frac{e^{-\beta b_r}}{Z(\beta)}.$$

$$Z(\beta) = \sum_{i=1}^{r} e^{-\beta b_i} = \sum_{i=1}^{r}(p_i)^\beta$$

Previoulsy, we refer to the Minkowski-Bouligand dimension. It happens that there is a more general way to quantify fractals, the Rényi dimension.

The Rényi dimension is defined in the $\epsilon \to 0$ or $V = -\ln \epsilon \to \infty$ limits.

$$D(\beta) = -\lim_{V \to \infty (I_\beta / V)}$$

As in physical and computer experiments $\epsilon > 0 \ \forall \epsilon$, that is, there is only finite modes of precision, we define the Rényi information per volume V

$$\frac{I_\beta}{V} = \frac{1}{(\beta - 1)V}$$

Besides the Rényi dimension, there is a Rényi analog also for entropy that generalizes several notions.

$$H_\alpha(X) = \frac{1}{1-\alpha} \log \sum_{i=1}^{n} p_i^\alpha$$

is the entropy of order α, $0 < \alpha < \infty$, $\alpha \neq 1$ and the definition in the limit $\gamma \to \alpha$, $\alpha = 0, 1, \infty$ is

$$H_\alpha(X) = \lim_{\gamma \to \alpha} (H_\gamma(X))$$

where X is a discrete random variable that assumes one at a time the value of the elements in the set $\mathcal{A} = \{x_1, x_2, x_3, \ldots, x_n\}$ with corresponding probabilities $p_i \doteq Pr(X = x_i)$ for $i = 1, \ldots, n$.

The utility in commenting briefly on fractal analysis resides in that we do not to have restrict ourselves merely to the study of chaos using Lyapunov exponents. There is, for example, the Kaplan-Yorke conjecture (214) that allows for the study of qualities further than chaos using tools of fractal analysis.

A.0.0.2 Fundamental thermodynamical relations

From now on until the end of this part section, we closely follow the demonstrations and presentation of results by Beck and Schogl (213). They are important to sediment the theory of dynamical systems as it is applied in our work. A fundamental result known as the Fundamental Thermodynamic Relation, can be formulated as

$$dU = TdS - \Pi dV$$

if the change of the number of particles in time is significant, we may write

$$dU = TdS - \Pi dV + \mu dN$$

where U refers to internal energy, T to temperature, S to entropy, Π to pressure, V to volume and N the conserved number of particles, see Figure A.0.0.2. This formula derives from the First Law of Thermodynamics and its related concepts of heat, work, and internal energy in a system. From this results we derive other significant formulations.

A tool of formalism that plays a distinguished role in the derivation of alternative formulations in thermodynamics is the Legendre transform.

Let a strictly convex real function $f(x)$. Then

$$p = df(x)$$

$$f^*(p) = -f(x(p)) + px(p)$$

and the Legendre Transform on x and f is

$$(x, f(x)) \to (p, f^*(p))$$

Energy E is distinguished as the generator of time shift and the most important constant of motion. Entropy S is highlighted as it is fully determined solely by the probability distribution. The Legendre transform provides a bridge between both.

Following Beck and Schogl (213), we proceed to derive other important results.

Gibbs' fundamental equation:

Consider the information gain from a generalized canonical distribution P, that is

$$P_i = e^{\Psi - \beta_\sigma M_i^\sigma}$$

to a perturbed one $P + \delta P$, which is obtained by a perturbation $\delta\beta_\sigma$ of the intensities β_σ

$$\begin{aligned} K(P + \delta P, P) &= \sum_i (P_i + \delta P_i)[\ln(P_i + \delta P_i) - \ln P_i] \\ &= -\delta S - \sum_i \delta P_i \ln P_i \\ &= -\delta S + \beta_\sigma \delta M^\sigma \geqslant 0 \end{aligned}$$

For infinitesimally small $\delta P_i \to 0$, we have

$$\left(\frac{\partial S}{\partial M^\sigma} - \beta_\sigma\right)\delta M^\sigma + \frac{1}{2}\frac{\partial^2 S}{\partial M^\sigma \partial M^\tau}\delta M^\sigma \delta M^\tau \leqslant 0$$

Taken that variations in δM are arbitrary in direction, we then have the relations

$$\frac{\partial S}{\partial M^\sigma} = \beta_\sigma$$

and that ∂S always assumes negative values.

$$\frac{\partial^2 S}{\partial M^\sigma \partial M^\tau} = \frac{\partial \beta_\sigma}{\partial M^\tau} = \delta M^\sigma \delta \beta_\sigma \leqslant 0$$

The entropy

$$S(M) = -\langle \ln P \rangle = -\Psi + \beta_\sigma M^\sigma$$

is the Legendre transform of $\Psi(\beta)$. And

$$\partial \Psi / \partial \beta_\sigma = M^\sigma$$

Then we derive the Gibbs fundamental equation for the grand canonical ensemble with fluctuating volume

$$dE = TdS - \Pi dV + \mu dN$$

S, V and N are *extensities* that increase proportionally with the increase of the amount of physical matter given the substantial composition and the external conditions are the same. T, Π and μ are *intensities*, coefficients in the total differential of E that remain constant given systems of different sizes. Π and μ differ from the coefficients β_{sigma} only by the factor $1/T$. The equilibrium state of a system can be described alternatively by the entire set of extensities or by the entire set of intensities, or by a mixed set of variables (213). In the context taken thus far, β_σ and M^σ are thermal conjugates of each other.

The Helmholtz free energy

$$F = E - TS$$

is a Legendre transform from $E(S, V, N)$ to $F(T, V, N)$. Using F, the Gibbs fundamental equation can be assumed as

$$dF = -\Pi dV + \mu dN - SdT$$

.

Chosen as independent variables V, N, T that occur in this equation as differentials, then

$$\partial F/\partial V = -\Pi, \quad \partial F/\partial N = \mu, \quad \partial F/\partial T = -S.$$

Quantities V, N, T are called the natural variables of F and form a complete set of variables for description of thermodynamics. By deriving F with respect to the natural variables we obtain another set, akin to the mechanical connection between forces and potentials. Therefore F, as a function of its natural variables, is a potential. Via Legendre transformation we proceed to other thermodynamical potentials, such as the Gibbs free energy

$$G = F + \Pi V$$

that is connected with F by a Legendre transformation from the variable V to the variable Π. The Gibbs fundamental equation assumes the following

$$dG = Vd\Pi + \mu dN - SdT$$

Therefore T, Π and N are the natural variables of G. For $G(T, \Pi, N)$ this means

$$\partial G/\partial \Pi = V, \partial G/\partial N = \mu, \partial G/\partial T = -S$$

Generally in the context of thermodynamics, by expression of the Gibbs fundamental equation as a total differential, the variables that occur as independent differentials are the *natural variables* of the thermodynamic quantity. The thermodynamic quantity as a function of the just corresponding natural variables is the corresponding thermodynamic potential. The analogy to mechanics goes beyond relations between forces and potentials and extends to the fact that a mechanical equilibrium is determined by a minimum of the potential. Thermodynamic potentials possess an extremum as well (6.3). Factor T aside, the different thermodynamic potentials are varied Legendre transforms of the entropy. The entropy $S(M)$ itself is a thermodynamic potential according to eq. (7.2.4).

The previous definitions can be simplified for homogenous systems, that is, if its physical properties and dynamical laws are the same in all of its spatial parts. Entropy

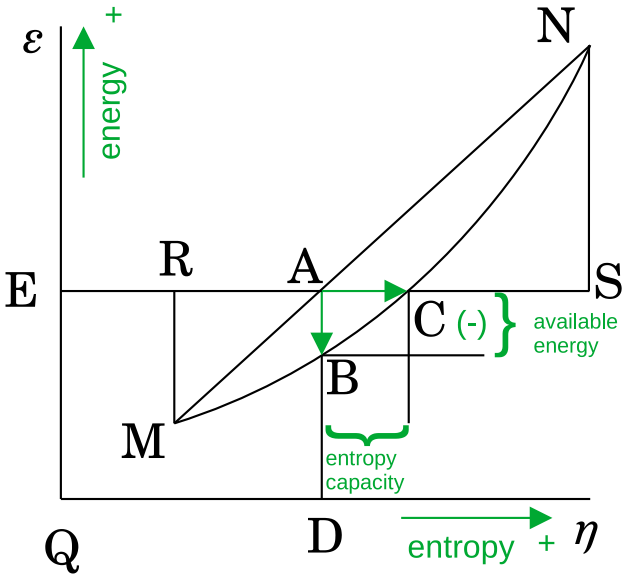

Figure 138 – Gibbs free energy diagram. Letters represent states of the reversible work that goes back and forth as a system. For example, for a system at state R to attain state D, it must pass first through states M (or A, and then B) and D.
Source: By the author.

fulfills here an important role due to its linear relation with every derivation of the fundamental relation, given that the system in question is homogeneous. Another fact about the entropy is that it is concave in the probability space as well, as a function of probabilities.

Beck and Schogl (213) explain the derivations for different types of homogeneous, including multiparticle, systems.

For the purposes of this work we focus on the *simplified* Gibbs-Duhem equation which has the form

$$G = \mu N$$

which has general form

$$S = \beta_\sigma M^\sigma$$

Thermodynamics exhibit susceptibilities and fluctuations that decrease as the size of the system increases, which allows study of a system using statistical tools given the system is *large enough*. Susceptibities and fluctuations lead to phase transitions, phenomena that depend on a critical event. Examples of phase transitions are solid-liquid and liquid-gas transitions, transitions between paramagnetic and ferromagnetic states, transitions between different crystal structures, transitions between homogeneous and inhomogenous states of liquid mixtures, transitions between the normal conducting and the supercon-

ducting statem and the transition between the normal fluid and the superfluid state of He^4 (213). Thereare also non-equilibrium phase transitions between diverse nonstationary nonequilibrium states.

Phase transitions are classified following the analytical behavior of the corresponding thermodynamical potential, and if the k-th derivative of the generalized free energy with respect to the relevant thermal variable does not exist at the critical point, whereas the $k+1$-th derivative does indeed exist, the phase transition is said to be of k-th order.

Critical exponents either diverge or go to zero at second order phase transitions under appropriate order parameters.

Scaling near the critical temperature T_c there is the specific heat for constant volume

$$c_V = -T\left(\frac{\partial^2 F}{\partial T^2}\right)_V$$

or the compressibility

$$\kappa_T = -\frac{1}{V}\left(\frac{\partial^2 G}{\partial \Pi^2}\right)_V$$

at the point where the coexistence of the two phases of liquid and vapor are no more.

$$\begin{aligned} c_V &\sim |\tau|^{-\alpha} \quad \alpha = 0.11 \\ \kappa_T &\sim |\tau|^{-\gamma} \quad \gamma = 1.25 \end{aligned}$$

And

$$\tau = (T - T_c)/T_c$$

a relative deviation of the temperature from the critical point, and it is dimensionless. τ need not be a temperature difference but it is the relative deviation of a fit control parameter from the critical value.

An order parameter f scales along critical exponent

$$\gamma = \lim_{\tau \to 0} \frac{\ln |f(\tau)|}{\ln |\tau|}$$

as

$$|f(\tau)| \sim |\tau|^{\gamma}$$

in the case of one-dimensional chaotic dynamics, this is the critical exponent. In multidirectional chaotic dynamics, the largest critical exponent is associated with the dominating directon of the dynamics.

A.0.0.3 Partition function and the Gibbs measure

For classical discrete systems, the canonical partition function is defined as

$$Z = \sum_i e^{-\beta E_i}$$

where i is the index for the microstates of the system, β is the thermodynamic beta, defined as $\frac{1}{k_B T}$ where k_B is Boltzmann's constant and E_i is the total energy of the system in the respective microstate. The exponential factor $e^{-\beta E_i}$ is the Boltzmann factor.

The main purpose of a partition function is to bring a meaningful view of some property of a given system – not just thermodynamical systems – in relation to other properties and also as a function of other properties. This bridges the microscopic states of a system and its whole equilibrium. If we realize that a certain state of the system has very low probability of occurring, due to the interplay between its properties, these low – otherwise high – probabilities serve as information about the system. The partition function, in defining the actual strength of the relation between the diverse properties in a manner that allows direct application of probability theory, effectively helps one to study the system at hand. From there we go through the concept of ensembles of systems, as frequentism states that the true probability of an event is calculated as the limit of its relative frequency in an unbounded number of trials.

For the canonical ensemble, the energy is not known a priori but the total number of particles. There is also the microcanonical ensemble, where both the energy of the system and the number of particles are fixed to predetermined values, and the grand canonical ensemble, where neither the energy nor the number of particles are known a priori. The canonical ensemble is appealing for application in chaotic orbits as by fixing the number of particles, the states of a dynamical system and its orbits with several points can be taken as appropriately defined parameters. The energy for a dissipative system like the logistic map it is indeed not known a priori and it is via numerical computations that we get an estimate.

The rate of separation, measured by means of the Lyapunov exponent, helps perform the separation of ensembles (215), which in turn lets us locate patterns. While the local variation for Lyapunov exponent on the logistic map does indeed provide valuable information, the dissipative and multifractal nature of maps like the logistic map makes it to an extent risky to rely on the evolution of the Lyapunov exponent within a single orbit

only as a reliable gauge. It surfaces, thus, the need to use ensembles of logistic map orbits, where each orbit correspond to a state. Moreover, when dealing with random processes the Lyapunov exponent alone is a necessary but not sufficient parameter for addressing the behavioral mixture of order and stochasticity.

Assume that if we test several such systems, with properly tuned parameters, then we faithfully represent the whole entity. Of course, it is not doable to experiment with every possible configuration of parameters. Nevertheless, for experimental purposes (216) locality of the scope is enough to measure the functional *faithfully enough*. A significant advantage of computer simulations over physical thermodynamical systems is that the parameters can be finely tuned which adds to the practical robustness of the measure.

From the bifurcation diagram we see that for low values of $r < 3.8$, their orbits show heterogenicity. As the value approaches $r = 4$, we witness that their behavior is more homogeneous, like a single system where the macro conditions are largely similar but the microstates are different to each other.

Restricting ourselves to one-dimensional maps and a test function

$$\phi(x) = -\beta \ln |f'(x)|$$

for each β there is an invariant Gibbs measure μ_β that minimizes the free energy. The outstanding measure with $\beta = 1$ is called the Sinai-Ruelle-Bowen measure.

As we restrict ourselves to expanding systems, the natural invariant measure coincides with the SRB measure. We may, however, also generalize our concept and consider Rényi entropies for arbitrary Gibbs measures μ_q parametrized by a temperature $1/q$. These are denoted by $K(\beta/q)$. Notice that $K(1, q) = h([\mu_q])$ and $K(\beta\ , 1) = K(\beta)$.

The Rényi entropies are defined by the asymptotic scaling relation

$$\textstyle\sum_j (P_j^{(N)})^\beta \sim e^{[N(1-\beta)K(\beta,q)]}, \quad N \to \infty.$$

The probabilities P_j are related to the Gibbs measure μ_q by

$$P_j^{(N)} = \int_{J_j^N} d\mu_q(x)$$

They scale as

$$P_j^N \sim (1/Z_N^{top})(l_j^{(N)})^q,$$

where with $Z_N^{top} \approx \tilde{Z}_N^{top}$

$$Z_N^{top} \sim \sum_j (l_j^N)^q \sim e^{N\mathscr{P}(q)}, \quad N \to \infty$$

Hence

$$\sum_j (P_j^N)^\beta \sim e^{-N\beta\mathscr{P}(q)} \sum_j (l_j^N)^{q\beta}$$
$$\sim e^{-N\beta\mathscr{P}(q)} e^{N\mathscr{P}(q\beta)}$$
$$\sim e^{N(1-\beta)K(\beta,q)}$$

.

We obtain

$$K(\beta, q) = \frac{1}{1-\beta}[\mathscr{P}(\beta q) - \beta\mathscr{P}(q)]$$

In particular for the case $q - 1$:

$$K(\beta) = \frac{1}{1-\beta}[\mathscr{P}(\beta) - \beta\mathscr{P}(1)].$$

$-\mathscr{P}(1)$ is the escape rate κ and there follows a relation between Rényi entropy, topological pressure, and escape rate

$$K(\beta) = \frac{1}{1-\beta}[\mathscr{P}(\beta) + \kappa\beta]$$

An important special case is $K(0) = \mathscr{P}(0)$, which relates the topological entropy to the topological pressure. To obtain a relation for the KS entropy K(1) that is similar to the Shannon entropy, we assume that $\mathscr{P}(\beta)$ is smooth, i.e., that there is the following series expansion

$$\mathscr{P}(\beta) = \mathscr{P}(1) + (\beta - 1)\mathscr{P}'(1) + O((\beta - 1)^2).$$

Inserting this into

$$K(\beta) = \frac{1}{1-\beta}[\mathscr{P} - \beta\mathscr{P}(1)]$$

and taking the limit $\beta \to 1$, we obtain

$$K(1) = -\mathscr{P}'(1)$$

$\mathscr{P}(1)$ is the negative escape rate, but what is the "physical" meaning of $\mathscr{P}'(1)$? The topological pressure is given by

$$\mathscr{P}(q) = \lim_{N\to\infty} \frac{1}{N} \ln \sum_j e^{-qNE_N(x_0^{(j)})}$$

.

Differentiating we obtain

$$\mathscr{P}'(q) = -\lim_{N\to\infty} \sum_j P_j^N E_N(x_0^{(j)}) = -\langle E\rangle(q)$$

.

The quantity $\langle E\rangle(q)$ is the mean expansion rate with respect to the Gibbs measure μ_q. In the one-dimensional case $\langle E\rangle(1)$ is simply the Lyapunov exponent λ. Hence,

$$K(1) = \lambda - \kappa$$

This equation relates the KS entropy, the Lyapunov exponent, and the escape rate of a one-dimensional expanding map. Among physicists it became well-known from a paper of Kantz and Grassberger (217), and it is also discussed in another work (218). We recognize that the KS entropy and the Lyapunov exponent of a one-dimensional system only coincide if there is no escape ($\kappa = 0$).

The measure leads to a Markov partition that holds representation both in thermodynamics and one-dimensional dynamical maps. From the Markov partition we draw a symbolic representation of the dynamical system (M, φ) such that the map φ becomes the shift map. However, we will not depthen our focus further on the symbolic dynamics, which would let us to other subjects like N-cylinders and local measures. Back to the significance of the Gibbs free energy, the mean expansion rate points to a phase transition, and bifurcations – which are the route to chaos – also point to a phase transition in chaotic systems. Again, we are concerned with average variables of several realizations within an ensemble for a system.

Table 21 – Classification performance as a preliminary test of DTW capabilities, with accuracy reported in percentages. 1-NN DTW is the classical nearest neighbor classifier, applied on a LLNA matrix as a matrix of time series with the temporal evolution for every node taken as one time series. The other results come from the SVM classifier. 'S' is the Shannon entropy, 'wl' the word length and 'lzc' the Lempel-Ziv complexity.

dataset	1-NN DTW	structural	LLNA	LLNA (S)	LLNA (wl)	LLNA (lzc)	LLNA-BP	LLNA-DTEP
Animals	80.34±3.92	88.39±1.18	82.41±4.26	83.55±4.47	81.06±3.77	25.92±6.54	44.14±4.47	25.36±3.85
Fungi	38.34±5.36	42.53±4.22	41.13±5.25	41.59±5.72	41.57±6.00	26.44±7.03	36.43±4.69	47.78±3.90
Plant	71.45±6.99	67.27±4.24	73.79±5.97	74.92±8.16	74.03±6.59	36.36±6.92	50.82±4.51	56.73±4.09
Actinobacteria	86.59±1.89	88.08±0.59	91.95±1.28	92.77±1.06	92.04±1.16	41.89±0.71	41,92±0.00	41.92±0.00
Kingdom	88.45±2.02	88.24±0.93	89.47±1.79	93.83±1.63	72.55±2.58	28.01±2.66	73.43±1.49	69.01±1.27
Protist	45.89±9.62	69.39±2.60	39.61±10.40	46.25±8.56	39.61±8.91	29.00±8.19	61.68±6.21	64.18±5.16
Firmicutes-Bacillis	78.15±1.34	82.06±0.66	74.96±1.72	78.28±1.36	76.45±1.72	47.21±0.99	31.50±0.00	31.50±0.00
Scale-Free	70.80±0.86	55.17±3.60	62.05±2.93	70.26±1.48	62.42±2.53	71.78±1.33	57.68±6.13	72.43±1.56
4-Models	54.55±1.26	56.50±1.40	83.63±0.67	66.18±0.64	80.74±0.81	72.09±0.33	81.35±4.84	92.59±0.17

Source: By the author.

Table 22 – Results for the SP800-22 Rev. 1 tests on the k-logistic map (base 2), $k = 0$, $r \sim 4$.

NIST test	p-value	result
monobit_test	2.3827519899843513e-62	FAIL
frequency_within_block_test	4.558896651993508e-44	FAIL
runs_test	0.0	FAIL
longest_run_ones_in_a_block_test	5.390829886304116e-208	FAIL
binary_matrix_rank_test	0.0	FAIL
dft_test	0.0	FAIL
non_overlapping_template_matching_test	0.9735784873666354	PASS
overlapping_template_matching_test	0.0	FAIL
maurers_universal_test	0.0	FAIL
linear_complexity_test	0.13972712023032216	PASS
serial_test	0.0	FAIL
approximate_entropy_test	0.0	FAIL
cumulative_sums_test	0.0	FAIL
random_excursion_test	1.5580586817350368e-09	FAIL
random_excursion_variant_test	0.030030509583329566	PASS

Source: By the author.

Table 23 – Results for the SP800-22 Rev. 1 tests on the k-logistic map (base 2), $k = 5$, $r \sim 4$.

NIST test	p-value	result
monobit_test	9.176227605259399e-41	FAIL
frequency_within_block_test	1.6578377990919188e-20	FAIL
runs_test	0.0	FAIL
longest_run_ones_in_a_block_test	4.182049324089779e-31	FAIL
binary_matrix_rank_test	0.0001710996768343542	FAIL
dft_test	4.972895358937442e-09	FAIL
non_overlapping_template_matching_test	0.99710647113403	PASS
overlapping_template_matching_test	6.847940135893526e-87	FAIL
maurers_universal_test	0.0	FAIL
linear_complexity_test	0.09150783433635766	PASS
serial_test	0.0	FAIL
approximate_entropy_test	0.0	FAIL
cumulative_sums_test	0.0	FAIL
random_excursion_test	0.06654930782449124	PASS
random_excursion_variant_test	0.043383782537769144	PASS

Source: By the author.

Table 24 – Results for the SP800-22 Rev. 1 tests on the k-logistic map (base 2), $k = 10$, $r \sim 4$.

NIST test	p-value	result
monobit_test	3.302106437084046e-39	FAIL
frequency_within_block_test	1.5705675235174104e-18	FAIL
runs_test	0.0	FAIL
longest_run_ones_in_a_block_test	6.016442359041556e-17	FAIL
binary_matrix_rank_test	0.6249432078831807	PASS
dft_test	0.3431274192315742	PASS
non_overlapping_template_matching_test	0.998351387710893	PASS
overlapping_template_matching_test	1.4967210165057915e-07	FAIL
maurers_universal_test	4.3354492321367287e-218	FAIL
linear_complexity_test	0.6409650680235172	PASS
serial_test	1.024091266631848e-266	FAIL
approximate_entropy_test	4.542233051057409e-264	FAIL
cumulative_sums_test	0.0	FAIL
random_excursion_test	0.000247681075586224	FAIL
random_excursion_variant_test	0.018117131435231654	PASS

Source: By the author.

Table 25 – Results for the SP800-22 Rev. 1 tests on the k-logistic map (base 2), $k = 15$, $r \sim 4$.

NIST test	p-value	result
monobit_test	0.0006416764336790679	FAIL
frequency_within_block_test	0.40503431927538897	PASS
runs_test	0.030342291562359576	PASS
longest_run_ones_in_a_block_test	0.6403128801292115	PASS
binary_matrix_rank_test	0.43867733360125044	PASS
dft_test	0.6144332929130587	PASS
non_overlapping_template_matching_test	1.0133848011662423	PASS
overlapping_template_matching_test	0.4773467764994301	PASS
maurers_universal_test	4.5791965993733364e-07	FAIL
linear_complexity_test	0.7421067354675733	PASS
serial_test	0.0010925226361813438	FAIL
approximate_entropy_test	0.010092169290521339	FAIL
cumulative_sums_test	0.0006047372242032889	FAIL
random_excursion_test	0.04424005463282892	PASS
random_excursion_variant_test	0.053015150095932696	PASS

Source: By the author.

Table 26 – Results for the SP800-22 Rev. 1 tests on the k-logistic map (base 2), $k = 20$, $r \sim 4$.

NIST test	p-value	result
monobit_test	0.3420587587680123	PASS
frequency_within_block_test	0.9876712206261564	PASS
runs_test	0.4699413414650103	PASS
longest_run_ones_in_a_block_test	0.48086487308929565	PASS
binary_matrix_rank_test	0.6215989225728945	PASS
dft_test	0.4343347635639268	PASS
non_overlapping_template_matching_test	0.9295933666036253	PASS
overlapping_template_matching_test	0.8478998861474993	PASS
maurers_universal_test	0.8720733227307572	PASS
linear_complexity_test	0.6228006913968536	PASS
serial_test	0.7520820448253139	PASS
approximate_entropy_test	0.8699776998998009	PASS
cumulative_sums_test	0.23836391812798374	PASS
random_excursion_test	0.0477906869404608	PASS
random_excursion_variant_test	0.18620167167153337	PASS

Source: By the author.

Table 27 – Results for the SP800-22 Rev. 1 tests on the k-logistic map (base 2), $k = 25$, $r \sim 4$.

NIST test	p-value	result
monobit_test	0.5818094909803402	PASS
frequency_within_block_test	0.47663515051129085	PASS
runs_test	0.7530284155277838	PASS
longest_run_ones_in_a_block_test	0.7109509623095214	PASS
binary_matrix_rank_test	0.33002772626488786	PASS
dft_test	0.7786198431222331	PASS
non_overlapping_template_matching_test	1.003443692587977	PASS
overlapping_template_matching_test	0.5880256112005683	PASS
maurers_universal_test	0.1723861937396658	PASS
linear_complexity_test	0.6480947604926023	PASS
serial_test	0.4666428059552852	PASS
approximate_entropy_test	0.7944133524617399	PASS
cumulative_sums_test	0.631399425016614	PASS
random_excursion_test	0.1870209278743739	PASS
random_excursion_variant_test	0.14898297980928107	PASS

Source: By the author.

Table 28 – Results for the SP800-22 Rev. 1 tests on the k-logistic map (base 2), $k = 30$, $r \sim 4$.

NIST test	p-value	result
monobit_test	0.44910437680772725	PASS
frequency_within_block_test	0.44881335466065825	PASS
runs_test	0.5745162829980621	PASS
longest_run_ones_in_a_block_test	0.1853092436890685	PASS
binary_matrix_rank_test	0.9848833193802344	PASS
dft_test	0.5887208644655226	PASS
non_overlapping_template_matching_test	0.9998043301032872	PASS
overlapping_template_matching_test	0.4485708511288196	PASS
maurers_universal_test	0.20167117003579957	PASS
linear_complexity_test	0.34064974482925486	PASS
serial_test	0.798798634779099	PASS
approximate_entropy_test	0.9020460248579646	PASS
cumulative_sums_test	0.7134393489475217	PASS
random_excursion_test	0.030857144395142543	PASS
random_excursion_variant_test	0.08448401495056913	PASS

Source: By the author.

Table 29 – Results for the SP800-22 Rev. 1 tests on eight k-logistic maps (base 2), $k = 0$, $r \sim 4$.

NIST test	p-value	result
monobit_test	1.9236879166074266e-44	FAIL
frequency_within_block_test	5.940154582683162e-32	FAIL
runs_test	0.0	FAIL
longest_run_ones_in_a_block_test	2.322518376989553e-175	FAIL
binary_matrix_rank_test	0.22156453917451643	PASS
dft_test	0.0	FAIL
non_overlapping_template_matching_test	0.9999947131760454	PASS
overlapping_template_matching_test	0.0	FAIL
maurers_universal_test	0.0	FAIL
linear_complexity_test	0.5285615712167111	PASS
serial_test	0.0	FAIL
approximate_entropy_test	0.0	FAIL
cumulative_sums_test	0.0	FAIL
random_excursion_test	9.879169286439331e-20	FAIL
random_excursion_variant_test	0.35029775729363855	PASS

Source: By the author.

Table 30 – Results for the SP800-22 Rev. 1 tests on eight k-logistic maps (base 2), $k = 5$, $r \sim 4$.

NIST test	p-value	result
monobit_test	5.224325179211946e-42	FAIL
frequency_within_block_test	1.7487934611460903e-22	FAIL
runs_test	0.0	FAIL
longest_run_ones_in_a_block_test	4.311415888165863e-32	FAIL
binary_matrix_rank_test	0.8553789321995459	PASS
dft_test	9.140785945851863e-13	FAIL
non_overlapping_template_matching_test	1.0000004374452784	PASS
overlapping_template_matching_test	2.6180227290751655e-109	FAIL
maurers_universal_test	9.229295726733283e-143	FAIL
linear_complexity_test	0.6808626494811644	PASS
serial_test	0.0	FAIL
approximate_entropy_test	0.0	FAIL
cumulative_sums_test	0.0	FAIL
random_excursion_test	0.32497235698354915	PASS
random_excursion_variant_test	0.21251033577373268	PASS

Source: By the author.

Table 31 – Results for the SP800-22 Rev. 1 tests on eight k-logistic maps (base 2), $k = 10$, $r \sim 4$.

NIST test	p-value	result
monobit_test	2.9029133237398203e-22	FAIL
frequency_within_block_test	1.009721298709369e-10	FAIL
runs_test	0.0	FAIL
longest_run_ones_in_a_block_test	0.5103356009303526	PASS
binary_matrix_rank_test	0.19014056367201881	PASS
dft_test	0.4253434920213056	PASS
non_overlapping_template_matching_test	1.0000094963731496	PASS
overlapping_template_matching_test	0.005047228744379414	FAIL
maurers_universal_test	0.13583866551989054	PASS
linear_complexity_test	0.06477016117298422	PASS
serial_test	0.0	FAIL
approximate_entropy_test	0.0	FAIL
cumulative_sums_test	0.0	FAIL
random_excursion_test	0.34117964932055617	PASS
random_excursion_variant_test	0.14330779839421232	PASS

Source: By the author.

Table 32 – Results for the SP800-22 Rev. 1 tests on eight k-logistic maps (base 2), $k = 15$, $r \sim 4$.

NIST test	p-value	result
monobit_test	0.00034219929621498614	FAIL
frequency_within_block_test	0.17630701538280963	PASS
runs_test	0.6187260433463151	PASS
longest_run_ones_in_a_block_test	0.8051820618599712	PASS
binary_matrix_rank_test	0.46410830583671653	PASS
dft_test	0.9020141311151602	PASS
non_overlapping_template_matching_test	0.9997386988804778	PASS
overlapping_template_matching_test	0.49721500830586424	PASS
maurers_universal_test	0.48232908726770024	PASS
linear_complexity_test	0.24579211162515333	PASS
serial_test	0.011850877677044675	PASS
approximate_entropy_test	0.011834206712466036	PASS
cumulative_sums_test	0.0002780185579982497	FAIL
random_excursion_test	0.04741825997673954	PASS
random_excursion_variant_test	0.2155581682390581	PASS

Source: By the author.

Table 33 – Results for the SP800-22 Rev. 1 tests on eight k-logistic maps (base 2), $k = 20$, $r \sim 4$.

NIST test	p-value	result
monobit_test	0.5261295920589557	PASS
frequency_within_block_test	0.2676672787579463	PASS
runs_test	0.11112575706202862	PASS
longest_run_ones_in_a_block_test	0.4297670595931066	PASS
binary_matrix_rank_test	0.4254708787016212	PASS
dft_test	0.7668423540581595	PASS
non_overlapping_template_matching_test	1.035339370190724	PASS
overlapping_template_matching_test	0.5996612121299701	PASS
maurers_universal_test	0.607051019099476	PASS
linear_complexity_test	0.96817792289452	PASS
serial_test	0.23846171012026143	PASS
approximate_entropy_test	0.2385242705732872	PASS
cumulative_sums_test	0.6014750975045908	PASS
random_excursion_test	0.5020093765535916	PASS
random_excursion_variant_test	0.3211016358872025	PASS

Source: By the author.

Table 34 – Results for the SP800-22 Rev. 1 tests on eight k-logistic maps (base 2), $k = 25$, $r \sim 4$.

NIST test	p-value	result
monobit_test	0.07612120740226914	PASS
frequency_within_block_test	0.2736156564277943	PASS
runs_test	0.25952225939092777	PASS
longest_run_ones_in_a_block_test	0.15056812485973037	PASS
binary_matrix_rank_test	0.25653848046671945	PASS
dft_test	0.6108326505633858	PASS
non_overlapping_template_matching_test	1.00897736023073	PASS
overlapping_template_matching_test	0.5140736326029121	PASS
maurers_universal_test	0.38303741797402857	PASS
linear_complexity_test	0.6034944410578652	PASS
serial_test	0.08014313050616924	PASS
approximate_entropy_test	0.0800569324917207	PASS
cumulative_sums_test	0.061090273170142595	PASS
random_excursion_test	0.3044760258466065	PASS
random_excursion_variant_test	0.26174124619035677	PASS

Source: By the author.

Table 35 – Results for the SP800-22 Rev. 1 tests on eight k-logistic maps (base 2), $k = 30$, $r \sim 4$.

NIST test	p-value	result
monobit_test	0.24230697139445445	PASS
frequency_within_block_test	0.5875893423724292	PASS
runs_test	0.09221453270074537	PASS
longest_run_ones_in_a_block_test	0.6741184439088131	PASS
binary_matrix_rank_test	0.38242319380582573	PASS
dft_test	0.20807532681356897	PASS
non_overlapping_template_matching_test	0.6419132735095406	PASS
overlapping_template_matching_test	0.17125607761878903	PASS
maurers_universal_test	0.3673235180195126	PASS
linear_complexity_test	0.5813789354767293	PASS
serial_test	0.499800100300948	PASS
approximate_entropy_test	0.4997572051159123	PASS
cumulative_sums_test	0.3284233871231679	PASS
random_excursion_test	0.1050771368059274	PASS
random_excursion_variant_test	0.301186031333336	PASS

Source: By the author.

Table 36 – Results for the SP800-22 Rev. 1 tests on the composition of k-logistic map (base 2) and LFSR, $k = 0$, $r \sim 4$.

NIST test	p-value	result
monobit_test	3.619449494211668e-53	FAIL
frequency_within_block_test	1.9757890751008757e-28	FAIL
runs_test	0.0	FAIL
longest_run_ones_in_a_block_test	0.6507455747501423	PASS
binary_matrix_rank_test	0.5676337464716236	PASS
dft_test	0.7011890238950875	PASS
non_overlapping_template_matching_test	1.0229292693353715	PASS
overlapping_template_matching_test	0.8343946583293789	PASS
maurers_universal_test	0.6523854126525218	PASS
linear_complexity_test	0.12065817304030364	PASS
serial_test	1.58321071474897e-229	FAIL
approximate_entropy_test	4.838500184604797e-232	FAIL
cumulative_sums_test	0.0	FAIL
random_excursion_test	0.10812006712273357	PASS
random_excursion_variant_test	0.04783853310152687	PASS

Source: By the author.

Table 37 – Results for the SP800-22 Rev. 1 tests on the composition of k-logistic map (base 2) and LFSR, $k = 5$, $r \sim 4$.

NIST test	p-value	result
monobit_test	1.9541560442563856e-44	FAIL
frequency_within_block_test	5.364501279657009e-19	FAIL
runs_test	0.0	FAIL
longest_run_ones_in_a_block_test	0.16556042566593554	PASS
binary_matrix_rank_test	0.05111395869507869	PASS
dft_test	0.1756434208875754	PASS
non_overlapping_template_matching_test	1.016356427185101	PASS
overlapping_template_matching_test	0.04635706079361955	PASS
maurers_universal_test	0.8717520015748969	PASS
linear_complexity_test	0.20397695104523345	PASS
serial_test	2.4562304767176107e-157	FAIL
approximate_entropy_test	9.604642291816074e-159	FAIL
cumulative_sums_test	0.0	FAIL
random_excursion_test	0.09474597962620576	PASS
random_excursion_variant_test	0.07666538365048903	PASS

Source: By the author.

Table 38 – Results for the SP800-22 Rev. 1 tests on the composition of k-logistic map (base 2) and LFSR, $k = 10$, $r \sim 4$.

NIST test	p-value	result
monobit_test	2.845368819923513e-23	FAIL
frequency_within_block_test	1.9530847050864257e-11	FAIL
runs_test	0.0	FAIL
longest_run_ones_in_a_block_test	0.49835692405572674	PASS
binary_matrix_rank_test	0.6445333485175885	PASS
dft_test	0.8914615010116311	PASS
non_overlapping_template_matching_test	1.0005220132233799	PASS
overlapping_template_matching_test	0.6968462105804429	PASS
maurers_universal_test	0.09909306383184191	PASS
linear_complexity_test	0.017422208762384383	PASS
serial_test	6.7298909609988065e-43	FAIL
approximate_entropy_test	4.698923701928685e-43	FAIL
cumulative_sums_test	0.0	FAIL
random_excursion_test	0.12723108330461327	PASS
random_excursion_variant_test	0.018491814238434916	PASS

Source: By the author.

Table 39 – Results for the SP800-22 Rev. 1 tests on the composition of k-logistic map (base 2) and LFSR, $k = 15$, $r \sim 4$.

NIST test	p-value	result
monobit_test	0.018521370152336545	PASS
frequency_within_block_test	0.4274497400158695	PASS
runs_test	4.441339947774052e-05	FAIL
longest_run_ones_in_a_block_test	0.3409248070539498	PASS
binary_matrix_rank_test	0.6695332331542784	PASS
dft_test	0.1822786366693676	PASS
non_overlapping_template_matching_test	0.9914710158400607	PASS
overlapping_template_matching_test	0.969486934362284	PASS
maurers_universal_test	0.6468006215368085	PASS
linear_complexity_test	0.4615916314810023	PASS
serial_test	0.001266034499334617	FAIL
approximate_entropy_test	0.0012660687106366651	FAIL
cumulative_sums_test	0.010521671891545736	PASS
random_excursion_test	0.005270891666712246	FAIL
random_excursion_variant_test	0.08831004568676523	PASS

Source: By the author.

Table 40 – Results for the SP800-22 Rev. 1 tests on the composition of k-logistic map (base 2) and LFSR, $k = 20$, $r \sim 4$.

NIST test	p-value	result
monobit_test	0.02364180549732688	PASS
frequency_within_block_test	0.4693010745871361	PASS
runs_test	0.2251418071347988	PASS
longest_run_ones_in_a_block_test	0.8130247241694208	PASS
binary_matrix_rank_test	0.33857984509320666	PASS
dft_test	0.7967769408641836	PASS
non_overlapping_template_matching_test	0.6499963329935932	PASS
overlapping_template_matching_test	0.4843471339345114	PASS
maurers_universal_test	0.8990869379854897	PASS
linear_complexity_test	0.5464084251813275	PASS
serial_test	0.1979086569485854	PASS
approximate_entropy_test	0.19791073372902082	PASS
cumulative_sums_test	0.03189228706970848	PASS
random_excursion_test	0.1968478849087879	PASS
random_excursion_variant_test	0.4047339749643348	PASS

Source: By the author.

Table 41 – Results for the SP800-22 Rev. 1 tests on the composition of k-logistic map (base 2) and LFSR, $k = 25$, $r \sim 4$.

NIST test	p-value	result
monobit_test	0.4282213996291674	PASS
frequency_within_block_test	0.769575730920922	PASS
runs_test	0.07953833050981193	PASS
longest_run_ones_in_a_block_test	0.39834964676691764	PASS
binary_matrix_rank_test	0.7719115918348235	PASS
dft_test	0.02497671317945234	PASS
non_overlapping_template_matching_test	0.9992486219371063	PASS
overlapping_template_matching_test	0.4206893220979453	PASS
maurers_universal_test	0.09879451849144369	PASS
linear_complexity_test	0.8797406512437945	PASS
serial_test	0.6801395384808412	PASS
approximate_entropy_test	0.6802238358982927	PASS
cumulative_sums_test	0.5185226092203554	PASS
random_excursion_test	0.2713374352040706	PASS
random_excursion_variant_test	0.29422233637909956	PASS

Source: By the author.

Table 42 – Results for the SP800-22 Rev. 1 tests on the composition of k-logistic map (base 2) and LFSR, $k = 30$, $r \sim 4$.

NIST test	p-value	result
monobit_test	0.9069025639941026	PASS
frequency_within_block_test	0.4115441509004894	PASS
runs_test	0.5169758765519051	PASS
longest_run_ones_in_a_block_test	0.02391417264384779	PASS
binary_matrix_rank_test	0.04162072257297781	PASS
dft_test	0.37593051724786886	PASS
non_overlapping_template_matching_test	1.0043519542806818	PASS
overlapping_template_matching_test	0.5107804883258552	PASS
maurers_universal_test	0.6328983670430154	PASS
linear_complexity_test	0.3818133858711697	PASS
serial_test	0.622426308931932	PASS
approximate_entropy_test	0.7511341248386715	PASS
cumulative_sums_test	0.5727834526750604	PASS
random_excursion_test	0.12768400771070418	PASS
random_excursion_variant_test	0.30931501762191027	PASS

Source: By the author.

Table 43 – Results for the SP800-22 Rev. 1 tests on the composition of eight k-logistic maps (base 2) and LFSR, $k = 0$, $r \sim 4$.

NIST test	p-value	result
monobit_test	6.127618556527771e-43	FAIL
frequency_within_block_test	1.958839275937847e-21	FAIL
runs_test	0.0	FAIL
longest_run_ones_in_a_block_test	0.3463059565448864	PASS
binary_matrix_rank_test	0.39774383829387666	PASS
dft_test	0.005360945360539859	FAIL
non_overlapping_template_matching_test	1.0013100345640316	PASS
overlapping_template_matching_test	0.416853795674755	PASS
maurers_universal_test	0.5642137003150811	PASS
linear_complexity_test	0.3897516414261191	PASS
serial_test	2.93342965523939e-37	FAIL
approximate_entropy_test	2.959710114894473e-37	FAIL
cumulative_sums_test	0.0	FAIL
random_excursion_test	0.2122984152399528	PASS
random_excursion_variant_test	0.02121134866552893	PASS

Source: By the author.

Table 44 – Results for the SP800-22 Rev. 1 tests on the composition of eight k-logistic maps (base 2) and LFSR, $k = 5$, $r \sim 4$.

NIST test	p-value	result
monobit_test	8.915404928109522e-34	FAIL
frequency_within_block_test	8.332840305450766e-14	FAIL
runs_test	0.0	FAIL
longest_run_ones_in_a_block_test	0.9253916840917283	PASS
binary_matrix_rank_test	0.5927944841054639	PASS
dft_test	0.029471162927216275	PASS
non_overlapping_template_matching_test	0.10341350012704421	PASS
overlapping_template_matching_test	0.9775534342456327	PASS
maurers_universal_test	0.9016229276934482	PASS
linear_complexity_test	0.4681574740206957	PASS
serial_test	1.9490950370091873e-29	FAIL
approximate_entropy_test	1.8690832960856065e-29	FAIL
cumulative_sums_test	0.0	FAIL
random_excursion_test	0.0002636085097975721	FAIL
random_excursion_variant_test	0.0034956728980962254	FAIL

Source: By the author.

Table 45 – Results for the SP800-22 Rev. 1 tests on the composition of eight k-logistic maps (base 2) and LFSR, $k = 10$, $r \sim 4$.

NIST test	p-value	result
monobit_test	8.844665040682314e-27	FAIL
frequency_within_block_test	2.179543243928932e-06	FAIL
runs_test	0.0	FAIL
longest_run_ones_in_a_block_test	0.1161460739142732	PASS
binary_matrix_rank_test	0.7237352490176504	PASS
dft_test	0.1058908265259405	PASS
non_overlapping_template_matching_test	1.00003312131871	PASS
overlapping_template_matching_test	0.2575436199059855	PASS
maurers_universal_test	0.6948343119911653	PASS
linear_complexity_test	0.270008843263696	PASS
serial_test	1.149683089334974e-21	FAIL
approximate_entropy_test	1.1512019089750539e-21	FAIL
cumulative_sums_test	0.0	FAIL
random_excursion_test	0.2955428889632254	PASS
random_excursion_variant_test	0.0029456735994761053	FAIL

Source: By the author.

Table 46 – Results for the SP800-22 Rev. 1 tests on the composition of eight k-logistic maps (base 2) and LFSR, $k = 15$, $r \sim 4$.

NIST test	p-value	result
monobit_test	0.003959163662387468	FAIL
frequency_within_block_test	0.1558001532211176	PASS
runs_test	0.9431077493460726	PASS
longest_run_ones_in_a_block_test	0.6923701550798846	PASS
binary_matrix_rank_test	0.870030931199496	PASS
dft_test	0.0820289045012617	PASS
non_overlapping_template_matching_test	0.6338484587274295	PASS
overlapping_template_matching_test	0.9613766280526963	PASS
maurers_universal_test	0.330931470262244	PASS
linear_complexity_test	0.723015328732378	PASS
serial_test	0.1632635308880512	PASS
approximate_entropy_test	0.16325916029090892	PASS
cumulative_sums_test	0.007135597170982777	FAIL
random_excursion_test	0.0105451906096164	PASS
random_excursion_variant_test	0.03066516454427745	PASS

Source: By the author.

Table 47 – Results for the SP800-22 Rev. 1 tests on the composition of eight k-logistic maps (base 2) and LFSR, $k = 20$, $r \sim 4$.

NIST test	p-value	result
monobit_test	0.21082371788418128	PASS
frequency_within_block_test	0.9445647472828872	PASS
runs_test	0.7858290063100128	PASS
longest_run_ones_in_a_block_test	0.805820297326962	PASS
binary_matrix_rank_test	0.685661520684859	PASS
dft_test	0.07472894801620793	PASS
non_overlapping_template_matching_test	0.9031213586131517	PASS
overlapping_template_matching_test	0.5878937296323016	PASS
maurers_universal_test	0.3168395601298556	PASS
linear_complexity_test	0.7869443481381304	PASS
serial_test	0.1852515771335178	PASS
approximate_entropy_test	0.24819958607502093	PASS
cumulative_sums_test	0.266660269417472	PASS
random_excursion_test	0.25072168548831053	PASS
random_excursion_variant_test	0.051536252807687914	PASS

Source: By the author.

Table 48 – Results for the SP800-22 Rev. 1 tests on the composition of eight k-logistic maps (base 2) and LFSR, $k = 25$, $r \sim 4$.

NIST test	p-value	result
monobit_test	0.7803693988038884	PASS
frequency_within_block_test	0.6644485056210444	PASS
runs_test	0.14591201393769954	PASS
longest_run_ones_in_a_block_test	0.743387771308943	PASS
binary_matrix_rank_test	0.5662080397822106	PASS
dft_test	0.5035351016627687	PASS
non_overlapping_template_matching_test	1.001156770796747	PASS
overlapping_template_matching_test	0.07008880711274676	PASS
maurers_universal_test	0.5580912986830577	PASS
linear_complexity_test	0.2903673989927815	PASS
serial_test	0.29462991024972146	PASS
approximate_entropy_test	0.29469898410341205	PASS
cumulative_sums_test	0.6976870863022167	PASS
random_excursion_test	0.009565069257363794	FAIL
random_excursion_variant_test	0.09178656884278973	PASS

Source: By the author.

Table 49 – Results for the SP800-22 Rev. 1 tests on the composition of eight k-logistic maps (base 2) and LFSR, $k = 30$, $r \sim 4$.

NIST test	p-value	result
monobit_test	0.47926083957297844	PASS
frequency_within_block_test	0.20684305332889918	PASS
runs_test	0.6213828384486311	PASS
longest_run_ones_in_a_block_test	0.1839086594409937	PASS
binary_matrix_rank_test	0.9548471032107839	PASS
dft_test	0.4135257994617516	PASS
non_overlapping_template_matching_test	1.0005246835042152	PASS
overlapping_template_matching_test	0.9549396563835839	PASS
maurers_universal_test	0.6338691419039044	PASS
linear_complexity_test	0.32528091991284636	PASS
serial_test	0.46510978522122787	PASS
approximate_entropy_test	0.46499289049322495	PASS
cumulative_sums_test	0.33373752708106097	PASS
random_excursion_test	0.039857802950306234	PASS
random_excursion_variant_test	0.28417865770324124	PASS

Source: By the author.

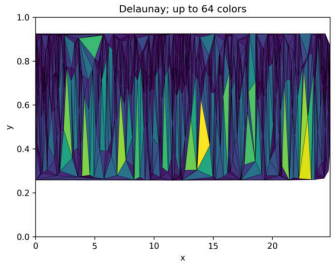

“k-logistic map with $k = 0$, 1”

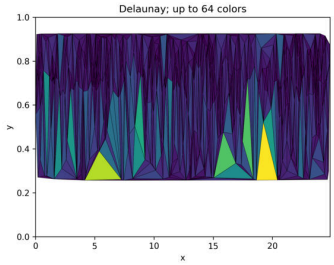

“k-logistic map with $k = 0$, 2”

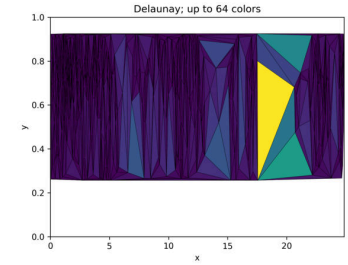

“k-logistic map with $k = 0$, 3”

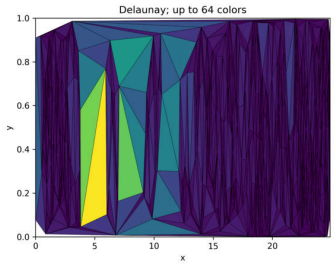

“k-logistic map with $k = 1$, 1”

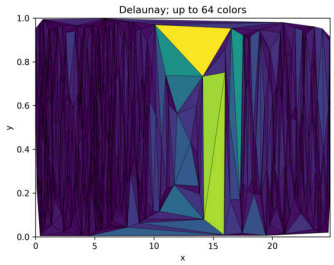

“k-logistic map with $k = 1$, 2”

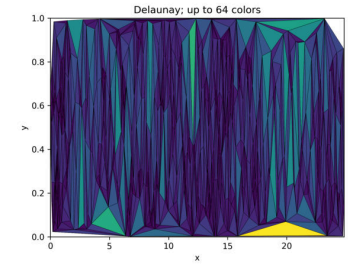

“k-logistic map with $k = 1$, 3”

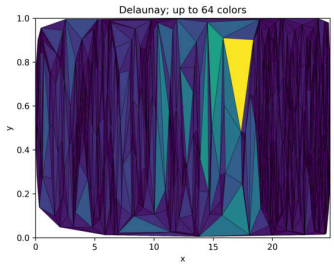

“k-logistic map with $k = 2$, 1”

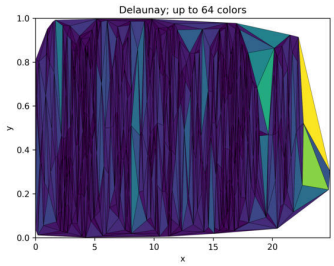

“k-logistic map with $k = 2$, 2”

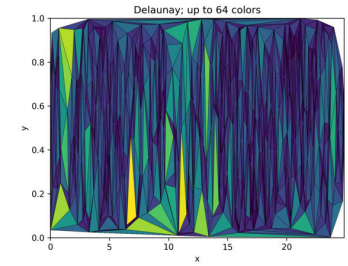

“k-logistic map with $k = 2$, 3”

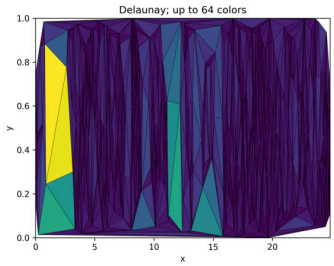

“k-logistic map with $k = 3$, 1”

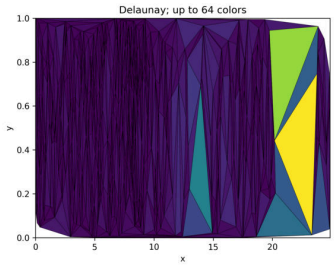

“k-logistic map with $k = 3$, 2”

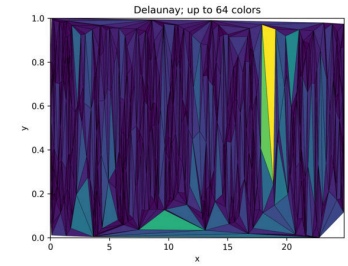

“k-logistic map with $k = 3$, 3”

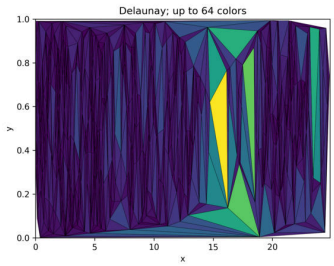

“k-logistic map with $k = 4$, 1”

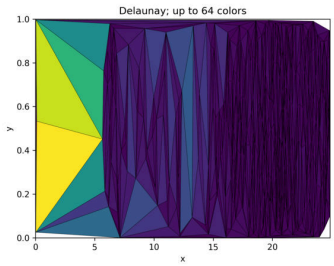

“k-logistic map with $k = 4$, 2”

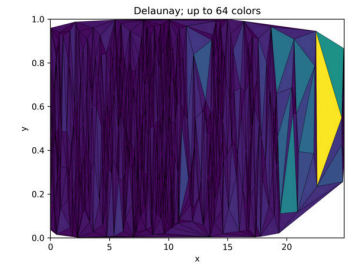

“k-logistic map with $k = 4$, 3”

Figure 139 – Delaunay triangulations of baseline complex networks for networks with 5,000 vertices, k-logistic map from $k = 0$ to $k = 4$, $r = 3.7$.
Source: By the author.

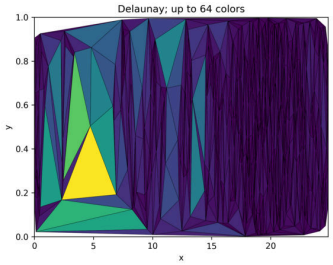

“k-logistic map with $k = 5$, 1”

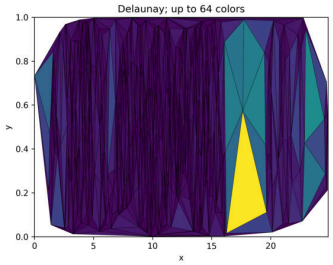

“k-logistic map with $k = 5$, 2”

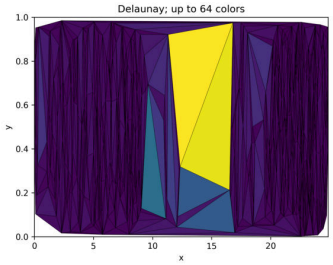

“k-logistic map with $k = 5$, 3”

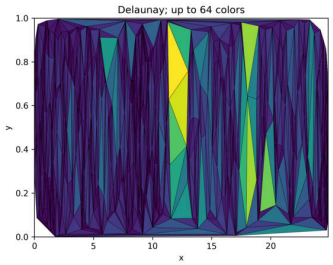

“k-logistic map with $k = 6$, 1”

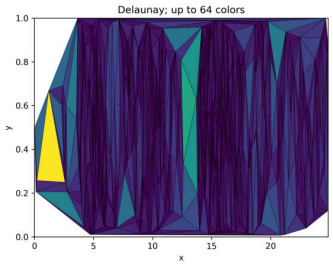

“k-logistic map with $k = 6$, 2”

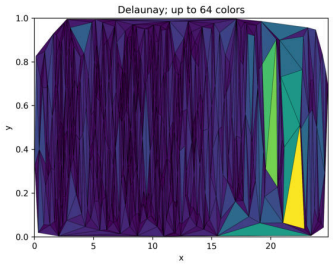

“k-logistic map with $k = 6$, 3”

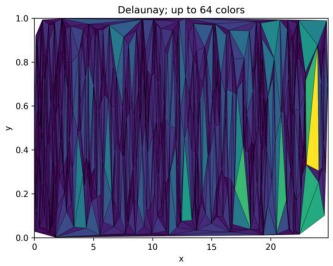

“k-logistic map with $k = 7$, 1”

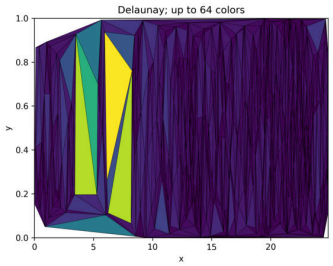

“k-logistic map with $k = 7$, 2”

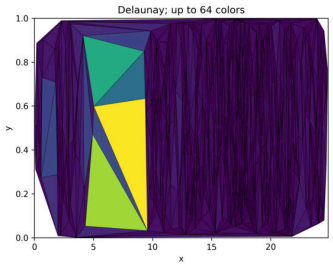

“k-logistic map with $k = 7$, 3”

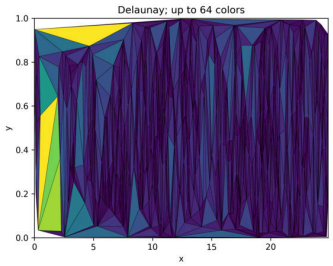

“k-logistic map with $k = 8$, 1”

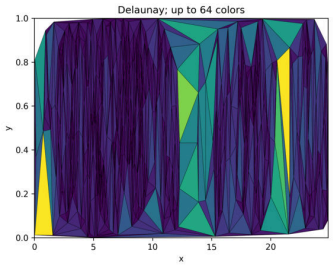

“k-logistic map with $k = 8$, 2”

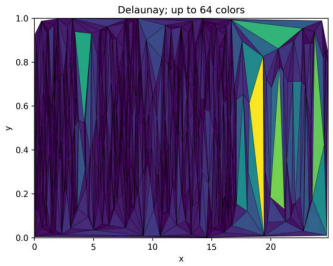

“k-logistic map with $k = 8$, 3”

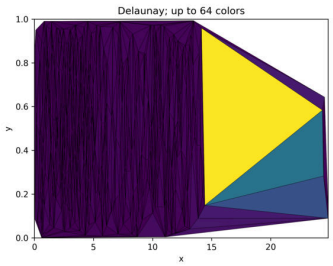

“k-logistic map with $k = 9$, 1”

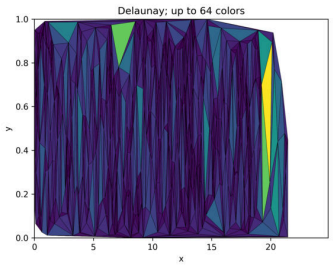

“k-logistic map with $k = 9$, 2”

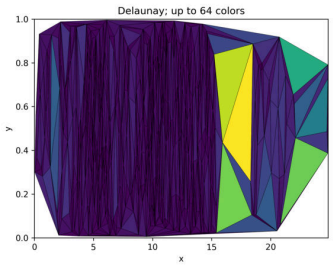

“k-logistic map with $k = 9$, 3”

Figure 140 – Delaunay triangulations of baseline complex networks for networks with 5,000 vertices, k-logistic map from $k = 5$ to $k = 9$, $r = 3.7$.
Source: By the author.

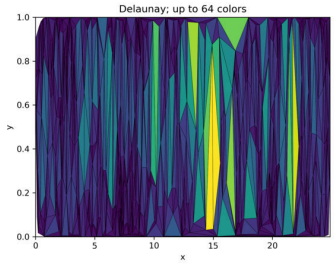

“k-logistic map with $k = 0$, 1”

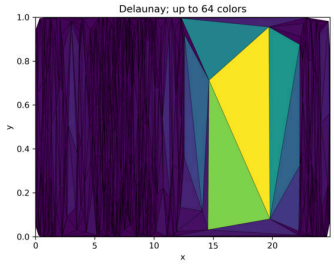

“k-logistic map with $k = 0$, 2”

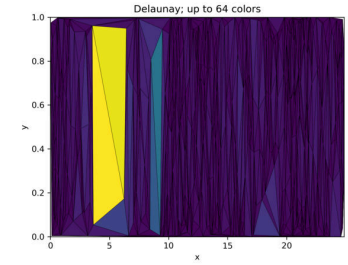

“k-logistic map with $k = 0$, 3”

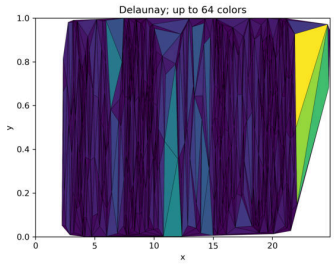

“k-logistic map with $k = 1$, 1”

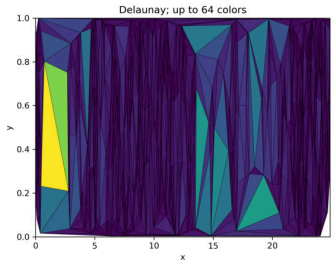

“k-logistic map with $k = 1$, 2”

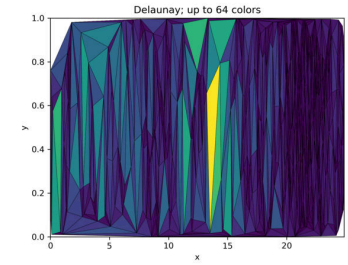

“k-logistic map with $k = 1$, 3”

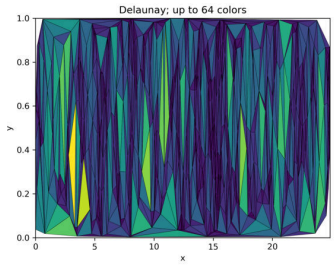

“k-logistic map with $k = 2$, 1”

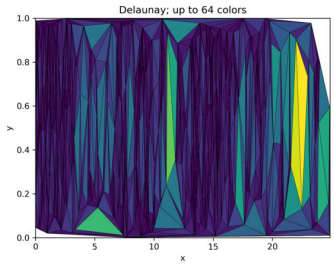

“k-logistic map with $k = 2$, 2”

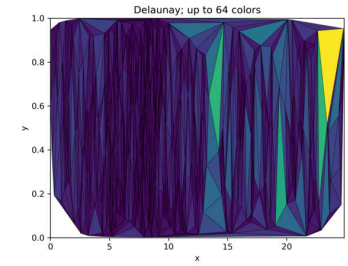

“k-logistic map with $k = 2$, 3”

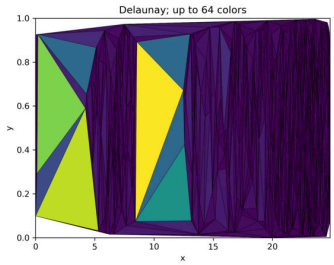

“k-logistic map with $k = 3$, 1”

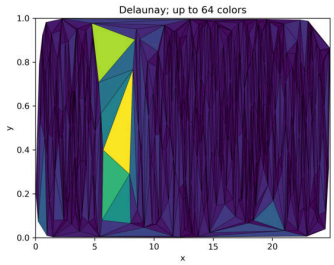

“k-logistic map with $k = 3$, 2”

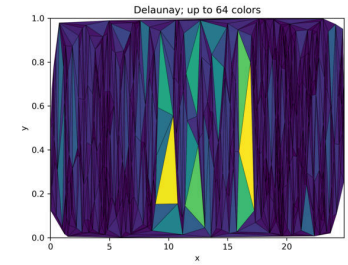

“k-logistic map with $k = 3$, 3”

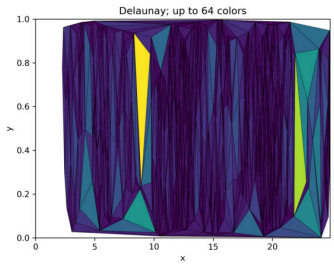

“k-logistic map with $k = 4$, 1”

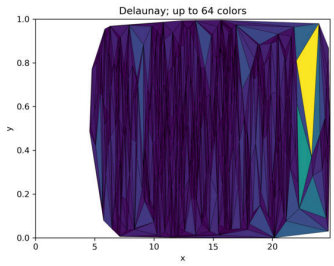

“k-logistic map with $k = 4$, 2”

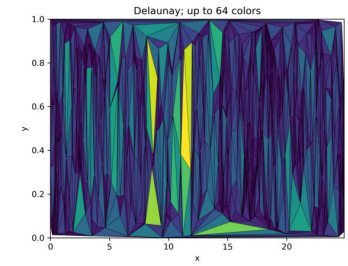

“k-logistic map with $k = 4$, 3”

Figure 141 – Delaunay triangulations of baseline complex networks for networks with 5,000 vertices, k-logistic map from $k = 0$ to $k = 4$, $r = 3.99999$.
Source: By the author.

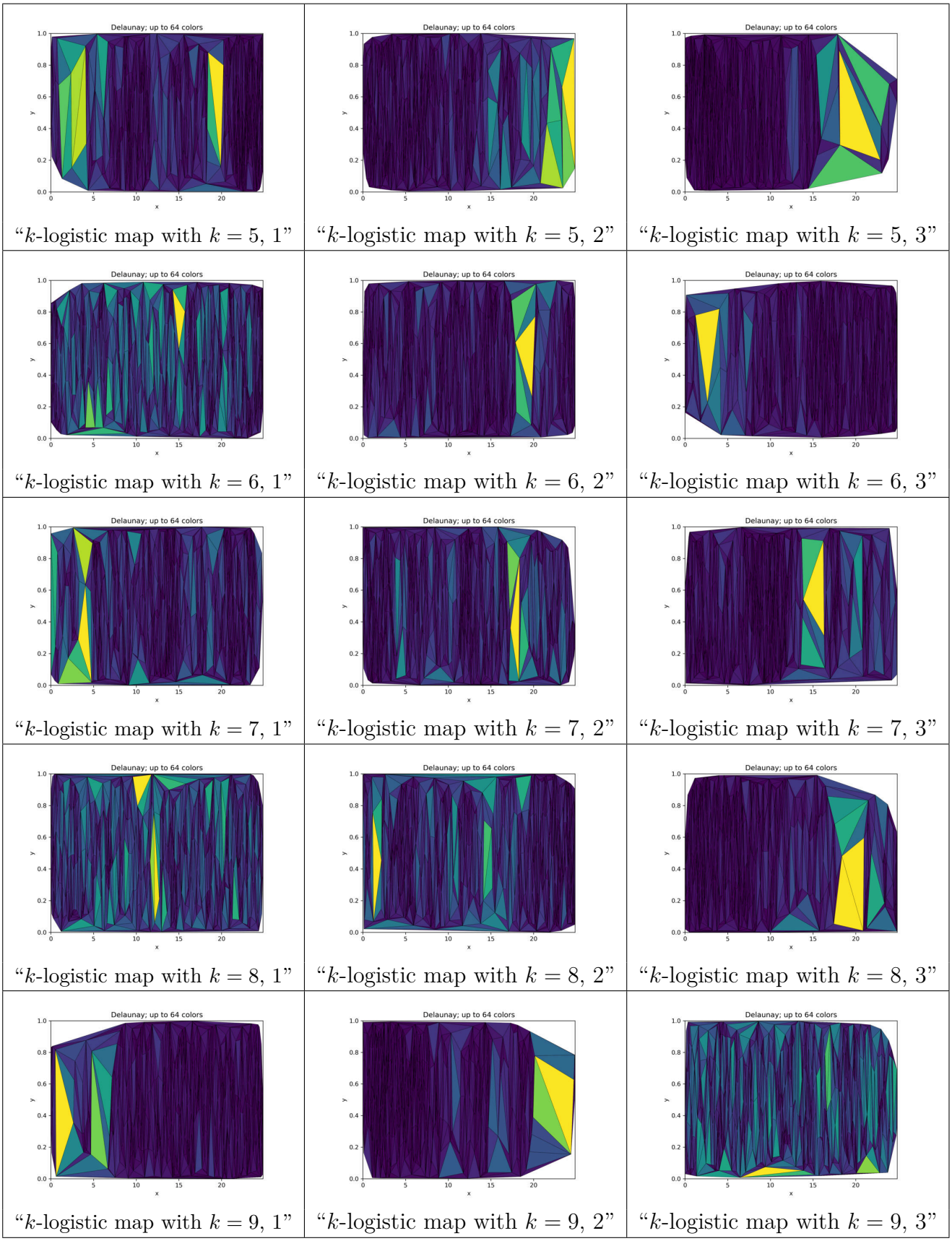

“k-logistic map with $k = 5$, 1” “k-logistic map with $k = 5$, 2” “k-logistic map with $k = 5$, 3”

“k-logistic map with $k = 6$, 1” “k-logistic map with $k = 6$, 2” “k-logistic map with $k = 6$, 3”

“k-logistic map with $k = 7$, 1” “k-logistic map with $k = 7$, 2” “k-logistic map with $k = 7$, 3”

“k-logistic map with $k = 8$, 1” “k-logistic map with $k = 8$, 2” “k-logistic map with $k = 8$, 3”

“k-logistic map with $k = 9$, 1” “k-logistic map with $k = 9$, 2” “k-logistic map with $k = 9$, 3”

Figure 142 – Delaunay triangulations of baseline complex networks for networks with 5,000 vertices, k-logistic map from $k = 5$ to $k = 9$, $r = 3.99999$.
Source: By the author.

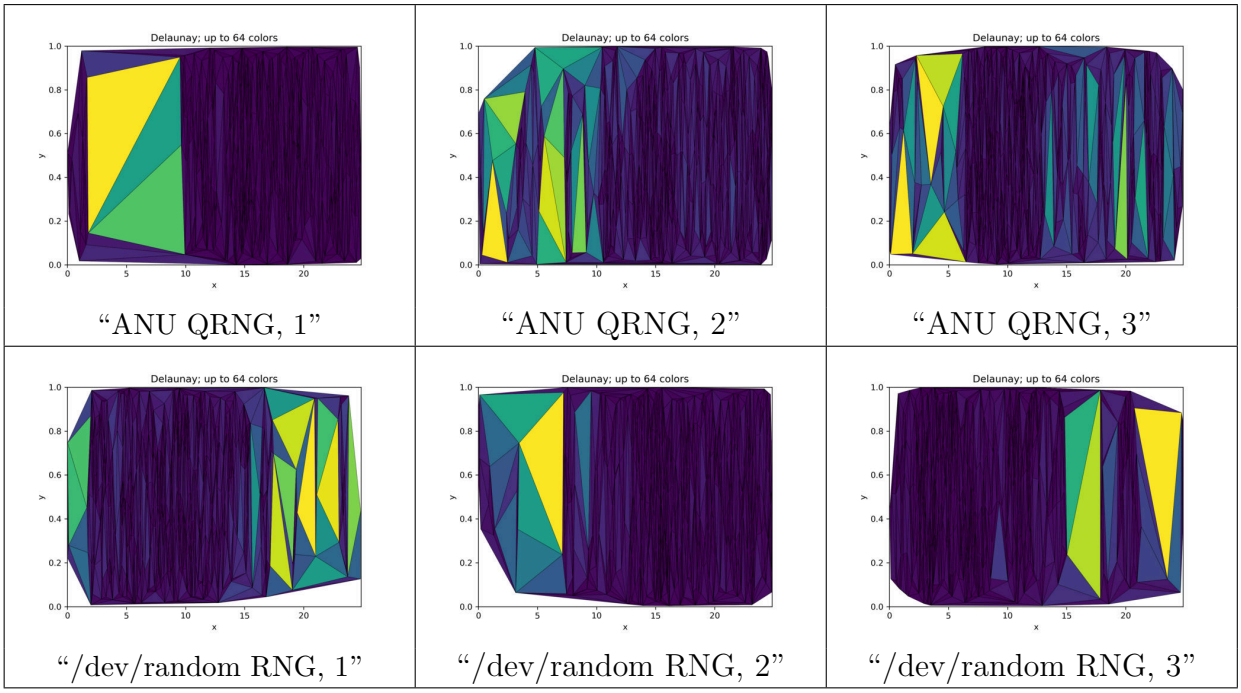

Figure 143 – Delaunay triangulations of baseline complex networks for networks with 5,000 vertices. ANU Quantum and Linux /dev/random RNGs.
Source: By the author.

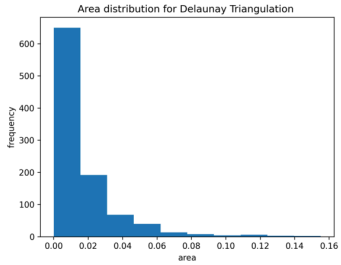

“k-logistic map with $k = 0$, 1”

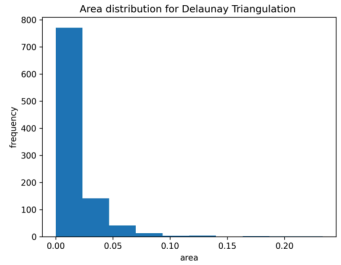

“k-logistic map with $k = 0$, 2”

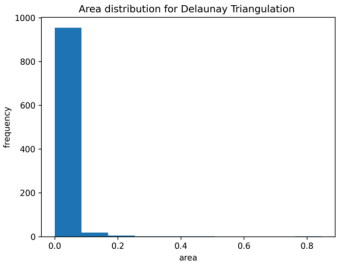

“k-logistic map with $k = 0$, 3”

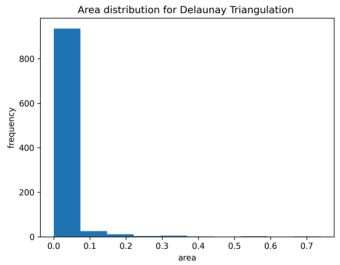

“k-logistic map with $k = 1$, 1”

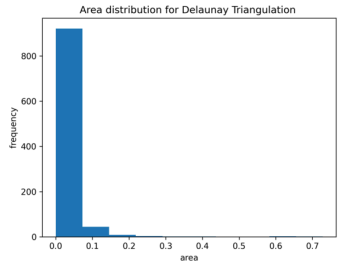

“k-logistic map with $k = 1$, 2”

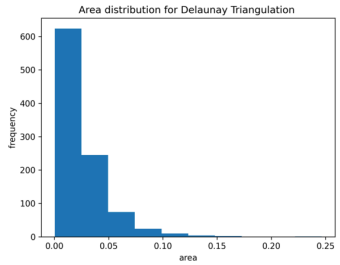

“k-logistic map with $k = 1$, 3”

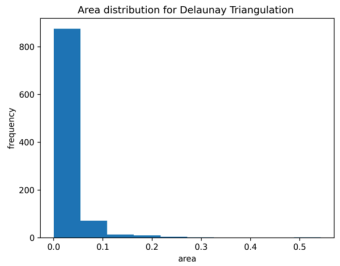

“k-logistic map with $k = 2$, 1”

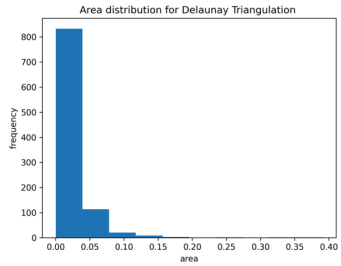

“k-logistic map with $k = 2$, 2”

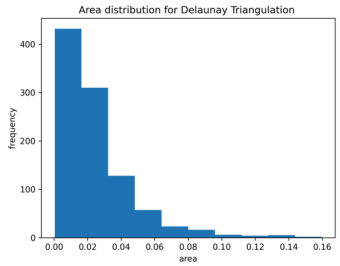

“k-logistic map with $k = 2$, 3”

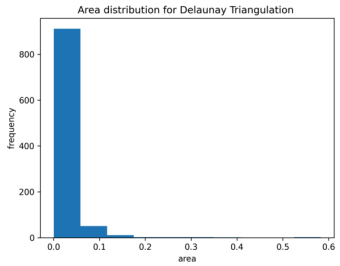

“k-logistic map with $k = 3$, 1”

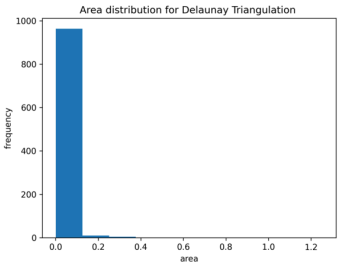

“k-logistic map with $k = 3$, 2”

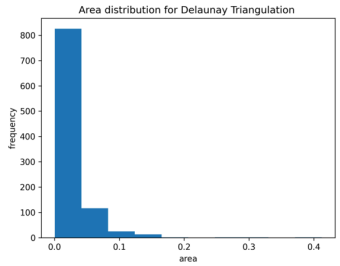

“k-logistic map with $k = 3$, 3”

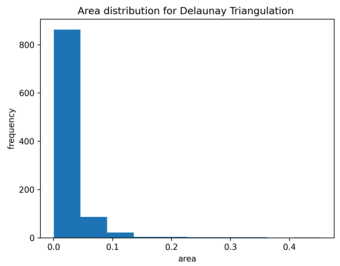

“k-logistic map with $k = 4$, 1”

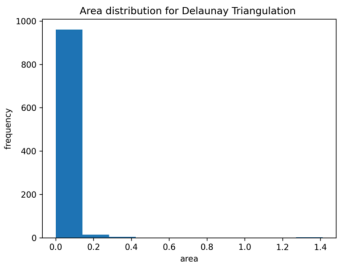

“k-logistic map with $k = 4$, 2”

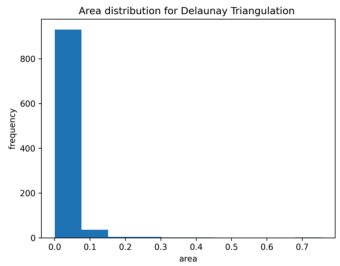

“k-logistic map with $k = 4$, 3”

Figure 144 – Histograms for Delaunay triangulations of baseline complex networks for networks with 5,000 vertices, k-logistic map from $k = 0$ to $k = 4$, $r = 3.7$. Source: By the author.

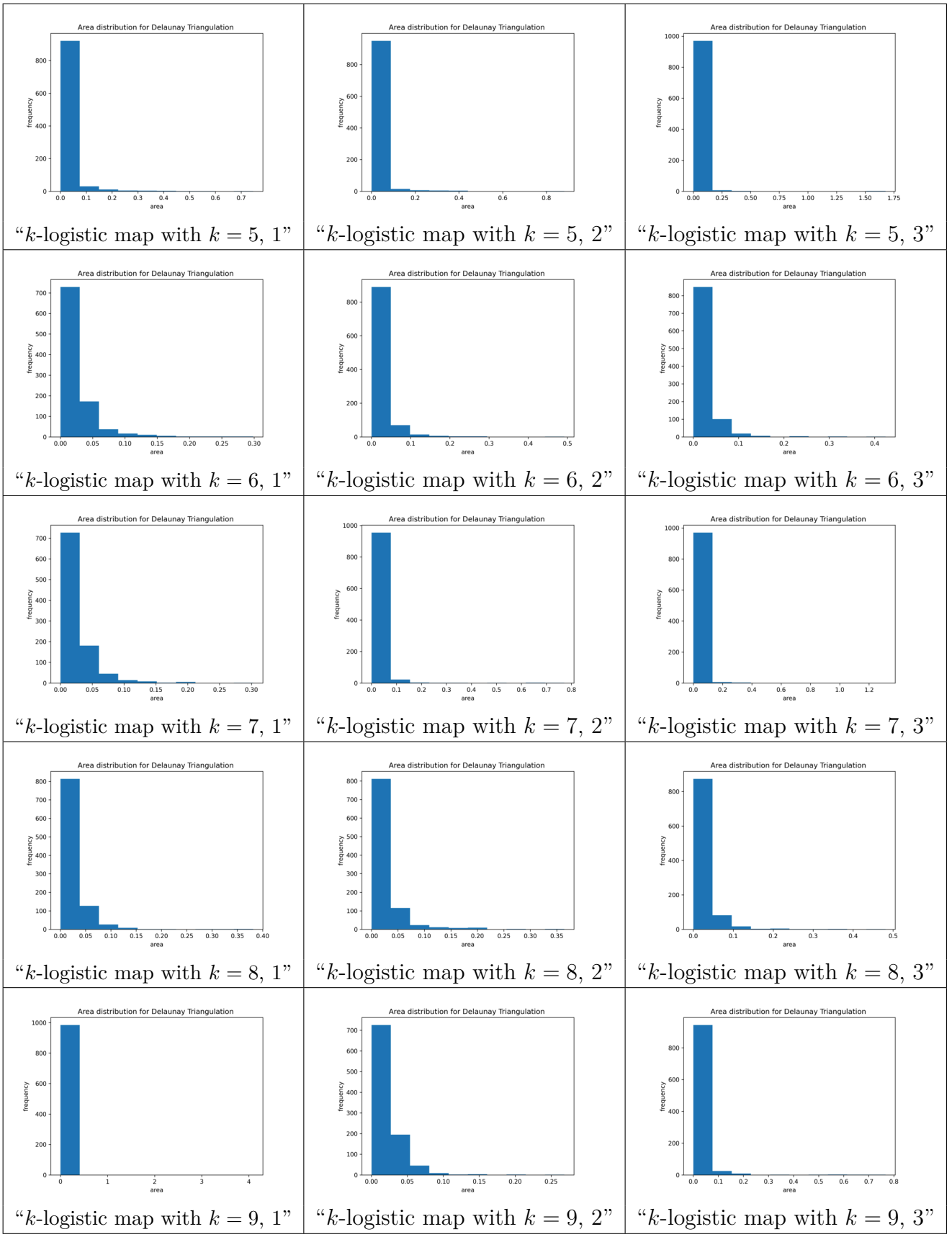

Figure 145 – Histograms for Delaunay triangulations of baseline complex networks for networks with 5,000 vertices, k-logistic map from $k = 5$ to $k = 9$, $r = 3.7$. Source: By the author.

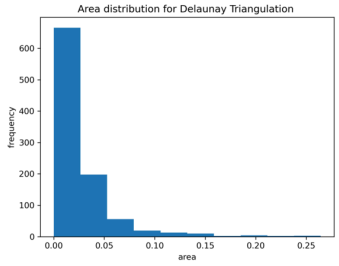

“k-logistic map with $k = 0$, 1”

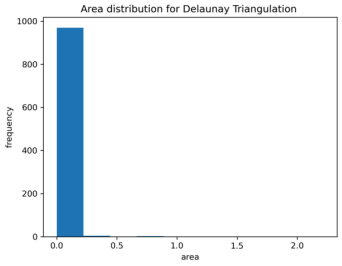

“k-logistic map with $k = 0$, 2”

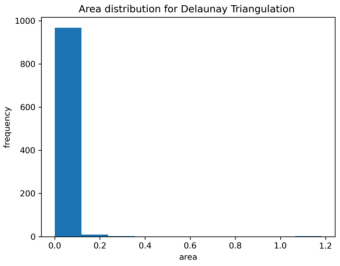

“k-logistic map with $k = 0$, 3”

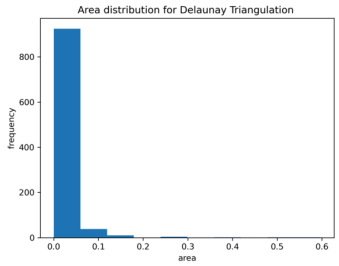

“k-logistic map with $k = 1$, 1”

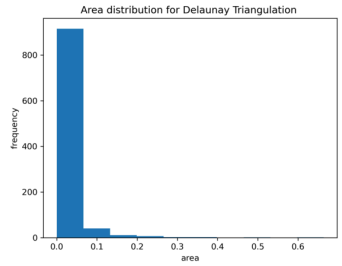

“k-logistic map with $k = 1$, 2”

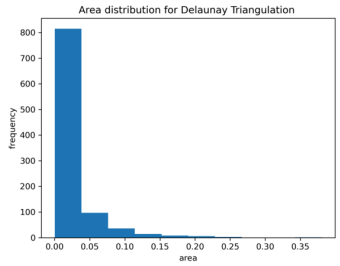

“k-logistic map with $k = 1$, 3”

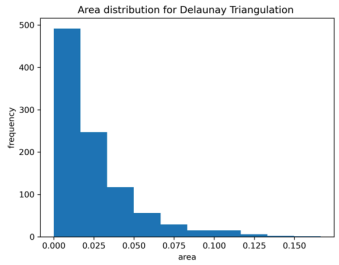

“k-logistic map with $k = 2$, 1”

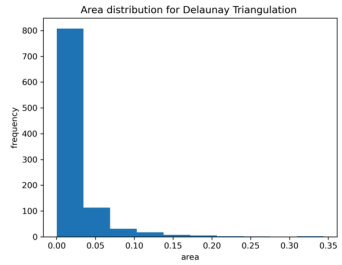

“k-logistic map with $k = 2$, 2”

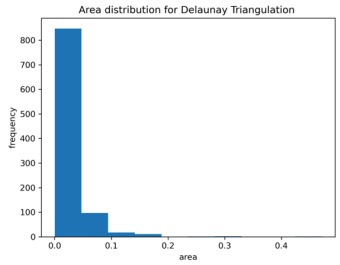

“k-logistic map with $k = 2$, 3”

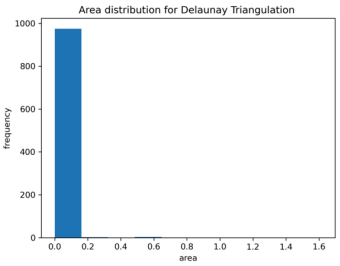

“k-logistic map with $k = 3$, 1”

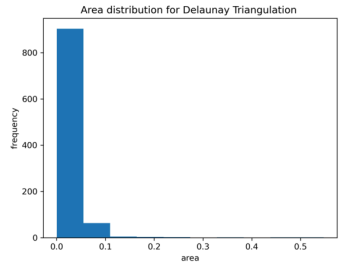

“k-logistic map with $k = 3$, 2”

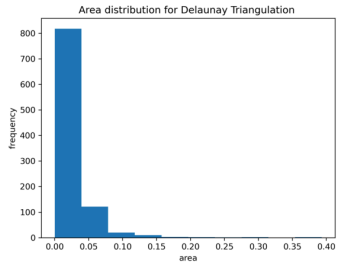

“k-logistic map with $k = 3$, 3”

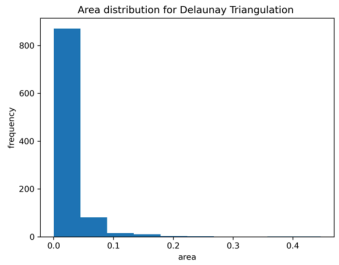

“k-logistic map with $k = 4$, 1”

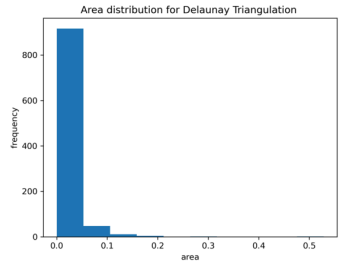

“k-logistic map with $k = 4$, 2”

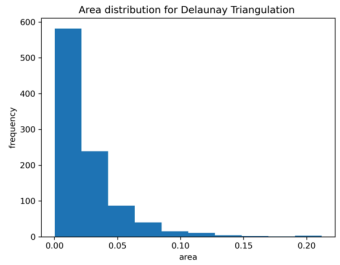

“k-logistic map with $k = 4$, 3”

Figure 146 – Histograms for Delaunay triangulations of baseline complex networks for networks with 5,000 vertices, k-logistic map from $k = 0$ to $k = 4$, $r = 3.99999$.
Source: By the author.

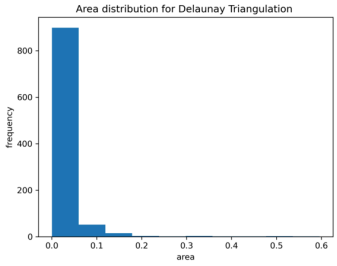

“k-logistic map with $k = 5$, 1”

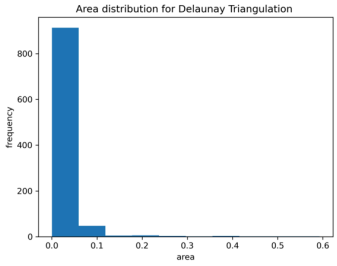

“k-logistic map with $k = 5$, 2”

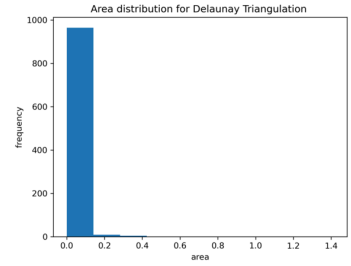

“k-logistic map with $k = 5$, 3”

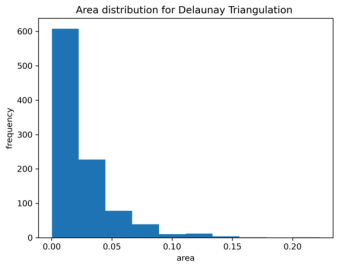

“k-logistic map with $k = 6$, 1”

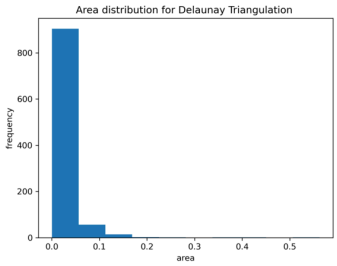

“k-logistic map with $k = 6$, 2”

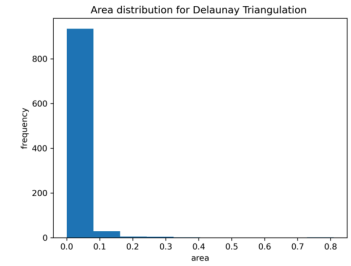

“k-logistic map with $k = 6$, 3”

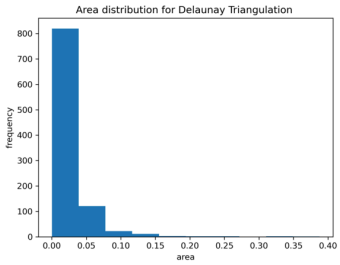

“k-logistic map with $k = 7$, 1”

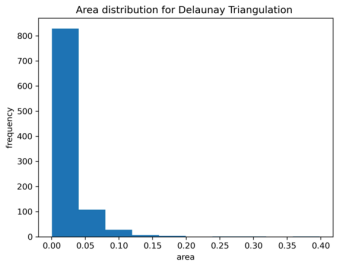

“k-logistic map with $k = 7$, 2”

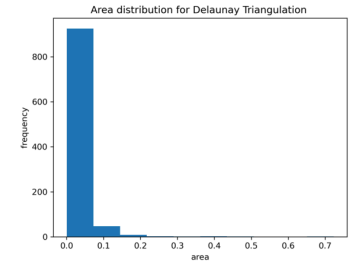

“k-logistic map with $k = 7$, 3”

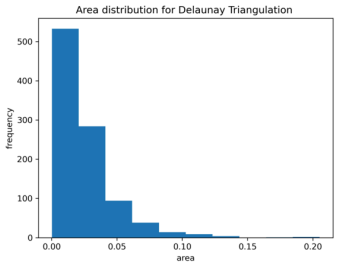

“k-logistic map with $k = 8$, 1”

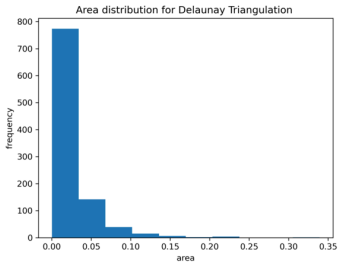

“k-logistic map with $k = 8$, 2”

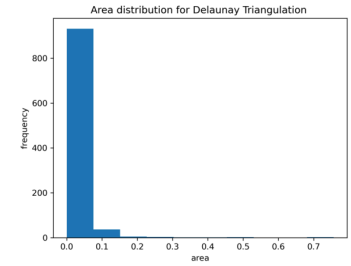

“k-logistic map with $k = 8$, 3”

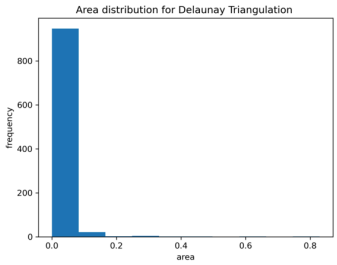

“k-logistic map with $k = 9$, 1”

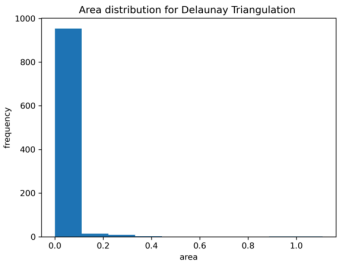

“k-logistic map with $k = 9$, 2”

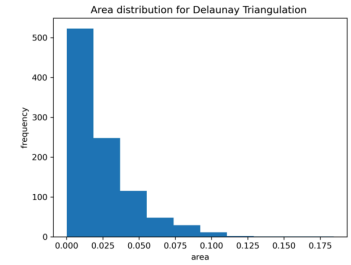

“k-logistic map with $k = 9$, 3”

Figure 147 – Histograms for Delaunay triangulations of baseline complex networks for networks with 5,000 vertices, k-logistic map from $k = 5$ to $k = 9$, $r = 3.99999$.
Source: By the author.

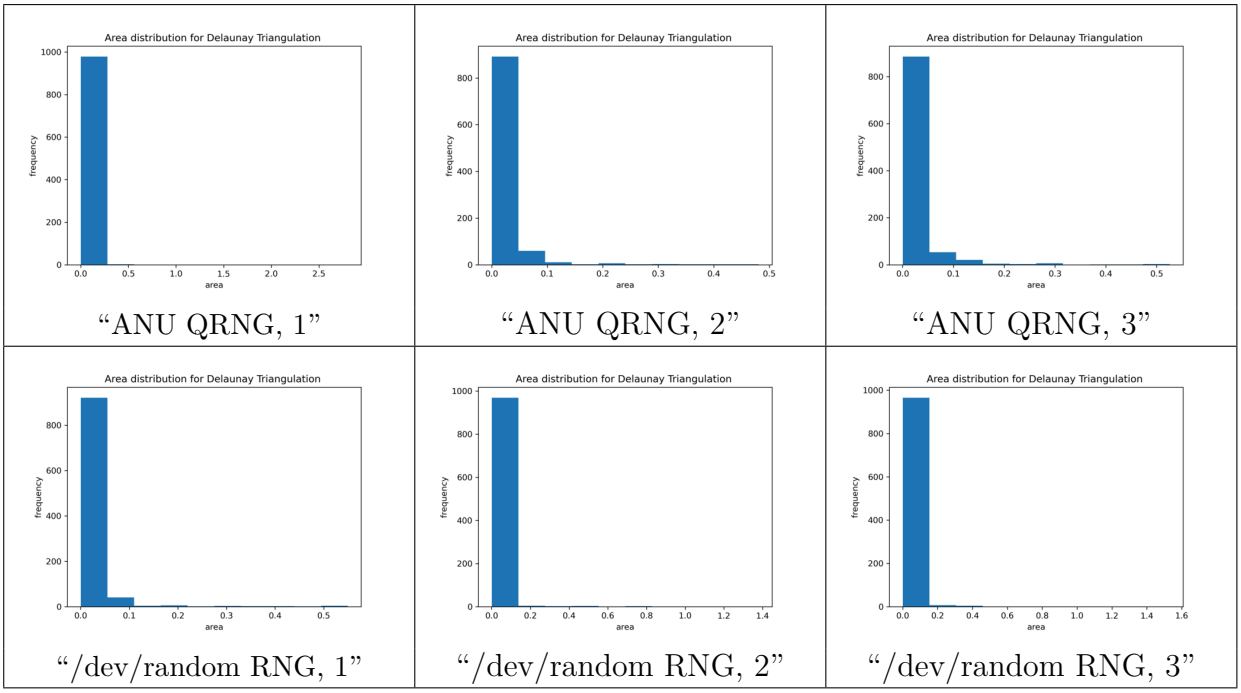

Figure 148 – Histograms for Delaunay triangulations of baseline complex networks for networks with 5,000 vertices. ANU Quantum and Linux /dev/random RNGs. Source: By the author.

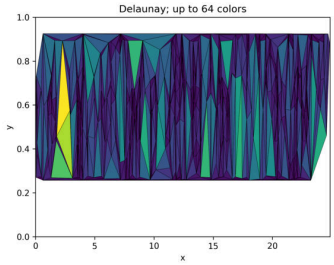

“k-logistic map with $k = 0$, 1”

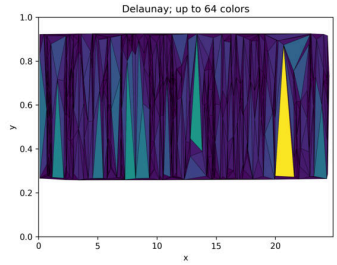

“k-logistic map with $k = 0$, 2”

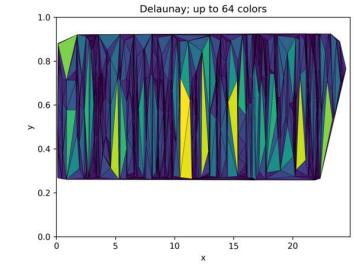

“k-logistic map with $k = 0$, 3”

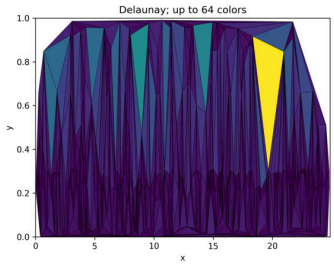

“k-logistic map with $k = 1$, 1”

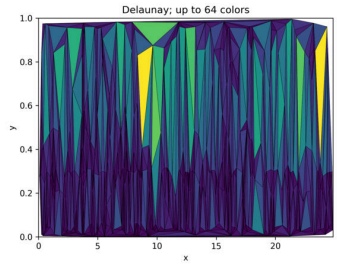

“k-logistic map with $k = 1$, 2”

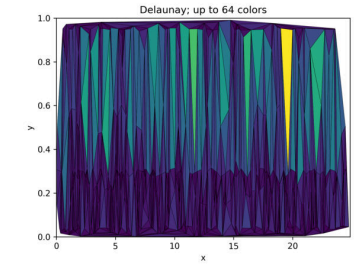

“k-logistic map with $k = 1$, 3”

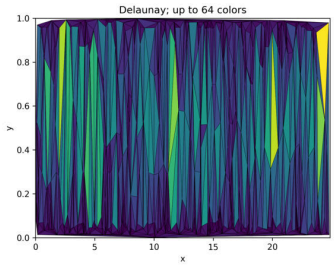

“k-logistic map with $k = 2$, 1”

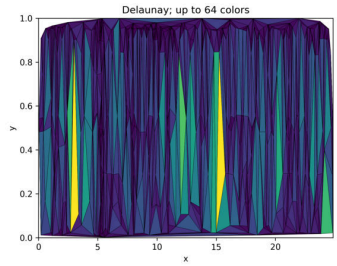

“k-logistic map with $k = 2$, 2”

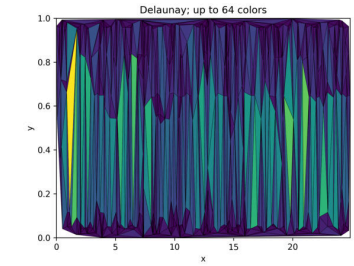

“k-logistic map with $k = 2$, 3”

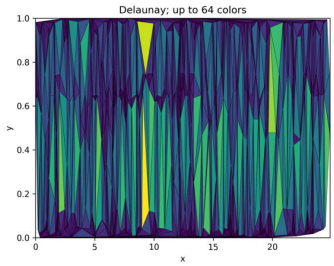

“k-logistic map with $k = 3$, 1”

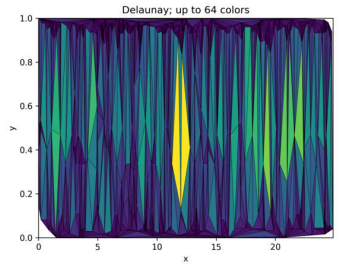

“k-logistic map with $k = 3$, 2”

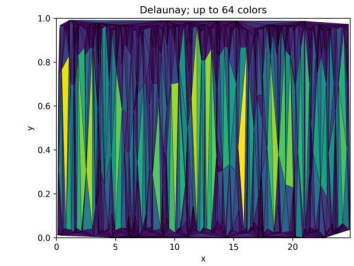

“k-logistic map with $k = 3$, 3”

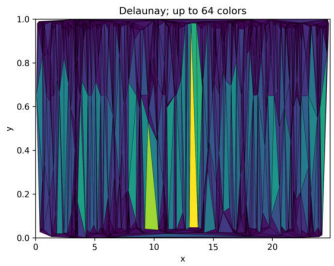

“k-logistic map with $k = 4$, 1”

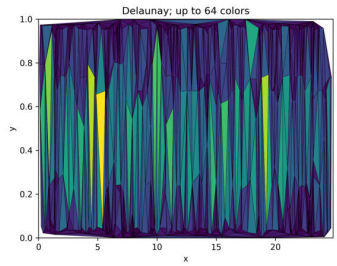

“k-logistic map with $k = 4$, 2”

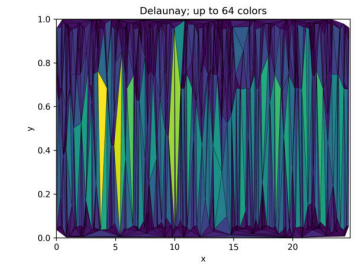

“k-logistic map with $k = 4$, 3”

Figure 149 – Delaunay triangulations of $> 1\sigma$ complex networks for networks with 5,000 vertices, k-logistic map from $k = 0$ to $k = 4$, $r = 3.7$.
Source: By the author.

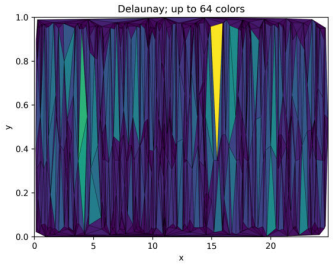

“k-logistic map with $k = 5$, 1”

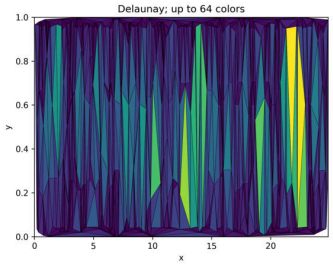

“k-logistic map with $k = 5$, 2”

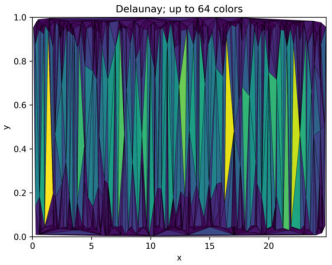

“k-logistic map with $k = 5$, 3”

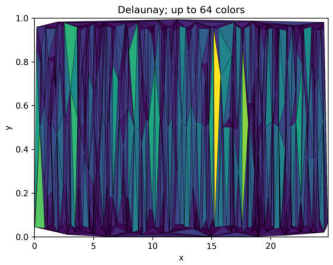

“k-logistic map with $k = 6$, 1”

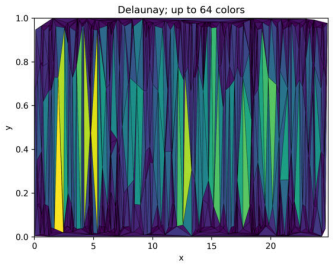

“k-logistic map with $k = 6$, 2”

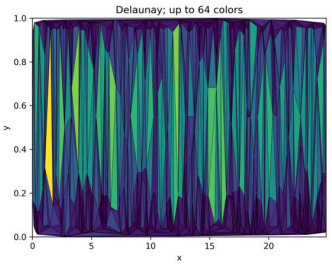

“k-logistic map with $k = 6$, 3”

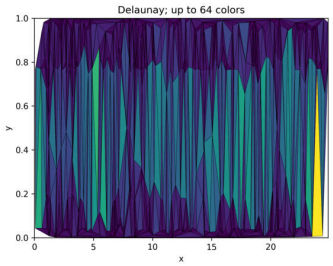

“k-logistic map with $k = 7$, 1”

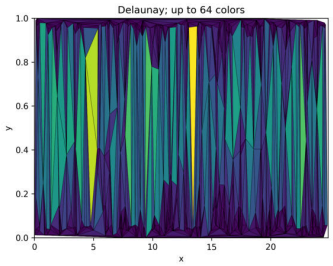

“k-logistic map with $k = 7$, 2”

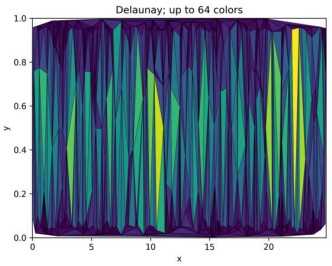

“k-logistic map with $k = 7$, 3”

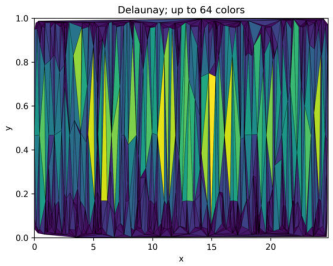

“k-logistic map with $k = 8$, 1”

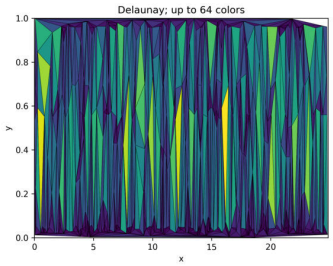

“k-logistic map with $k = 8$, 2”

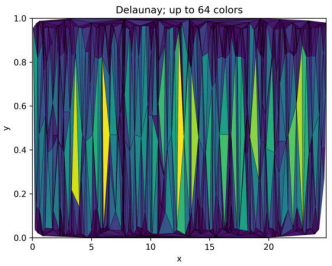

“k-logistic map with $k = 8$, 3”

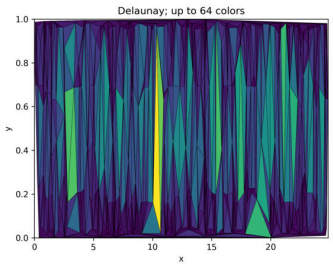

“k-logistic map with $k = 9$, 1”

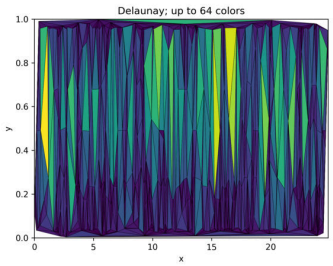

“k-logistic map with $k = 9$, 2”

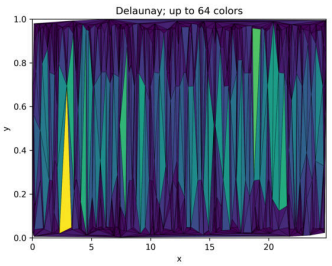

“k-logistic map with $k = 9$, 3”

Figure 150 – Delaunay triangulations of $> 1\sigma$ complex networks for networks with 5,000 vertices, k-logistic map from $k = 5$ to $k = 9$, $r = 3.7$.
Source: By the author.

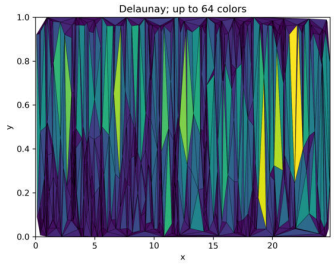

“k-logistic map with $k = 0$, 1”

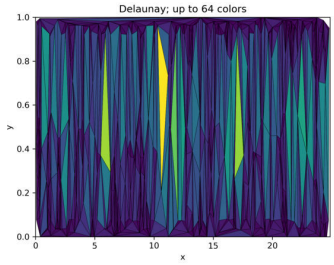

“k-logistic map with $k = 0$, 2”

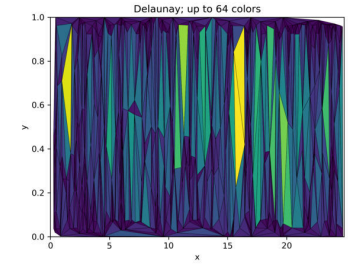

“k-logistic map with $k = 0$, 3”

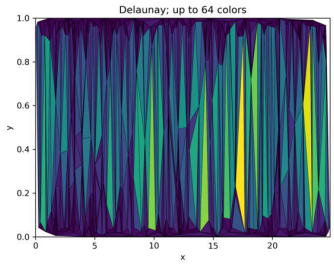

“k-logistic map with $k = 1$, 1”

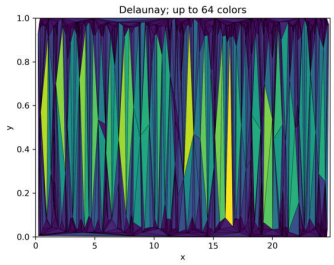

“k-logistic map with $k = 1$, 2”

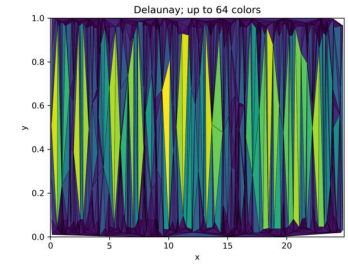

“k-logistic map with $k = 1$, 3”

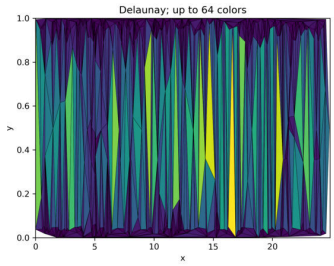

“k-logistic map with $k = 2$, 1”

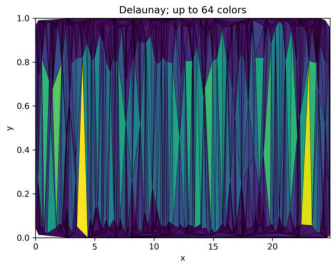

“k-logistic map with $k = 2$, 2”

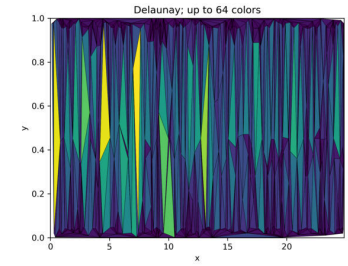

“k-logistic map with $k = 2$, 3”

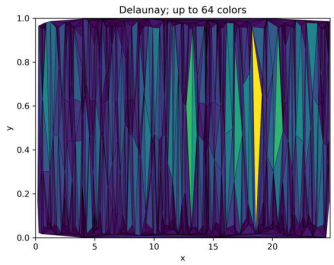

“k-logistic map with $k = 3$, 1”

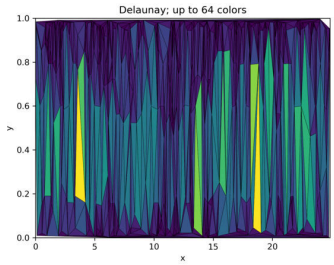

“k-logistic map with $k = 3$, 2”

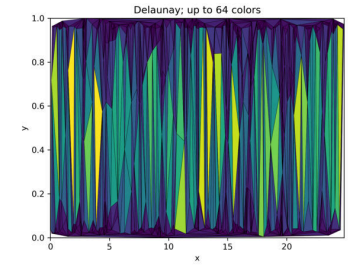

“k-logistic map with $k = 3$, 3”

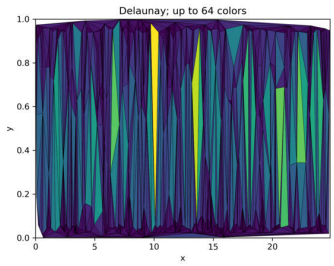

“k-logistic map with $k = 4$, 1”

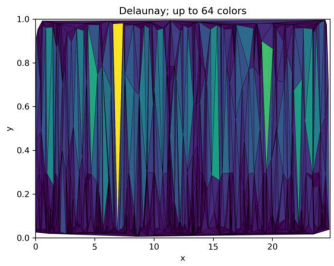

“k-logistic map with $k = 4$, 2”

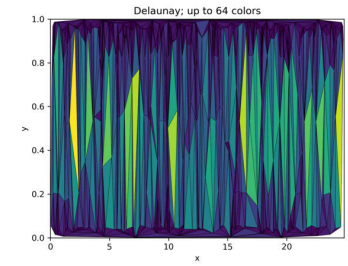

“k-logistic map with $k = 4$, 3”

Figure 151 – Delaunay triangulations of $> 1\sigma$ complex networks for networks with 5,000 vertices, k-logistic map from $k = 0$ to $k = 4$, $r = 3.99999$.
Source: By the author.

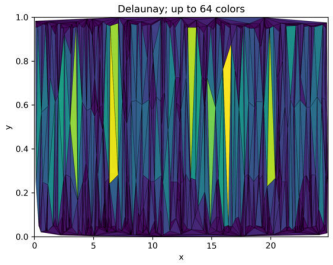

“k-logistic map with $k = 5$, 1”

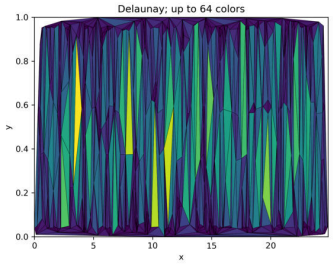

“k-logistic map with $k = 5$, 2”

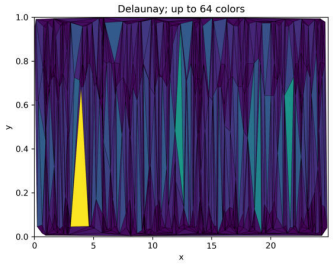

“k-logistic map with $k = 5$, 3”

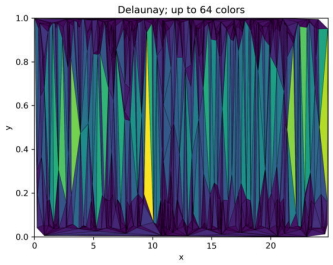

“k-logistic map with $k = 6$, 1”

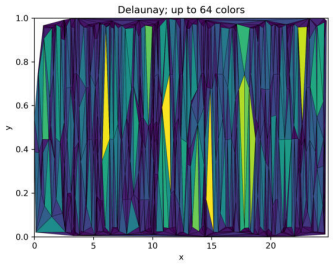

“k-logistic map with $k = 6$, 2”

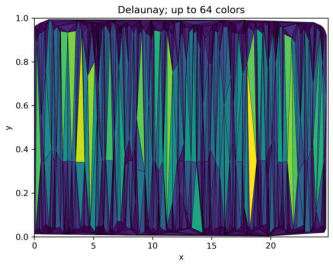

“k-logistic map with $k = 6$, 3”

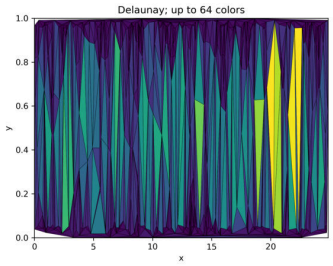

“k-logistic map with $k = 7$, 1”

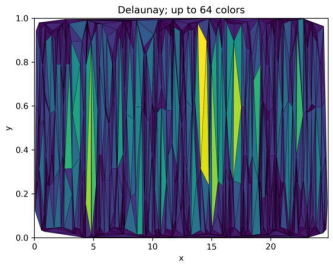

“k-logistic map with $k = 7$, 2”

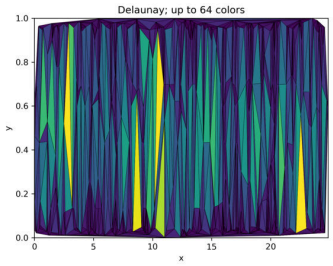

“k-logistic map with $k = 7$, 3”

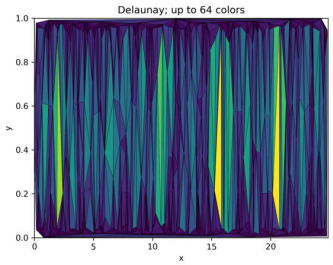

“k-logistic map with $k = 8$, 1”

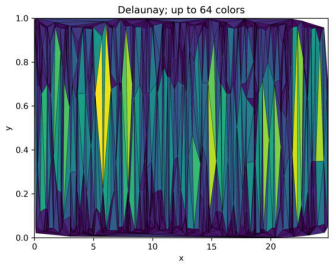

“k-logistic map with $k = 8$, 2”

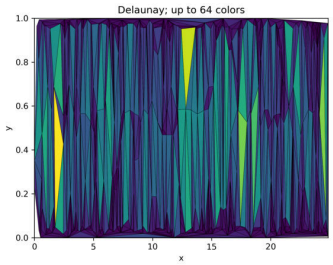

“k-logistic map with $k = 8$, 3”

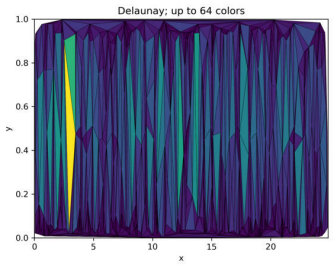

“k-logistic map with $k = 9$, 1”

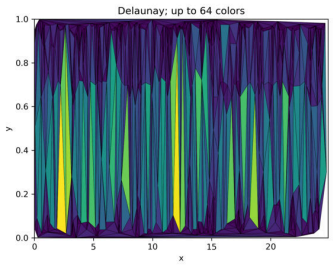

“k-logistic map with $k = 9$, 2”

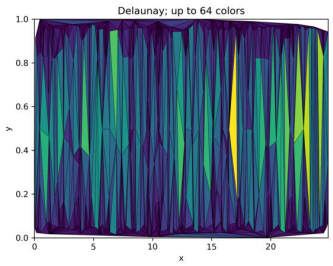

“k-logistic map with $k = 9$, 3”

Figure 152 – Delaunay triangulations of $> 1\sigma$ complex networks for networks with 5,000 vertices, k-logistic map from $k = 5$ to $k = 9$, $r = 3.99999$.
Source: By the author.

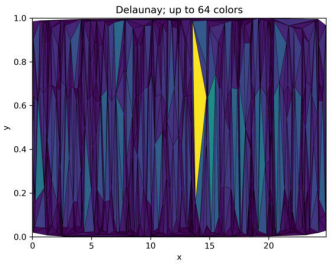

“ANU QRNG, 1”

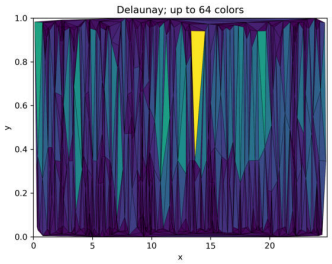

“ANU QRNG, 2”

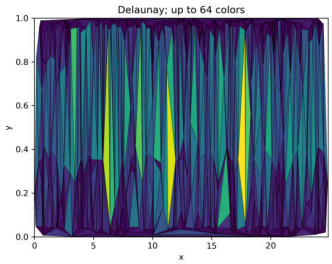

“ANU QRNG, 3”

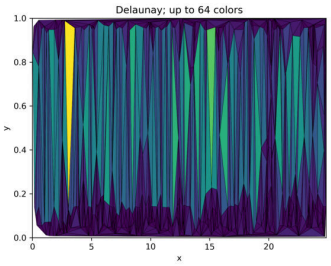

“/dev/random RNG, 1”

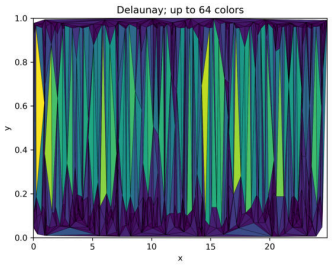

“/dev/random RNG, 2”

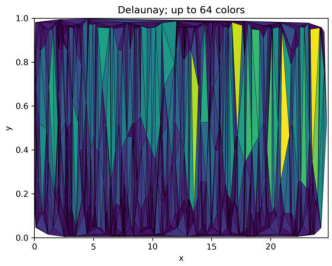

“/dev/random RNG, 3”

Figure 153 – Delaunay triangulations of $> 1\sigma$ complex networks for networks with 5,000 vertices. ANU Quantum and Linux /dev/random RNGs.
Source: By the author.

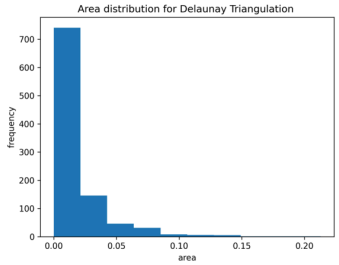

“k-logistic map with $k = 0$, 1”

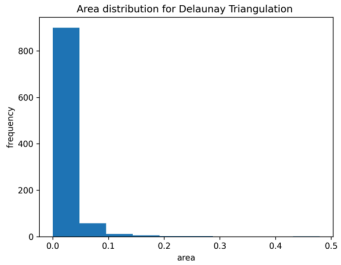

“k-logistic map with $k = 0$, 2”

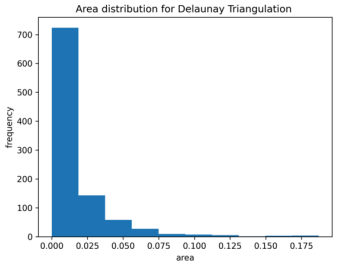

“k-logistic map with $k = 0$, 3”

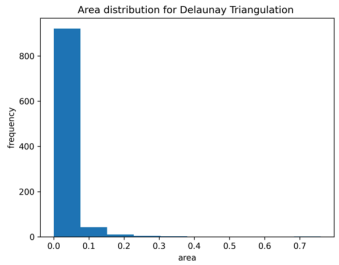

“k-logistic map with $k = 1$, 1”

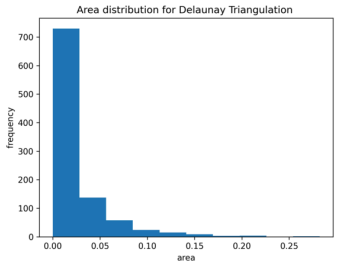

“k-logistic map with $k = 1$, 2”

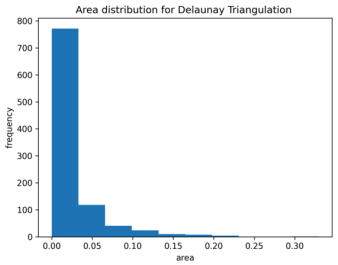

“k-logistic map with $k = 1$, 3”

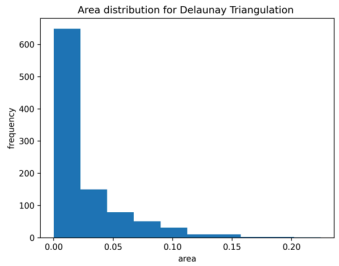

“k-logistic map with $k = 2$, 1”

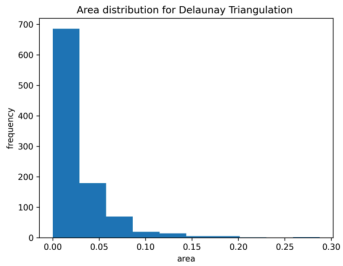

“k-logistic map with $k = 2$, 2”

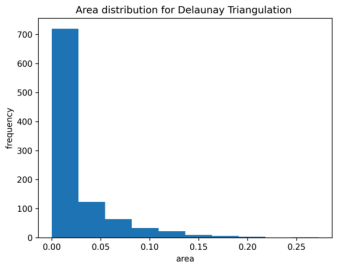

“k-logistic map with $k = 2$, 3”

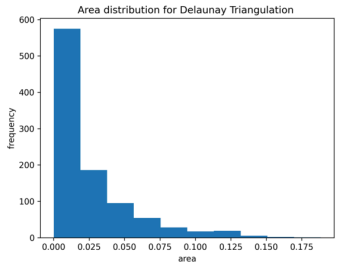

“k-logistic map with $k = 3$, 1”

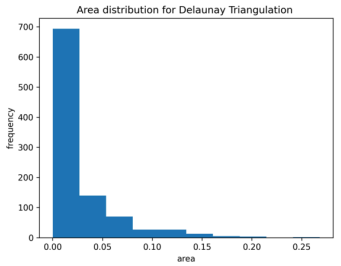

“k-logistic map with $k = 3$, 2”

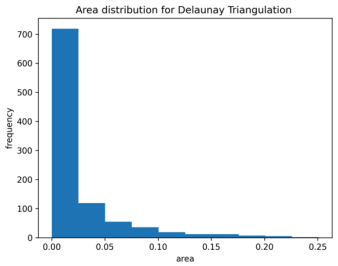

“k-logistic map with $k = 3$, 3”

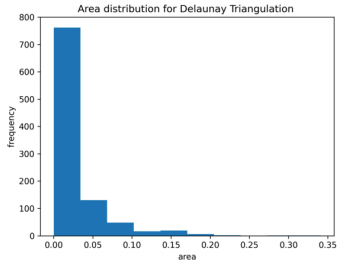

“k-logistic map with $k = 4$, 1”

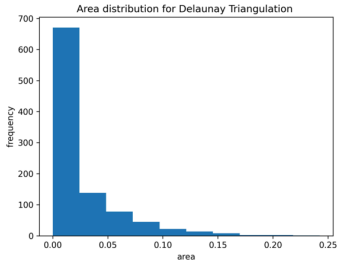

“k-logistic map with $k = 4$, 2”

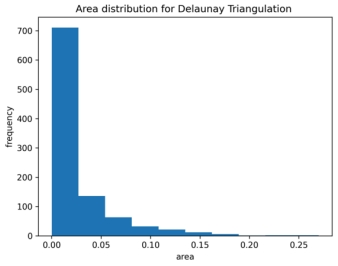

“k-logistic map with $k = 4$, 3”

Figure 154 – Histograms for Delaunay triangulations of $> 1\sigma$ complex networks for networks with 5,000 vertices, k-logistic map from $k = 0$ to $k = 4$, $r = 3.7$.
Source: By the author.

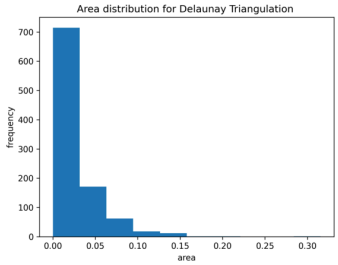

“k-logistic map with $k = 5$, 1”

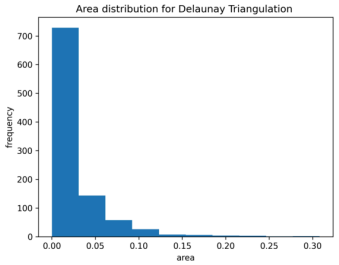

“k-logistic map with $k = 5$, 2”

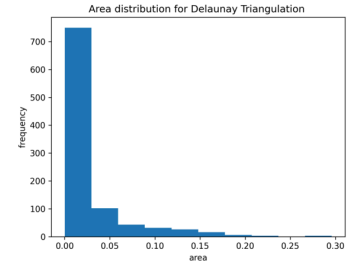

“k-logistic map with $k = 5$, 3”

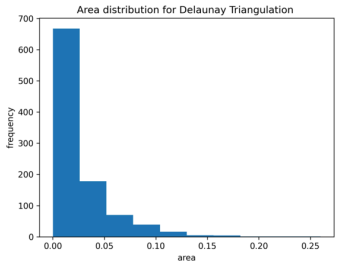

“k-logistic map with $k = 6$, 1”

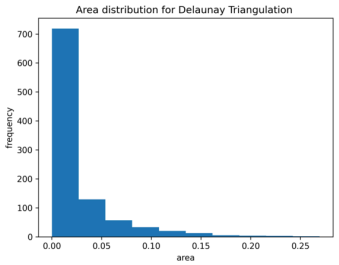

“k-logistic map with $k = 6$, 2”

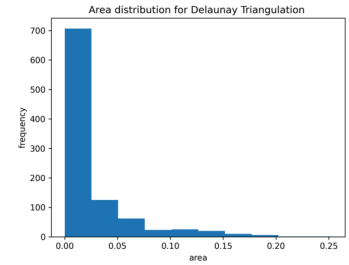

“k-logistic map with $k = 6$, 3”

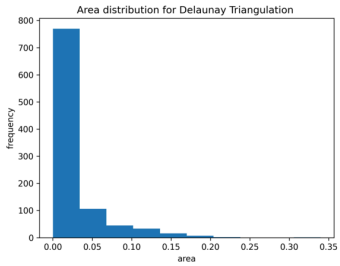

“k-logistic map with $k = 7$, 1”

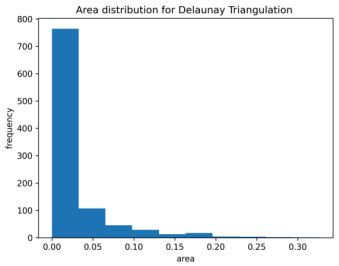

“k-logistic map with $k = 7$, 2”

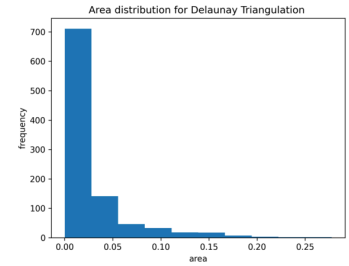

“k-logistic map with $k = 7$, 3”

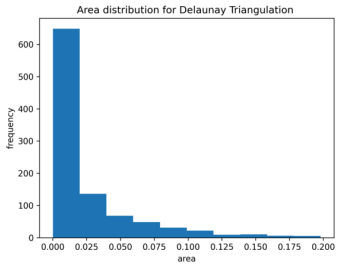

“k-logistic map with $k = 8$, 1”

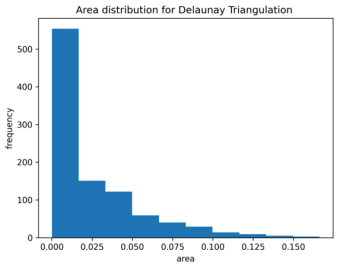

“k-logistic map with $k = 8$, 2”

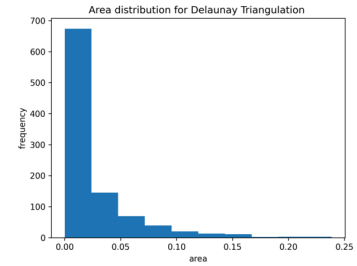

“k-logistic map with $k = 8$, 3”

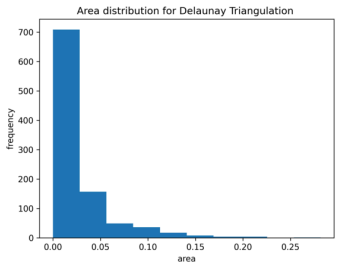

“k-logistic map with $k = 9$, 1”

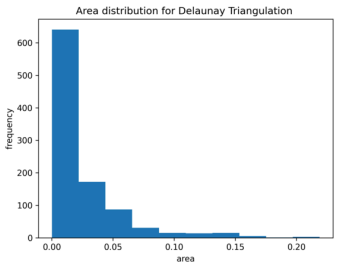

“k-logistic map with $k = 9$, 2”

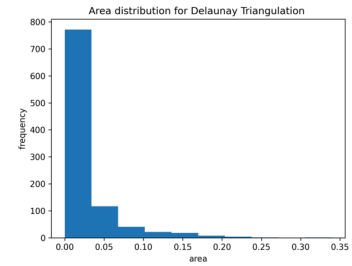

“k-logistic map with $k = 9$, 3”

Figure 155 – Histograms for Delaunay triangulations of $> 1\sigma$ complex networks for networks with 5,000 vertices, k-logistic map from $k = 5$ to $k = 9$, $r = 3.7$.
Source: By the author.

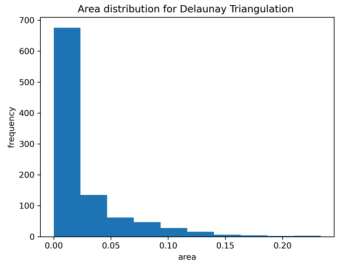

“k-logistic map with $k = 0$, 1”

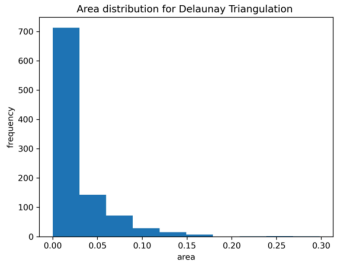

“k-logistic map with $k = 0$, 2”

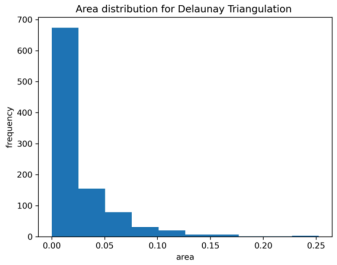

“k-logistic map with $k = 0$, 3”

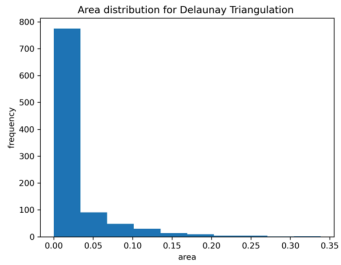

“k-logistic map with $k = 1$, 1”

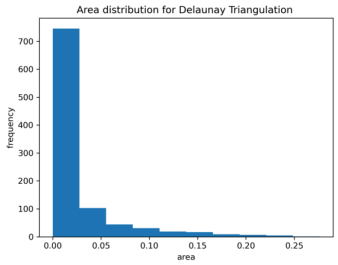

“k-logistic map with $k = 1$, 2”

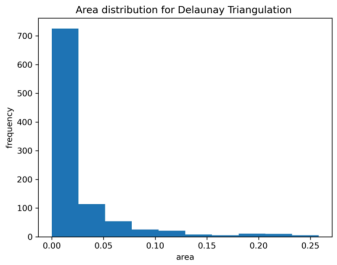

“k-logistic map with $k = 1$, 3”

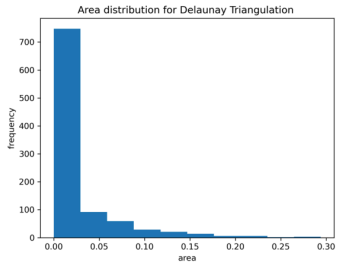

“k-logistic map with $k = 2$, 1”

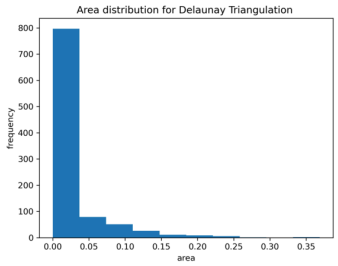

“k-logistic map with $k = 2$, 2”

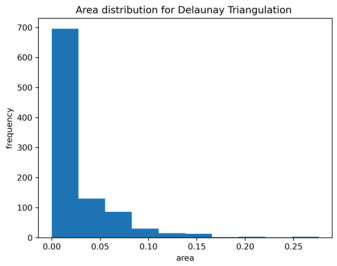

“k-logistic map with $k = 2$, 3”

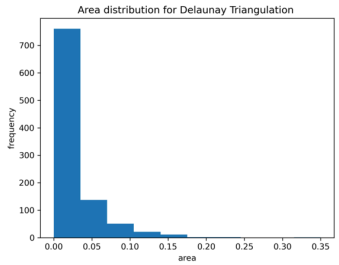

“k-logistic map with $k = 3$, 1”

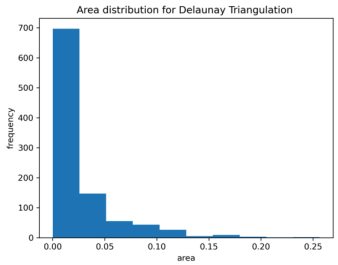

“k-logistic map with $k = 3$, 2”

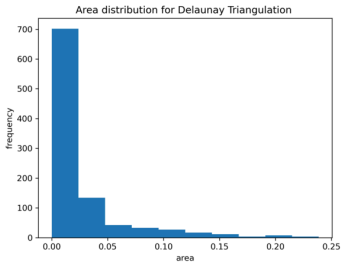

“k-logistic map with $k = 3$, 3”

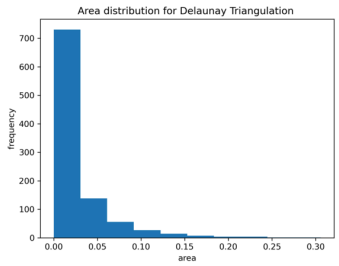

“k-logistic map with $k = 4$, 1”

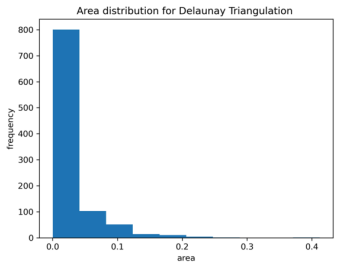

“k-logistic map with $k = 4$, 2”

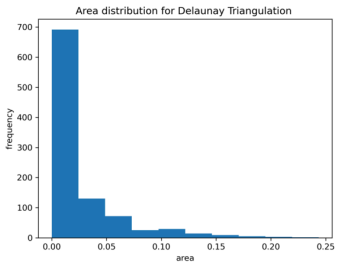

“k-logistic map with $k = 4$, 3”

Figure 156 – Histograms for Delaunay triangulations of $> 1\sigma$ complex networks for networks with 5,000 vertices, k-logistic map from $k = 0$ to $k = 4$, $r = 3.99999$. Source: By the author.

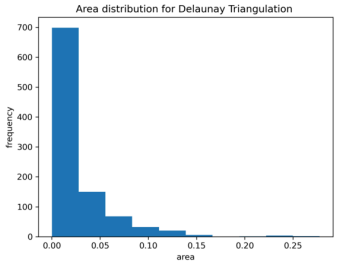

“k-logistic map with $k = 5$, 1”

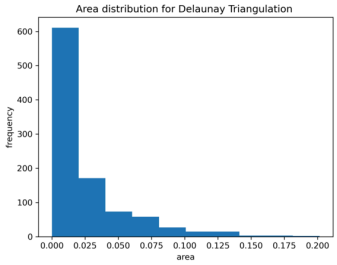

“k-logistic map with $k = 5$, 2”

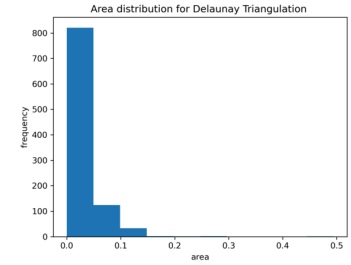

“k-logistic map with $k = 5$, 3”

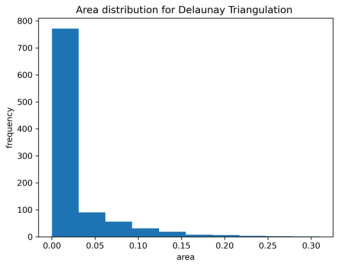

“k-logistic map with $k = 6$, 1”

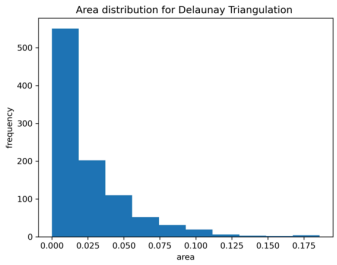

“k-logistic map with $k = 6$, 2”

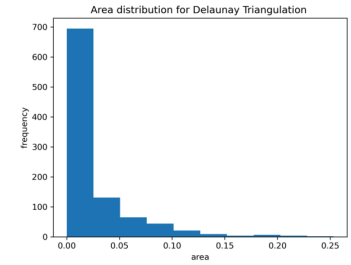

“k-logistic map with $k = 6$, 3”

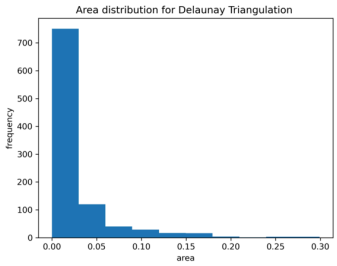

“k-logistic map with $k = 7$, 1”

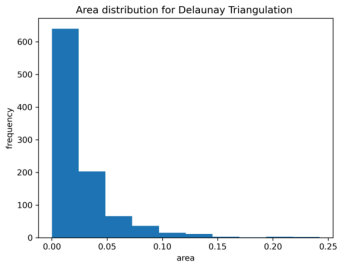

“k-logistic map with $k = 7$, 2”

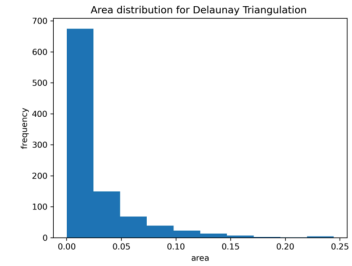

“k-logistic map with $k = 7$, 3”

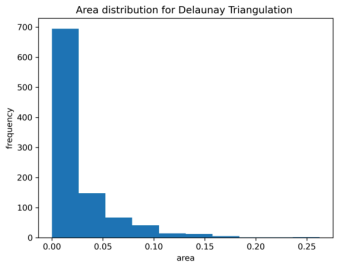

“k-logistic map with $k = 8$, 1”

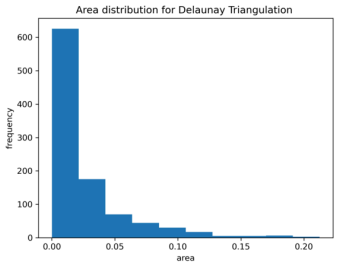

“k-logistic map with $k = 8$, 2”

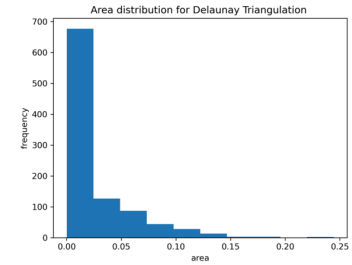

“k-logistic map with $k = 8$, 3”

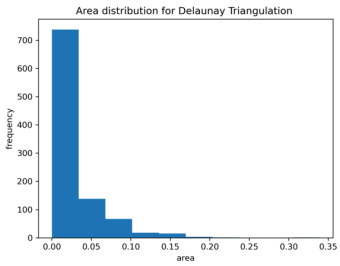

“k-logistic map with $k = 9$, 1”

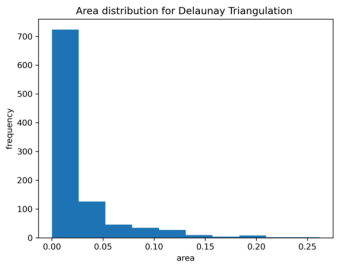

“k-logistic map with $k = 9$, 2”

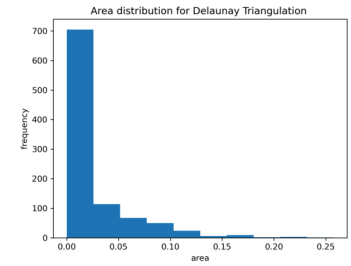

“k-logistic map with $k = 9$, 3”

Figure 157 – Histograms for Delaunay triangulations of $> 1\sigma$ complex networks for networks with 5,000 vertices, k-logistic map from $k = 5$ to $k = 9$, $r = 3.99999$. Source: By the author.

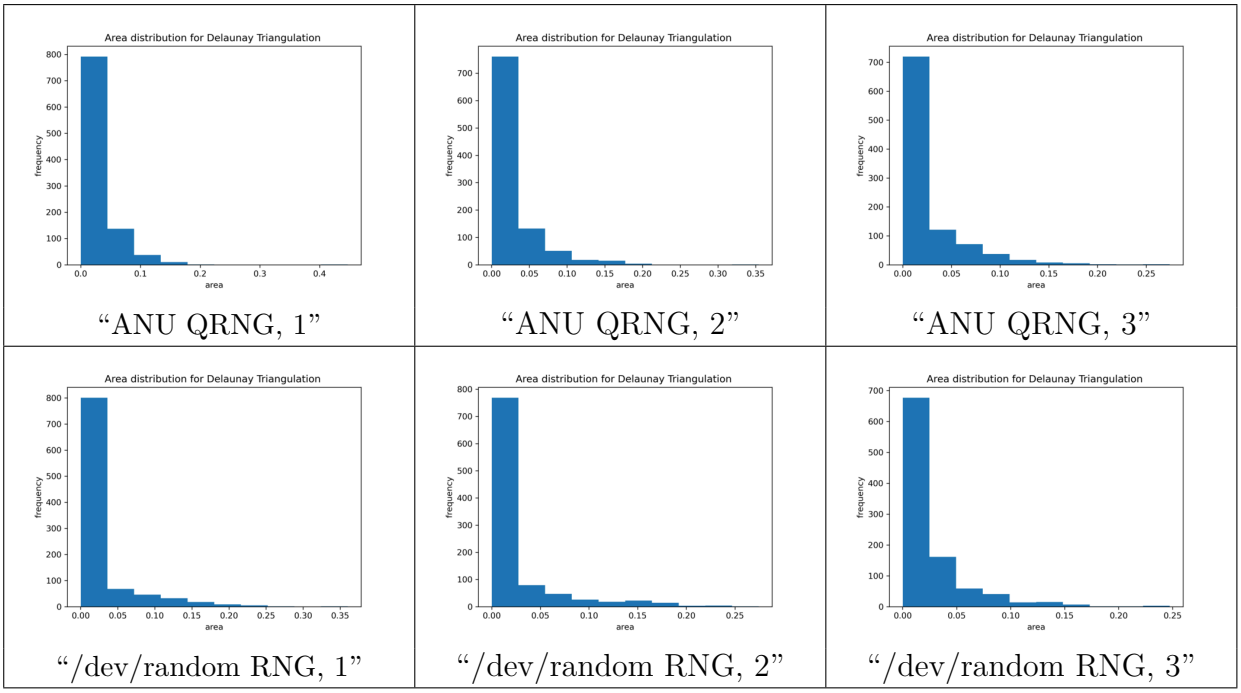

Figure 158 – Histograms for Delaunay triangulations of $> 1\sigma$ complex networks for networks with 5,000 vertices. ANU Quantum and Linux /dev/random RNGs. Source: By the author.

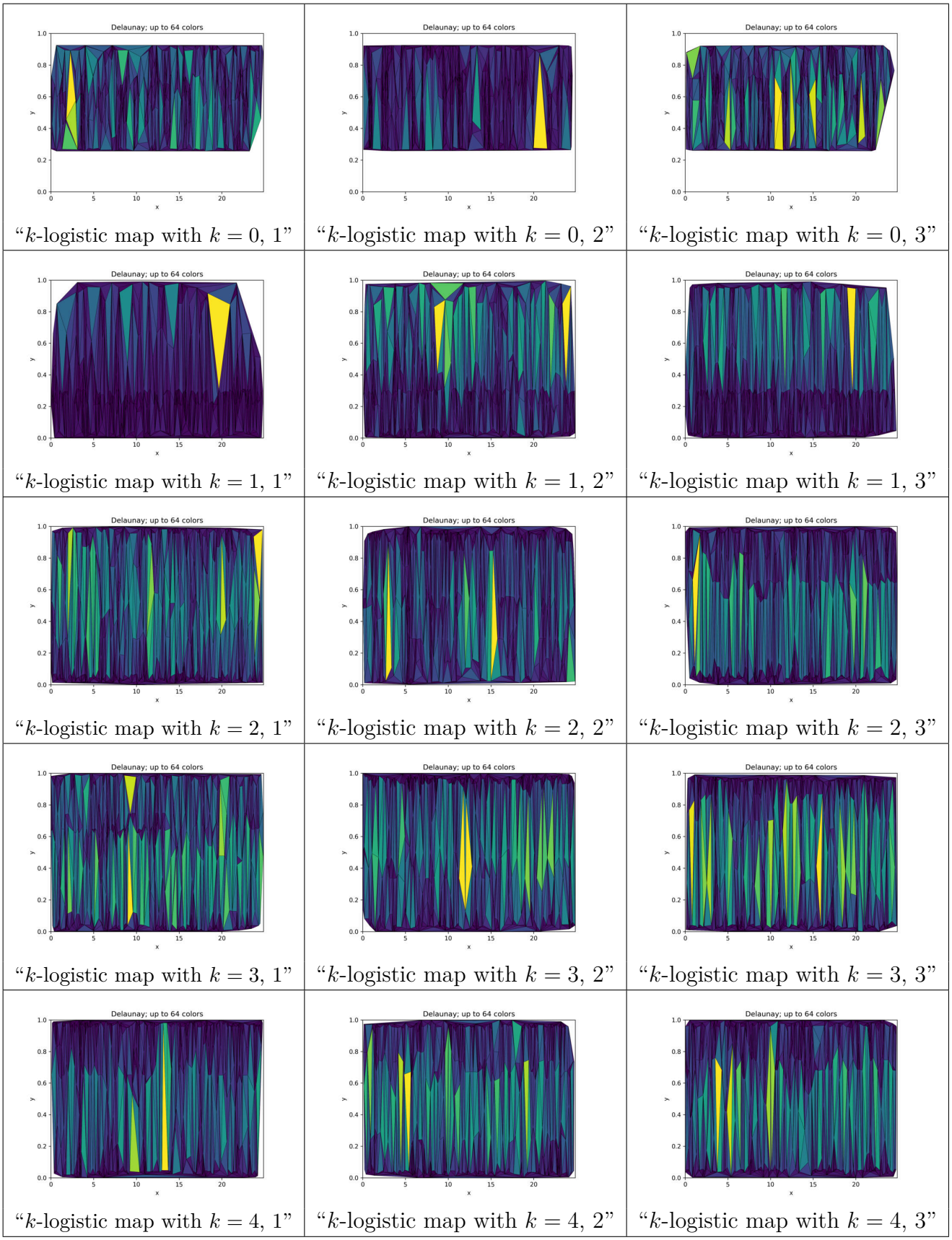

Figure 159 – Delaunay triangulations of $> 2\sigma$ complex networks for networks with 5,000 vertices, k-logistic map from $k = 0$ to $k = 4$, $r = 3.7$.
Source: By the author.

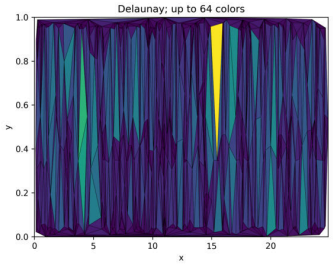

“k-logistic map with $k = 5$, 1”

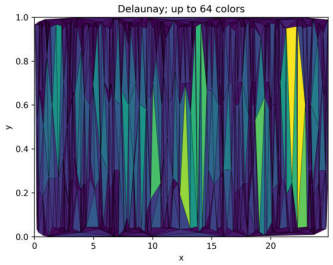

“k-logistic map with $k = 5$, 2”

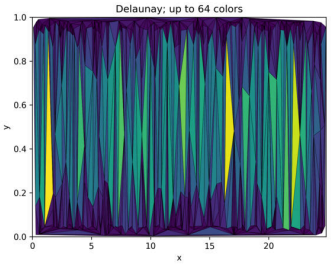

“k-logistic map with $k = 5$, 3”

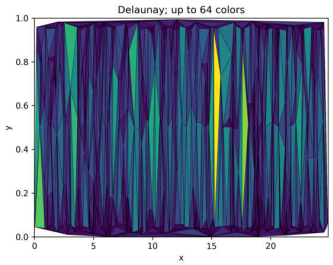

“k-logistic map with $k = 6$, 1”

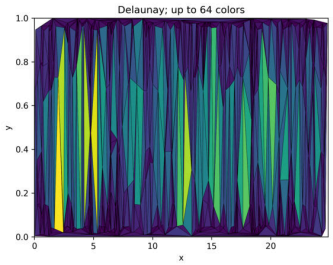

“k-logistic map with $k = 6$, 2”

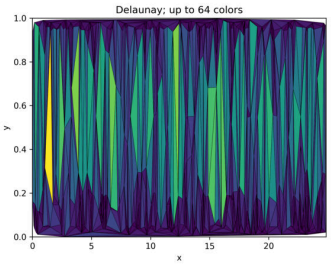

“k-logistic map with $k = 6$, 3”

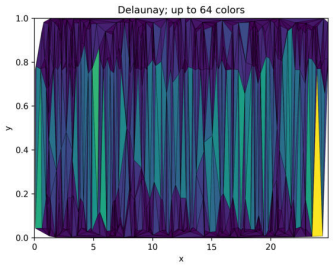

“k-logistic map with $k = 7$, 1”

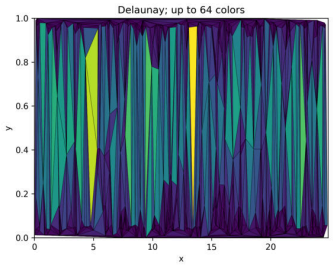

“k-logistic map with $k = 7$, 2”

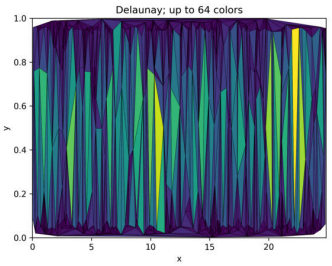

“k-logistic map with $k = 7$, 3”

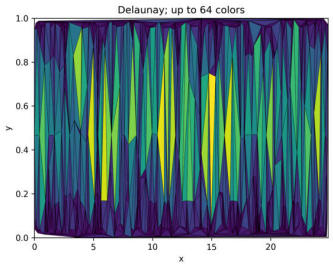

“k-logistic map with $k = 8$, 1”

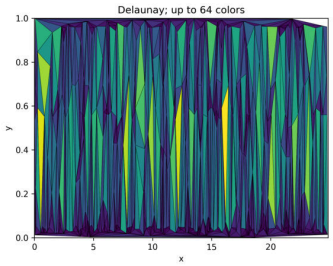

“k-logistic map with $k = 8$, 2”

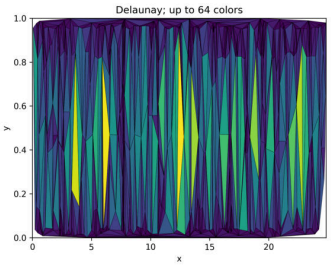

“k-logistic map with $k = 8$, 3”

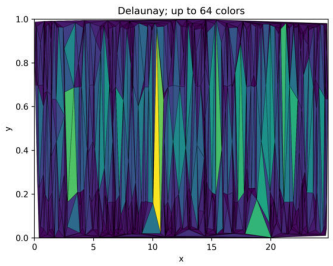

“k-logistic map with $k = 9$, 1”

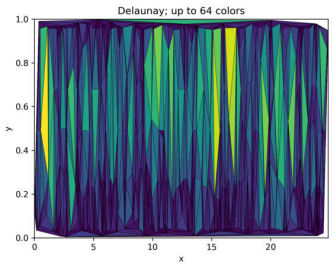

“k-logistic map with $k = 9$, 2”

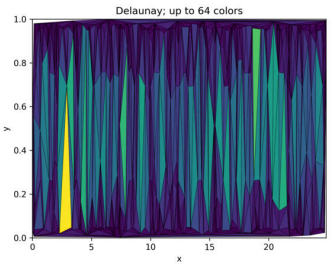

“k-logistic map with $k = 9$, 3”

Figure 160 – Delaunay triangulations of $> 2\sigma$ complex networks for networks with 5,000 vertices, k-logistic map from $k = 5$ to $k = 9$, $r = 3.7$.
Source: By the author.

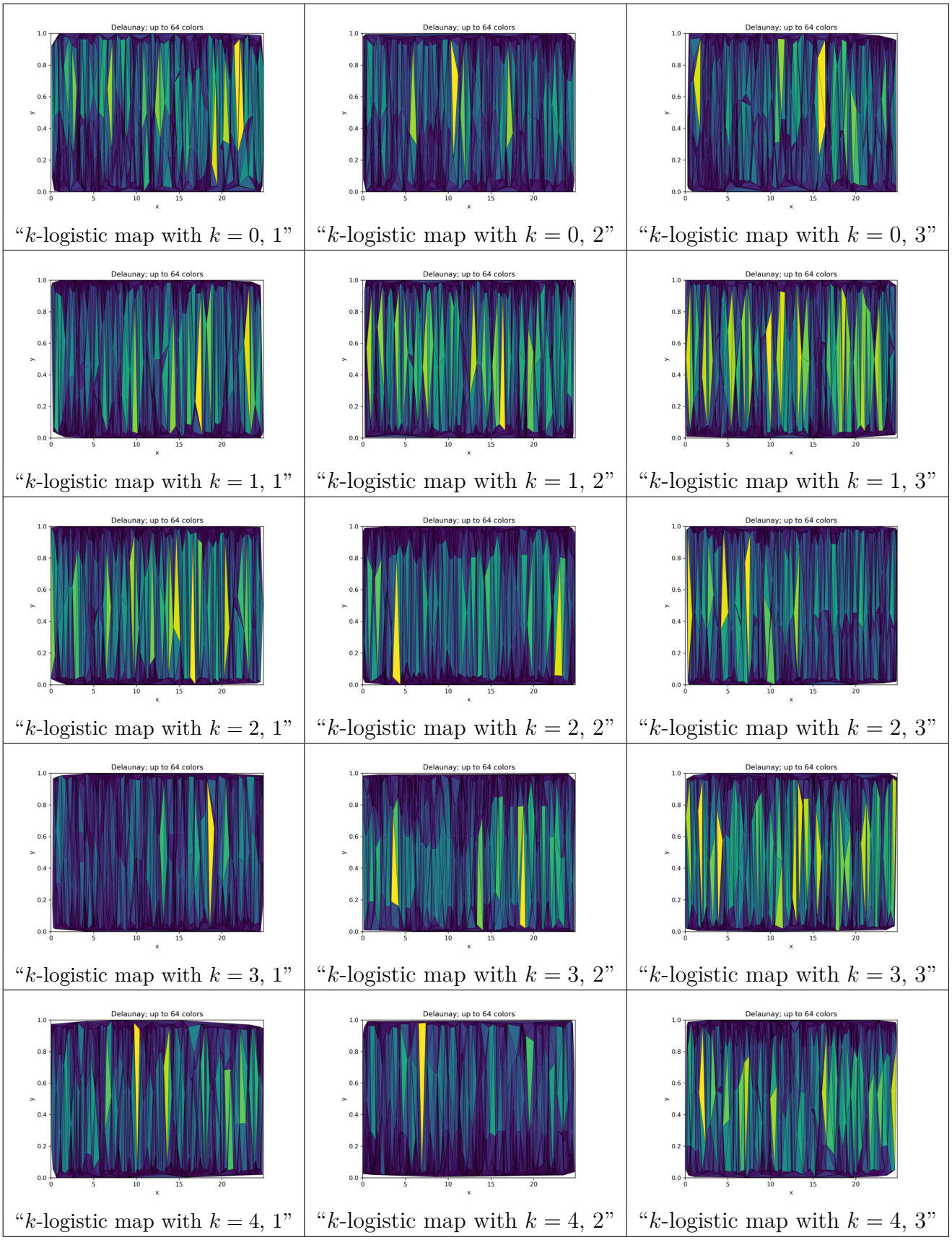

Figure 161 – Delaunay triangulations of $> 2\sigma$ complex networks for networks with 5,000 vertices, k-logistic map from $k = 0$ to $k = 4$, $r = 3.99999$.
Source: By the author.

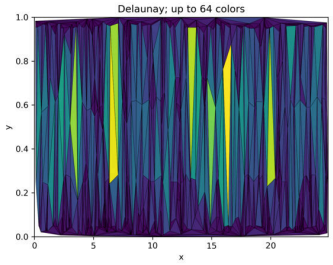

“k-logistic map with $k = 5$, 1”

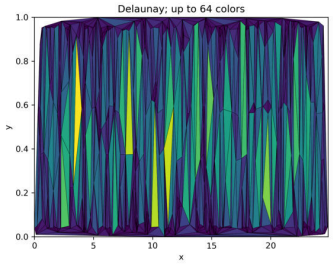

“k-logistic map with $k = 5$, 2”

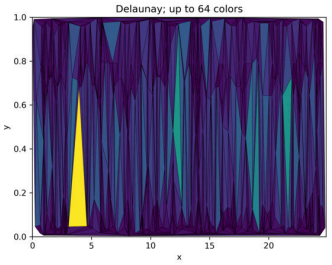

“k-logistic map with $k = 5$, 3”

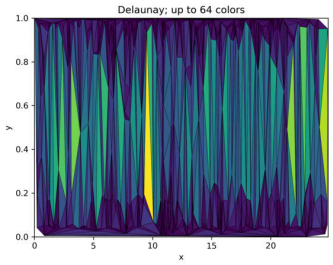

“k-logistic map with $k = 6$, 1”

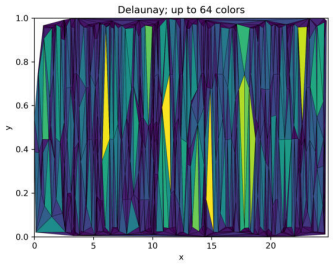

“k-logistic map with $k = 6$, 2”

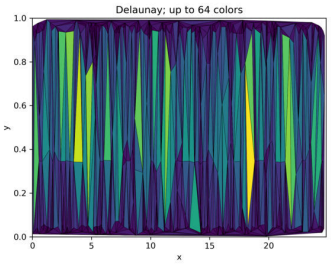

“k-logistic map with $k = 6$, 3”

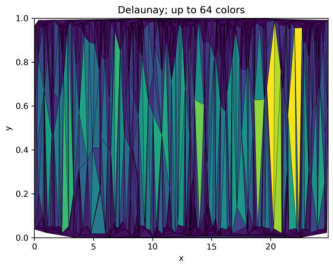

“k-logistic map with $k = 7$, 1”

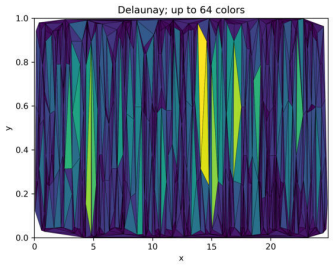

“k-logistic map with $k = 7$, 2”

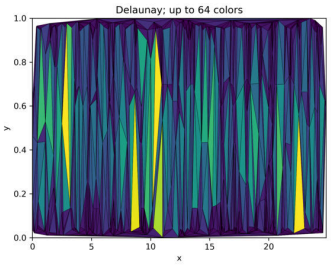

“k-logistic map with $k = 7$, 3”

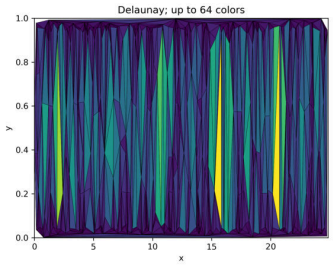

“k-logistic map with $k = 8$, 1”

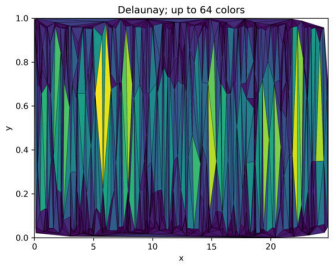

“k-logistic map with $k = 8$, 2”

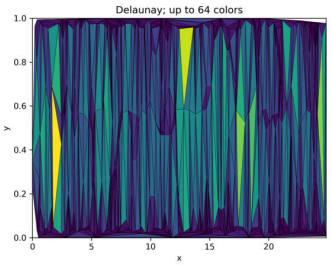

“k-logistic map with $k = 8$, 3”

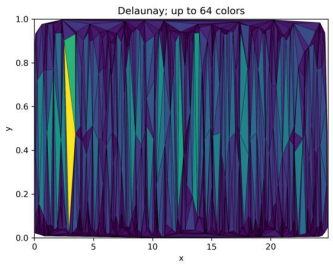

“k-logistic map with $k = 9$, 1”

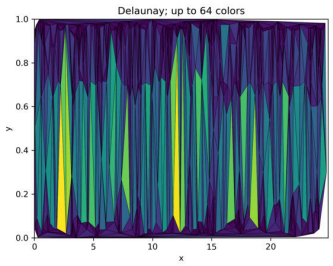

“k-logistic map with $k = 9$, 2”

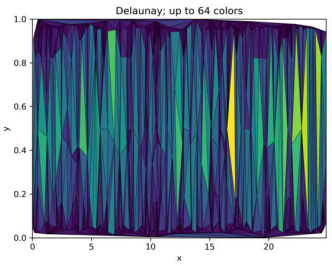

“k-logistic map with $k = 9$, 3”

Figure 162 – Delaunay triangulations of $> 2\sigma$ complex networks for networks with 5,000 vertices, k-logistic map from $k = 5$ to $k = 9$, $r = 3.99999$.
Source: By the author.

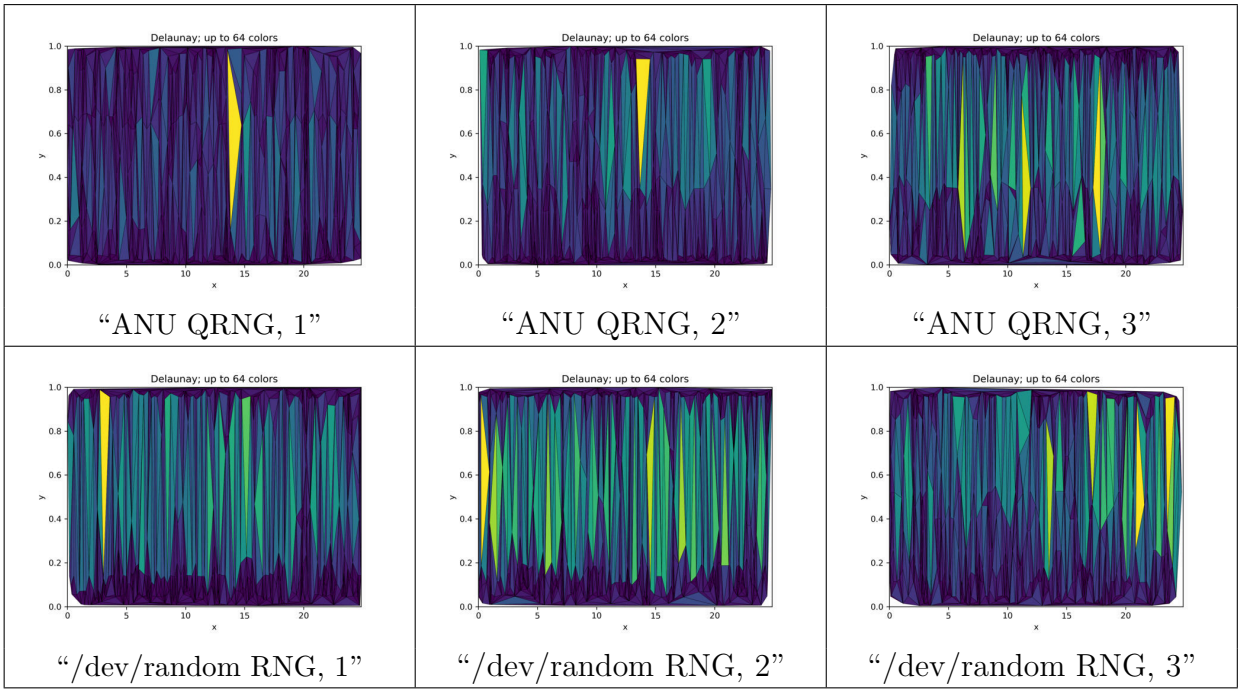

Figure 163 – Delaunay triangulations of $> 2\sigma$ complex networks for networks with 5,000 vertices. ANU Quantum and Linux /dev/random RNGs.
Source: By the author.

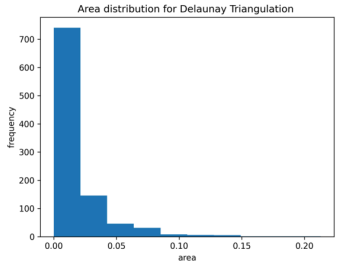

“k-logistic map with $k = 0$, 1”

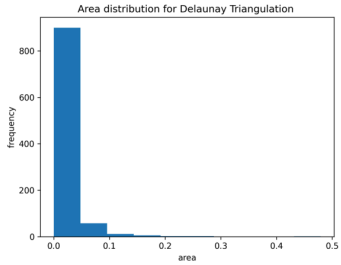

“k-logistic map with $k = 0$, 2”

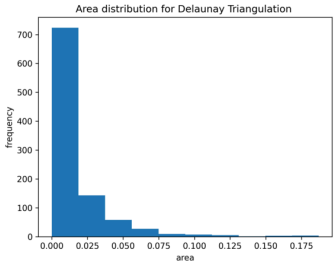

“k-logistic map with $k = 0$, 3”

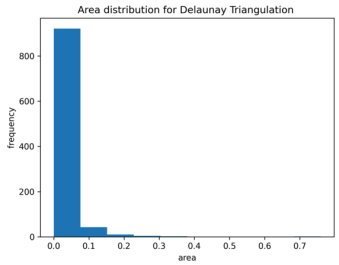

“k-logistic map with $k = 1$, 1”

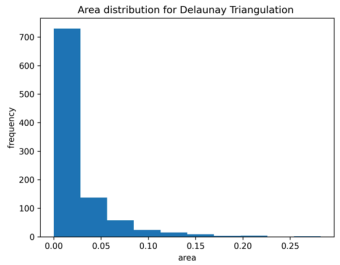

“k-logistic map with $k = 1$, 2”

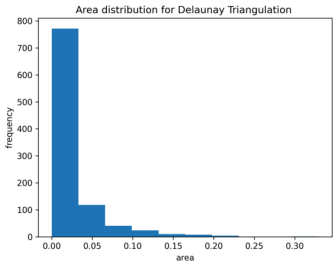

“k-logistic map with $k = 1$, 3”

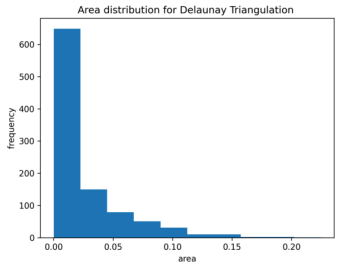

“k-logistic map with $k = 2$, 1”

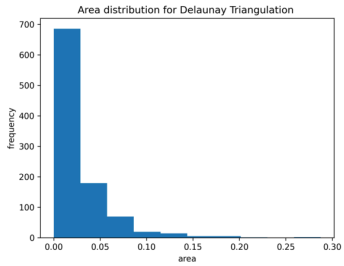

“k-logistic map with $k = 2$, 2”

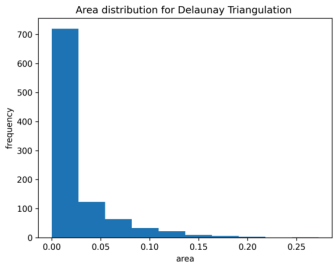

“k-logistic map with $k = 2$, 3”

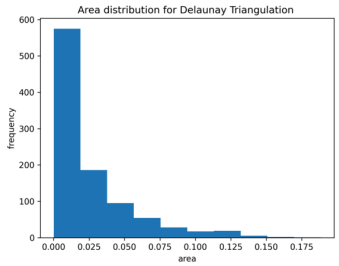

“k-logistic map with $k = 3$, 1”

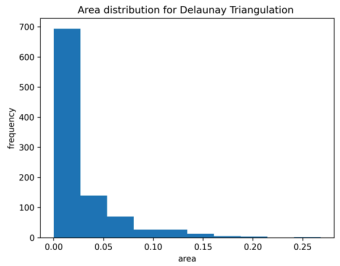

“k-logistic map with $k = 3$, 2”

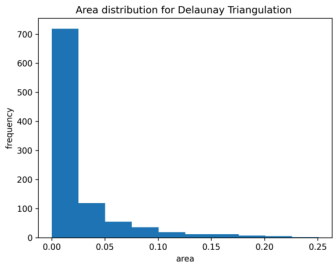

“k-logistic map with $k = 3$, 3”

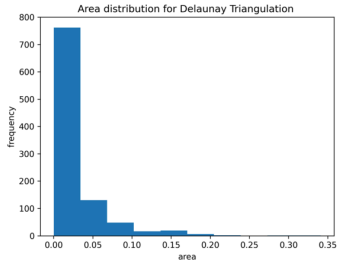

“k-logistic map with $k = 4$, 1”

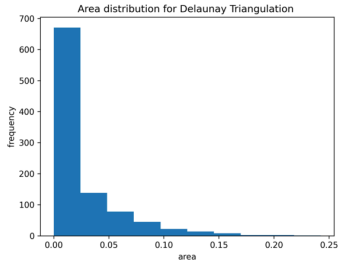

“k-logistic map with $k = 4$, 2”

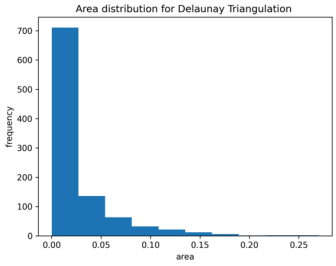

“k-logistic map with $k = 4$, 3”

Figure 164 – Histograms for Delaunay triangulations of $> 2\sigma$ complex networks for networks with 5,000 vertices, k-logistic map from $k = 0$ to $k = 4$, $r = 3.7$.
Source: By the author.

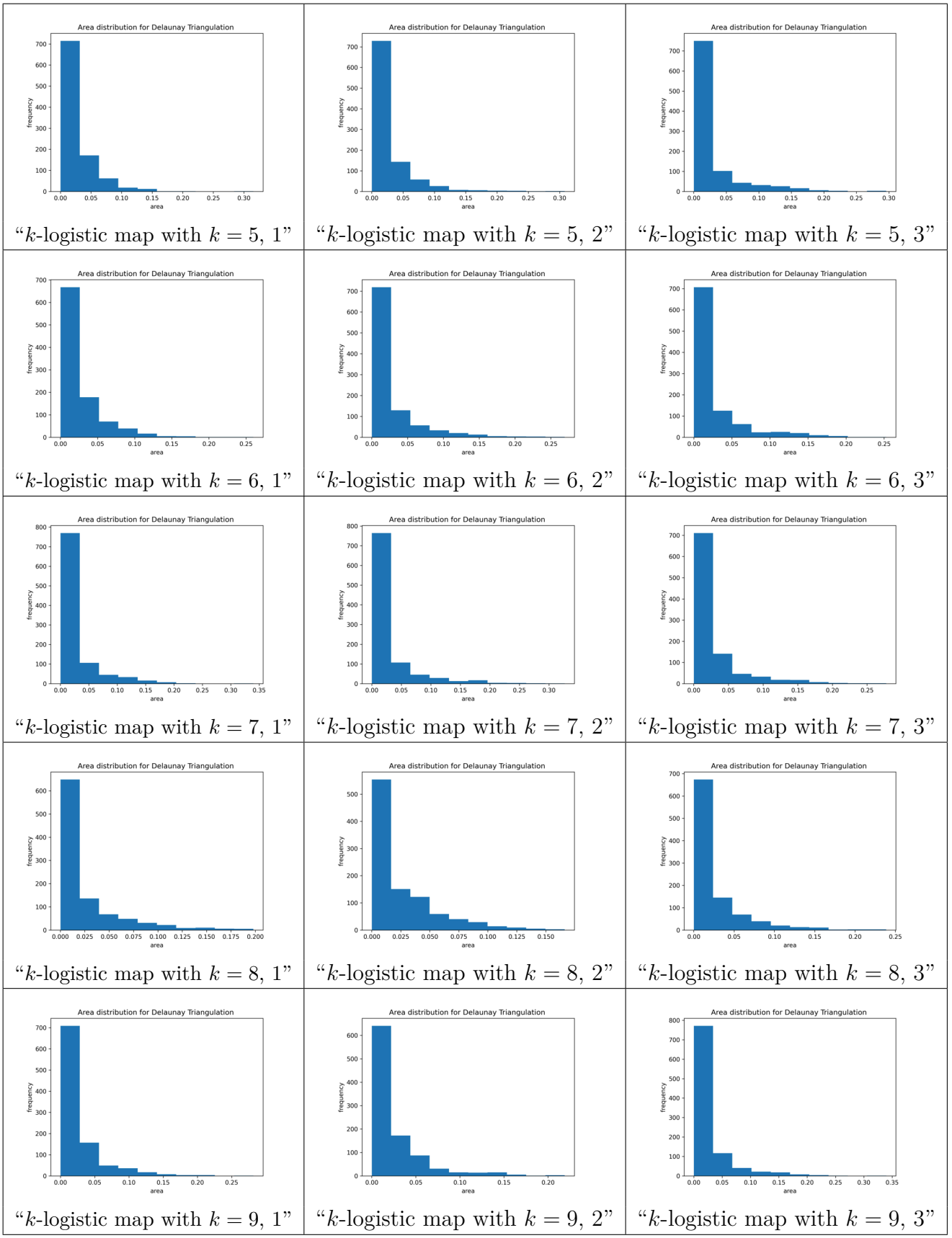

“k-logistic map with $k = 5$, 1” “k-logistic map with $k = 5$, 2” “k-logistic map with $k = 5$, 3”

“k-logistic map with $k = 6$, 1” “k-logistic map with $k = 6$, 2” “k-logistic map with $k = 6$, 3”

“k-logistic map with $k = 7$, 1” “k-logistic map with $k = 7$, 2” “k-logistic map with $k = 7$, 3”

“k-logistic map with $k = 8$, 1” “k-logistic map with $k = 8$, 2” “k-logistic map with $k = 8$, 3”

“k-logistic map with $k = 9$, 1” “k-logistic map with $k = 9$, 2” “k-logistic map with $k = 9$, 3”

Figure 165 – Histograms for Delaunay triangulations of $> 2\sigma$ complex networks for networks with 5,000 vertices, k-logistic map from $k = 5$ to $k = 9$, $r = 3.7$.
Source: By the author.

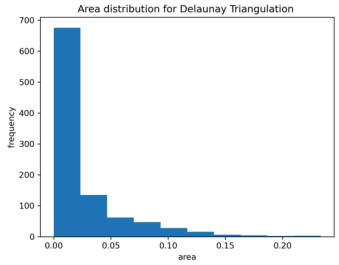

“k-logistic map with $k = 0$, 1”

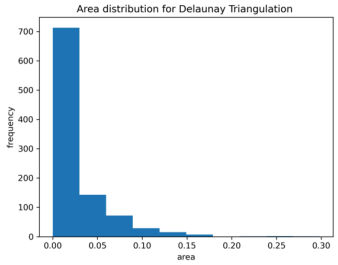

“k-logistic map with $k = 0$, 2”

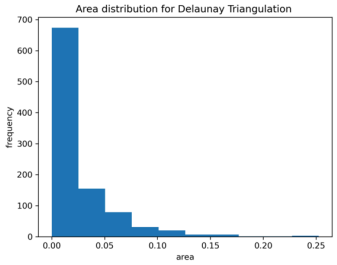

“k-logistic map with $k = 0$, 3”

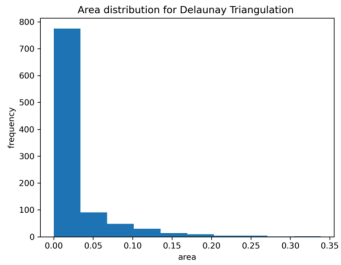

“k-logistic map with $k = 1$, 1”

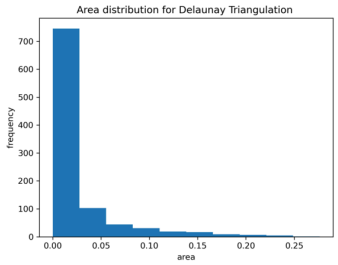

“k-logistic map with $k = 1$, 2”

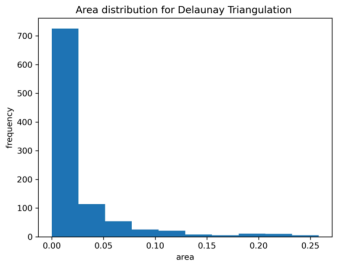

“k-logistic map with $k = 1$, 3”

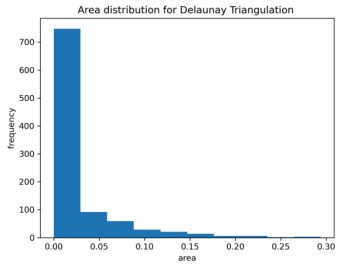

“k-logistic map with $k = 2$, 1”

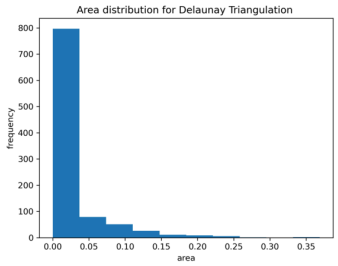

“k-logistic map with $k = 2$, 2”

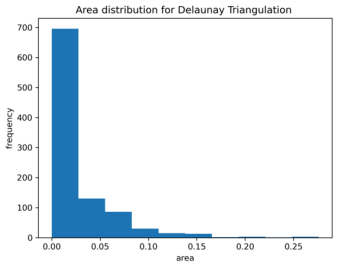

“k-logistic map with $k = 2$, 3”

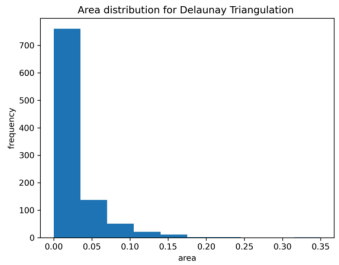

“k-logistic map with $k = 3$, 1”

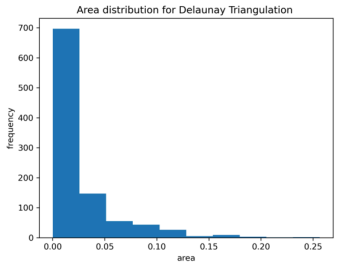

“k-logistic map with $k = 3$, 2”

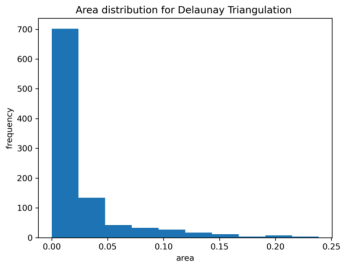

“k-logistic map with $k = 3$, 3”

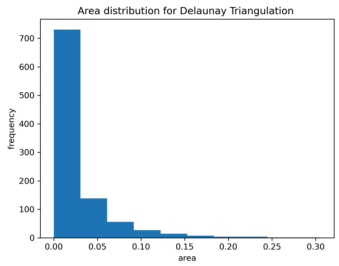

“k-logistic map with $k = 4$, 1”

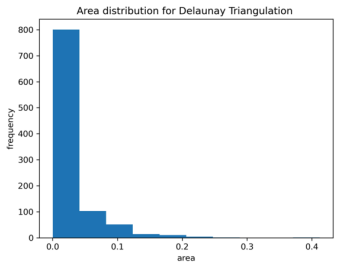

“k-logistic map with $k = 4$, 2”

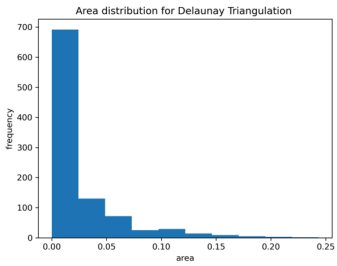

“k-logistic map with $k = 4$, 3”

Figure 166 – Histograms for Delaunay triangulations of $> 2\sigma$ complex networks for networks with 5,000 vertices, k-logistic map from $k = 0$ to $k = 4$, $r = 3.99999$. Source: By the author.

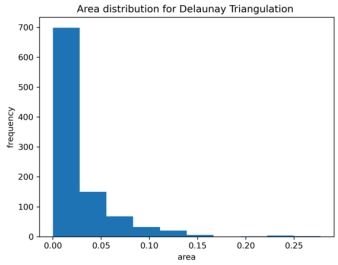

“k-logistic map with $k = 5$, 1”

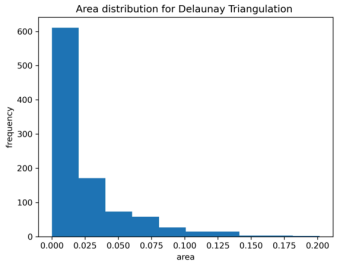

“k-logistic map with $k = 5$, 2”

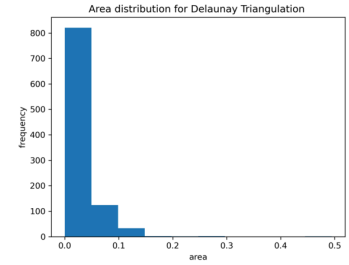

“k-logistic map with $k = 5$, 3”

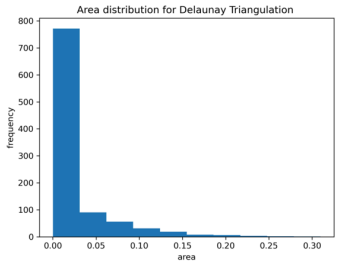

“k-logistic map with $k = 6$, 1”

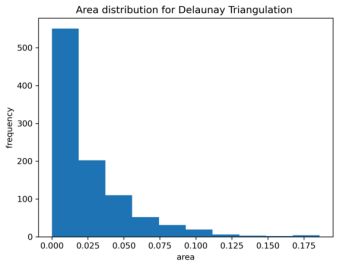

“k-logistic map with $k = 6$, 2”

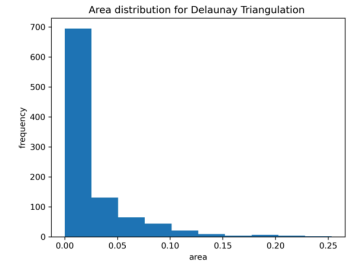

“k-logistic map with $k = 6$, 3”

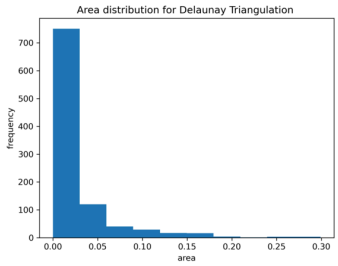

“k-logistic map with $k = 7$, 1”

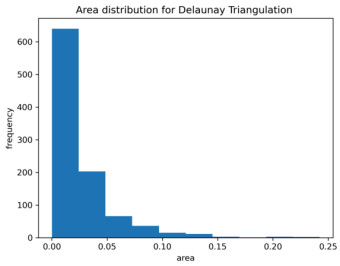

“k-logistic map with $k = 7$, 2”

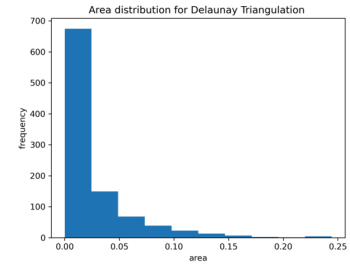

“k-logistic map with $k = 7$, 3”

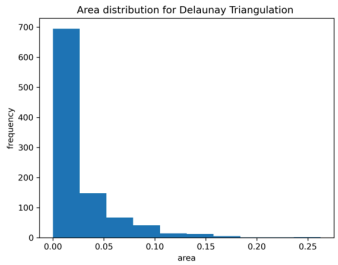

“k-logistic map with $k = 8$, 1”

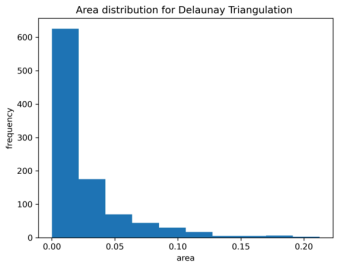

“k-logistic map with $k = 8$, 2”

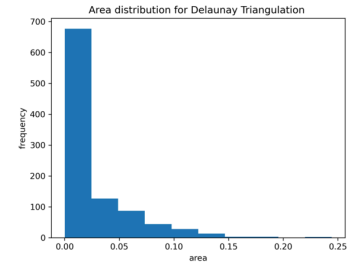

“k-logistic map with $k = 8$, 3”

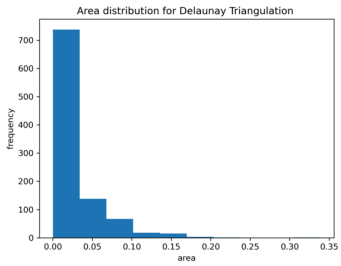

“k-logistic map with $k = 9$, 1”

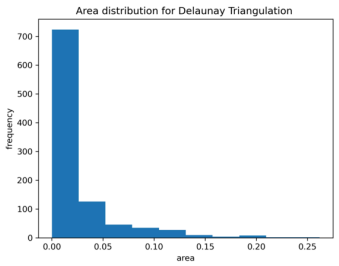

“k-logistic map with $k = 9$, 2”

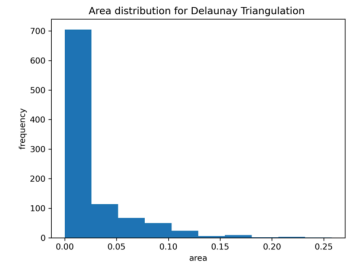

“k-logistic map with $k = 9$, 3”

Figure 167 – Histograms for Delaunay triangulations of $> 2\sigma$ complex networks for networks with 5,000 vertices, k-logistic map from $k = 5$ to $k = 9$, $r = 3.99999$. Source: By the author.

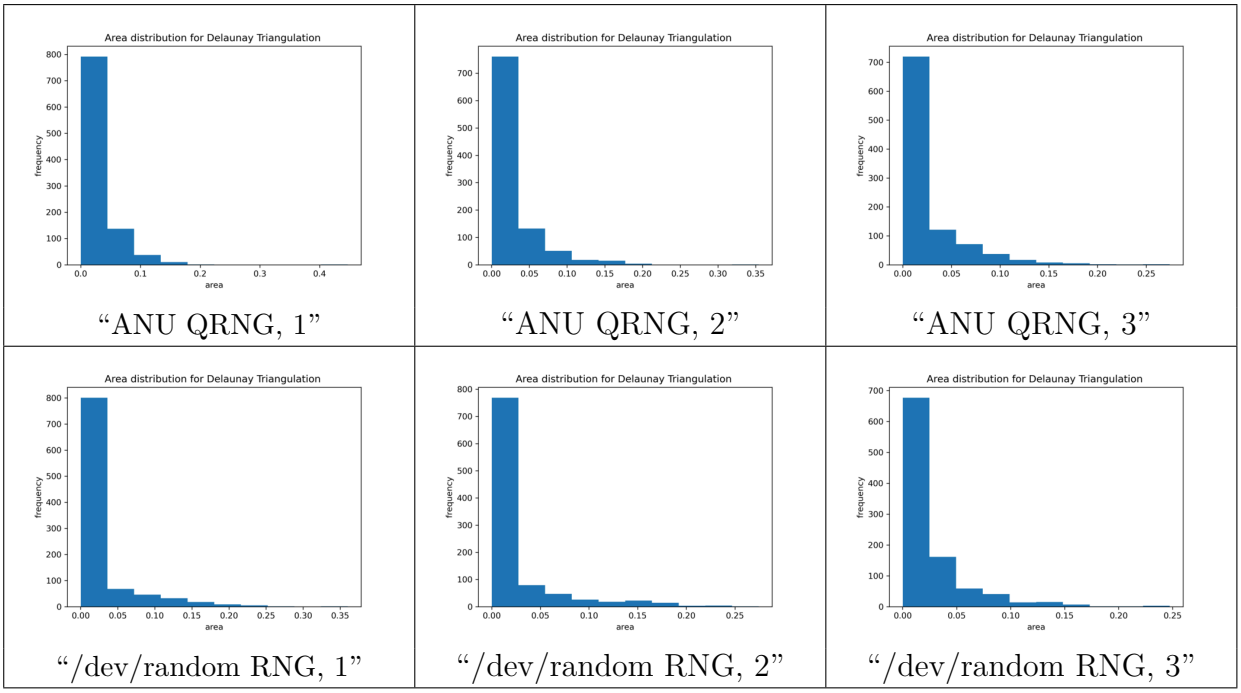

Figure 168 – Histograms for Delaunay triangulations of $> 2\sigma$ complex networks for networks with 5,000 vertices. ANU Quantum and Linux /dev/random RNGs. Source: By the author.

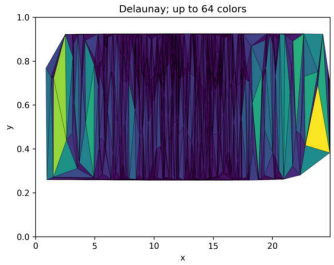

“k-logistic map with $k = 0$, 1”

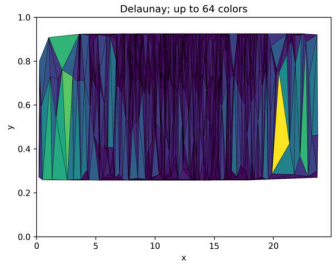

“k-logistic map with $k = 0$, 2”

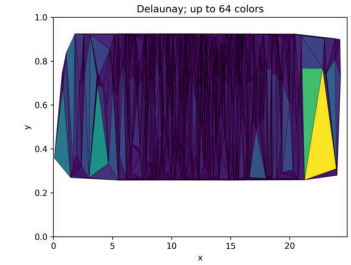

“k-logistic map with $k = 0$, 3”

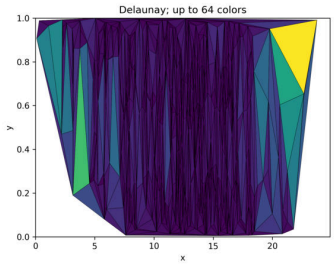

“k-logistic map with $k = 1$, 1”

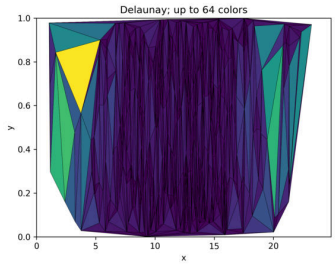

“k-logistic map with $k = 1$, 2”

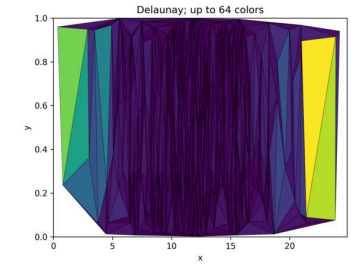

“k-logistic map with $k = 1$, 3”

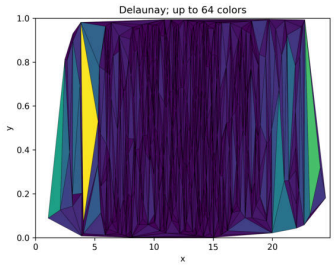

“k-logistic map with $k = 2$, 1”

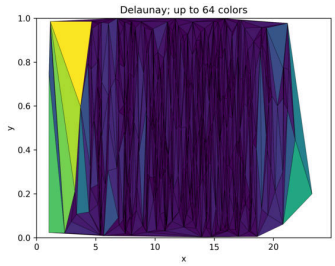

“k-logistic map with $k = 2$, 2”

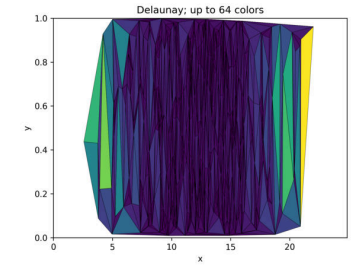

“k-logistic map with $k = 2$, 3”

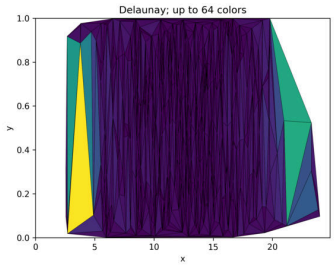

“k-logistic map with $k = 3$, 1”

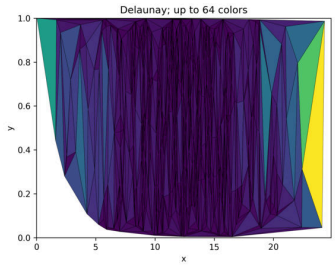

“k-logistic map with $k = 3$, 2”

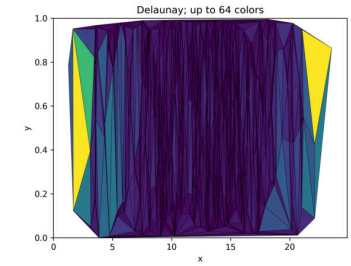

“k-logistic map with $k = 3$, 3”

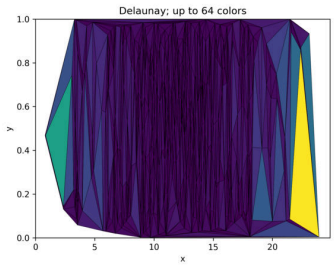

“k-logistic map with $k = 4$, 1”

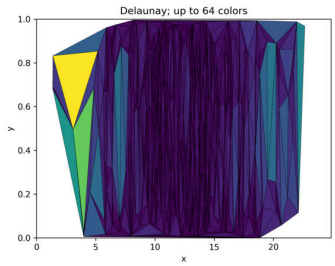

“k-logistic map with $k = 4$, 2”

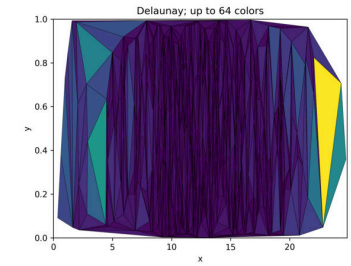

“k-logistic map with $k = 4$, 3”

Figure 169 – Delaunay triangulations of $< -1\sigma$ complex networks for networks with 5,000 vertices, k-logistic map from $k = 0$ to $k = 4$, $r = 3.7$.
Source: By the author.

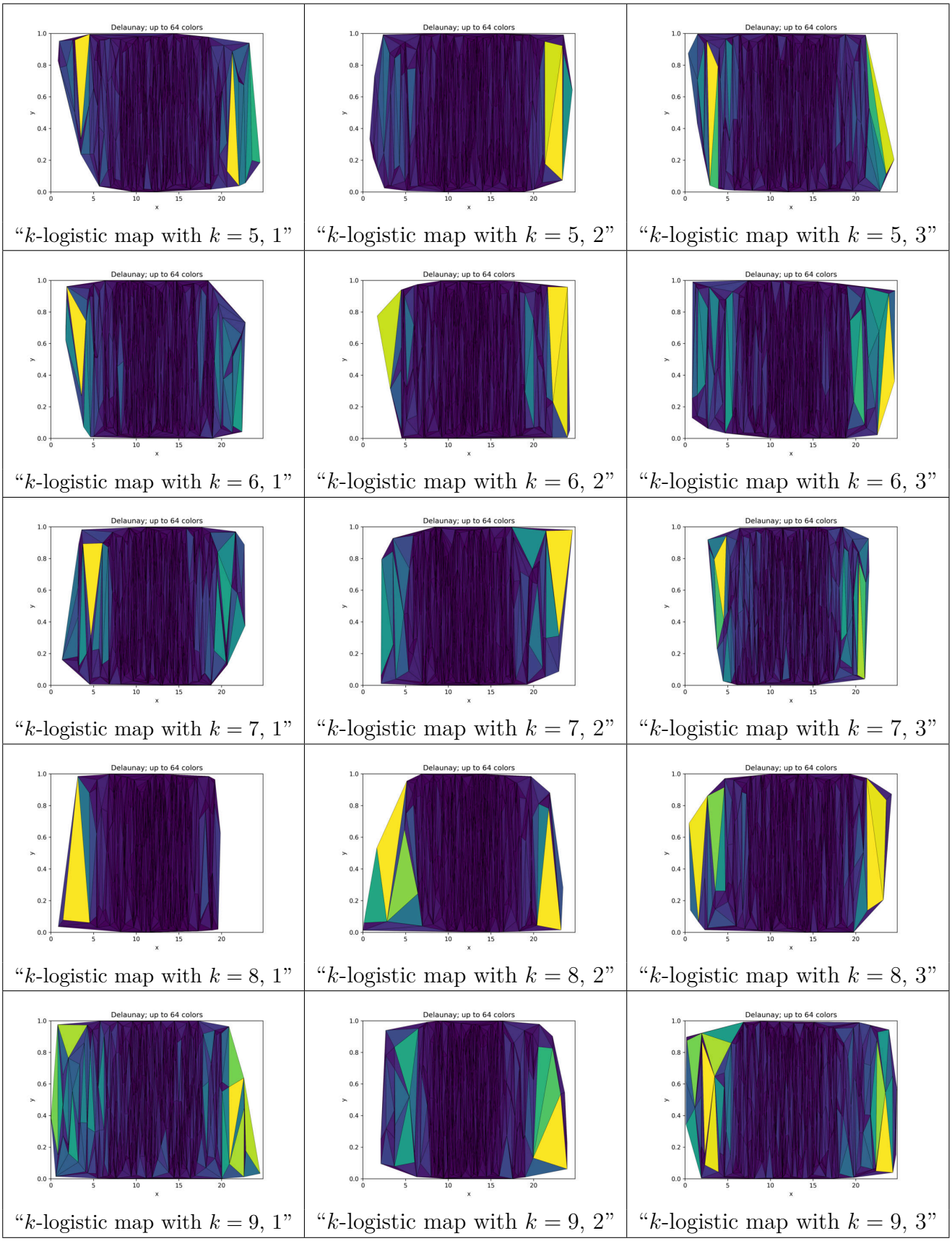

Figure 170 – Delaunay triangulations of $< -1\sigma$ complex networks for networks with 5,000 vertices, k-logistic map from $k = 5$ to $k = 9$, $r = 3.7$.
Source: By the author.

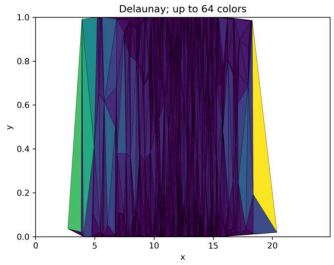

“k-logistic map with $k = 0$, 1”

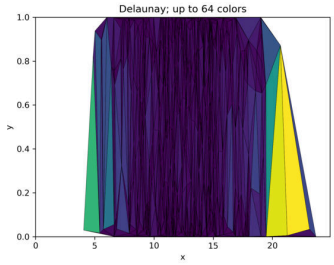

“k-logistic map with $k = 0$, 2”

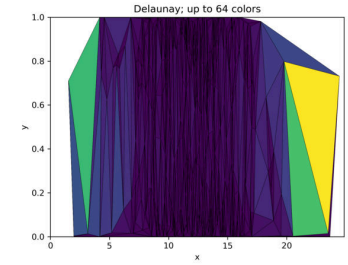

“k-logistic map with $k = 0$, 3”

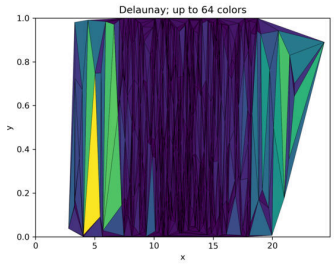

“k-logistic map with $k = 1$, 1”

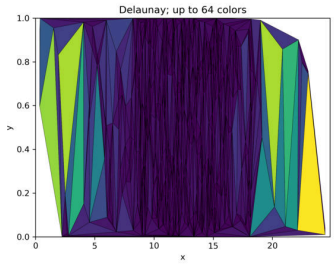

“k-logistic map with $k = 1$, 2”

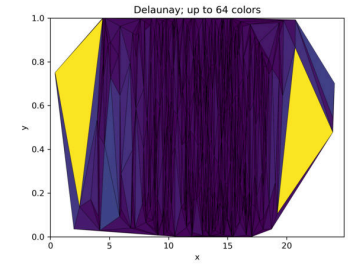

“k-logistic map with $k = 1$, 3”

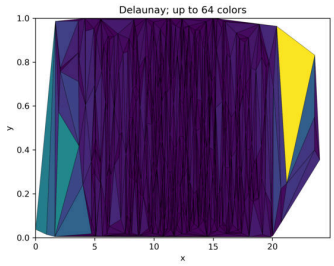

“k-logistic map with $k = 2$, 1”

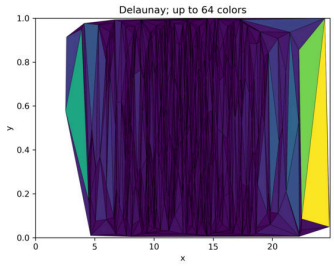

“k-logistic map with $k = 2$, 2”

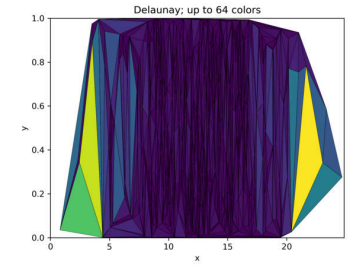

“k-logistic map with $k = 2$, 3”

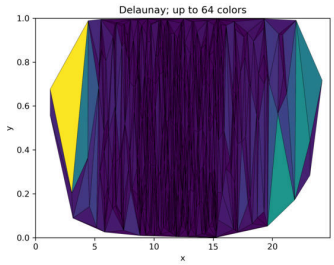

“k-logistic map with $k = 3$, 1”

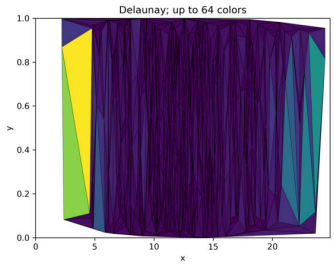

“k-logistic map with $k = 3$, 2”

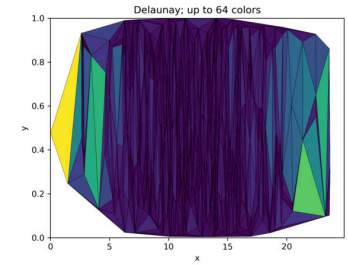

“k-logistic map with $k = 3$, 3”

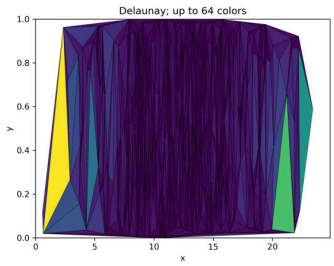

“k-logistic map with $k = 4$, 1”

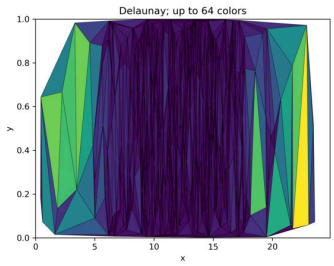

“k-logistic map with $k = 4$, 2”

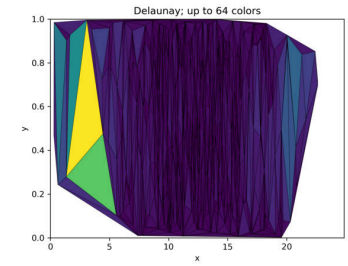

“k-logistic map with $k = 4$, 3”

Figure 171 – Delaunay triangulations of $< -1\sigma$ complex networks for networks with 5,000 vertices, k-logistic map from $k = 0$ to $k = 4$, $r = 3.99999$.
Source: By the author.

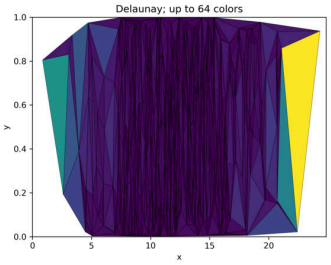

“k-logistic map with $k = 5$, 1”

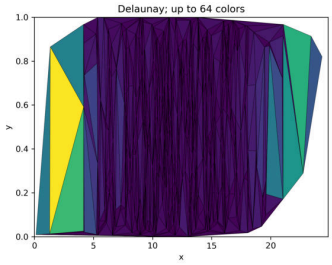

“k-logistic map with $k = 5$, 2”

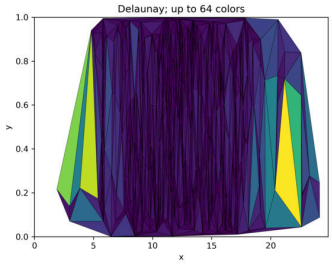

“k-logistic map with $k = 5$, 3”

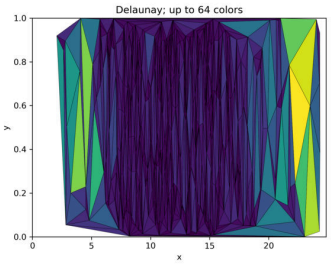

“k-logistic map with $k = 6$, 1”

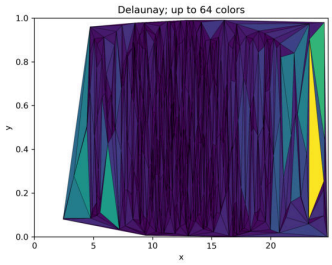

“k-logistic map with $k = 6$, 2”

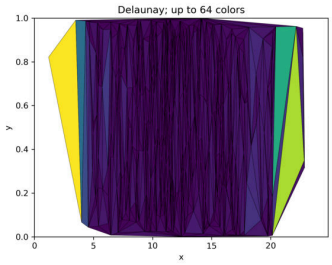

“k-logistic map with $k = 6$, 3”

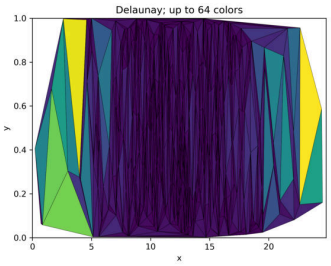

“k-logistic map with $k = 7$, 1”

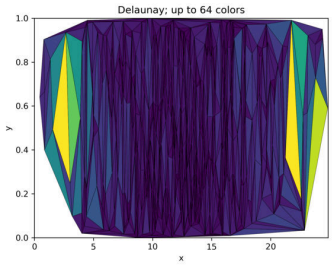

“k-logistic map with $k = 7$, 2”

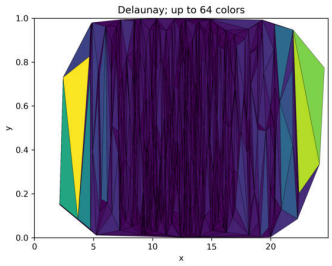

“k-logistic map with $k = 7$, 3”

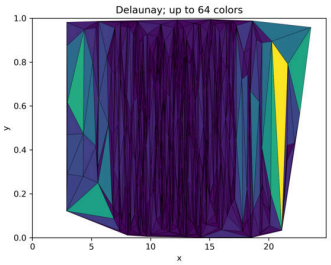

“k-logistic map with $k = 8$, 1”

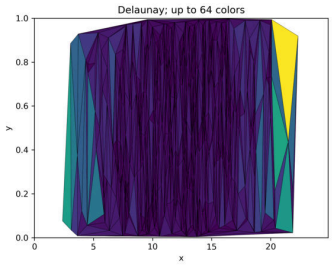

“k-logistic map with $k = 8$, 2”

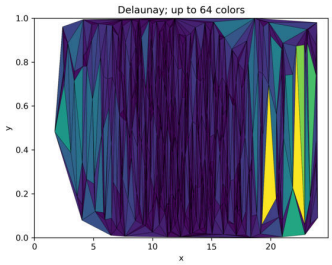

“k-logistic map with $k = 8$, 3”

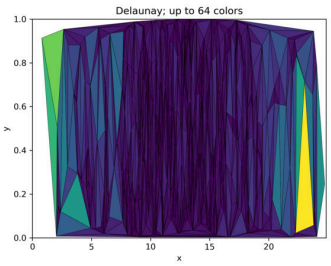

“k-logistic map with $k = 9$, 1”

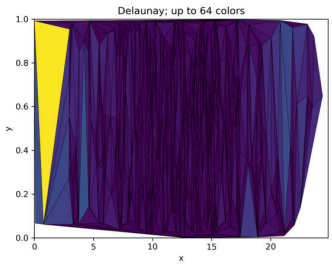

“k-logistic map with $k = 9$, 2”

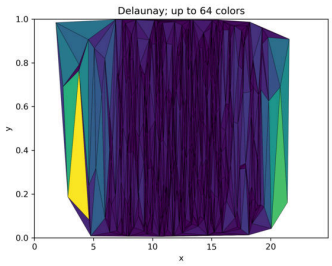

“k-logistic map with $k = 9$, 3”

Figure 172 – Delaunay triangulations of $< -1\sigma$ complex networks for networks with 5,000 vertices, k-logistic map from $k = 5$ to $k = 9$, $r = 3.99999$.
Source: By the author.

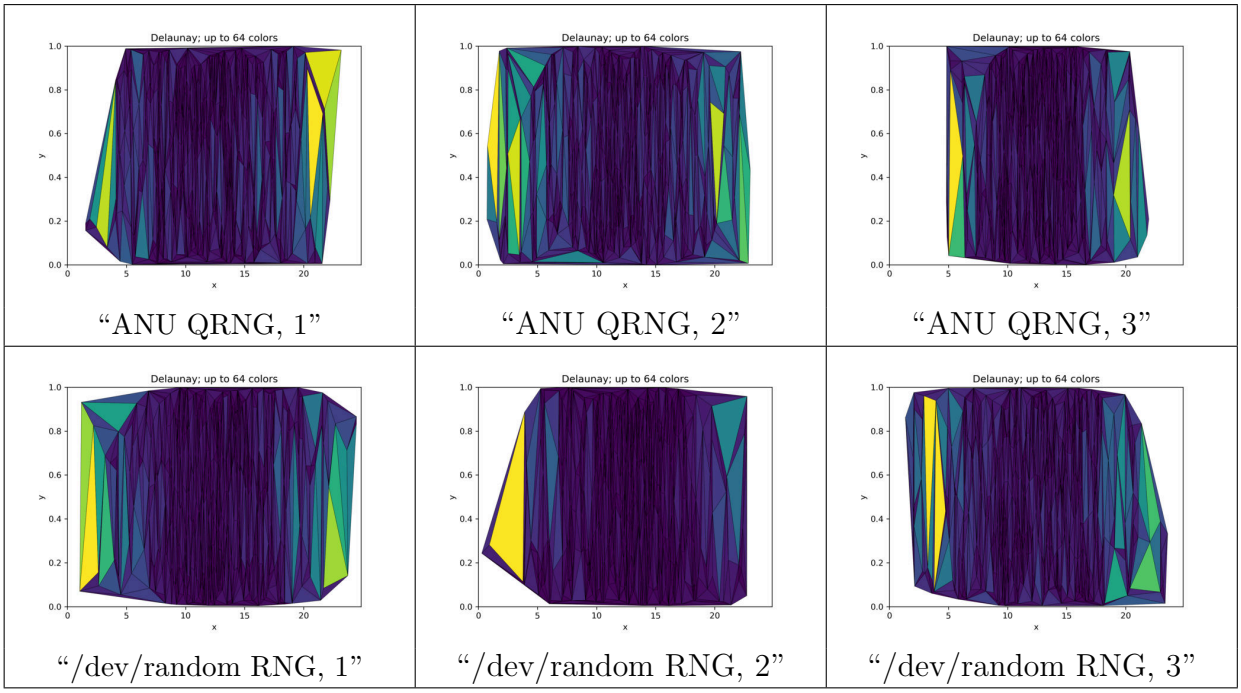

Figure 173 – Delaunay triangulations of $< -1\sigma$ complex networks for networks with 5,000 vertices. ANU Quantum and Linux /dev/random RNGs.
Source: By the author.

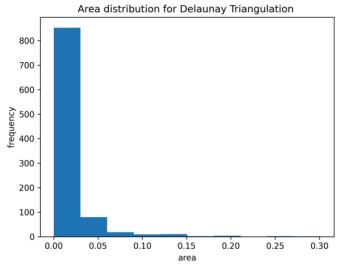

“k-logistic map with $k = 0$, 1”

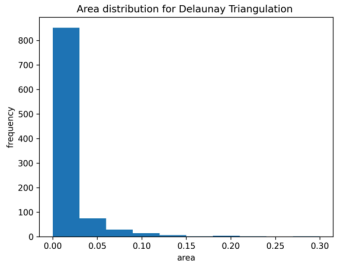

“k-logistic map with $k = 0$, 2”

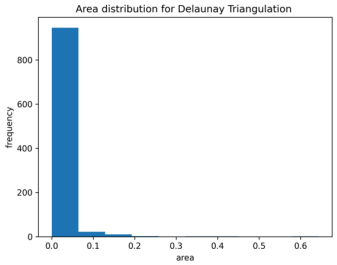

“k-logistic map with $k = 0$, 3”

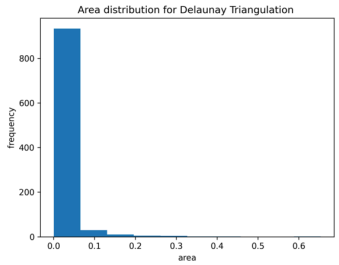

“k-logistic map with $k = 1$, 1”

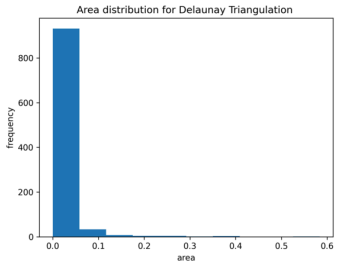

“k-logistic map with $k = 1$, 2”

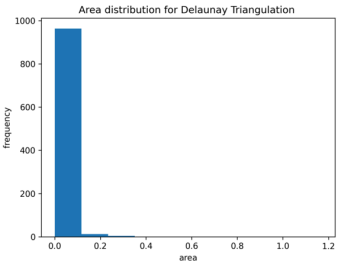

“k-logistic map with $k = 1$, 3”

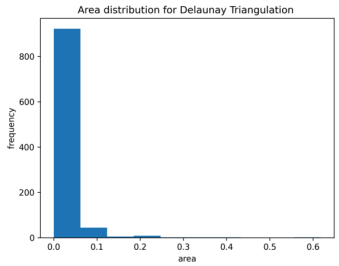

“k-logistic map with $k = 2$, 1”

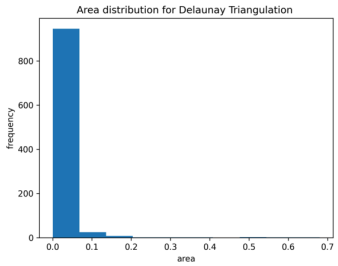

“k-logistic map with $k = 2$, 2”

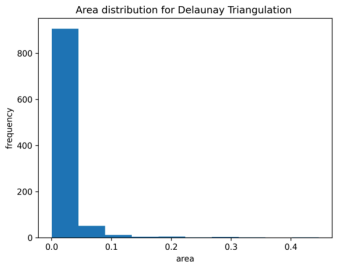

“k-logistic map with $k = 2$, 3”

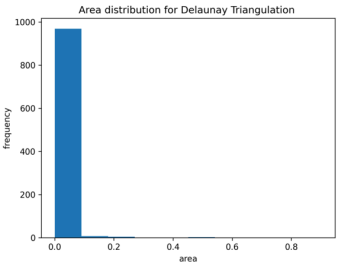

“k-logistic map with $k = 3$, 1”

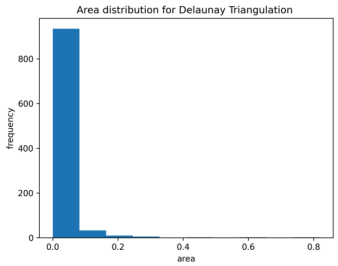

“k-logistic map with $k = 3$, 2”

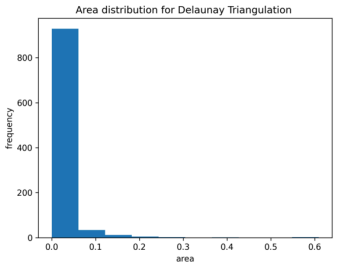

“k-logistic map with $k = 3$, 3”

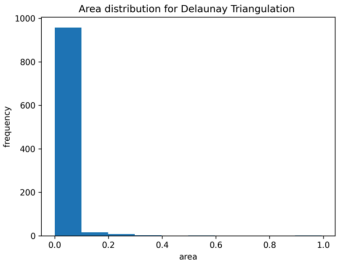

“k-logistic map with $k = 4$, 1”

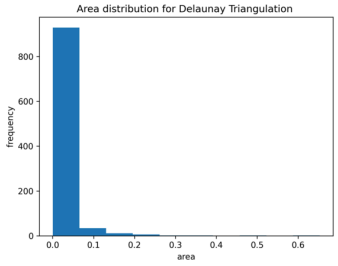

“k-logistic map with $k = 4$, 2”

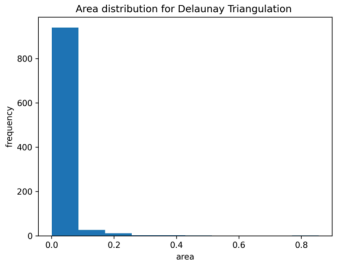

“k-logistic map with $k = 4$, 3”

Figure 174 – Histograms for Delaunay triangulations of $< -1\sigma$ complex networks for networks with 5,000 vertices, k-logistic map from $k = 0$ to $k = 4$, $r = 3.7$. Source: By the author.

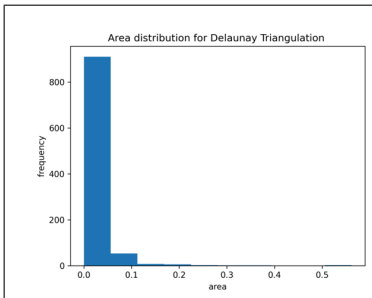

“k-logistic map with $k = 5$, 1”

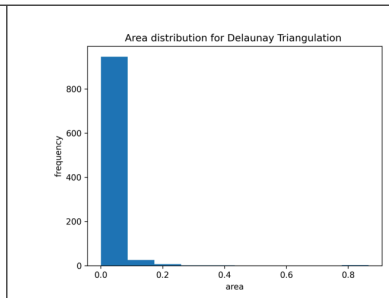

“k-logistic map with $k = 5$, 2”

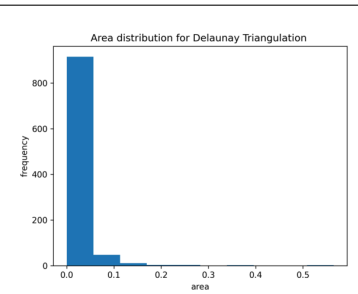

“k-logistic map with $k = 5$, 3”

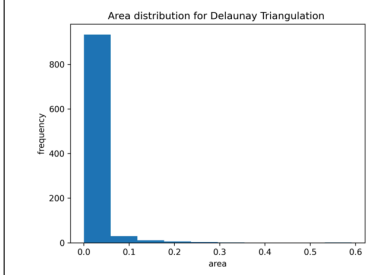

“k-logistic map with $k = 6$, 1”

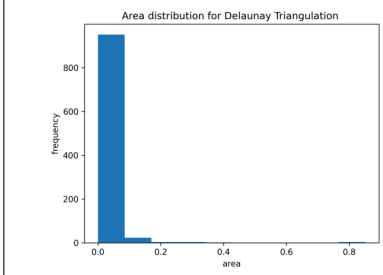

“k-logistic map with $k = 6$, 2”

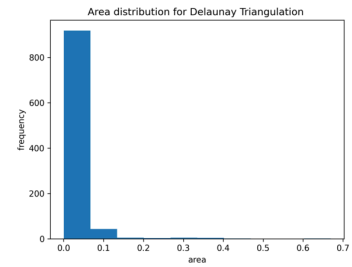

“k-logistic map with $k = 6$, 3”

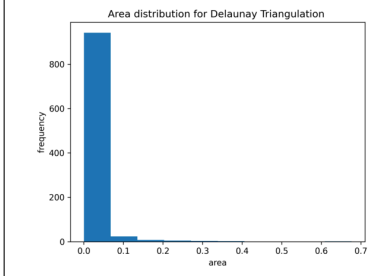

“k-logistic map with $k = 7$, 1”

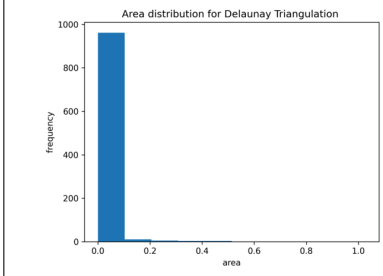

“k-logistic map with $k = 7$, 2”

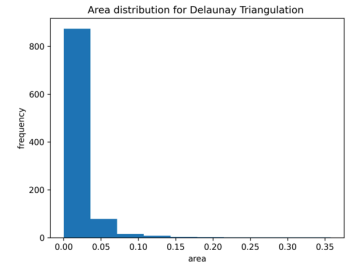

“k-logistic map with $k = 7$, 3”

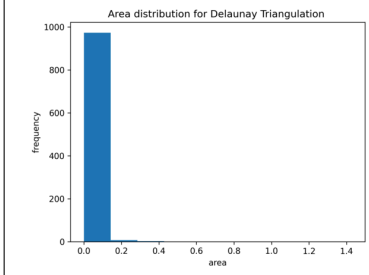

“k-logistic map with $k = 8$, 1”

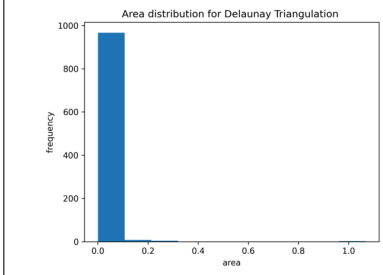

“k-logistic map with $k = 8$, 2”

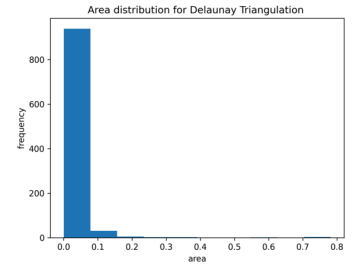

“k-logistic map with $k = 8$, 3”

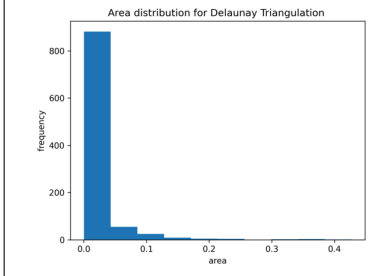

“k-logistic map with $k = 9$, 1”

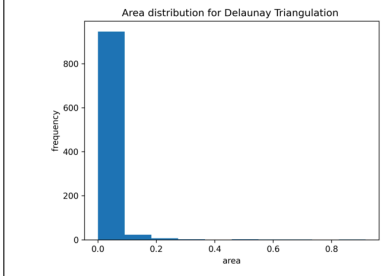

“k-logistic map with $k = 9$, 2”

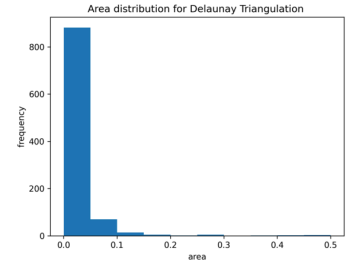

“k-logistic map with $k = 9$, 3”

Figure 175 – Histograms for Delaunay triangulations of $< -1\sigma$ complex networks for networks with 5,000 vertices, k-logistic map from $k = 5$ to $k = 9$, $r = 3.7$. Source: By the author.

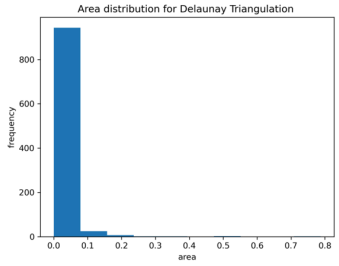

“k-logistic map with $k = 0$, 1”

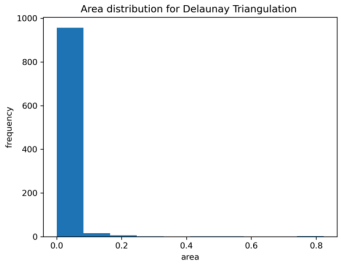

“k-logistic map with $k = 0$, 2”

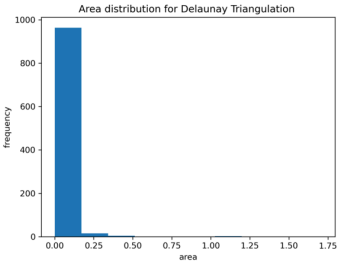

“k-logistic map with $k = 0$, 3”

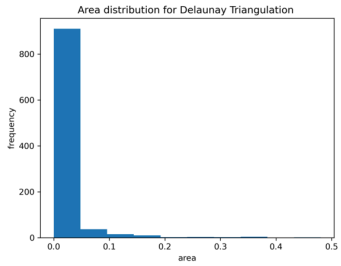

“k-logistic map with $k = 1$, 1”

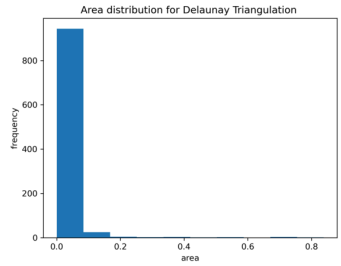

“k-logistic map with $k = 1$, 2”

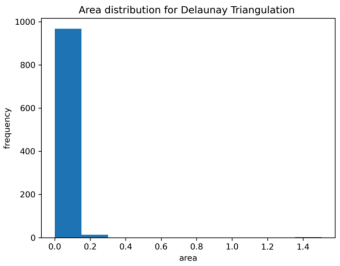

“k-logistic map with $k = 1$, 3”

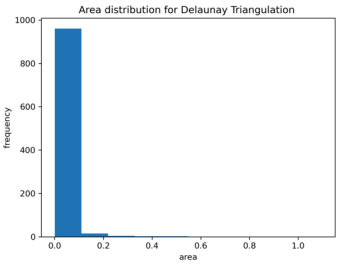

“k-logistic map with $k = 2$, 1”

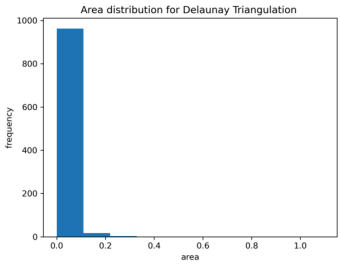

“k-logistic map with $k = 2$, 2”

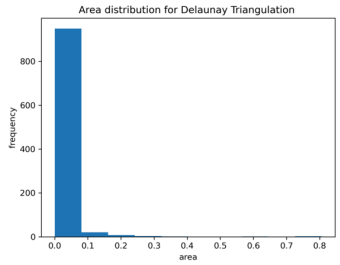

“k-logistic map with $k = 2$, 3”

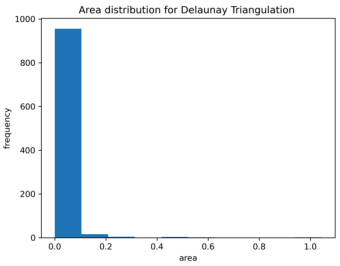

“k-logistic map with $k = 3$, 1”

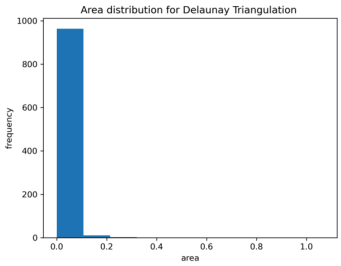

“k-logistic map with $k = 3$, 2”

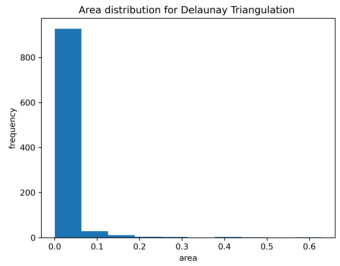

“k-logistic map with $k = 3$, 3”

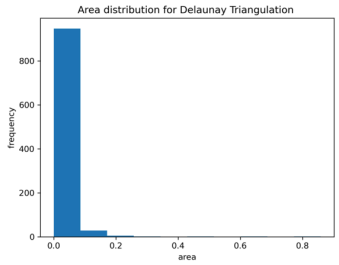

“k-logistic map with $k = 4$, 1”

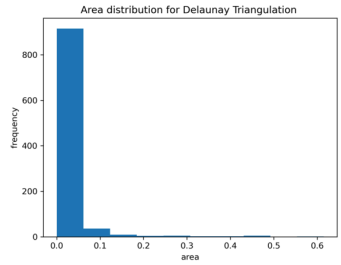

“k-logistic map with $k = 4$, 2”

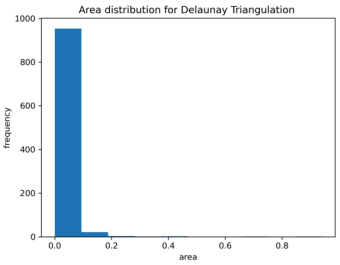

“k-logistic map with $k = 4$, 3”

Figure 176 – Histograms for Delaunay triangulations of $< -1\sigma$ complex networks for networks with 5,000 vertices, k-logistic map from $k = 0$ to $k = 4$, $r = 3.99999$.
Source: By the author.

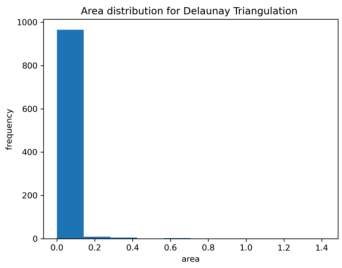

“k-logistic map with $k = 5$, 1”

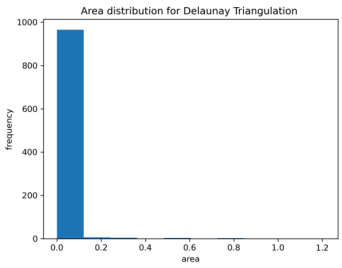

“k-logistic map with $k = 5$, 2”

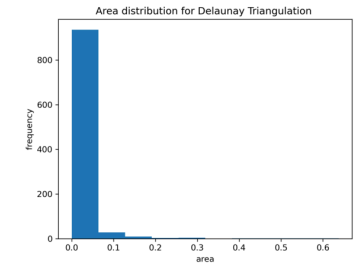

“k-logistic map with $k = 5$, 3”

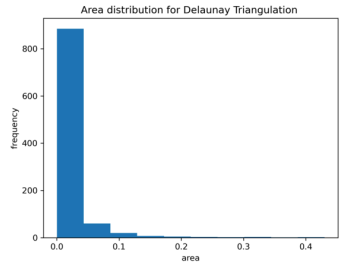

“k-logistic map with $k = 6$, 1”

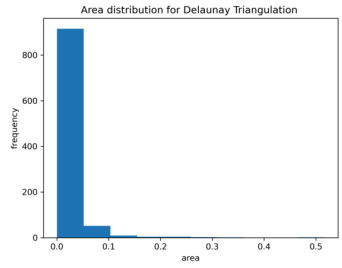

“k-logistic map with $k = 6$, 2”

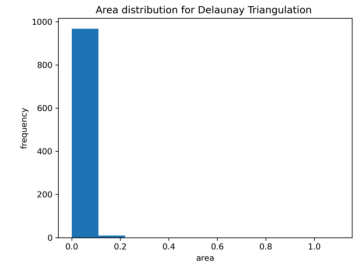

“k-logistic map with $k = 6$, 3”

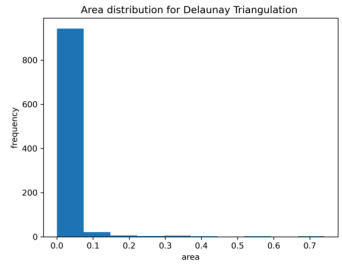

“k-logistic map with $k = 7$, 1”

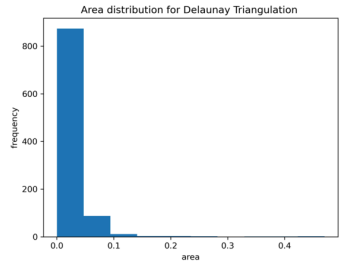

“k-logistic map with $k = 7$, 2”

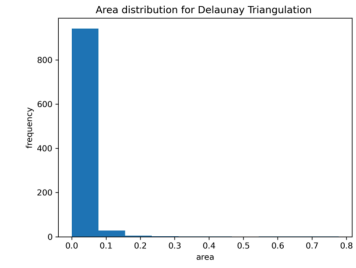

“k-logistic map with $k = 7$, 3”

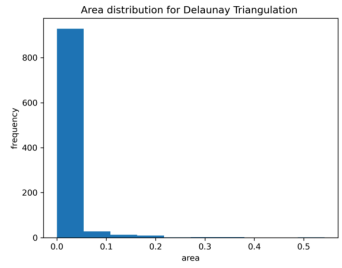

“k-logistic map with $k = 8$, 1”

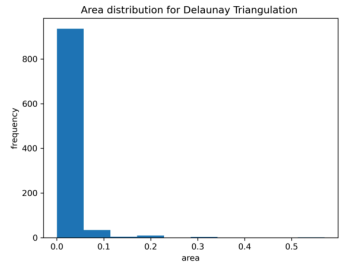

“k-logistic map with $k = 8$, 2”

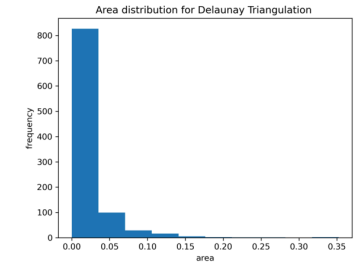

“k-logistic map with $k = 8$, 3”

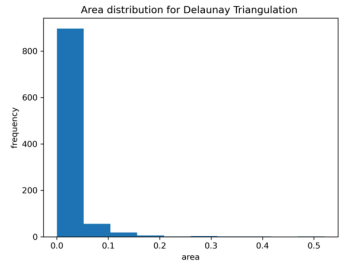

“k-logistic map with $k = 9$, 1”

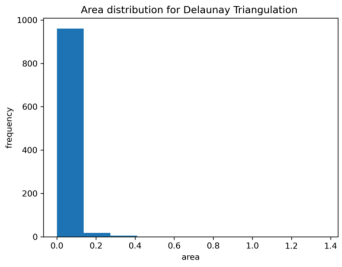

“k-logistic map with $k = 9$, 2”

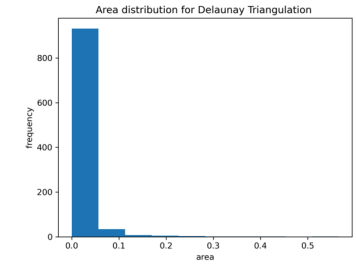

“k-logistic map with $k = 9$, 3”

Figure 177 – Histograms for Delaunay triangulations of $< -1\sigma$ complex networks for networks with 5,000 vertices, k-logistic map from $k = 5$ to $k = 9$, $r = 3.99999$.
Source: By the author.

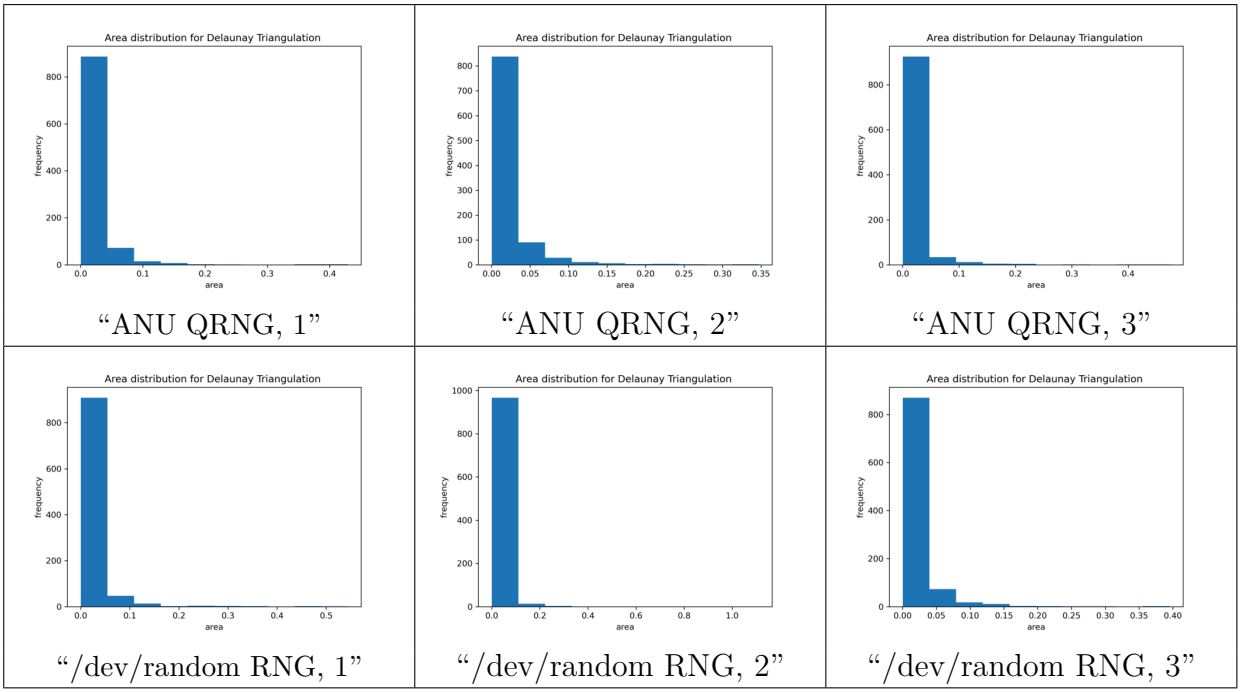

Figure 178 – Histograms for Delaunay triangulations of $< -1\sigma$ complex networks for networks with 5,000 vertices. ANU Quantum and Linux /dev/random RNGs. Source: By the author.

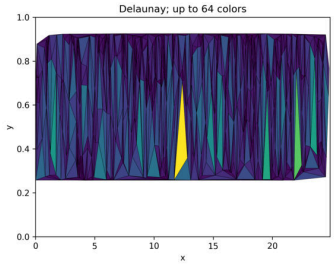

“k-logistic map with $k = 0$, 1”

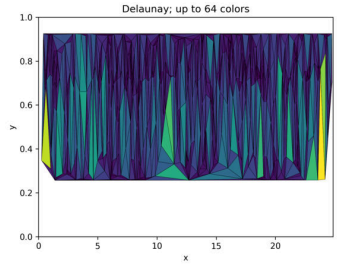

“k-logistic map with $k = 0$, 2”

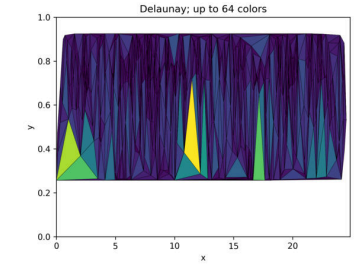

“k-logistic map with $k = 0$, 3”

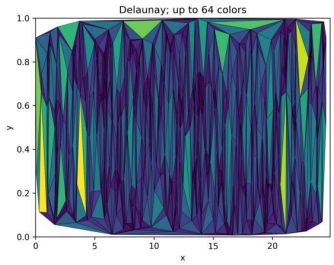

“k-logistic map with $k = 1$, 1”

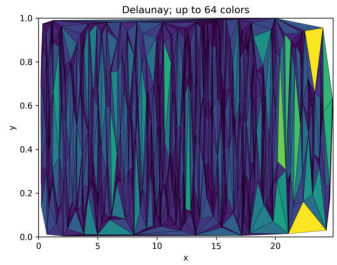

“k-logistic map with $k = 1$, 2”

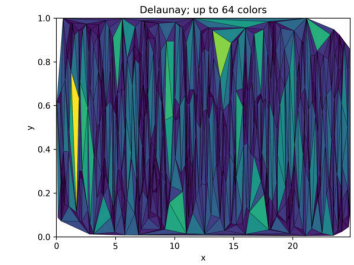

“k-logistic map with $k = 1$, 3”

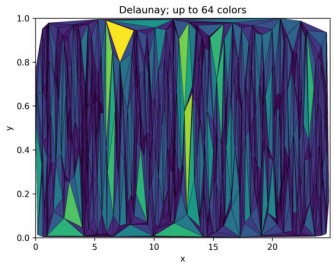

“k-logistic map with $k = 2$, 1”

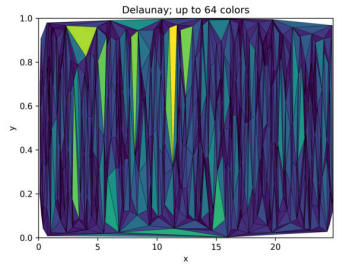

“k-logistic map with $k = 2$, 2”

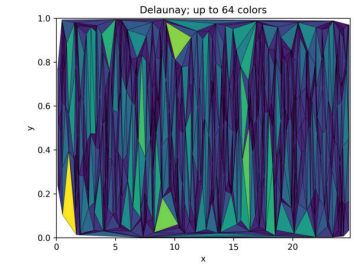

“k-logistic map with $k = 2$, 3”

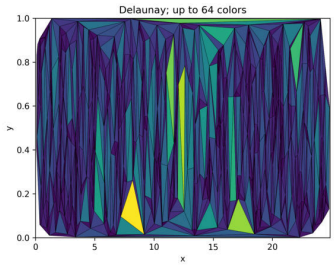

“k-logistic map with $k = 3$, 1”

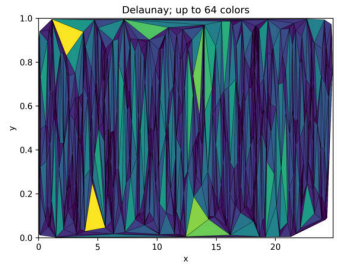

“k-logistic map with $k = 3$, 2”

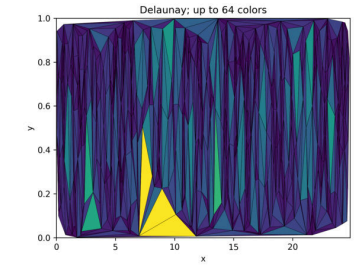

“k-logistic map with $k = 3$, 3”

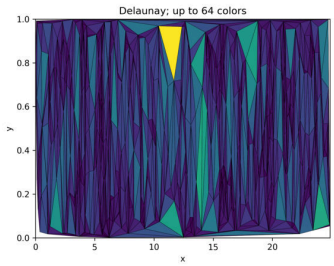

“k-logistic map with $k = 4$, 1”

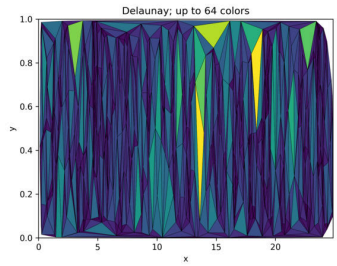

“k-logistic map with $k = 4$, 2”

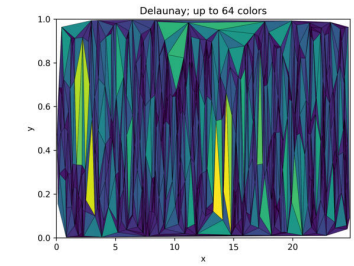

“k-logistic map with $k = 4$, 3”

Figure 179 – Delaunay triangulations of $< -2\sigma$ complex networks for networks with 5,000 vertices, k-logistic map from $k = 0$ to $k = 4$, $r = 3.7$.
Source: By the author.

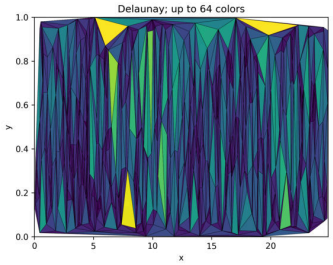

“k-logistic map with $k = 5$, 1”

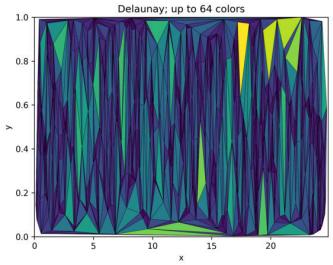

“k-logistic map with $k = 5$, 2”

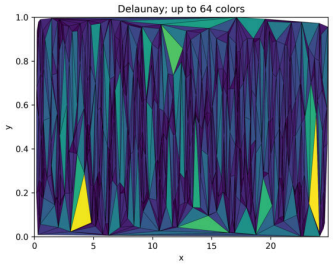

“k-logistic map with $k = 5$, 3”

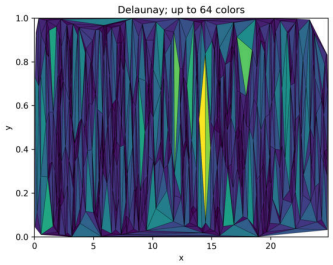

“k-logistic map with $k = 6$, 1”

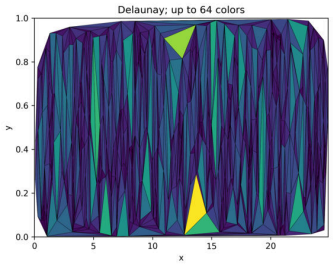

“k-logistic map with $k = 6$, 2”

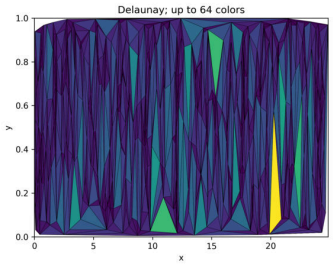

“k-logistic map with $k = 6$, 3”

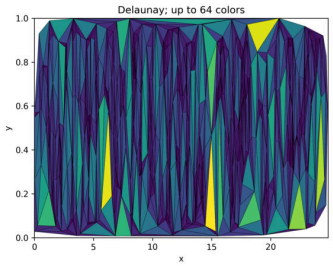

“k-logistic map with $k = 7$, 1”

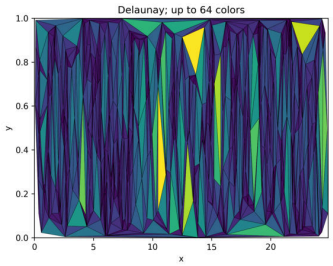

“k-logistic map with $k = 7$, 2”

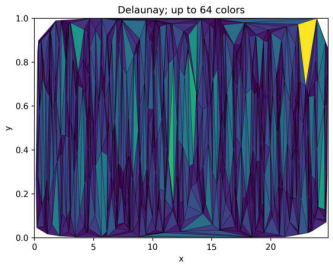

“k-logistic map with $k = 7$, 3”

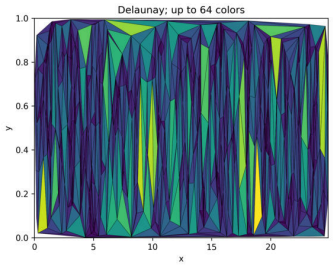

“k-logistic map with $k = 8$, 1”

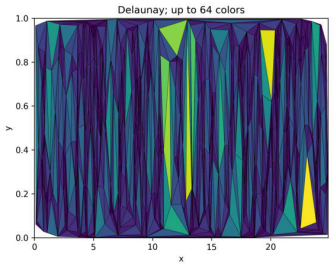

“k-logistic map with $k = 8$, 2”

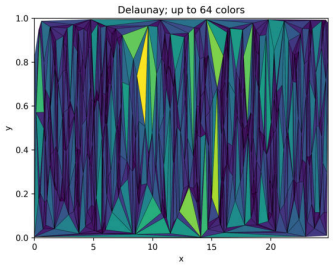

“k-logistic map with $k = 8$, 3”

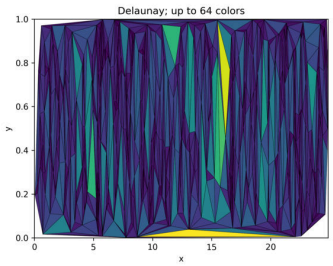

“k-logistic map with $k = 9$, 1”

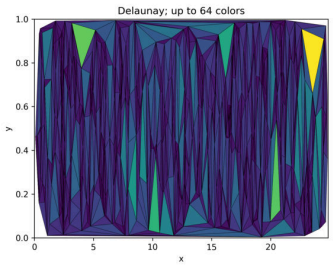

“k-logistic map with $k = 9$, 2”

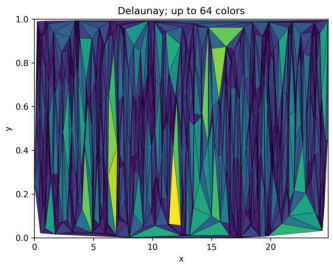

“k-logistic map with $k = 9$, 3”

Figure 180 – Delaunay triangulations of $< -2\sigma$ complex networks for networks with 5,000 vertices, k-logistic map from $k = 5$ to $k = 9$, $r = 3.7$.
Source: By the author.

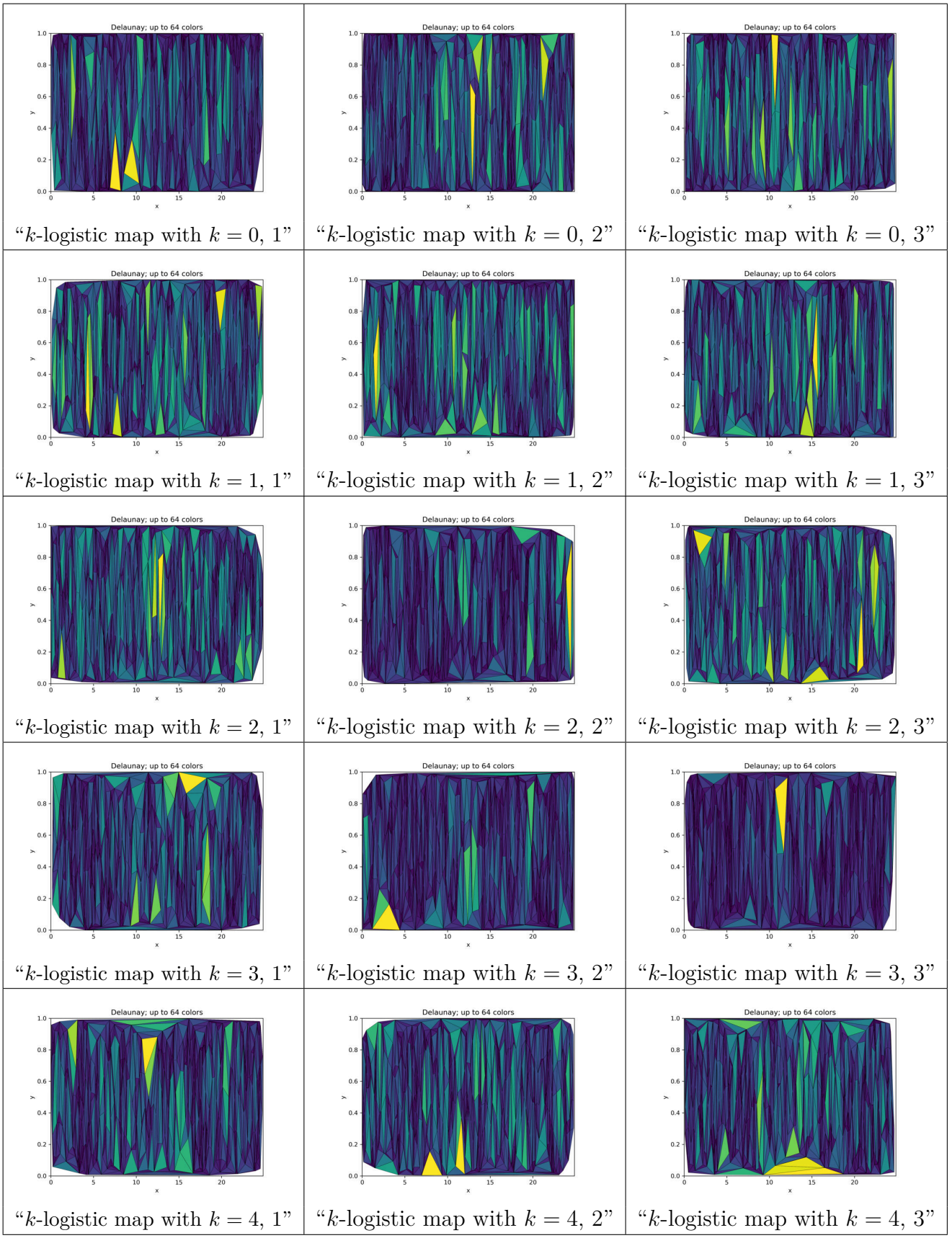

Figure 181 – Delaunay triangulations of $< -2\sigma$ complex networks for networks with 5,000 vertices, k-logistic map from $k = 0$ to $k = 4$, $r = 3.99999$.
Source: By the author.

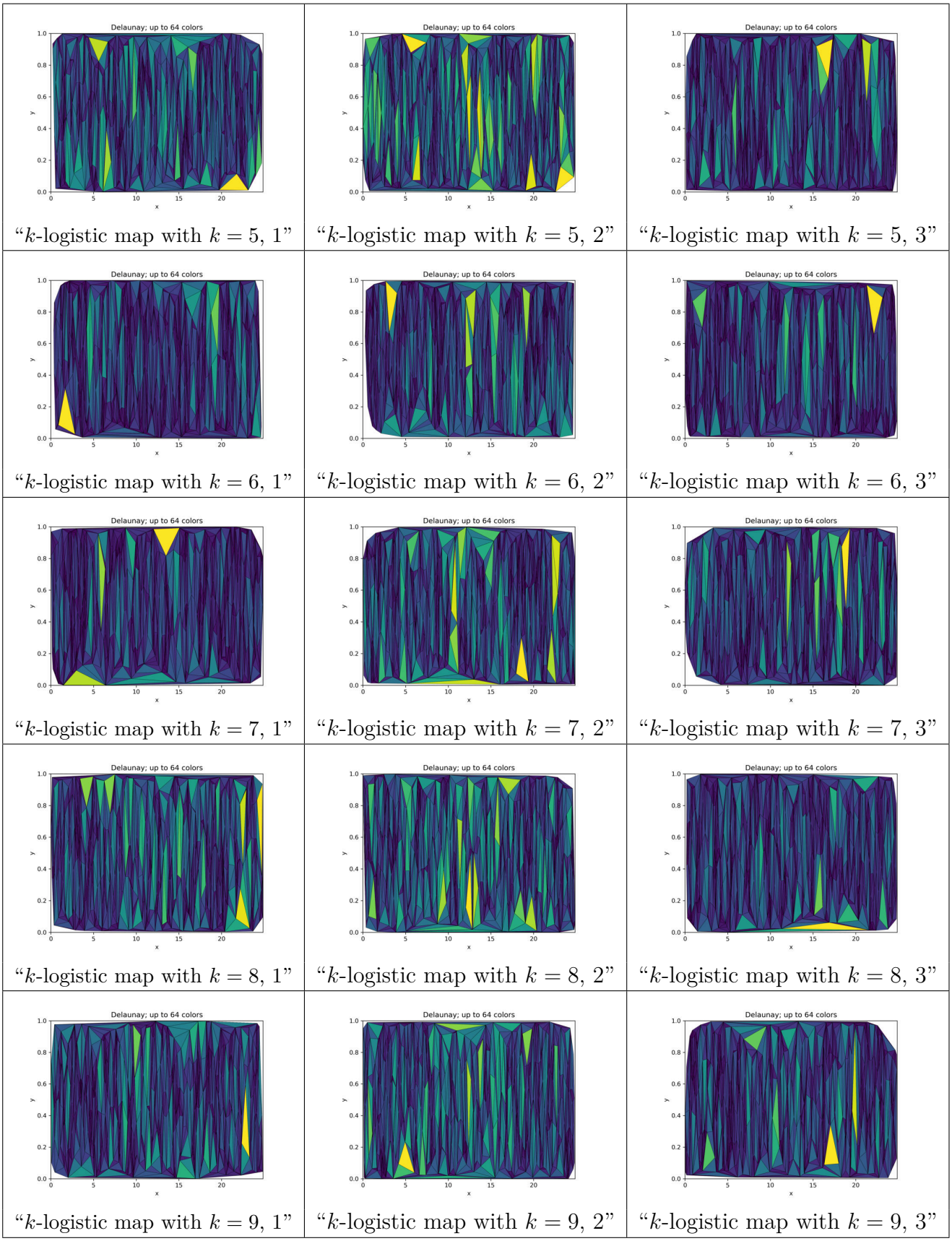

Figure 182 – Delaunay triangulations of $< -2\sigma$ complex networks for networks with 5,000 vertices, k-logistic map from $k = 5$ to $k = 9$, $r = 3.99999$.
Source: By the author.

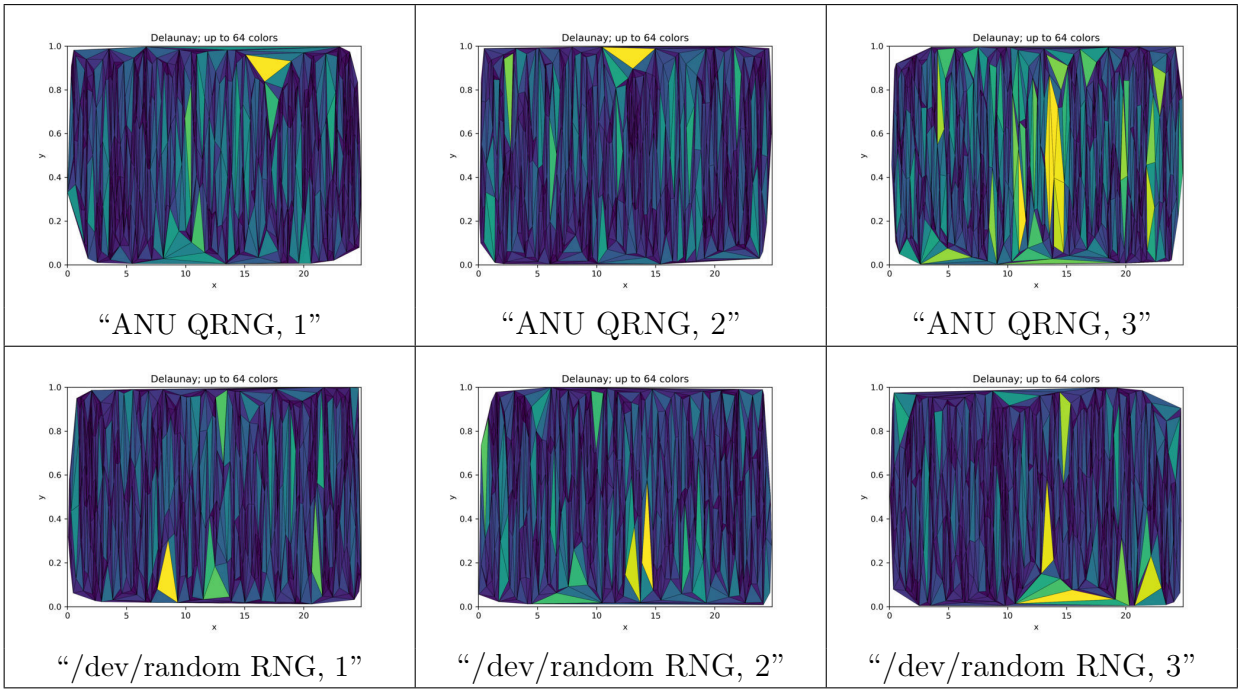

Figure 183 – Delaunay triangulations of $< -2\sigma$ complex networks for networks with 5,000 vertices. ANU Quantum and Linux /dev/random RNGs.
Source: By the author.

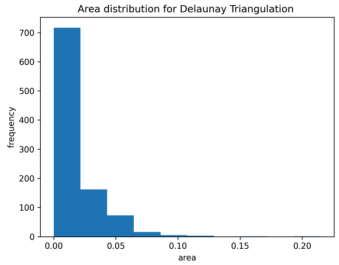

“k-logistic map with $k = 0$, 1”

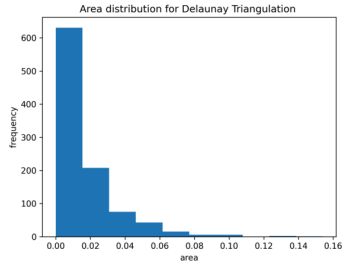

“k-logistic map with $k = 0$, 2”

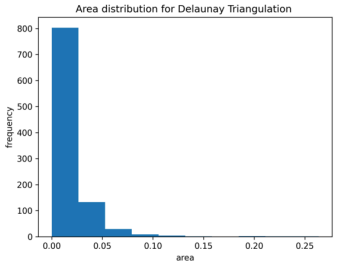

“k-logistic map with $k = 0$, 3”

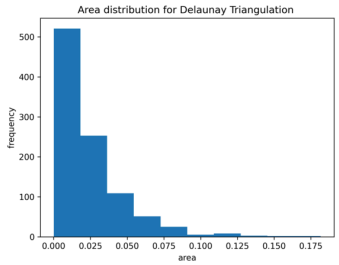

“k-logistic map with $k = 1$, 1”

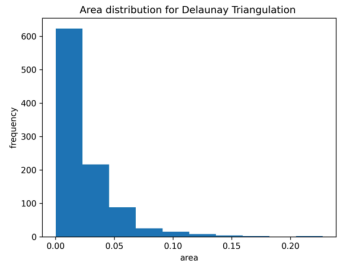

“k-logistic map with $k = 1$, 2”

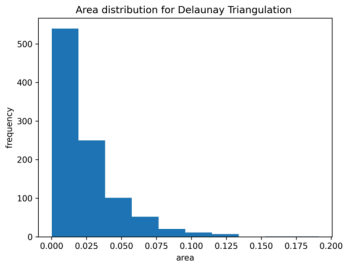

“k-logistic map with $k = 1$, 3”

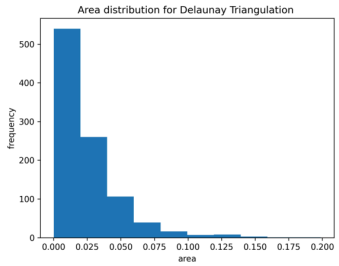

“k-logistic map with $k = 2$, 1”

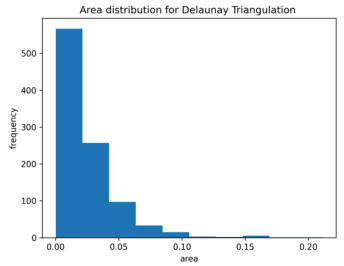

“k-logistic map with $k = 2$, 2”

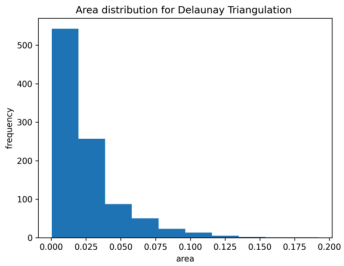

“k-logistic map with $k = 2$, 3”

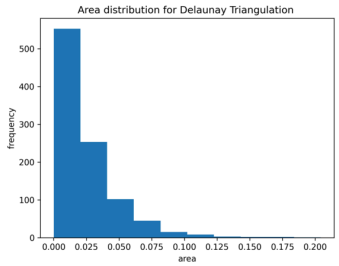

“k-logistic map with $k = 3$, 1”

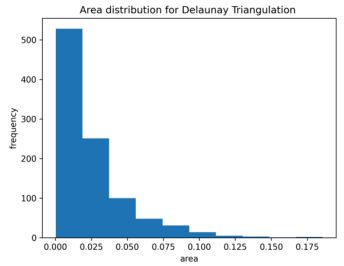

“k-logistic map with $k = 3$, 2”

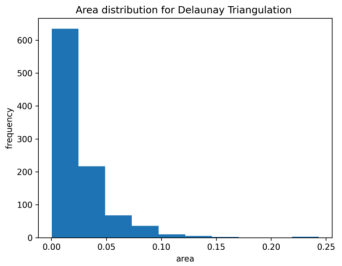

“k-logistic map with $k = 3$, 3”

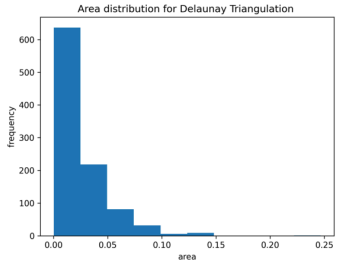

“k-logistic map with $k = 4$, 1”

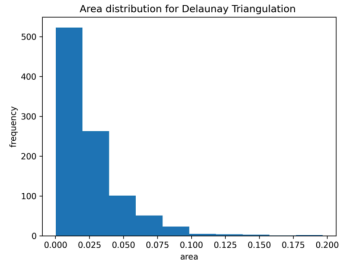

“k-logistic map with $k = 4$, 2”

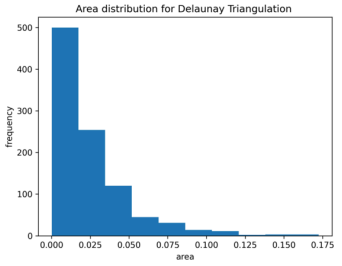

“k-logistic map with $k = 4$, 3”

Figure 184 – Histograms for Delaunay triangulations of $< -2\sigma$ complex networks for networks with 5,000 vertices, k-logistic map from $k = 0$ to $k = 4$, $r = 3.7$. Source: By the author.

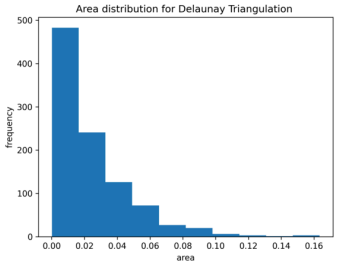

“k-logistic map with $k = 5$, 1”

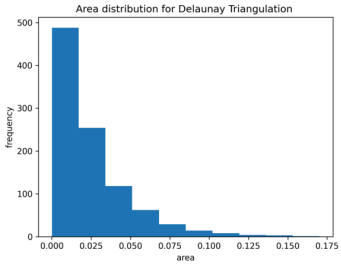

“k-logistic map with $k = 5$, 2”

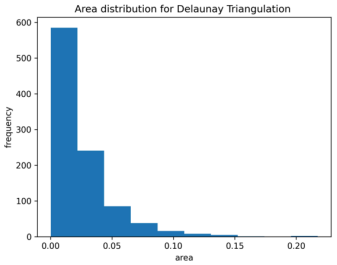

“k-logistic map with $k = 5$, 3”

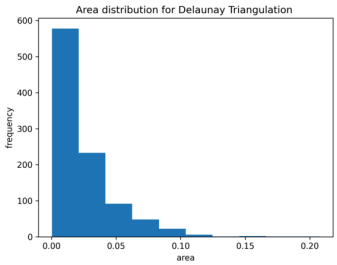

“k-logistic map with $k = 6$, 1”

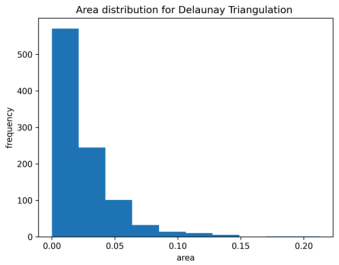

“k-logistic map with $k = 6$, 2”

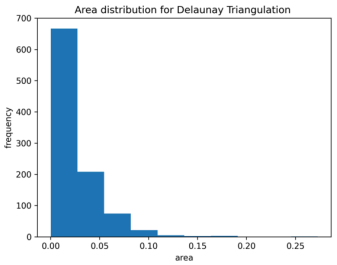

“k-logistic map with $k = 6$, 3”

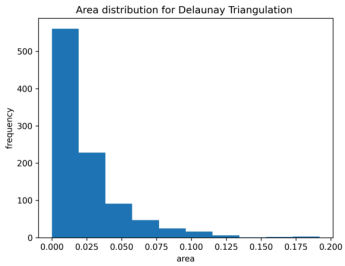

“k-logistic map with $k = 7$, 1”

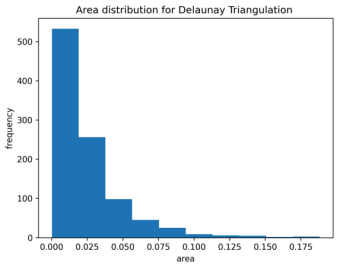

“k-logistic map with $k = 7$, 2”

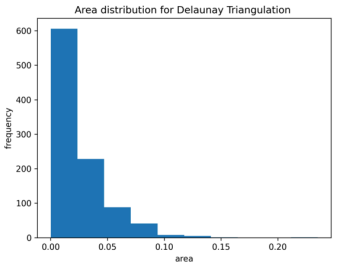

“k-logistic map with $k = 7$, 3”

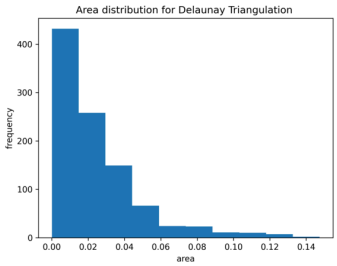

“k-logistic map with $k = 8$, 1”

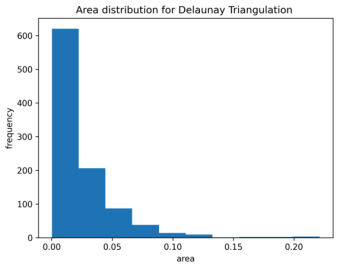

“k-logistic map with $k = 8$, 2”

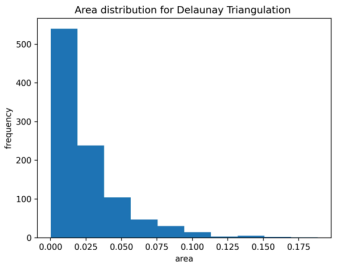

“k-logistic map with $k = 8$, 3”

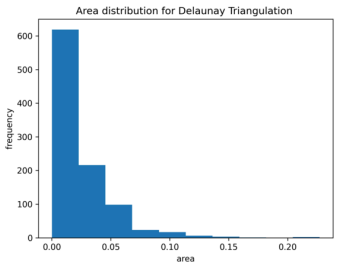

“k-logistic map with $k = 9$, 1”

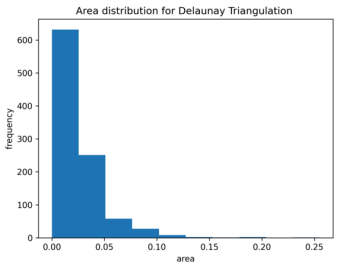

“k-logistic map with $k = 9$, 2”

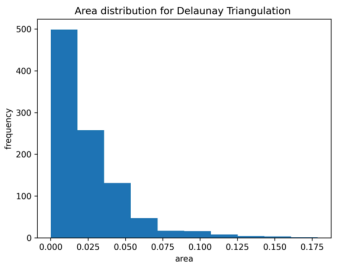

“k-logistic map with $k = 9$, 3”

Figure 185 – Histograms for Delaunay triangulations of $< -2\sigma$ complex networks for networks with 5,000 vertices, k-logistic map from $k = 5$ to $k = 9$, $r = 3.7$. Source: By the author.

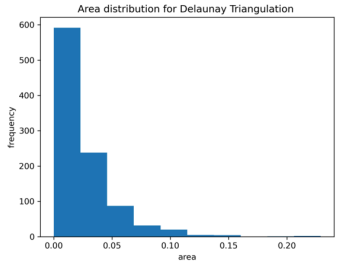

“k-logistic map with $k = 0$, 1”

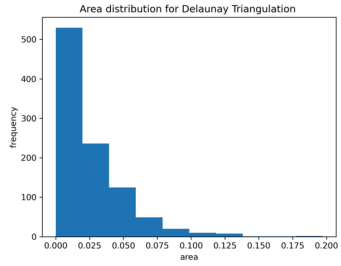

“k-logistic map with $k = 0$, 2”

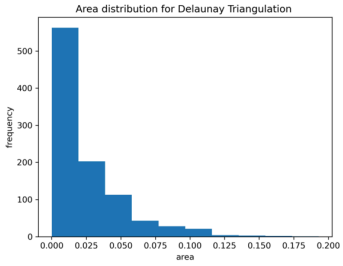

“k-logistic map with $k = 0$, 3”

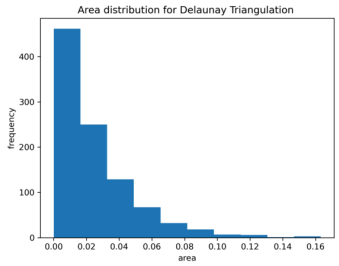

“k-logistic map with $k = 1$, 1”

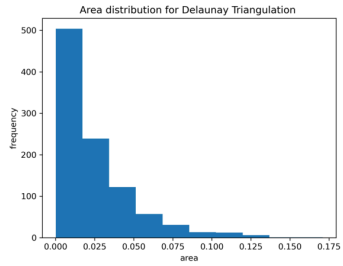

“k-logistic map with $k = 1$, 2”

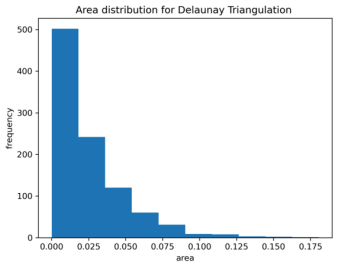

“k-logistic map with $k = 1$, 3”

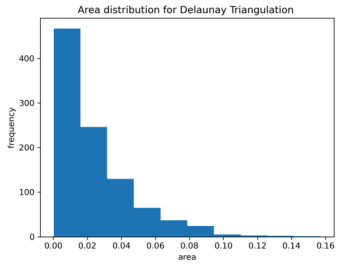

“k-logistic map with $k = 2$, 1”

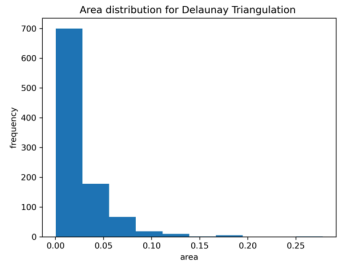

“k-logistic map with $k = 2$, 2”

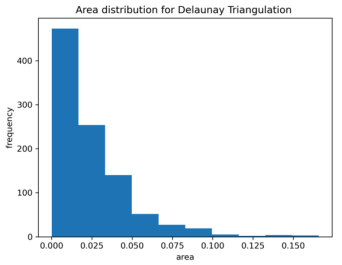

“k-logistic map with $k = 2$, 3”

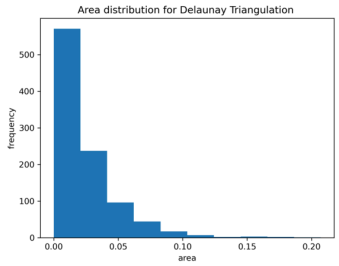

“k-logistic map with $k = 3$, 1”

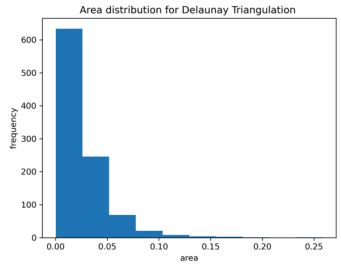

“k-logistic map with $k = 3$, 2”

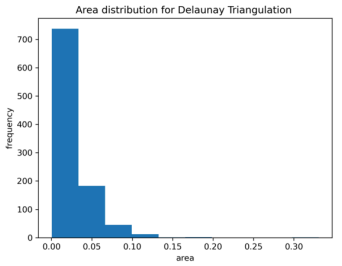

“k-logistic map with $k = 3$, 3”

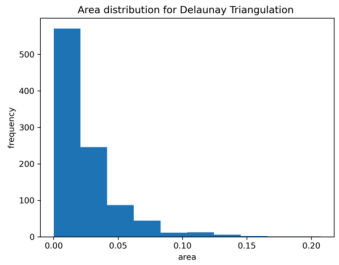

“k-logistic map with $k = 4$, 1”

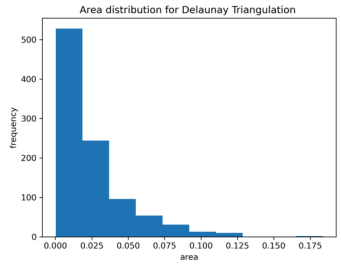

“k-logistic map with $k = 4$, 2”

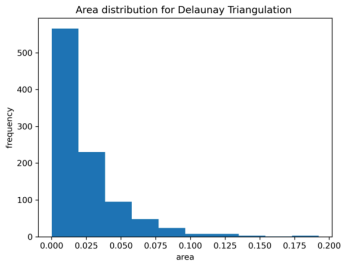

“k-logistic map with $k = 4$, 3”

Figure 186 – Histograms for Delaunay triangulations of $< -2\sigma$ complex networks for networks with 5,000 vertices, k-logistic map from $k = 0$ to $k = 4$, $r = 3.99999$.
Source: By the author.

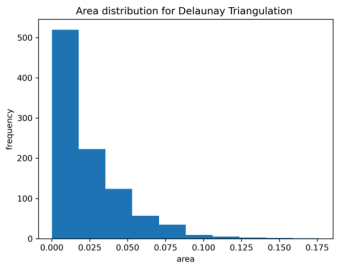

“k-logistic map with $k = 5$, 1”

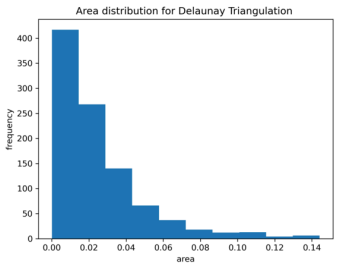

“k-logistic map with $k = 5$, 2”

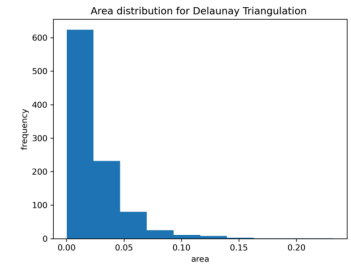

“k-logistic map with $k = 5$, 3”

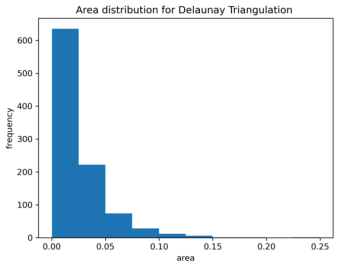

“k-logistic map with $k = 6$, 1”

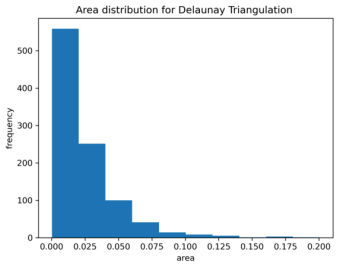

“k-logistic map with $k = 6$, 2”

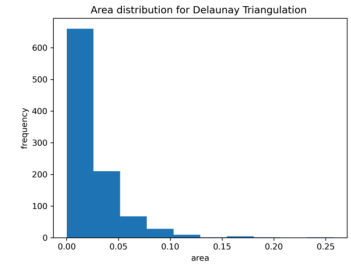

“k-logistic map with $k = 6$, 3”

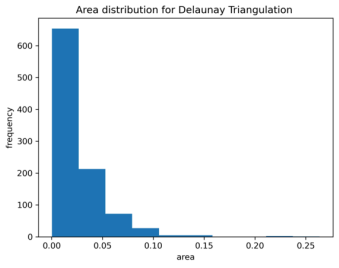

“k-logistic map with $k = 7$, 1”

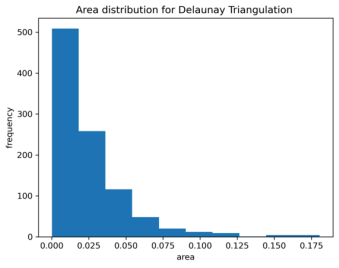

“k-logistic map with $k = 7$, 2”

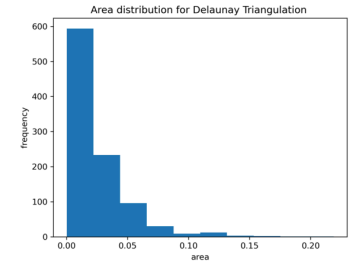

“k-logistic map with $k = 7$, 3”

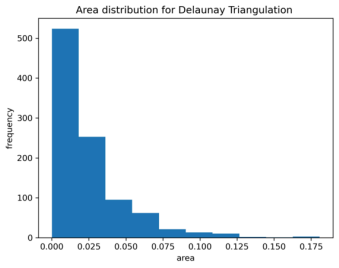

“k-logistic map with $k = 8$, 1”

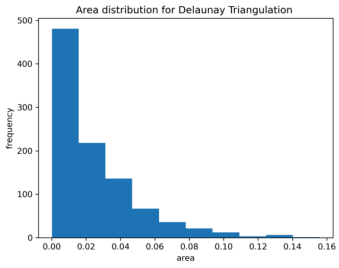

“k-logistic map with $k = 8$, 2”

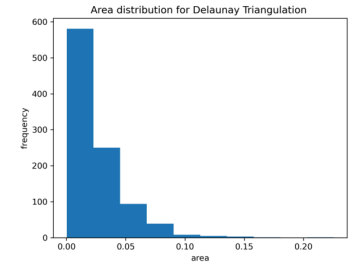

“k-logistic map with $k = 8$, 3”

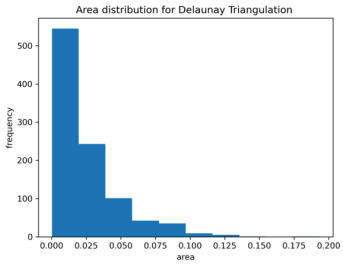

“k-logistic map with $k = 9$, 1”

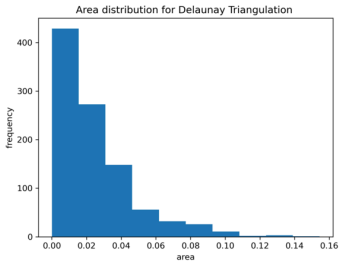

“k-logistic map with $k = 9$, 2”

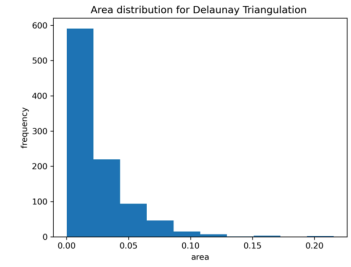

“k-logistic map with $k = 9$, 3”

Figure 187 – Histograms for Delaunay triangulations of $< -2\sigma$ complex networks for networks with 5,000 vertices, k-logistic map from $k = 5$ to $k = 9$, $r = 3.99999$.
Source: By the author.

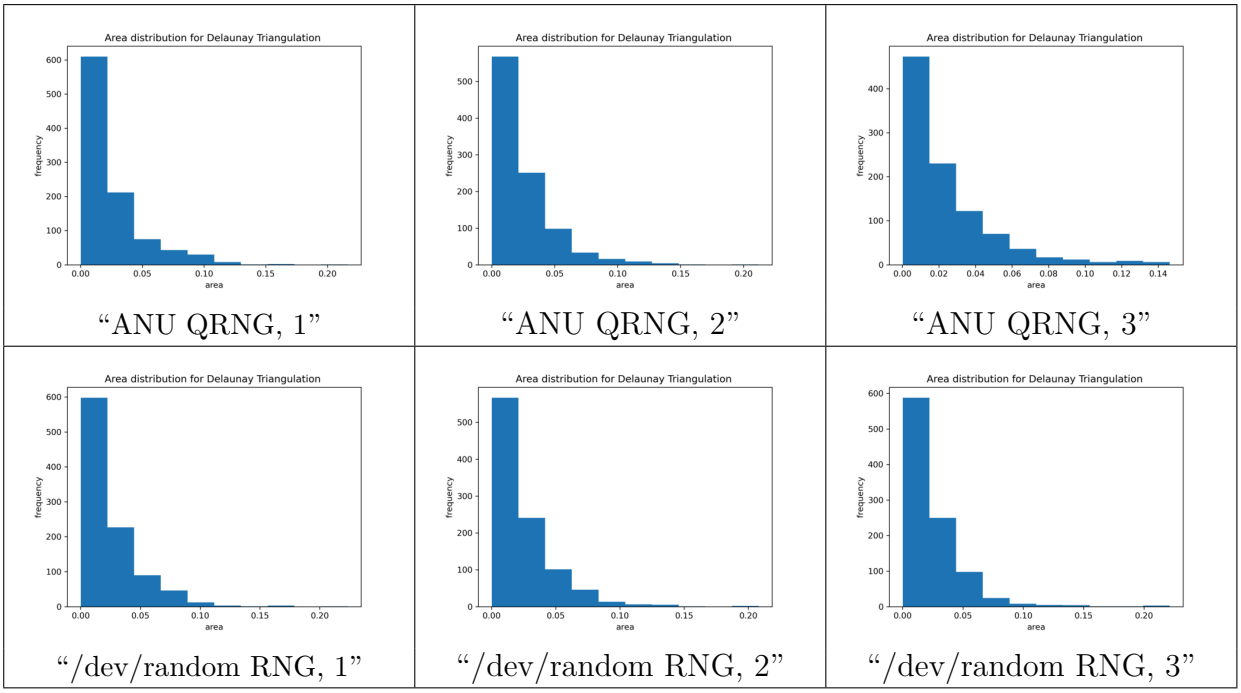

Figure 188 – Histograms for Delaunay triangulations of $< -2\sigma$ complex networks for networks with 5,000 vertices. ANU Quantum and Linux /dev/random RNGs. Source: By the author.